DEFORMATION MECHANICS AND MICROSTRUCTURE EVOLUTION DURING MICROFORMING OF METALS

by

Marzyeh Moradi

B.S. in Material Science and Engineering, University of Tehran, 2003

M.S. in Material Science and Engineering, University of Tehran, 2008

M. S. in Industrial Engineering, University of Pittsburgh, 2013

Submitted to the Graduate Faculty of

Swanson School of Engineering in partial fulfillment

of the requirements for the degree of

Doctor of Philosophy

University of Pittsburgh

2015

UNIVERSITY OF PITTSBURGH

SWANSON SCHOOL OF ENGINEERING

This dissertation was presented

by

Marzyeh Moradi

It was defended on

August 26, 2015

and approved by

Bopaya Bidanda, Ph.D., Ernest E. Roth Professor

Department of Industrial Engineering, University of Pittsburgh

Ian Nettleship, Ph.D., Associate Professor

Department of Mechanical Engineering and Material Science, University of Pittsburgh

Markus Chmielus, Ph.D., Assistant Professor

Department of Mechanical Engineering and Material Science, University of Pittsburgh

Dissertation Director: M. Ravi Shankar, Ph.D., Associate Professor

Department of Industrial Engineering, University of Pittsburgh

Dissertation Co-director: Jörg M.K. Wiezorek, Ph.D., Professor

Department of Mechanical Engineering and Material Science, University of Pittsburgh

DEFORMATION MECHANICS AND MICROSTRUCTURE EVOLUTION DURING MICROFORMING OF METALS

Marzyeh Moradi, Ph.D.

University of Pittsburgh, 2015

Deformation mechanics including dynamic strain, strain-rate and rotation of material elements and its spatio-temporal scaling behavior was studied using *in situ* characterization of *prototypical microforming operations*- Equal Channel Angular Pressing (ECAP), Indirect Extrusion (IE) and Deep Drawing (DD) across length scales (sub-millimeter and micron). Microforming devices including ECAP, IE and DD dies in plane strain condition were designed and fabricated to manifest process outcomes/anomalies in small length-scale deformations for a range of imposed strains: severe (ECAP), moderate (IE) and low (DD). This was captured by conducting *in situ* experiments on commercially pure metals: Ni 200, Oxygen Free High Conductivity (OFHC) Cu, Al 1100 and Pb.

Set up microforming stages capable of in-situ observation in various length scales were implemented to employ Digital Image Correlation (DIC) technique in order to quantify the mechanics of deformation particularly in deformation zone where the temperature filed captured by *in situ* Infra-Red (IR) thermography completed the detailed understanding of thermomechanical phenomena prevail in microforming operations. To do this, ECAP and IE devices were designed with a transparent viewing window made of Sapphire block enables the imaging of the material flow during deformation using high-speed (CCD) and IR cameras. While DD of metallic sheets was performed in a microforming setup that sits inside the chamber of

Scanning Electron Microscope (SEM) enables *in situ* characterization of material flow behavior using SEM based DIC. Pre and post–Mortem Microstructure analysis was carried out by performing Orientation Imaging Microscopy (OIM) across the microformed machine elements aiming to correlate spatially evolved microstructures/textures across the deformation zone with the mechanics of deformation obtained by *in situ* observations for the given materials system. In microforming, variables such as initial microstructure, process configuration and tooling design along with the deformation process parameters are known as crucial factors that determine the deformation behavior of material and therefore the process consequences including failure characteristics and quality of microparts surface finish. In the present dissertation, the effect of process parameters and scaling was studied and the role of characteristics of prior microstructures such as grain size and its distribution, grain morphology, twin size and density, pre-existing textures, etc. and their contribution in improving or disproving the formability was delineated for different deformation geometries and material systems.

These studies revealed the strong dependence of the morphology and characteristics of plastic deformation zone (PDZ) to the process outcomes e.g. microstructure evolution, surface roughening, sudden failure, etc. which are the results of the mechanical/microscopical responses of material to the geometric confinements and strain gradients. The systematic studies of the effect of microscopic/macroscopic boundary conditions allows to determine the presence of any spatial confinement switchover in the mechanism of microscopic material response that will be eventually appeared in the quality of micro-machined components.

Keywords: Microforming, Mechanics of deformation, *In situ* characterization, DIC, Microstructure engineering.

TABLE OF CONTENTS

LIST OF TABLES

LIST OF FIGURES

PREFACE

To my Mother and Father!

1.0 INTRODUCTION

Metal forming operations rely on the constant geometric and tribological boundary conditions to achieve the desired process and product outcomes. Often, these processes feature heterogeneous deformation zone geometries within which microstructures evolve as a function of strain, strain-rate and temperature. The microstructure of the fabricated component controls its structural and functional performance. Empirical (e.g. using Digital Image Correlation (DIC)(S. Basu & M. R. Shankar, 2014a)), analytical (e.g. using Slip Line Fields (SLF)(Chakrabarty, 2012)) and numerical (e.g. using Finite Element Methods (FEM)(Yen, Jain, & Altan, 2004)) techniques exist for characterizing deformation zone geometries.

While the geometry of deformation zone and its heterogeneity is influenced by complexity of deformation boundary conditions in typical large length-scale manufacturing operations, further complexities can emerge when the scale of deformation shrinks(M. Geiger, M. Kleiner, R. Eckstein, N. Tiesler, & U. Engel, 2001). A straightforward scale down of machine tools/process in order to achieve this is generally not possible owing to nonlinear changes in the material behavior at small length-scales. For example, when the forming processes are miniaturized to the sub-mm/micron scale wherein the size of the deformation zone is comparable to the scale of the microstructure, unexpected process anomalies and failures are observed(Fu & Chan, 2013). Analogues microstructural anomalies are observed in machining-based processes when material removal occurs at the micrometer-scales(S. Basu & M. R. Shankar, 2014b).

Unfortunately, there is a lack of a direct observation of the mechanics of forming processes with decreasing length-scales and a delineation of the resulting microstructural evolution. The interaction of the mechanics and the microstructure will underpin the process outcomes.

There has been a considerable effort directed to the design of cold forming based operation for creating mm and sub (mm) – scale components(Fu & Chan, 2011; H. J. Lee, Lee, Lee, Lee, & Kim, 2006). These approaches are collectively referred to as microforming. Prior work has noted various sources of process failures and anomalies that are tractable to the interaction of the mechanics, microstructure and the tribological boundary conditions(Engel & Eckstein, 2002; Fu & Chan, 2013). However, the underlying sources of the process anomalies remain unexplored due to the lack of direct insight into the scaling of the mechanics across length-scales, the trajectories of microstructural evolution as a function of the process parameters. Doing so, will help refine computational models and motivate new microstructure-based models.

The focus if this thesis is predominantly to delineate the micromechanics of deformation and the resulting microstructure evolution during imposing different levels of strain in small sized machine elements by varying the extrinsic (e.g. volumetric, geometric, deformation rate, etc.) and intrinsic (e.g. initial microstructure features such as grain size, texture, grain boundary characteristics, etc.) parameters using three different microforming devices: ECAP, indirect extrusion and deep drawing. These are efficient and commercially viable routes for industrial scale manufacture of wide variety of metallic machine elements(Fu & Chan, 2013; W.F. Hosford & Caddell, 2011). Miniaturized processing using these methods is useful to fabricate a range of semi and final products such as micro pins, micro screws, micro gears, micro bolts, etc. (Engel & Eckstein, 2002; F. Vollertsen, Niehoff, & Hu, 2006). Different metallic materials systems were

used in this study for performing experiment. Commercially-Pure Lead (Pb) and Aluminum (Al 1100) were used as prototypical non-work/work hardening materials and Ni 200 and Oxygen Free High Conductivity (OFHC) Cu as three different industry relevant polycrystalline metals.

In situ imaging in combination with cross-correlation-based analysis can resolve salient features of the deformation zone such as strain, strain-rate and rotation fields(S. Basu & M. R. Shankar, 2014b; Moradi, Basu, & Shankar, 2015). Following *in situ* characterization of the mechanics as a function of the geometry and length-scale, effect of initial microstructure on mechanical behavior and microstructure evolution was investigated. Additionally, *in situ* IR thermography was performed to find the temperature fields during microforming and correlate to microstructure responses. Subsequently, simulation of texture evolution in deformed products was performed for some condition in indirect extrusion using a Visco-Plastic Self-Consistent (VPSC) model(Wang, Wu, Tomé, & Huang, 2010) coupled with *in situ* characterization and results were verified by results found in Orientation Image Microscopy (OIM) observations. The resulting process-structure mappings offer a framework for controlling and enhancing process outcomes in forming-based processes across length scales.

The context of present thesis is organized in six primary sections. First section provides an overview on the microforming literature and crystal plasticity theories. Second section is about identifying the major challenges/obstacles in microforming and discusses investigation necessities of mechanics of deformation in microforming scenarios by providing process-performance-response linkages. In this section, the main objective/global research hypothesis is explained. Next three sections describe the three different microforming devices utilized in present work. The details of specific research hypothesis/plan and methodologies are explained individually for each device and later on the results/observations will be presented and discussed

followed by concluding remarks. This will give primary insights into the micromechanics of deformation that offer strategies for microstructure control, process optimization and miniaturization of metallic components. In the last chapter, conclusions and potential future works from this study are outlined.

2.0 LITERATURE REVIEW

Deformation of material with the dimensions in sub-millimeter scale is called microforming. Microforming is a promising method to fabricate miniaturized products that become a critical requirement in recent years for various sectors of industry (M Geiger, M Kleiner, R Eckstein, N Tiesler, & U Engel, 2001). Technological skills in design and tooling of microforming were well established and a comprehensive knowledge about size effect (extrinsic and intrinsic material length-scale) was provided (Greer & De Hosson, 2011).

However, there is glaring lack of understanding of physical phenomena and mechanisms underpinning microstructural impacts on material behavior during microforming. In deformation of microparts, simplify assumptions of isotropy breakdowns and comprehensive macroforming knowledge of microstructural design is no longer valid. Indeed, interactive effects between workpiece size and parameters of microstructure in response to the macroscopic deformation boundary conditions determine performance of microforming and quality of microparts.

This chapter aims at reviewing principals of plasticity in materials and then discussing the size effect-related deformation behaviors followed by presenting some of the state-of-the-art microforming processes related to the objectives of the present thesis.

2.1 OVERVIEW ON CRYSTAL PLASTICITY

Permanent plastic deformation in crystalline solid structures involves the relative sliding of atomic planes through the motion of linear crystal defects-dislocations (Rice, 1971). At microscopic level, dislocation motion involves rupture and deformation of inter-atomic bonds that makes plastic deformation easier at smaller stresses than the theoretical stress required to deform perfect crystals (Barrett & Massalski, 1966). Direction of motion of dislocations depends on the type of dislocation-edge and screw- where edge dislocations move by slip and climb introducing compressive, tensile, and shear strains while screw dislocations move by slip and cross-slip introducing only shear strain. There is a strain field around dislocations causes interaction between them in the form of repletion (same sign or direction of burgers vector) and attraction/annihilation (opposite sign). Interaction between dislocations results in formation of sharp breaks in dislocation line that creates hindrance toward the their easy motion (Barrett & Massalski, 1966). Dislocation density is defined as the number of dislocations in a material or in fact the total dislocation length per unit volume or the number of dislocations intersecting a unit area. By imposing of strain, the number of dislocations in material increases progressively during plastic deformation. Dislocations generate from existing dislocations, grain boundaries and surfaces. Dislocation densities can vary from ~10^{13} m^{-2} and 10^{14} m^{-2} for material in annealed state to ~ 10^{16} m^{-2} for heavily deformed metals (Nes, 1997).

Typically, grains deforms via slipping to maintain strain continuity where dislocations move in specific directions (slip-directions) on specific planes (slip-planes) called slip system. Generally, slip plane is the plane of highest atomic density, and the slip direction is the close packed direction within the slip plane.

Three distinct stages of deformation are identified in both single and polycrystalline materials. These three regimes are commonly called Stage I, Stage II and Stage III hardening (Nes, 1997). Stage I refers to the onset of plastic deformation in single crystals and is accommodated by dislocations flowing on only one activated slip system. Multiple slip systems are activated in stage II of plastic deformation and linear strain hardening is observed. In stage III, cross-slip happens and dislocation cells are formed. Stage I hardening governs by crystallographic orientation of the crystal; stage II hardening is inherently temperature independent and is it is also insensitive to strain-rate, its value is almost constant in the range of G/200−G/100 (where G is the shear modulus); and stage III is very sensitive to temperature and strain-rate.

Generally, three approaches are perused in plasticity theory towards finding stress and strain states of material during plastic deformation (William F Hosford & Caddell, 1993). One widely used in continuum mechanics is yield criterion, which predicts stress states and their resulting strains disregarding deformation mechanisms.

Second approach focuses on the crystallographic mechanisms of deformation such as slip and twining. It explains anisotropic behavior of material and it dependency to the crystallographic texture. Since then, many efforts were put to connect these two approaches and relate plastic yield to resolved shear stress required for slip in different slip systems which it was firstly suggested by Schmid (Schmid & Boas). This is known as Schmid law that states minimum shear stress required to initiate slip (critical resolved shear stress), which is independent of the orientation of the tensile axis.

Third approach is based on the dislocation theory and how dislocations contribute in slip and twining. Since the predicted critical stress showed several order of the magnitude higher than

experimental stress required for shear, dislocation based theory explain the discrepancy through introducing mechanisms e.g. dislocation climb and cross slip to overcome obstacles and facilitate their motion.

In Schmid law, single crystal deforms when a critical shear stress is reached in a slip system. Using this criterion, Sachs (Sachs, 1928) assumed that all the grains are deformed by single slip neglecting the strain compatibility at grain boundaries. Taylor and Bishop-Hill (Bishop & Hill, 1951; Geoffrey Ingram Taylor, 1938) introduce an upper bound model for polycrystalline deformation, whereby all the grains are subjected to the same strain while in the lower-bound models, e.g. Sachs grains are subjected to the same stress. Taylor suggested that a minimum five independent slip system is required to accommodate deformation. He also introduced grain orientation factor, which is called Taylor factor (M). This factor relates macroscopic tension stress to shear stress and was predicted to have a value of 3.06 for random FCC polycrystalline material. This is in contrast to the value found by Sachs as 2.24. Kocks (Kocks, Kallend, Wenk, Rollett, & Wright, 1995) proposed that less than five slip systems can be activated in order to maintain strain continuity and slips may not necessary pass through the whole grain. Followed by this idea, Leffers (Mughrabi et al., 1981) suggested that when the slip planes reaches the grain boundary that acts like an obstacle, stress starts building up which will eventually get relaxed by the activation of second slip in the neighboring grains. All the aforementioned models are illustrated in Figure 1.

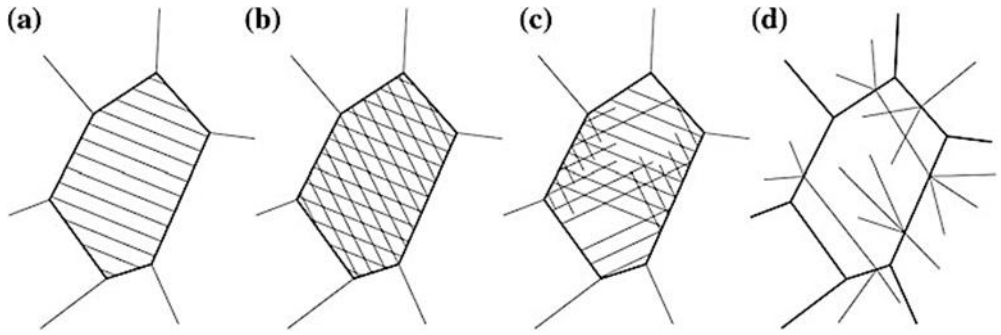

Figure 1: Activation slip systems in polycrystalline materials modeled by: (a) Sachs, (b) Taylor, (c) Kocks and (d) Leffers(M. W. Fu & W. L. Chan, 2014).

Self-consistent scheme introduced by (Kroner, 1978) that considers grains as inclusions embedded in homogeneous matrix. They have shown that the stress and strain state is uniform within the inclusion if it has an ellipsoidal shape. In the self-consistent models the interaction between the grains and the pseudo polycrystalline is incorporated in the model, but the direct grain-to-grain interaction is not taken into account. It uses a fully elastic coupling between the grains and the matrix, and therefore it predicts very low deformation heterogeneity in the polycrystalline. The self-consistent modeling scheme proposed by of (Hill, 1965; Hutchinson, 1976) introduces the elastic-plastic coupling between the grains and the matrix, which predicts more realistic deformation heterogeneity in the polycrystalline.

Strain gradient plasticity models (N. Fleck & J. Hutchinson, 1997) suggest that in addition to the strain, plastic flow of materials depends also on the strain gradient. Therefore, geometrically necessary dislocations (GND) from plastic deformation gradients are also added to the total generated dislocations during deformation. This is used to predict the size-dependent response of material in the presence of macroscopic strain gradients during deformation, which is

highly dependent on the geometry of deformation. Unlike statistically stored dislocations (SSD), GNDs are stored in the crystal when it is subjected to a gradient of plastic strain due to the either geometry of the deformation or material itself. Presence of the non-deformed second phases or hard particles in the microstructure results in strain gradient in the matrix surrounded them. Generally, strain gradient are inversely proportional to the length-scale over which plastic deformation occurs. Therefore, strain gradient becomes important when the material length-scale decreases as what is observed in microforming.

2.2 TEXTURE AND ANISOTROPY

In a polycrystalline material, the crystallographic axes of the grains can be oriented randomly with respect to each other, or they can be oriented so that there is a non-random distribution. If there is a preferred orientation, then we say that the material has crystallographic texture (Bunge, 1979; Mathur & Dawson, 1989). Crystallographic texture determines the degree of the anisotropic behavior of material where the physical or mechanical properties of material are different along the different axes. An aggregate with randomly distributed orientations has isotropic properties. Texture analysis is a statistical methodology for analyzing the distribution of crystallographic orientation in polycrystalline materials. The Orientation Distribution (OD), which is a central concept in texture analysis and anisotropy, is represented in the form Pole Figure (PF) or Orientation Distribution Function (ODF) plots (Bunge, 1979). Each point in the orientation distribution represents a single specific orientation or texture component. OD can be used to determine presence/absence of components and their volume fractions and predict anisotropic properties of polycrystalline materials. ODs can be defined mathematically in any space appropriate to continuous description of rotations (Euler angles, axis-angle, etc.).

The Euler angle space is generally used because the series expansion representation depends on the generalized spherical harmonics (Wenk, 2002). Pole Figure (PF) is 2D representation of orientation distribution in which a specified crystallographic axis (or pole) from each of a representative number of crystallites is plotted in a stereographic projection, along with directions relevant to the material's processing history. Orientation Distribution Function (ODF) is a mathematical function describes the (continuous) orientation density. Normalized probability distribution typically denoted by "*f*" in Euler space is used to parameterize orientation. Typically 3 Euler angles are used and OD is written as $f(\varphi_1, \Phi, \varphi_2)$. The OD is closely related to the frequency of occurrence of any given texture component, which means that $f \geq 0$. For a random orientation g, f (g) denotes the volume fraction of that orientation within a certain region of orientation space. It is usually represented as intensity lines of 2D sections of Euler space.

2.3 SIZE EFFECT IN SMALL LENGTH-SCALE DEFORMATION

Size effect generally refers to interactive effects consequences arise from the interaction between workpiece size and microstructure parameters in response to the loading and deformation boundary conditions (M Geiger et al., 2001). Results of the many studies conducted to understand size effect on flow behavior of material show a significant changes in flow stress by varying the specimen size and grain size. They have shown that flow stress of material decreases with the reduction of specimen size and the increase of grain size (Figure 2a, b) (Ming Wang Fu & Wai Lun Chan, 2014). However, this effect is strongly dependent on the range of the dimension of the specimen that undergoes deformation. Results of uniaxial deformation experiments on metallic test specimens with dimension in the order of micron and sub-micron unambiguously demonstrate higher yield and ultimate tensile strength sometimes very close to

the theoretical strength of material, which proves the new-known statement “smaller is stronger” (Figure 2c) (Greer & De Hosson, 2011). Therefore, unknown nature of size effect-related phenomena affected by both intrinsic (i.e. microstructural) and extrinsic (i.e. sample size) dimensions have a critical role in material deformation response and mechanical properties of material during deformation.

It can therefore be concluded that there is a threshold in test specimen dimension below which strengthening behavior of material undergoes a significant changes and flow stress drastically increases. It is believed that the effects due to the deformation volume and strain gradient are more prominent for such length-scales.

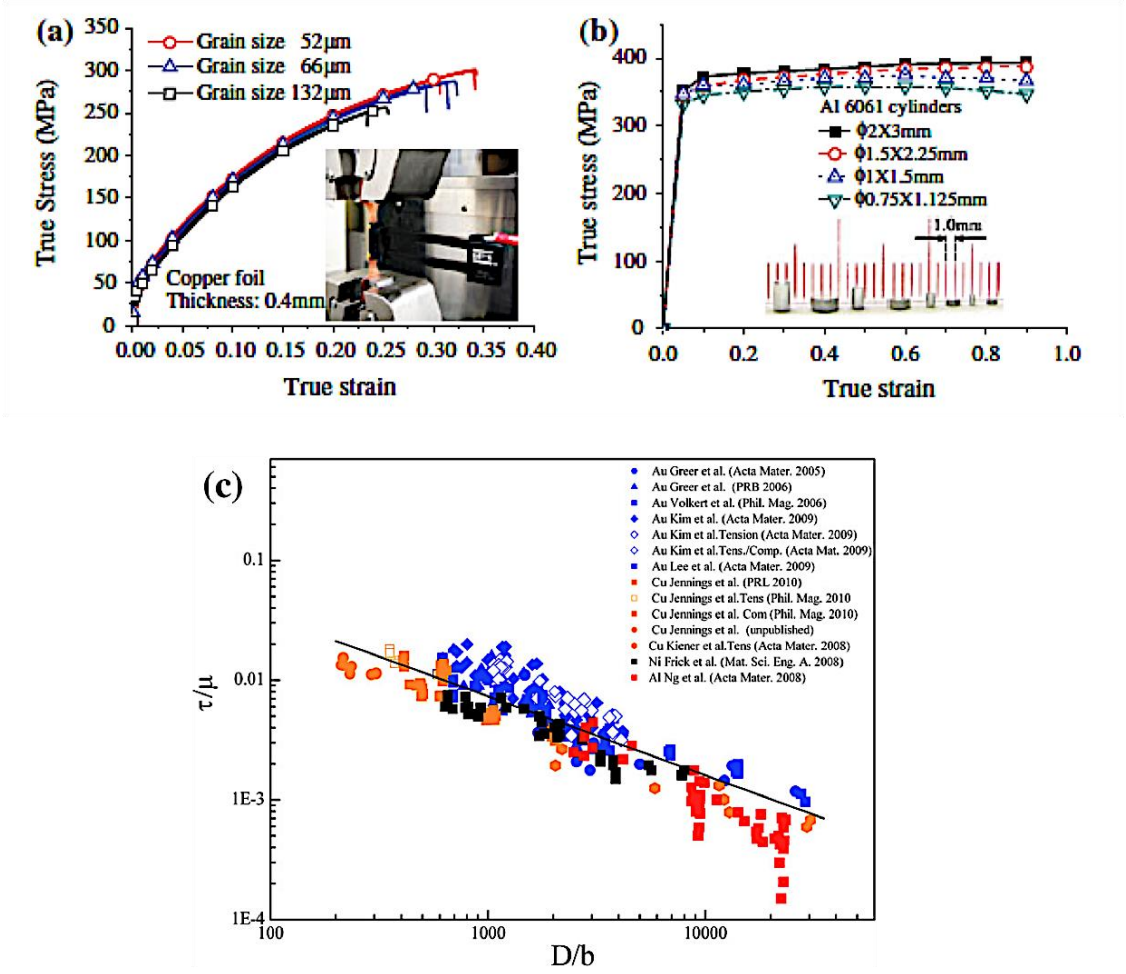

Figure 2: Grain and specimen size effects on flow stress in (a) tensile and (b) compression tests. (c) Shear flow stress normalized by shear modulus FCC metallic micro- and nano-pillars tested in compression and tension (Ming Wang Fu & Wai Lun Chan, 2014; Greer & De Hosson, 2011; Tiesler & Engel, 2000).

Another issue regarding to the size effect is fracture behavior of metallic components. Ductile mode of fracture has been observed in microforming as a result of strain localization. Hence, controlling the amount and uniformity of deformation in each forming operation is

critical to avoid fracture, which is strongly dependent on the geometry of the deformation and ratio of the sample size to grain size (Tiesler & Engel, 2000).

Controlling the dimensional accuracy in microproducts is another challenging issue. One important factor that affects the geometrical accuracy of microproducts in the form of thin sheets and foils is springback (Gau, Principe, & Yu, 2007). This behavior arises from elastic recovery after deformation. It is revealed that springback increases significantly with the decreasing ratio of specimen thickness to grain size. Surface roughening in microforming also affects the geometrical accuracy and quality of micro-formed parts (Manabe, Shimizu, Koyama, Yang, & Ito, 2008). In fact, roughening on the surface is created because of the deformation interaction among surface grains that strongly dependent on the orientations. Surface roughness is attributed to the heterogeneity of deformation that arises from orientation of individual grains and local texture (Kanjarla, Van Houtte, & Delannay, 2010).

2.4 MICROFORMING PROCESSES

Several microforming processes have been developed for forming bulk and sheet metal parts in small length-scale. Micro-deep drawing (Gong, Guo, Wang, & Shan, 2010; Frank Vollertsen & Hu, 2010) and microextrusion (Krishnan, Cao, & Dohda, 2007; Saotome & Iwazaki, 2001) are widely used to study microforming performance for a range of materials with various workpiece dimension and microstructure grain size. Figure 3 shows the configurations used for both aforementioned microforming processes. In microforming processes, size effect-related phenomena should be considered in order to determine process parameters and tooling design for better microforming performance.

Micro-deep drawing/micro blanking of copper sheets to form cup-shaped parts was performed in order to study the size effect and its consequences on deformation behavior and quality of the products. It was shown that the deformation load decreases with the increase of grain size. This decrease in loading force is explained based on the fact that in microparts ratio of surface area to volume of material undergoing deformation increases, so the fraction of less constraint grains (surface grains) increases. Surface grains show lower flow stress compared to the fully constraint inner grains. So the overall flow stress decreases as the fraction of surface grains increases. Additionally, the volume of grain boundaries decreases, which therefore results in decreasing flow stress based on grain boundary strengthening mechanisms. It was also reported that larger grain size lead to non-homogeneous deformation and rough surface finish in drawn cups (Chan & Fu, 2011).

Microextrusion is a commercially viable microforming process that can be widely used to produce microparts for different purposes. Size effects were also investigated for different type of microextrusion (forward, backward) in order to improve quality of microparts using this method (Chan, Fu, & Yang, 2011). It was shown that deformation load varies significantly by changing the grain size while it is not the case for backward extrusion. The non-uniform material flow was observed in the case of large grain size in microextrusion that results in irregular cup height. Some work showed that applying ultrasonic vibration in microextrusions helps reduce deformation load and enhance surface finish of the micro-formed parts.

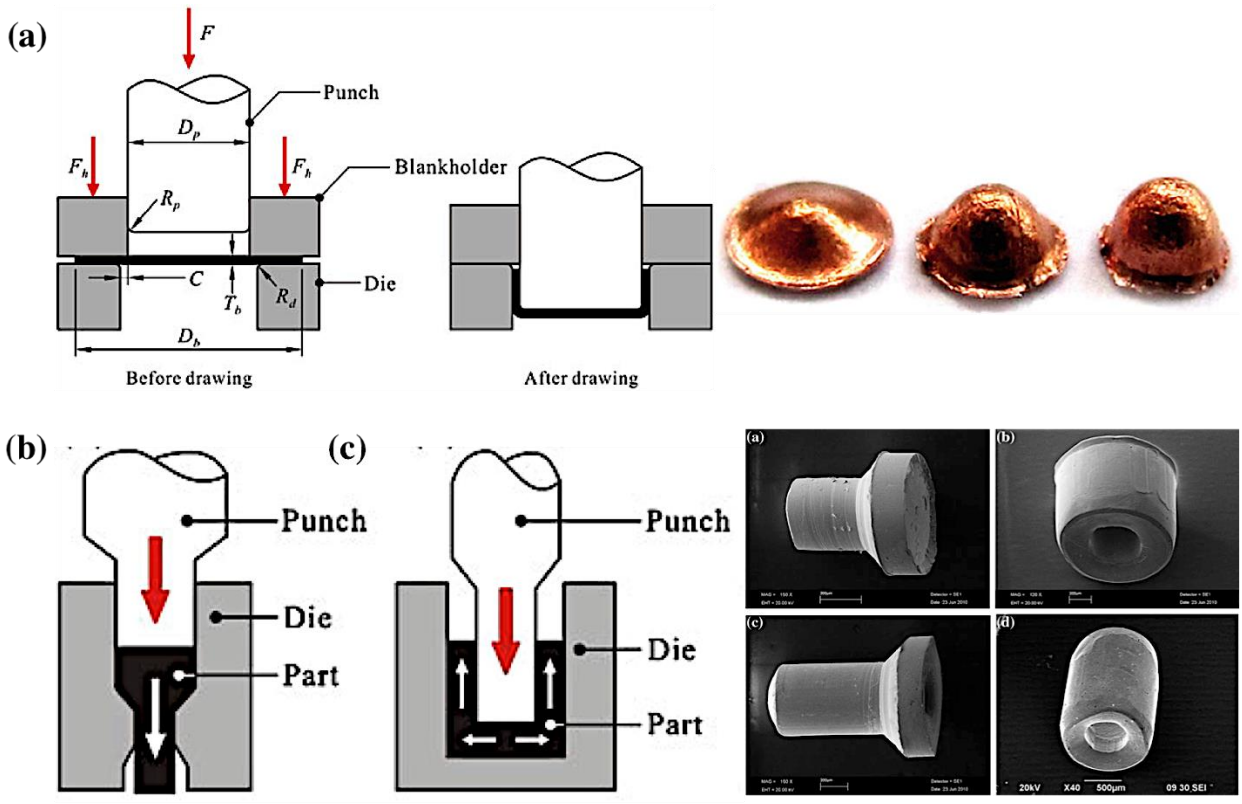

Figure 3: (a) Design parameters in micro deep drawing of a cylindrical cup, (b) schematic of microextrusion for (b) forward extrusion, (c) backward extrusion (Ming Wang Fu & Wai Lun Chan, 2014).

3.0 PROBLEM STATEMENT AND MOTIVATION

3.1 CHALLENGES AND OBSTACLES IN MICROFORMING

Although product miniaturization has a tremendous growing trend in various industrial sectors, there exist a number of technological challenges related to size effect. Generally, size effect refers to the issues arise from the effect of workpiece size/geometry of the deformation (macroscopic dimensions) and grain size/features size (microscopic dimensions). Effectively, physical principles and dimensional analysis that are legitimate in macroforming processes cannot be simply scaled down for the manufacturing of micro-parts. For instance, existing constitutive models that describe deformation behavior and mechanical response of material in large length-scale may not predict accurately the deformation behavior in small length-scales, thus basic assumptions of local homogeneity of internal forces and deformation are breakdown. It was shown that decreasing the grain size simultaneously and proportionally with scaling down the workpiece dimension reduces anomalies occur during microforming (Frank Vollertsen, 2008). But, it is still difficult to predict and control deformation behavior and avoid heterogeneity in microforming because of the complexity of the process and its unknown underlying physical mechanisms.

Another problem in miniaturization is related to the modeling of microforming processes with respect to the factors such as strain gradient that becomes significant in micrometer scale metal forming processes. Essentially, classical plasticity models such as the Taylor full

constraints model, Sachs model, Taylor relaxed model and rate sensitivity full constraints model are based on the assumptions that the dimensions of deformation zone are much larger than the material intrinsic length scales e.g. grain/sub grain size and material is subjected to deformation in either homogenous strain or stress (Roters et al., 2010). Typically, there is a significance deviation from homogeneity in microforming that promotes strain localization and accelerates onset of failure due to the formation of crack, neck, etc. Even under the homogenous macroscopic imposed strain, deformation heterogeneity exists in microscopic level due to the grain kinematics. Thus, a revised and improved crystal plasticity model is required to correctly address deformation behavior of material in micrometer length-scale and reflect physical mechanisms of deformation.

Simulation techniques based on FEM combined with crystal plasticity models (CPFEM) (Bate, 1999) are proposed to compute mechanical response and predict microstructure evolution of material during deformation. Despite these improvements, large inconsistencies still exist between numerically predicted mechanical behavior and what is observed experimentally. Because the mechanics of deformation that is determined by variables such as strain, strain-rate, temperature and microstructure fields become very complicated for complex deformation geometries and materials systems with respect to the deformation history. Simulation time extremely increases in such cases and it is almost impractical to employ such models to predict process outcomes (Simof & Hughes, 2008), importantly deformation distribution/local strains because of the complexity and effect of previous deformation paths. Hence, *in situ* experimental characterization using real time imaging methods (Shi, Pang, Zhang, Liu, & Ying, 2004) can resolve the dynamic details of a complex deformation system. The information obtained from

these methods, which correctly address deformation history of material, can be used as input in computational models.

In summary challenges, issues and obstacles in microforming is categorized as following:

(1) Major challenge: multi scale physics-based models of material behavior in manufacturing regimes

- Advise optimal processing routes and thermo-mechanical conditions needed

(2) Applications domain issues

- Surface integrity in component manufacture
- Scalability of processing (material, dimension)
- Novel processes for advanced technologies

(3) Obstacles

- Controlled high resolution deformation frameworks
- Characterizing process anomalies in micro/nano length scales

Process-performance-response linkages- Deformation behavior of material is determined by central variables of plasticity including s*train, strain-rate, rotation* fields along with *temperature and microstructure* fields that define the mechanics of plasticity for a given material system and determine the process outcomes for a wide-array of metal forming-based manufacturing operations. In addition to aforementioned variables, *strain gradient* plays an important role in microforming processes due to the effect of length scale. For deformation geometry defined by a chosen manufacturing process, these central variables are unique functions of prior microstructure, deformation temperature, length-scale, rate and tribological

boundary conditions that link initial microforming parameters to the process outcomes, including the deformed microstructure, forces, residual stresses etc. (Figure 4).

Process outcomes are consequences of the central variables can be calculated if and only if the dynamic fields of the central variables are well delineated that require an *in situ* characterization. However, such a paradigm for experimental characterization of the central variables has proven to be elusive. This inability has limited achievement of fundamental insights into the thermomechanics of micrometer-scale deformation fields such as those in microforming.

In addition to the poorly understood dependence of the central variables of deformation in microforming on the deformation geometry, rate and boundary conditions, the effect of microstructure offers another level of complexity. Process outcomes cannot be easily predicted especially when the effect of both microstructural parameters (e.g., grain misorientation, grain size and its distribution, crystallographic texture etc.), and local stresses are considered. Here, there is a glaring lack of understanding of the *crystallographic details* on how the *starting microstructure* accommodates the strain, strain-rates and rotation of material elements and transforms during the course of micro-deformation while manifesting process outcomes. Nonetheless, experimental evidence in the literature is unambiguous that microstructural effects demonstrably modify the process and the resulting properties in the microproducts.

It is anticipated that the effort proposed here to pursue the *in situ* characterization of variables of deformation mechanics and their effect on the microstructure field in deformation zone during microforming can offer fundamentally new insights into the aforementioned interactions and suggest a framework for the design and simulation of micrometer-scale metal forming processes. We envision a transformative potential of this study in enabling specific

designs of microstructural characteristics that result in tailored mechanical properties, a capability that impacts an array of engineering sectors.

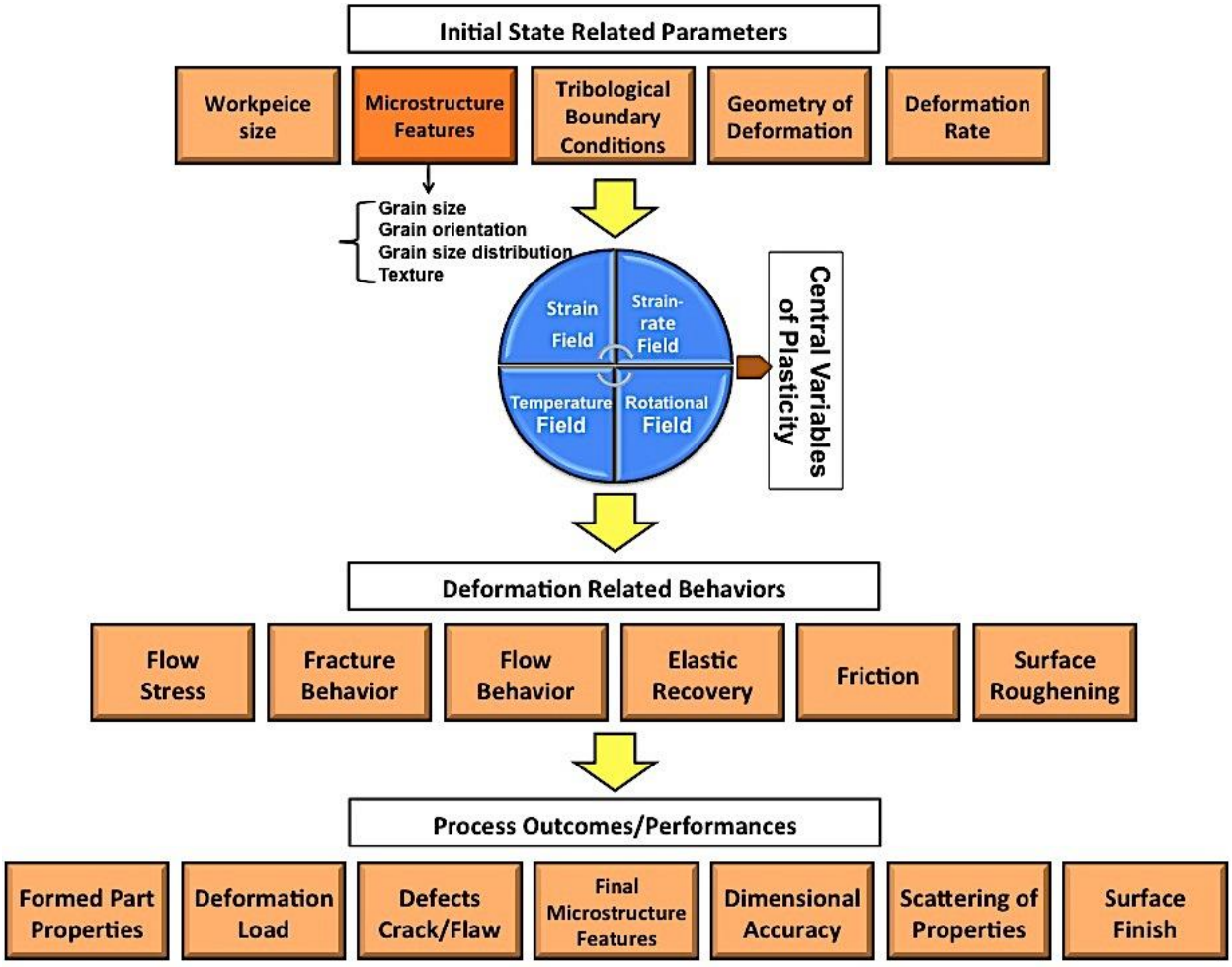

Figure 4: Process-performance-response linkages show how input variables modify central variables of deformation that eventually determine deformation behavior and consenquently process outcomes/responces.

3.2 OBJECTIVES AND PLANS

The ***main objective*** in this research is to study the deformation characteristics of different starting microstructures during microforming with the overarching goal of establishing methodologies of engineering microstructures for better process performance. This will be achieved by integrating high resolution *in situ* measurements of mechanics of deformation with rigorous characterization of microstructure evolution to understand in depth the subtleties and intricacies of deformation behavior of metallic alloys in microforming. *In situ* measurement of mechanics would include delineation of strain, strain-rate and rotational fields in the deformation zones of utilized microforming geometries. Using extensive experimentation, the present study aims to examine the effect of the initial-state related parameters (Figure 4) on the aforementioned deformation mechanics with respect to initial microstructure, finally coupling the same with characteristics of the evolved microstructure and process performance.

Doing this will reveal the role of prior microstructures and its characteristics with respect to geometry confinements and mechanics of deformation in the process outcomes and lead us to design and engineer suitable starting microstructures in order to enhance formability and improve the quality of micro-components. Insights gained from this will advise optimal processing routes and thermomechanical conditions needed to improve microfoming.

Therefore, the ***hypothesis*** is that there are certain prior microstructures and textures coming from the previous thermomechanical treatments on materials which their interactions with the mechanics of deformation depending on the geometry of process will result in less process anomalies and improve process performance. It is expected that by controlling the aforementioned thermomechanical treatments, desired microstructures can be engineered and designed for that purpose.

In next chapters we describe the methodologies and experimental procedures designed in order to find the material response to geometry constrictions and scaling and also to test various microstructure fields to optimize the microforming performance. To achieve this, three microforming stages are suggested in this research to test the scaling effects, different level of impose strains as well as the microscopical material response during microforming in complex geometries that can be relatable to the scale and geometry of microforming operations in industrial sectors. The aforementioned three microforming devices are including:

1. *Equal channel angular pressing (ECAP)*
2. *Indirect microextrusion (IE)*
3. *Micro-deep drawing* (DD)

Plane strain deformation conditions are used to characterize deformation mechanics using Digital Image Correlation (details in chapter 4). Pure effects arise from scaling and geometry constrictions are investigated using prototypical model material Pb to avoid any microstructural contribution in process performance during microforming. Furthermore, in order to test the staring microstructure effects, the following microstructure characteristics are altered in this study:

I. Grain size and distribution (uniform/multimodal/graded)
II. Grain morphology (lamellar/equi-axial)
III. Twin density/size/morphology
IV. Crystallographic texture and texture rotation

Details and rationales for testing each microstructure will be provided individually for specific devices and geometries in next chapters.

4.0 EQUAL CHANNEL ANGULAR PRESSING

Equal Channel Angular Pressing (ECAP) has been established as a scalable route for manufacturing Ultra Fine Grained (UFG)/nanostructured metals in bulk form (comprising large cross-sections) by imposing Severe Plastic Deformation (SPD) (Iwahashi, Horita, Nemoto, & Langdon, 1998; Iwahashi, Wang, Horita, Nemoto, & Langdon, 1996). The process involves pressing a ram against a workpiece (billet), which sits in a channel. Due to a bend in the channel, the workpiece undergoes deformation involving high levels of strain as it advances through the bend (Figure 5a). Here, grain refinement takes place during imposition of high levels of shear strain without any significant change in the cross section geometry of the workpiece, even after several deformation passes (Iwahashi et al., 1996). Imposition of SPD during ECAP to process fully-dense bulk forms is also facilitated by substantial hydrostatic pressure that prevails in its deformation zone (Raab, Soshnikova, & Valiev, 2004; Zehetbauer, Stüwe, Vorhauer, Schafler, & Kohout, 2003). Additionally, much like other plastic deformation processes, microstructure evolution here is governed by the spatio-temporal distribution of the strain, strain-rate and temperature in the deformation zone (Abolghasem, Basu, Shekhar, Cai, & Ravi Shankar, 2012). In ECAP, a steady state flow of material under plane strain conditions is associated with simple shear in a narrow zone at the intersection plane of entry and exit channels of die (Iwahashi et al., 1996).

4.1 QUESTIONS, HYPOTHESIS AND OBJECTIVES

The aim of this study is first to understand thoroughly the effects arise from length-scale and geometrical confinement in microforming scenarios under complicated stress conditions e.g. the interaction of the geometry and length-scale with mechanics of deformation. Here, length scale refers to extrinsic dimensions or sample/die size. Knowing this will help us to predict the microstructural response of material at those scales and hence the mechanical properties.

This brings up critical questions such as how is the flow behavior of material for example under sudden rotations in the constricted defamation zone geometry? Such as material rotation at the intersection of the channels during ECAP process. Is there any switchover in the mechanics of deformation with scaling down the processes? And what are the consequences of such switchover on the microstructure evolution mechanisms? Or what is the effect of length-scale on the heterogeneity of deformation and hence microstructure across the sample.

To answer these questions, the idea is to use a prototypical model material such as Pb with almost no work hardening capacity. Therefore, the effects arise from microstructural features (e.g. grain size and anisotropy) can be ignored and hence, geometry of deformation can be purely attributed to the process boundary conditions (later on in the next chapters, effects arise from microstructure parameters are investigated). Pb shows little work hardening and approximates the elastic-perfectly plastic behavior common in stress-saturated materials such as those featuring ultra-fine grained or nanostructured microstructures. Within such a prototype, experiments with Pb offer a simplified baseline that focuses on the modification of the deformation with shrinking scale of the process. Furthermore, Pb with Face Centered Cubic (FCC) crystal structure at room temperature can also encapsulate deformation behavior of this

family of polycrystalline materials at their approximately 0.5 homologous temperatures where thermally activated processes such as multiple slips and cross slips prohibit dislocation accumulations and motivate dynamic recovery and recrystallization(Kumar, Schwartz, & King, 2002; Rollett, Humphreys, Rohrer, & Hatherly, 2004). Here, the assumptions are almost equivalent to what is prevalent in Slip Line Field (SLF) theory in which there is no account for the effects of work hardening, heat generation and thermal gradients etc. on the deformation field(W.F. Hosford & Caddell, 2011; Rees, 2012).

In this suite of experiments, we are aiming to delineate the scaling effects and also effects arise by increasing the rate of deformation on the extension/spread of plastic deformation zone in sub (mm)-scale samples deformed by *ECAP*. Parameterization of deformation zone geometry is performed in Pb by studying the key elements of deformation mechanics (strain, strain-rate and rotation fields) in order to model deformation behavior for materials as a function of length scale and process parameters. Details are explained subsequently.

4.2 METHODOLOGIES AND EXPERIMENTAL TECHNIQUES

4.2.1 Mechanics of ECAP across length scales

An experimental setup for *in situ* observation of material flow during ECAP was implemented to image the PDZ and Digital Image Correlation (DIC) (Bruck, McNeill, Sutton, & Peters Iii, 1989; Srinivasan et al., 2005) was used to characterize this flow. In this manner, strain/strain-rate/rotation fields in the PDZ were characterized (described in the following sections). In addition to this, thermal characterization of the material flow through the PDZ was also performed. For thermomechanical characterization, ECAP die was fabricated using a transparent observation window made of sapphire (Figure 5a). The broad transmission spectrum of sapphire enables the imaging of the material flow using an Infra-Red (IR) camera. Characterization of flow mechanics through the PDZ during ECAP was performed for a host of used ECAP process parameters (geometries and deformation rate). By subsequent analysis of the flow mechanics (described in the following sections), the influence of process parameters on the same was delineated.

In addition to the sapphire observation window, the ECAP die was also retrofitted with adjustable tool steel plates for the top and bottom walls of channels. In this manner, effect of different die geometries-channel widths and outer corner angles- on material flow in the PDZ of ECAP could be studied. The fixed base was also made of tool steel (Figure 5a).

Commercially pure Lead (Pb) was used as the workpiece. In the configuration used, the extrusion direction was oriented vertically and the ram was advanced horizontally while performing ECAP. An unobstructed view of the PDZ was obtained using the sapphire window, making optical and thermal imaging of the material flow possible. Material flow through the PDZ was recorded using an optical high-speed Charged Coupled Device (CCD) camera (PCO

1200 HS) and a FLIR Infra-Red (IR) camera, for performing mechanical (strain, strain-rate, etc.) and thermal characterization, respectively. CCD camera was located in directly in front of the viewing sapphire window and a light source was used to illuminate sample and provide enough light and contrast for imaging.

In this setup, the recording frame rate was approximately 118 frame/second. Figure 5b illustrates the material flow through the deformation zone in a time-sequence of optical images obtained from the PCO camera. ECAP was performed on rectangular Pb samples. A die angle $\delta = 90°$ was used (Figure 6a). Channel widths of 1 mm and 2 mm were used (Figure 6a) and the ram was advanced at five different speeds (2 mm/s, 5 mm/s, 10 mm/s, 20 mm/s and 30 mm/s). Sharp and round-corner dies featuring $\psi = 0°, 45°$ and $90°$ were used (Figure 6a). In Figure 6a, inner and outer corners of ECAP die are marked as A and B respectively.

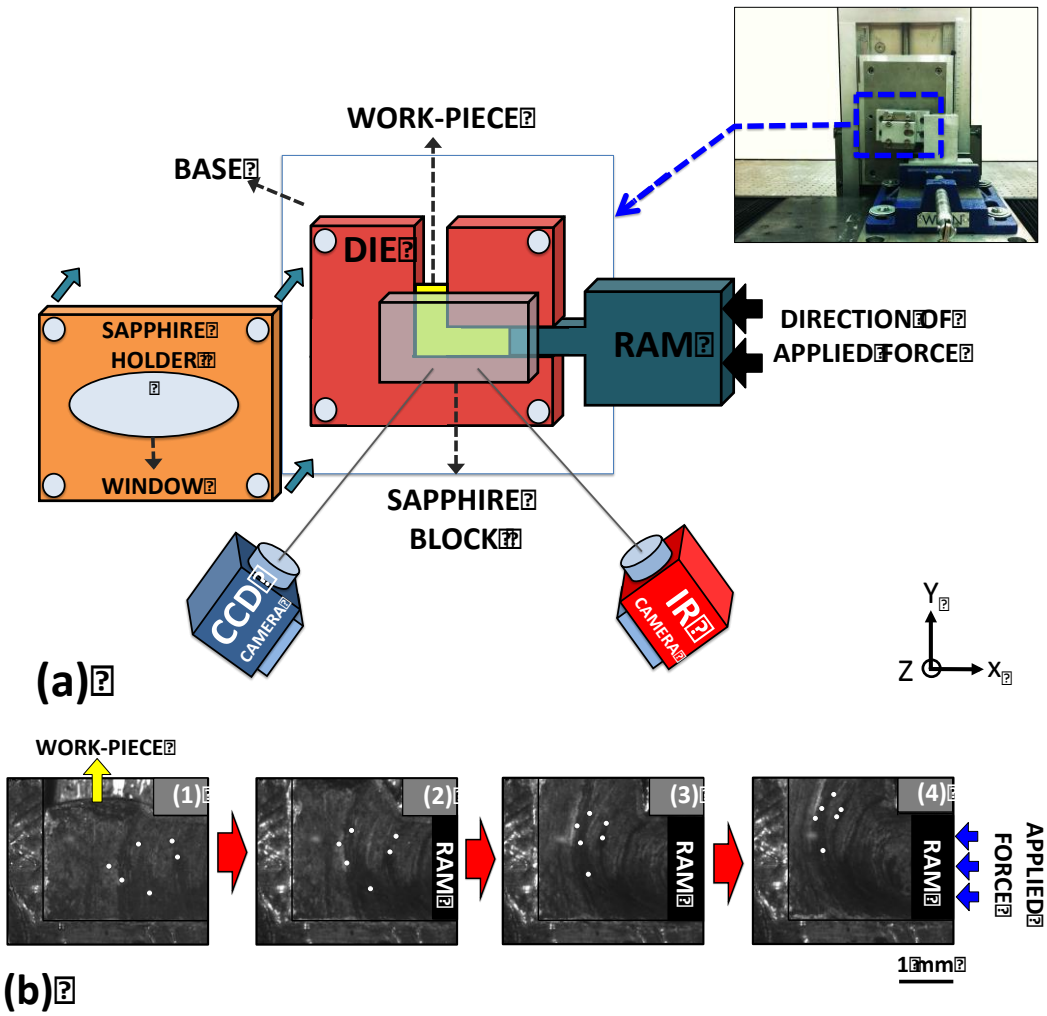

Figure 5: Equal Channel Angular Pressing (ECAP) die configuration made of transparent sapphire window for studying mechanics of deformation using CCD and IR cameras. b) Sequence of images using CCD camera for performing digital image correlation captured during deformation of Lead.

No lubricant was used while performing ECAP to prevent interference with the optical and IR imaging systems. The width of the workpiece in the Z direction (Figure 6a) was set at 2 mm. Table 1 and 2 list the ECAP process parameters studied here along with the theoretical

(assuming no friction between die wall and sample) von Misses equivalent strain for each condition, calculated using (Valiev & Langdon, 2006):

$$\varepsilon_{eq} = \frac{1}{\sqrt{3}}\left[2\cot\left(\frac{\delta+\psi}{2}\right) + \psi cosec\left(\frac{\delta+\psi}{2}\right)\right] \quad (1)$$

Deformation zone in ECAP was characterized using Digital Image Correlation (DIC). In this, image correlation algorithms were used to quantify the motion of asperities during ECAP, using which velocity and displacement fields in the PDZ were generated. Asperities are characteristic high contrast features inherently present on the surface of the workpiece undergoing deformation. The advancement of the ram results in movement of these asperities. Therefore, by tracking their motion through the sequence of optical images acquired by the high speed CCD camera during ECAP (Raffel, 2007), deformation imposed by the advancing ram can be assimilated. Thereafter, the strain-rate field in deformation zone was generated using spatiotemporal differentiation of the displacement field (Adrian, 1997; Raffel, 2007), from which, morphological parameters of the ensuing PDZ were extracted for the different ECAP process parameters used. Insets in Figure 6a show examples of the flow behavior of material and its corresponding extracted deformation filed obtained by DIC. In this Figure, L_S^* and L_{DMZ} are the length of shear zone and Dead Metal Zone (DMZ) in the deformation zone.

Deformation forces experienced by the ram along the X and Y directions – F_H and F_V (Figure 6b) were measured by mounting the die assembly on a three directional load cell (Model# TR3D-B-4K-Michigan Scientific). In fact, the load cell was located between the base plate (Figure 6a) and the die, connecting linear servo motor machine to the die assembly.

The idealized (frictionless) deformation geometries are similar in both machining and ECAP. Both constitute simple shear within a narrow zone (of thickness h (Palmer & Oxley, 1959). Hence, an upper bound analysis based approach similar to machining is used to analyze

deformation forces during ECAP. In doing this, ECAP is considered equivalent to machining with a fixed geometry of PDZ assuming that the undeformed and deformed chip thicknesses (a_0 and a_c, respectively) are equal (Palmer & Oxley, 1959). This implies a fixed shear plane angle (φ = 45°) during ECAP (Figure 6c). Therefore, using an approach similar to that in Ref. (Palmer & Oxley, 1959), the force resolved along the nominal shear direction (F_S), parallel to the shear plane is calculated using (Marusich & Ortiz, 1995; Palmer & Oxley, 1959):

$$F_S = F_H \cos\varphi - F_V \sin\varphi \quad (2)$$

where F_H, F_V and φ are the horizontal and vertical forces, and the shear angle (φ = 45°), respectively. In the aforementioned theory of machining (Palmer & Oxley, 1959), it is assumed that the average shear strain-rate in the PDZ is given by:

$$\dot{\gamma} = \frac{V_S}{h} \quad (3)$$

where V_S is the shear velocity and h is the thickness of the deformation zone.

Equation 3 in fact relates the thickness of the PDZ (h) to the shear strain-rate ($\dot{\gamma}$) and shear velocity (V_S). Here, empirical shear velocity (V_S^*, measured by DIC) was calculated using $V_S^* = V_{exit} - V_{entry}$ where V_{exit} and V_{entry} are exit and entry velocity vectors, respectively. During ECAP, $|V_{exit}| = |V_{entry}|$ due to conservation of density during plastic deformation. Therefore, $V_S^* = |V_S^*| = \sqrt{2}|V_{entry}|$ (Table 1 and 2).

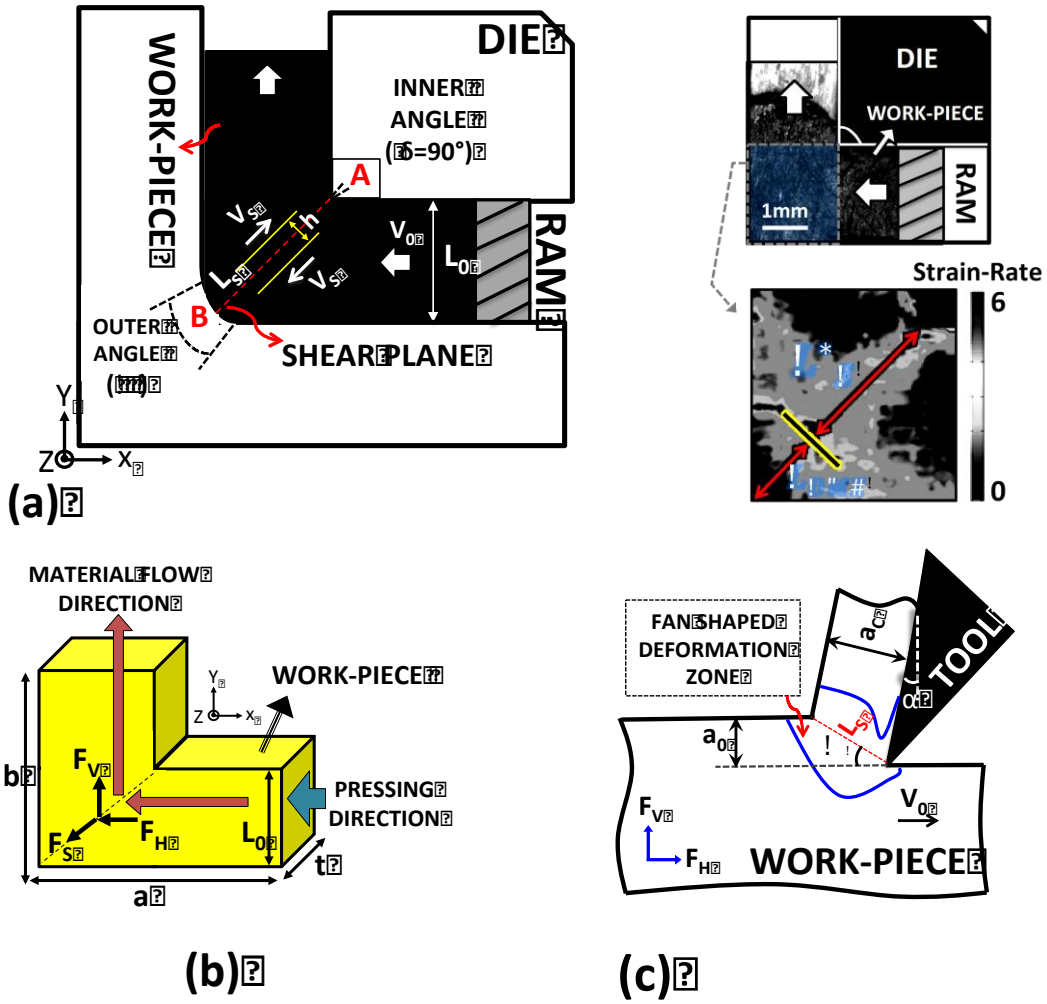

Figure 6: Schematic of Equal Channel Angular Pressing (ECAP) in a plane-strain configuration to measure the mechanics of deformation in simple shear using light and infrared high-speed photography from the side view of the deformation zone. a) The deformation parameters in ECAP are illustrated; insets are the images of the material flow captured through the transparent sapphire window while performing load and its corresponding deformation zone obtained by DIC. b) The forces measured along the X and Y directions using load cell correspond to horizontal and vertical forces (F_H , F_V) and F_S is the force along the shear plane that can be calculated using (F_H , F_V). c) Schematic of machining configuration, showing the deformation parameters.

Characterization of the mechanics of deformation was complemented with the measurement of the temperature field in the deformation zone using *in situ* calibrated Infra-Red (IR) thermography using a FLIR Infra-Red camera. Calibration was performed by coating a metallic sheet with black non-reflective stove paint to achieve uniform surface emissivity. This sheet was heated from room temperature (~300 K) to 500 K in steps of 5 K and subsequently observed through the IR camera, which produced a certain number of counts for every temperature. By recording the counts and tallying with the preset temperatures, a calibration curve was produced. Using this curve, counts obtained from the camera during ECAP were used to produce the deformation zone temperature field. Prior to performing ECAP, the workpiece was coated with the black stove paint for obtaining uniform emissivity and a region close to the deformation zone was observed through IR camera while performing ECAP.

4.2.2 Digital Image Correlation (DIC)

Motion of the surface asperities that appeared as light/dark spots are tracked for the consecutive set of images using cross correlation techniques to measure the mechanics of deformation over a range of length scales. Here, length scale refers to the thickness of the deformation zone (t) in each microforming configuration.

4.2.3 Strain-rate field

DIC algorithm determines the movement of asperities over an image pair within the sequence captured during deformation whereby a displacement field corresponding to material flow is delineated in finite time intervals. The strain-rate tensor field $\underline{D^P}$ was thereafter calculated from this by numerical spatiotemporal differentiation using:

$$\underline{D}^P = \begin{bmatrix} \frac{\partial^2 u}{\partial x \partial t} & 1/2\left(\frac{\partial^2 u}{\partial y \partial t} + \frac{\partial^2 v}{\partial x \partial t}\right) \\ 1/2\left(\frac{\partial^2 u}{\partial y \partial t} + \frac{\partial^2 v}{\partial x \partial t}\right) & \frac{\partial^2 v}{\partial y \partial t} \end{bmatrix} \quad (4)$$

where u and v are displacements in the X and Y directions in the plane of deformation respectively and t is time. The effective strain-rate field was calculated using:

$$\dot{\varepsilon}^P = \sqrt{\frac{2}{3}\underline{D}^P : \underline{D}^P}\ , \text{where } \underline{D}^P = \frac{\underline{L}+\underline{L}^T}{2} \quad (5)$$

Here, ':' refers to the inner product and $\underline{L}$ is the velocity gradient tensor.

4.2.4 Strain field

Pathline of a material points during microforming is being sought whereby the position of the original point is continuously updated. For calculating the effective strain e accumulated, numerical time integration of the effective strain-rate field was performed over the aforementioned pathline, given by:

$$\varepsilon = \oint_{\Gamma} \dot{\varepsilon}_p dt \quad (6)$$

where dt is the time between the image pairs in the sequence and Γ refers to the pathline and $\dot{\varepsilon}_p$ refers to the effective strain-rate that the material point experiences at time t in the pathline. It will be seen in the software that the *normxcorr2* function in MATLAB was used to calculate the cross correlation.

4.2.5 Rotation field

The rotational component of deformation imposed during indirect extrusion of Pb was determined from empirically measured and quantified pathlines using DIC. The rotation field was obtained by first calculating the displacement gradient tensor (∇u) and deformation gradient tensor (F) fields. This was done using:

$$\nabla u = \frac{\partial u_i}{\partial x_j} = \begin{pmatrix} \frac{\partial u}{\partial x} & \frac{\partial u}{\partial y} \\ \frac{\partial v}{\partial x} & \frac{\partial \mathrm{v}}{\partial y} \end{pmatrix}, \; F = I + \nabla u \tag{7}$$

where u and v are displacements in X and Y directions in the deformation plane respectively. Thereafter polar decomposition was performed whereby rotation tensor R could be obtained from F. This was done by reducing the deformation gradient tensor to the right Cauchy-Green tensor by performing the operation:

$$C = F^T F \tag{8}$$

From the eigenvalues of the Cauchy-Green tensor C and ($= {\lambda_i}^2$) eigenvectors of C ($= W_i$), the stretch tensor is obtained as:

$$U = \sum_i \lambda_i \, W_i \otimes W_i \tag{9}$$

where $\otimes$ is the tensor product. Eventually the rotation tensor $R(\omega)$is obtained by performing:

$$R(\omega) = F * U^{-1} \tag{10}$$

Subsequently, the rotation tensor R is related to the finite rotation angle, (ω), by the relation:

$$R(\omega) = \begin{pmatrix} cos\ \omega & -sin\ \omega \\ sin\ \omega & cos\ \omega \end{pmatrix} \quad (11)$$

Doing this for every point on the grid, a rotation field was obtained for the material undergoing deformation during indirect extrusion.

Table 1: Deformation parameters for die with 2 mm channel width and different geometries listed: ram velocity (V_0), measured velocity along the shear plane using DIC (V_S^*), measured length of the shear zone using DIC (L_S^*) [inset Figure 6a], measured equivalent strain using DIC (ε^*), normalized length of the DMZ [$h_{DMZ} = \frac{L_S - L_S^*}{L_S}$], average shear strain-rate in PDZ measured using DIC ($\dot{\gamma}$), calculated deformation thickness (h) [$h = V_S^*/\dot{\gamma}$], measured horizontal and vertical forces (F_H, F_V) along the X and Y directions using load cell attached to die assembly, calculated force along the shear plane (F_S) using Equation (2) [Figure 6b].

Die Geometry	V_0 (mm/s)	V_S^* (mm/s ±0.5	L_S^* (mm) ±0.05	ε^* ±0.05	h_{DMZ}	$\dot{\gamma}$ (1/s) ±0.5	h (mm)	F_H (N) ±5	F_V (N) ±5	F_S (N) ±5
$\delta = 90^\circ$ $\psi = 45^\circ$ $L_0 = 2\ mm$ $L_S = 2.42\ mm$ $\varepsilon_{Th} = 0.968$	2	1.54	2.2	0.77	0.09	2.28	0.67	370	117	177.1
	5	3.86	2.2	0.83	0.09	4.33	0.89	391	124	186.9
	10	7.8	2.15	0.86	0.11	5.92	1.31	404	137	186.9
	20	16.8	2.15	0.95	0.11	9.2	1.82	440	144	207.2
	30	32.3	1.9	1.08	0.21	11.55	2.79	485	153	232.4
$\delta = 90^\circ$ $\psi = 0^\circ$ $L_0 = 2\ mm$ $L_S = 2.85\ mm$ $\varepsilon_{Th} = 1.154$	2	1.43	1.9	0.85	0.33	2.88	0.49	400	124	193.2
	5	3.5	1.88	0.9	0.34	5.76	0.60	413	133	196
	10	7.62	1.8	0.96	0.36	6.87	1.10	450	142	215.6
	20	16.35	1.8	1.04	0.36	11.4	1.43	480	155	227.5
	30	31.7	1.75	1.2	0.38	13.2	2.40	516	169	242.9

Table 2: Deformation parameters for die with 1 mm channel width and different geometries listed: ram velocity (V_0), measured velocity along the shear plane using DIC (V_S^*), measured length of the shear zone using DIC (L_S^*) [inset Figure 6a], measured equivalent strain using DIC (ε^*), normalized length of the DMZ [$h_{DMZ} = \frac{L_S - L_S^*}{L_S}$], average shear strain-rate in PDZ measured using DIC ($\dot{\gamma}$), calculated deformation thickness (h) [$h = V_S^*/\dot{\gamma}$], measured horizontal and vertical forces (F_H, F_V) along the X and Y directions using load cell attached to die assembly, calculated force along the shear plane (F_S) using Equation (2) [Figure 6b].

Die Geometry	V_0 (mm/s)	V_S^* (mm/s ±0.5	L_S^* (mm) ±0.05	ε^* ±0.05	h_{DMZ}	$\dot{\gamma}$ (1/s) ±0.5	h (mm)	F_H (N) ±5	F_V (N) ±5	F_S (N) ±5
$\delta = 90^\circ$ $\psi = 90^\circ$ $L_0 = 1\ mm$ $L_S = 1\ mm$ $\varepsilon_{Th} = 0.9$	2	1.8	0.65	0.66	0.35	4.12	0.47	320	128	134.4
	5	4.2	0.67	0.7	0.33	5.4	0.77	331	141	133
	10	8.76	0.6	0.75	0.4	7.4	1.18	360	157	142.1
	20	19.2	0.64	0.8	0.36	11.8	1.62	391	163	159.6
	30	36.7	0.62	0.86	0.38	16.4	2.23	418	178	168
$\delta = 90^\circ$ $\psi = 0^\circ$ $L_0 = 1\ mm$ $L_S = 1.42\ mm$ $\varepsilon_{Th} = 1.154$	2	1.35	0.98	0.97	0.30	4.40	0.30	355	160	136.5
	5	3.67	0.87	1.05	0.38	6.76	0.54	369	169	140
	10	6.2	0.85	1.09	0.40	8.7	0.71	391	177	149.8
	20	15.3	0.8	1.2	0.43	13.8	1.10	435	184	175.7
	30	28.2	0.74	1.35	0.47	20.6	1.36	467	200	186.9

4.3 RESULTS AND DISCUSSION

ECAP was used to impose an effective strain of ~1 after one pass and the thermomechanics in the PDZ was quantified as a function of ram velocity, channel width and geometry of the die. *In situ* visible light and IR imaging was utilized to characterize the deformation. These characterizations were complemented by force measurements and the following sections detail the results. Result of calculations for each condition is given in Table 1 and 2 (Section 4.2).

4.3.1 Strain-rate fields in PDZ

Results of *in situ* mechanical characterization of the PDZ during ECAP using DIC are summarized in Figures 7 and 8. It is evident in Figure 7 that the PDZ during ECAP is localized in the vicinity of the intersection plane of the two channels *i.e.* the nominal shear plane. Morphology of the PDZ is found to be a function of the die geometry and the deformation rate (ram velocity). Same variation in the strain-rate is also found across the length of the PDZ.

In Figure 7, max intense strain-rate is found near the corner A and strain-rate decayed when approaching the outer corner B (A and B are marked in Figure 6a). Based on morphological characteristics arising from inhomogeneity of deformation through its length, the PDZ is conventionally divided into two distinct zones: a narrow region close to the inner corner A extended to the center of the workpiece, and a fan shaped region adjacent to the outer corner B (Stoica et al., 2005) .

In contrast to corner A in Figure 7, corner B is also characterized by a Dead Metal Zone (DMZ) as shown in inset Figure 6a. DMZs are seen for all ECAP process parameters studied here. It is also seen that on increasing ram velocities, the shape of the PDZ adopts a more curved shape and dead-metal zone extends further into the center of the channel. This is observed in

insets h, i and j in Figure 7. It is seen that at ram velocities above 10 mm/s, the PDZ adopts a more curved morphology, compared with the conventionally anticipated straight PDZ (insets a, b, f and g in Figure 7) that is oriented along the intersection plane of entry and exit channels. This is illustrated in insets d, e, i and j in Figure 7. The aforementioned curvature becomes significantly more prominent at ram velocities of 30 mm/s. It is seen that the ensuing PDZ here features a rigidly moving front of material ahead of the ram with deformation concentrated in its periphery (insets e and j in Figure 7).

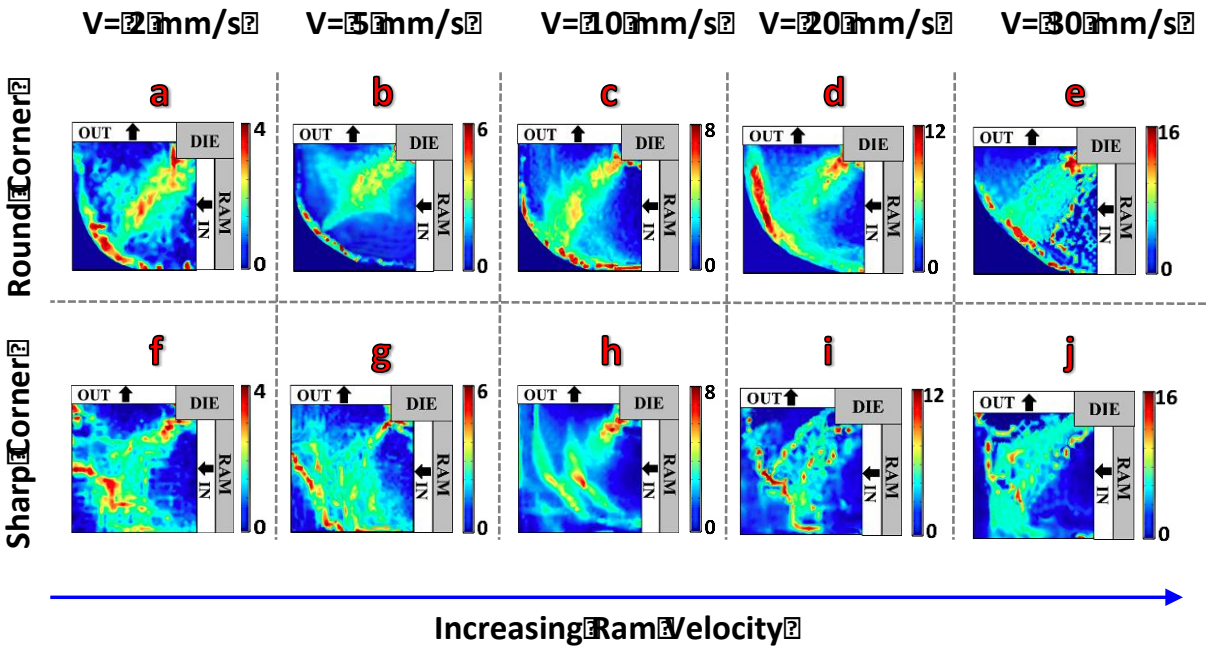

Figure 7: DIC of plastic deformation zone (PDZ) for 2 mm channel width in the dies with round and sharp corner radiuses for various ram velocities. The images show the strain-rate field changing with the curvature of the outer surface of the die as well as the deformation speed

The PDZs resulting in ECAP with a channel width of 1 mm exhibited some prominent differences with respect to those with channel width of 2 mm (Figure 8). It is seen that PDZs in the former are more localized around the shear plane for both round and sharp corner dies, implying a decrease in h with reducing channel width.

However, scaling down the ECAP process by decreasing the channel width results in the formation of a proportionately large dead-metal zone close to the outer corner B. This is delineated by normalizing the dimensions of the DMZ using $h_{DMZ} = \frac{L_S - L_S^*}{L_S}$ where L_S is the theoretically anticipated length of PDZ and L_S^* is the empirically observed counterpart. For measuringL_S^*, the DMZ close outer corner B (Figure 6a) is not considered as part of the PDZ of ECAP.

h_{DMZ} values for various conditions are listed in Table 1 and 2. As seen, DMZs during ECAP with smaller channel width (1 mm) are larger compared with those in the die with channel width (2 mm) particularly at higher ram velocities for the die with sharp corner angle B (insets I and J in Figure 8). This is due to the relatively increase in the surface-to-volume of material undergoing deformation for smaller channel width (1 mm) which is approximately 1.5 times larger than that in the die with 2 mm channel width for the geometries used in these experiments.

It is seen in Figure 8 that deformation is localized in three distinct regions during ECAP with round corner die geometries (corner B), particularly at lower ram velocities (insets a, b and c in Figure 8). The three zones comprise the shear plane, the inlet where the curvature of the corner commences and the analogous point where the curvature ends at the exit.

The geometry of deformation zone demonstrates an unexpected size effect, where the gradual deformation in the 2 mm channel in an integral deformation zone is replaced with discrete regions of concentrated deformation in the 1 mm channel.

However, this effect disappears at higher ram velocities (V>10 mm/s) and we observe a restoration of an integral deformation zone (insets d and e in Figure 8). For round and sharp corners in both 1 mm and 2 mm channel widths a curved deformation zone is observed for ram velocities > 10 mm/s (see insets d, e, i and j in Figures 7 and 8).

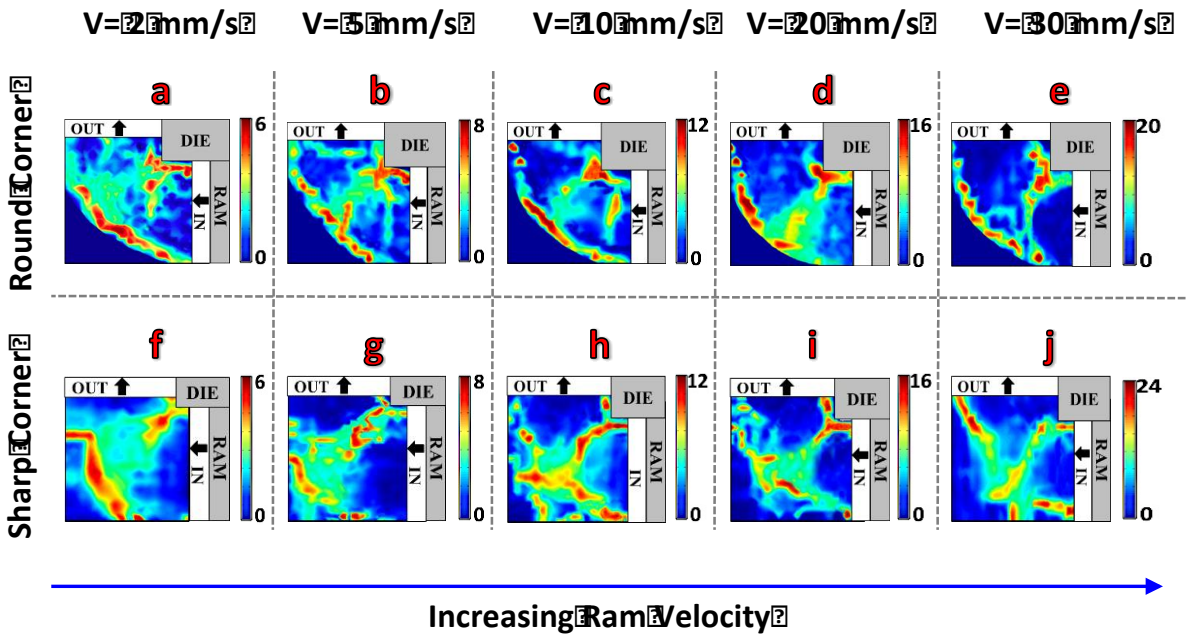

Figure 8: DIC of plastic deformation zone (PDZ) for 1 mm channel width in the dies with round and sharp corner radiuses for various ram velocities. The images show the strain-rate field changing with the curvature of the outer surface of the die as well as the deformation speed.

4.3.2 Shear zone parameters

To understand the effect of ECAP process parameters (ram velocity, geometry, etc.) on the mechanics of deformation, we measured the average effective strain-rate in the PDZ for the various conditions. Table 1 and 2 report the empirically obtained values (section 4.2). These are

obtained from zones in the PDZ by area averaging. Empirically observed lengths of the zones along the intersection plane of entry and exit channels (L_S^*, see Figure 6a) are also reported in Table 1 and 2.

Given the similarities between ECAP and machining, we drew insights from the machining literatures. Characteristics of the PDZ during machining (in machining relevant process parameters) were delineated by Oxley (PLB Oxley & Hastings, 1977) who showed that the average strain-rate prevalent within the aforementioned zone is proportional to the parameter $\frac{V_S}{L_S}$ *i.e.* $\dot{\gamma} = C\frac{V_S}{L_S}$. In this equation, V_S is the shear velocity, which is the velocity of material resolved along the shear plane and L_S is the length of the PDZ that is approximated as a plane. The parameter C (the Oxley parameter) was found to be constant for a given material and was shown to be approximately equal to $\frac{L_S}{h}$ implying constancy of $\frac{L_S}{h}$ for a material (PLB Oxley & Hastings, 1977). This relation predicts that the thickness of the deformation zone h is directly proportional to the length of the deformation zone L_S. Validity of these relations were verified across a wide range of machining process parameters (e.g. cutting speeds and undeformed chip thicknesses (PLB Oxley & Hastings, 1977)). Based on arguments of similarities in deformation geometries, it is expected that the analogous relations hold for ECAP (a simple shear based plastic deformation process, akin to machining).

However, empirical observations (Table 1 and 2) show that unlike in machining, thickness of the deformation (h) in ECAP of Pb not only depends on the length of the deformation zone (L_S^*) but also on the speed of advancement of the ram (*i.e.* deformation speed) (Lapovok, Tóth, Molinari, & Estrin, 2009). Although equation 3 somewhat overestimates h for ECAP with respect to empirical values obtained from the strain-rate fields (Figures 7 and 8), Table 1 and 2 show a clear increasing trend in h, with increasing the ram velocity. It appears that

increasing ram velocity instigates the formation of a larger DMZ, which results in a smaller L_S^*. However, this results in a more diffuse deformation zone as opposed to the conventionally anticipated thinner deformation zone.

Deformation zone thickness (h) in ECAP is also observed to be influenced by the die geometry. For instance, h is found to be higher during ECAP with a 1 mm wide channel when round outer corner is used, compared to the sharp outer corner counterpart. This is a consequence of the large curvature of outer corner ($\psi = 90°$), which has been previously shown to influence ensuing deformation characteristics during ECAP (Figure 8).

In order to probe this further, we plotted the average shear strain-rates $\dot{\gamma}$ vs. the empirical ($\frac{V_S^*}{L_S^*}$) for each set of experiments (Figure 9) It is evident from this diagram that a linear relationship is only valid for $\frac{V_S^*}{L_S^*}$ less than 10. For larger values of $\frac{V_S^*}{L_S^*}$, $\dot{\gamma}$ strays away from linear behavior with respect to $\frac{V_S^*}{L_S^*}$.

$\frac{V_S^*}{L_S^*}$ is increased by either decreasing the scale of deformation by reducing channel width (*i.e.* decreasing L_S^*) or by ram velocity (and hence shear velocity V_S^*). Nonetheless, there appears to be a universality to the variation of the average strain-rate as a function of $\frac{V_S^*}{L_S^*}$. It is concluded that in ECAP, the geometry of PDZ is not only a consequence of the material properties (Kim, Hong, & Seo, 2001; Kim, Seo, & Hong, 2001), but also of the process parameters (geometry of die and ram velocity). Furthermore, the influence becomes more pronounced when material flow is spatially confined.

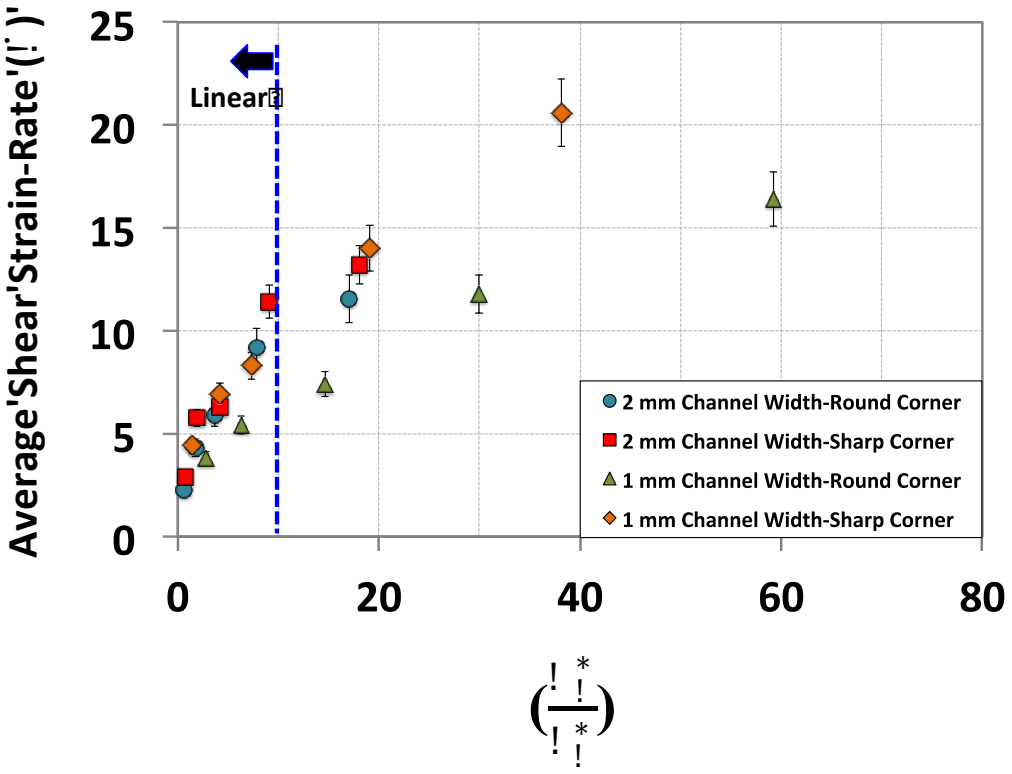

Figure 9: Average of strain-rate $(\dot{\gamma})$versus shear velocity over shear length $(\frac{V_S^*}{L_S^*})$ for different ECAP conditions, suggesting a universality of its scaling as a function of geometry and deformation rate.

4.3.3 Effective strain measurements for pathlines of material flow

The strain imposed on the workpiece was calculated along path-lines of material flow that went through the PDZ, identified using DIC. Results were obtained for three path-lines located in the upper, middle and lower regions of the workpiece (Figure 100). The calculation was performed by integrating the increments of strain accumulated in discrete sections of the path-lines of the material. The average values of effective strain (ε) obtained along the material flow pathlines in PDZ were plotted against the ram velocity for each processing condition (Figure 10).

Based on Equation 1, the magnitude of equivalent plastic strain (ε) imposed on the workpiece undergoing ECAP in one pass is dependent only on the inner angle (δ) and outer corner angles (ψ) that are marked on Figure 6a. The strains imposed are 1.154 for sharp outer corner ($\psi = 0$) and 0.96 and 0.9 for round outer corner ($\psi = 45^o$, $\psi = 90^o$) dies, respectively. They are assumed to be uniform throughout the workpiece. However, it is evident from Figure 10 that the measured values of equivalent strain across the thickness of the workpiece vary with scale, die geometry, deformation speed (ram velocity) and location in the workpiece. Pathline 3, which corresponds to a zone close to the outer corner B of the die consistently, exhibits the highest value of strain, compared with pathlines 1 and 2. This is due to the influence of the dead metal zone, which forms adjacent to outer corner and presumably influences pathline 3 more than pathlines 1 and 2. Thus, it is expected that more prominent dead metal zones would influence pathline 3 more significantly and resulting in larger strain inhomogeneity. This is indeed true as seen by a comparison of ECAP with a sharp outer die corner (channel width = 1 mm, ram velocity V= 30 mm/s) with a round outer die corner (channel width = 2 mm, ram velocity V = 2 mm/s). The former exhibits the largest normalized dead metal zone in the conditions studied and shows a strain inhomogeneity of ~ 1.1. On the other hand, the latter features the smallest normalized dead metal zone and shows a significantly smaller strain inhomogeneity of ~ 0.5. Here, strain homogeneity refers to $\varepsilon_3 - \varepsilon_1$ where ε_3 refers to strain accumulated by pathline 3, etc. Dimensions of the normalized dead metal zone were calculated using $\frac{L_S - L_S^*}{L_S}$ where L_S refers to the idealized length of the shear plane and L_S^* refers to that calculated empirically using DIC.

It remains to be seen how ram velocity influences dimensions of the dead metal zone. However, an increase in the ram velocity caused an increase in the normalized dimensions of the

dead metal zone (Table 1 and 2) in the ECAP process parameters studied here. This change significantly influences mechanics of material flow through the PDZ of ECAP, which plays an important role in instigating the deviation of expected strain-rate from $\dot{\gamma} = C\frac{V_S}{L_S}$ as described in the previous paragraph. As discussed previously, there is a deviation from the linearity beyond the cut off (Figure 9) that may promote instability in the material flow. Here, with increasing the ram velocity or scaling down the process, we also obtain higher deviation of the average equivalent effective strain from of the theoretically imposed strain (Equation 1). This also suggests strain localization for these conditions which promotes shear band formation and hence instability in the PDZ.

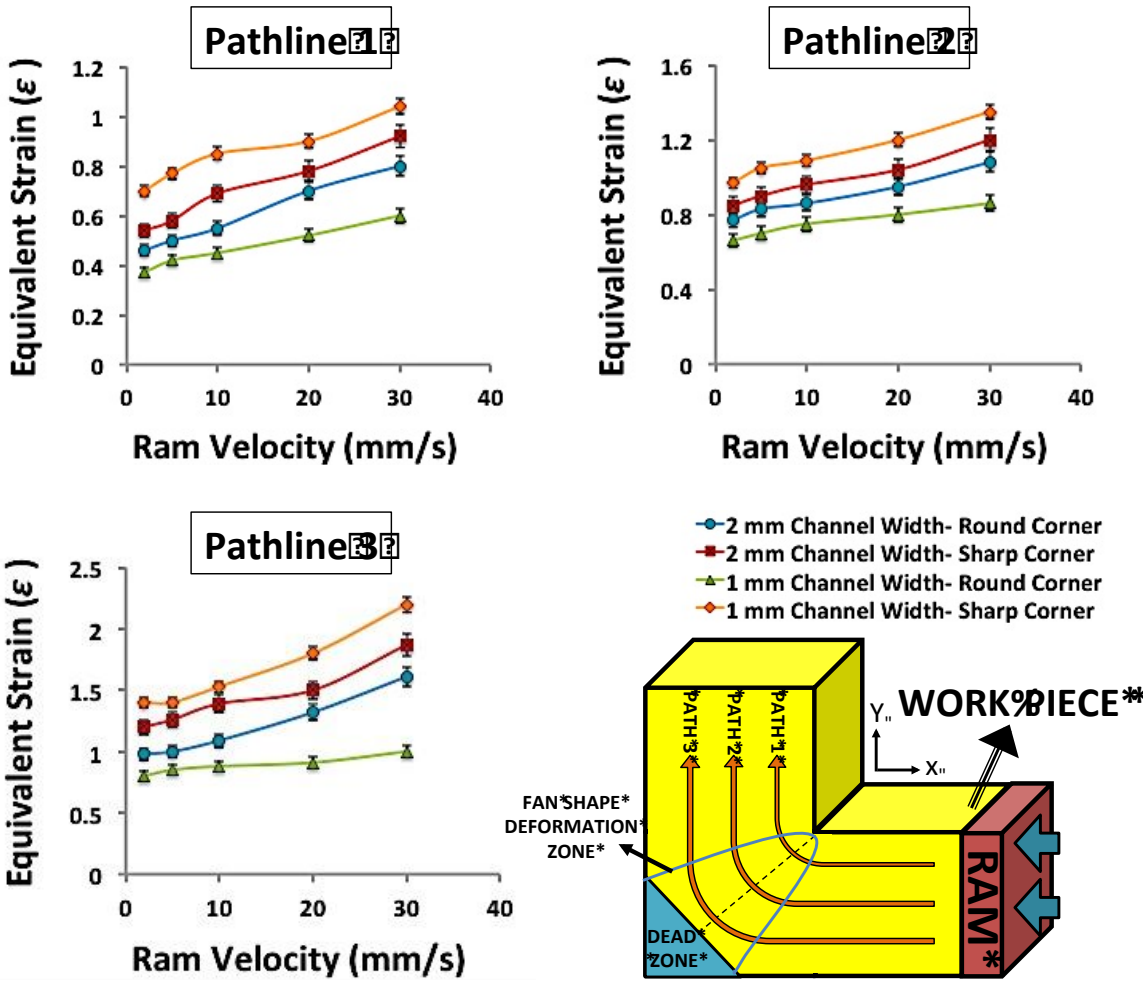

Figure 10: Equivalent Strain (ε) in the deformation zone along three pathlines located in the upper, middle and lower regions of the workpiece for 2 and 1 mm channel widths with round and sharp corners. Schematic on the bottom right shows the location of pathlines and the fan shape deformation zone in which the strain value was measured.

4.3.4 Temperature fields in PDZ

Following the characterization of PDZ using DIC, the temperature field was empirically characterized using Infrared (IR) imaging.

Figure 11 illustrates IR thermographs of PDZ obtained for two conditions: 10 and 30 mm/s ram speeds for 2 mm channel width with round corner. A portion of the work of the plastic deformation is dissipated as heat, which in turn modifies the temperature field in the deformation zone and can lead to a thermosmechanically-coupled state (Shashank Shekhar, Abolghashem, Basu, Cai, & Shankar, 2012; S Shekhar, Cai, Wang, & Shankar, 2009). In addition to the used die geometry, this thermomechanical coupling also affects the mechanics of material flow (Abolghasem, Basu, & Shankar, 2013).

We find that the temperature rise is localized in the vicinity of deformation zone as expected from results of DIC. It is also found that the higher ram velocity of 30 mm/s (

Figure 11 11b) results in a much more extensive zone, simultaneously involving higher magnitudes of temperature-rise. We also find that the IR thermography reveals an increase in the thickness of the deformation zone with increasing deformation speeds, which coincide with that observed in the strain-rate fields from DIC. This might be a combined effect of the higher rate of heat dissipation in the PDZ in larger ram velocities and the effect of thickening of the deformation zone as seen empirically in strain-rate fields, obtained from DIC. During ECAP, a significant portion of plastic work is converted into heat in the PDZ. For adiabatic conditions, temperature rise (ΔT) is given by (Dong, Zhang, Alexandrov, & Wang, 2012; Kim, 2001):

$$\Delta T = \eta \frac{\sigma \varepsilon}{\rho c} \tag{12}$$

where η is the percentage of total plastic work that is converted to heat, which is usually approximated as ~ 0.9 (Quang, Krishnaiah, Hong, & Kim, 2009). σ, ε, ρ and c, are flow stress at

the PDZ, deformation strain, density and the heat capacity of the workpiece, respectively. The values for the physical properties for Pb are: $\rho = 11340\ kgm^{-3}$, $c = 130\ Jkg^{-1}K^{-1}$. For σ in Equation (12) we utilized the deformation force resolved along the shear plane (F_S). This calculation was performed using Equation 2 with force data from Table 1 and 2. This approach for estimating the temperature field using the force resolved along the "shear plane" is reminiscent of that used in the machining literature, where it has been used to obtain reliable estimates of the temperature rise in analogous thermomechanically-coupled SPD (Palmer & Oxley, 1959). The relevant flow stress (σ) in the PDZ was obtained by dividing F_S over the area of shear plane ($t \times L_S$) where t is the thickness of the sample, which is 2 mm in both ECAP dies with 1 and 2 mm channel widths. The average equivalent strains (Table 1 and 2) measured from the DIC were used for each condition. The temperatures rise for 10 mm/s and 30 mm/s ram velocities for $\eta = 0.9$ was obtained to be 20 ℃ and 31 ℃ respectively.

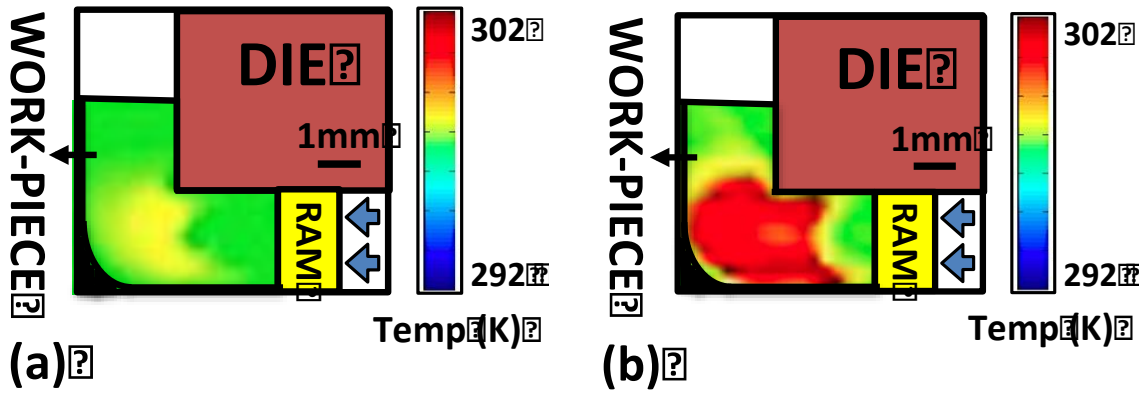

Figure 11: IR thermograph for ECAP of Lead in plane strain configuration. The temperature rise in the deformation zone is illustrated in the die with 2 mm channel width and for a) 10 mm/s and b) 30 mm/s ram velocities. It shows the temperature increment is higher for 30 mm/s ram velocity.

In contrast to these calculations, IR thermography revealed significantly lower temperature rise of 6 ℃ and 12 ℃ for 10 and 30 mm/s ram velocities respectively. One of the assumption we made in using Equation (12) is that 90 percent of plastic work is converting to heat which is not always the case especially for strains less than one(Mason, Rosakis, & Ravichandran, 1994; Ravichandran, Rosakis, Hodowany, & Rosakis, 2002). With the aid of *in situ* techniques of measuring temperature rise during metal forming processes, it has been argued that for strains less than 1, the value of η can decrease from conventional assumption (0.9) to even 0.3(Ravichandran et al., 2002). In addition, Equation (12) is likely true only for adiabatic processes where heat diffusion is completely neglected (Eisenlohr, Gutierrez-Urrutia, & Raabe, 2012). Here, the heat transfer of the workpiece-tooling interfaces is likely to modify the temperature field. ECAP occurs in a fully enclosed die, where the relatively simplistic assumptions that might be acceptable say, in thermal models for machining produce an overestimate of the temperature rise in ECAP.

4.3.5 Rotation fields in PDZ

The rotational component of deformation imposed during ECAP of Pb was determined from empirically measured and quantified path-lines using DIC. Figure 12a shows the results of DIC for ECAP with 2 mm/s ram velocity for 2 mm channel width with round corner. Also illustrated in Figure 12b is the corresponding rotation field (in degrees) obtained from these results.

Doing this for every point on the grid, a rotation field is obtained for the material undergoing deformation during ECAP (Figures 16b, 16c, 16d). Figure 12a shows the final configuration of a grid of points obtained from DIC using a sequence of high speed images of the ECAP process with deformation conditions: 2 mm/s ram velocity, 2 mm channel width with

round corner. Figures 16b, 16c and 16d show the rotation fields corresponding to ECAP with deformation conditions: 2 mm/s ram velocity, 2 mm channel width with round corner; 20 mm/s ram velocity, 2 mm channel width with round corner; 20 mm/s ram velocity, 2 mm channel width with sharp corner, respectively. That was obtained from their corresponding grids using the procedure described above. Furthermore, for obtaining these images, the DIC routine was stopped at an instant when a portion of the grid near the right edge (e.g. closer to A*B* in Figure 12b) was about to enter the deformation zone whereas the top left corner (e.g. closer to C* in Figure 12b) had crossed the deformation zone. Consequently, there is an unambiguous variation in the corresponding rotation fields which change from strongly negative (anti-clockwise near A*, shown in blue) to moderately positive (clockwise near C*, shown in red). In fact the average rotation angles calculated near points A*, B*, C* are -59˚, 1.1˚, 12.6˚ respectively (Figure 12a). In comparison, the average rotation angles calculated near points A**, B**, C** were -32.5˚, 28.5˚, 17.3˚ respectively (Figure 12c) and A***, B***, C*** were -86.5˚, 11.0˚, -2.9˚ respectively (Figure 12d), corresponding to 20 mm/s ram velocity, 2 mm channel width with round corner; 20 mm/s ram velocity, 2 mm channel width with sharp corner, respectively.

The deformation history is complicated due to effects arising from friction and pile up near the ECAP die corner. In fact, we have already seen in Figure 12 that the regions close to the bottom right of the grids exhibit strongly negative rotation fields. This is attributed to frictional effects arising from the bottom face of the channel resulting in anti-clockwise rotation. Using a similar reasoning, the positive rotation closer to the top right corner of the grid is explained, as the top face of the ECAP die would tend to rotate material in a clockwise fashion. It is also clear from Figures 16b, 16c and 16d that as material progresses through the deformation zone, the anti-clockwise rotation caused by the bottom face is reversed whereby material closer to C*D*

exhibits a less negative rotation field (when compared to material closer to A* which has undergone deformation imposed by the DMZ).

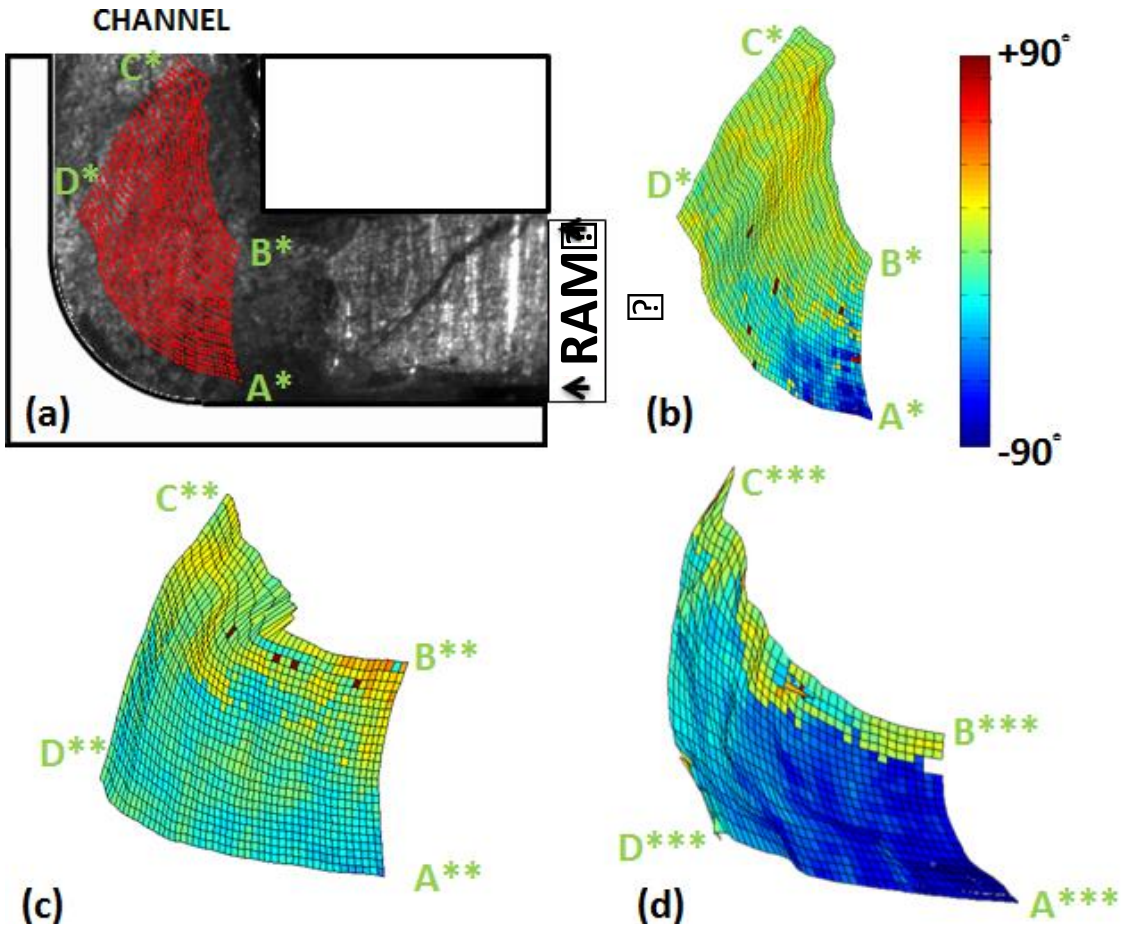

Figure 12: Final configuration of a grid of points obtained from DIC on high-speed image sequence acquired during ECAP. Deformation conditions: 2 mm/s ram velocity, 2 mm channel width with round corner. b) Rotation field corresponding to deformation conditions in (a). c) Rotation field for deformation conditions: 20 mm/s ram velocity, 2 mm channel width with round corner. (d) Rotation field for deformation conditions: V=20 mm/s ram velocity, 2 mm channel width with sharp corner. (* Refers to deformed configuration).

The observations mentioned here suggest that deformation zone heterogeneities are instigated by certain (sharp) deformation geometries and process parameters (high velocities). These heterogeneities are bound to result in accelerated microstructure evolution due strain path changes intrinsically associated to the deformation zone of ECAP. Such strain path changes are known to cause flow instabilities (Li, Hoferlin, Bael, Houtte, & Teodosiu, 2003; Paul, Baudin, & Brisset, 2011) as also evidenced in our experiments. For e.g. sharp corner dies with higher ram speeds exhibited large gradients in angular rotation (previous paragraph, Figure 12d), simultaneous with thin deformation zone morphologies indicative of flow localizations. On the other hand, round corner dies exhibited diffuse deformation zone geometries compared to sharp corner dies, especially at lower speeds *i.e.* no flow localizations.

4.4 SUMMARY AND FINDINGS

This study was set to explore the process anomalies and consequences of geometry confinements using model material Pb to avoid any participation of microstructure characteristics during deformation in sub-(mm) scale Equal Channel Angular Pressing due to the unique properties of Pb. It has identified the effect of geometric scaling and deformation rate on ensuing deformation zone and its parameters. The thermomechanics prevalent in the deformation zone was characterized *in situ* using DIC and IR thermography. A specially designed ECAP die housing an optical and IR transparent sapphire window was utilized for doing this. This study has also sought to know whether there is any switchover in the mechanism of deformation that can be quantified by measuring the key elements of deformation mechanics such as strain, strain rate and rotation field in deformation zone by scaling and applying die constrictions.

It is seen that, as conventionally observed in ECAP process, deformation zone is expanded in the region of two intersecting channels. It is shown that deformation zone is divided in two main regions: PDZ and DMZ. Using *in situ* analysis of deformation zone, it is demonstrated that varying the geometry and deformation rate influences the mechanics of the formation of PDZ and DMZ.

The deformation zone of ECAP is similar to that in machining where simple shear deformation occurs in a narrow shear zone. It is found that, similar to machining, the thickness of PDZ decreases with channel's dimensions. However, unlike machining process, in ECAP it increases with increasing deformation rate. The average strain-rate in the PDZ scaled linearly in proportion to $\frac{V_S^*}{L_S^*}$ till a threshold ~10. For larger $\frac{V_S^*}{L_S^*}$ values this scaling was no longer valid although a monotonic relation between average strain rate and $\frac{V_S^*}{L_S^*}$ persisted. Results from empirically measured strain parameter showed a larger inhomogeneity in deformation for higher

values of $\frac{V_S^*}{L_S^*}$ across the length of PDZ. Additionally, at higher $\frac{V_S^*}{L_S^*}$, the value of the average effective strain increases and its larger deviation from the theoretically predicted strain in PDZ can be an indication of strain localization and ensuing shear banding and instability in material flow.

Based on the similarity of deformation zone characteristics between machining and ECAP, theoretical estimates of temperature rise in the deformation zone were performed using this model and results seen to be in reasonable agreement with empirical counterparts.

Finally, the rotation fields of ECAP found by DIC analysis are shown to be affected by mechanics of formation of PDZ and DMZ. Broadening of DMZ under certain conditions result in a negative rotation of material elements that also suggests more instability in deformation.

5.0 INDIRECT MICROEXTRUSION

Extrusion is the process by which a block/billet of metal is reduced in cross section by forcing it to flow through a die under high pressure. Extrusion as an important bulk forming process offers a range of many advantages for industry such as optimal usage of material, high production rates with short piece-production times, accurate reproduction of dimensions and forms coupled with a good surface quality, good static and dynamic properties of the components due to the favorable fiber structure and work hardening (Kleiner, Geiger, & Klaus, 2003). Therefore, extrusion in sub (mm)–scales (microextrusion) is considered as an efficient and commercially viable candidate for the manufacture of widespread microproducts in innovative industries. Generally, there are three types of extrusions, namely forward, backward, and compound extrusions. Here, in this study we used indirect/backward extrusion process in which the stroke of punch moves in the opposite direction of the material flow.

5.1 QUESTIONS, HYPOTHESIS AND OBJECTIVES

Intrinsic length-scales e.g. grain/sub-grain size and its interaction with extrinsic length-scales e.g. sample size and geometry confinement add another crucial parameter to microforming performance. Hence, understanding the process anomalies in microfroming and the role of microstructure in decreasing or enhancing them will help us to design microstructures, which their interactions with mechanics and scale result in minimizing or removing the aforementioned anomalies. Therefore, in this chapter in addition to model the flow behavior of material using model material Pb as mentioned in the previous chapter, effect of microstructure parameters for poly crystalline materials (Al and Cu) is investigated.

In this regard, first step is to study the effect of the grain size having equiaxed morphology and random texture to purely relate the material deformation response to the grain size. It is expected that decreasing the grain size simultaneously with shrinking the size will improve uniformity in deformation and reduce process anomalies arise from anisotropy. But the question is to what extend we can decrease the grain size to maintain the ductility as well? Or in most methodologies used to produce ultrafine structures e.g. ECAP or other SPD methods there is always a strong and complicated texture evolved during deformation. So, do these textures and their orientation have the same or as important role as grain size in enhancement of micro-formability? Are there certain textures that their interaction with geometry constrictions results in achieving better formability and surface finish considering the fact that it is almost impossible to perform finishing steps on microparts.

It is known that pre-existing crystallographic textures influence microstructure evolution during imposition of subsequent deformation. It is seen that strain paths play a significant role in determining evolution of grain size during imposition of SPD. This study was

performed by comparing evolution of grain size during rolling with that during ECAP (route A), both performed to the same effective strain (~2). Excessive lattice rotation during ECAP in the beginning of the second pass due to conflicting textures left from the previous pass resulted in enhanced lattice rotation and grain fragmentation as opposed to rolling.

As mentioned above, attentions towards the use of ultrafine microstructures in microforming are increasing due to the effect of grain size in deformation homogeneity. However, these potentially interested candidates for starting microstructure have limitations due to their inherent lack of ductility that can be decreased by optimizing crystallographic texture. The aforementioned microstructural manifestations arising from conflicting crystallographic textures can be expected to become more significant in microforming, due to enhanced strain gradients and their well-known influence on microstructure evolution.

Hence, we are examined a new methodology for engineering starting microstructures for microforming applications with the overarching goal of improving process performance and quality of products. The successful completion of this study relies on delineation of crystallographic texture evolution during microforming of a randomly textured starting material. Using insights gained from studying crystallographic texture evolutions during indirect extrusion, process routes can be suggested whereby compatible textures in the starting material for indirect extrusion are produced. Subsequently, methodologies to improve process performance using these (suitably textured) starting materials are described. It is anticipated that the insights gained from this research is generalizable to a vast array of microforming applications. The methodology to create and test such textures will be explained in the next section.

5.2 METHODOLOGIES AND EXPERIMENTAL TECHNIQUES

5.2.1 Mechanics of Indirect microextrusion

Two different setups were fabricated, one suited for Pb and the other for commercially pure Al 1100 and (OFHC) Cu. In both cases, *in situ* characterization of flow fields (Figure 13a) was availed using Digital Image Correlation (described subsequently). The setup for Pb was designed to provide control over the deformation geometry that was varied to facilitate delineation of the effect of length scales. The second set of experiments (on commercially pure Al 1100 and (OFHC) Cu) was designed to study the effect of initial microstructure variables e.g. grain size, texture, etc. on the mechanics of deformation and hence, employed a fixed deformation geometry and speed during indirect extrusion while altering initial microstructure features.

Figure 13 illustrates the prototypical experimental deformation configuration uses commercially pure Lead (Pb) as the workpiece in a die comprises two adjustable plates made of D_2 tool steel forming the top and bottom walls of die cavity, with the fixed base made of alloy steel (Figure 13a). The plunger is also made of D_2 tool steel.

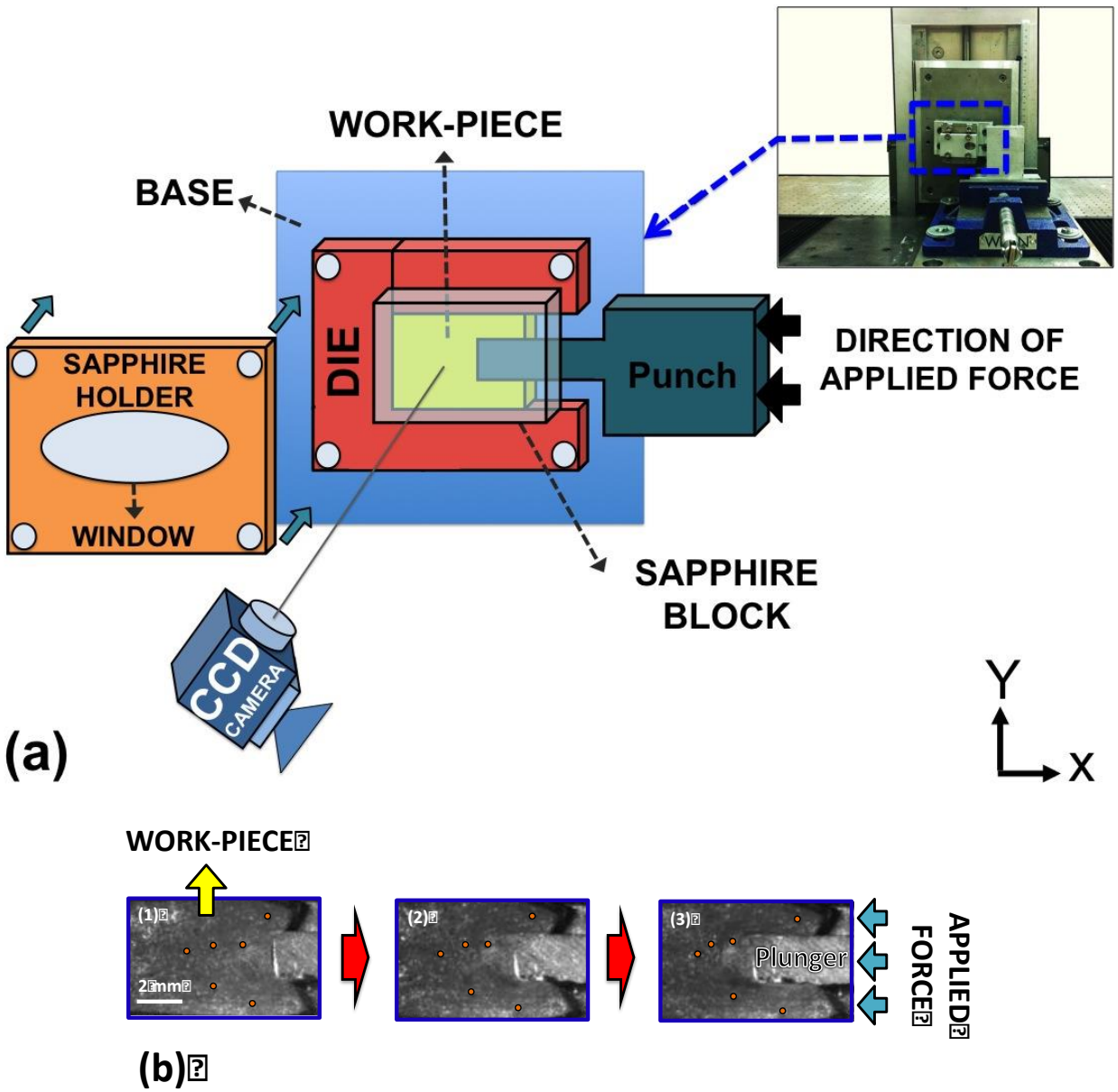

Figure 13: (a) Indirect microextrusion die configuration made of transparent sapphire window for studying mechanics of deformation using CCD camera. (b) Sequence of images captured using CCD camera for performing digital image correlation (DIC), motion of asperities is observed during deformation of Pb.

IE of lead (Pb) was performed in dies with different channel widths ranging from 1.5 mm through 5 mm and two punch widths = 1 mm and 2 mm. The initial length of the samples was set at 10 mm and the depth of punch advance into the die was limited to 5 mm across all experiments on Pb. The punch velocities (V_0) were set at 2, 5, 10, 15 and 20 mm/s in this suite of experiments. IE of Al was performed in a die featuring a width of 1.5 mm and length of 5 mm, using a punch with width = 0.5 mm. The punch velocity was set at 5 mm/s and travel was limited to 2.5 mm. Pb samples were tested as-received and were found to have the grain size of ~ 100 μm. The thickness of theses samples was 2 mm.

Figure 14a illustrates components of the assembled indirect extrusion for second set of experiment on work hardening materials. Here, the direction of extrusion was set parallel to Y (Figure 14b). A transparent sapphire window was installed facing the deformation zone. This configuration provided an unobstructed view of the deformation zone during indirect extrusion (IE). Components (including base) of the IE die were fabricated with D2 tool steel that was heat treated and subsequently tempered before assembly. Sapphire is almost transparent to visible light and features adequate strength and wear resistance for such experiments as evidenced by its previous use in other SPD based experimental frameworks(Moradi et al., 2015). During IE, the plunger was actuated with a servo driven linear actuator (actuator model: BG 2602A 200H-A5C), comprising a 5-phase stepper motor. A miniature load cell (Model# TR3D-B-4K-Michigan Scientific) was installed to avail measurement of extrusion forces. For actuating the plunger with in the cavity a servo driven linear actuator comprises an electric motor and a rotary-to-linear converter was used.

The linear provided from the Nippon Bearing (NB) Company uses a 5-phase stepper motor (42 square-geared built-in types AK-G series). A linear actuator is a device that develops a force and a motion through a straight line. A stepper motor-based linear actuator uses a stepping motor as the source of rotary power. Inside the rotor, there's a threaded precision nut instead of a shaft. The shaft is replaced by a lead-screw. As the rotor turns, linear motion is achieved directly through the nut and threaded screw. To derive the motor, a 5-phase microstepping motor driver model MD5-HD14 is used. PMC-1HS software is used to determine the position and control the speed of a pulse input of the stepping motor.

IE of Al 1100 and (OFHC) Cu samples was performed in a die featuring a width of 1.5 mm and length of 5 mm, using a punch with width = 0.5 mm. The punch velocity was set at 5 mm/s and travel was limited to 2.5 mm. Samples for IE were created from Al 1100 and (OFHC) Cu sheets had the thickness = 1 mm. Al and Cu samples were tested in as-received condition and also with different starting microstructures described previously.

Similar to ECAP, *In situ* characterization of the deformation zone was performed using Digital Image Correlation (DIC) using a Charged Coupled Device camera (PCO1200 HS) operating in full resolution mode (1280×1024). The region of interest is illuminated using a Cole Parmer fiber optic illuminator (catalog # 41723) directed obliquely with respect to the sapphire window whereby flooding of the CCD is avoided and adequate brightness and contrast are achieved. In this manner, a recording frame rate of ~118 fps is obtained. Illumination results in a concentration of asperities (light/dark spots) on the surface. Motion of these asperities that appeared as light/dark spots are tracked through the sequence of consecutive image pairs, originally acquired using the PCO high speed camera. This is done using cross correlation algorithms whereby velocity gradient tensor fields due to deformation imposed during IE are

generated. Subsequently, mechanics of deformation comprising strain, strain-rate and rotation fields prevalent during IE are extracted from the velocity gradient tensor fields using post-processing sub-routines. Accuracies of $<1\ s^{-1}$ in strain-rate fields extracted using this technique have been verified previously(S. Basu & M. R. Shankar, 2014b; S. Shekhar, Cai, Basu, Abolghasem, & Shankar, 2011).

Figure 14c shows a time-sequence of images of the material flow for Al through the deformation zone captured by CCD camera during IE. Motion of some asperities is also marked in this figure. DIC is performed on the sets of images in which the flow of material reached to steady state condition. Here, steady state refers to an approximate stationary flow of material during forming process, which is independent of time(Zienkiewicz, 1974).

The experimental matrix and measured parameters using DIC, load cell, etc. are provided in Table 3-5 for some conditions. The details of the measurements/calculations for each condition will be explained in details subsequently (next chapter).

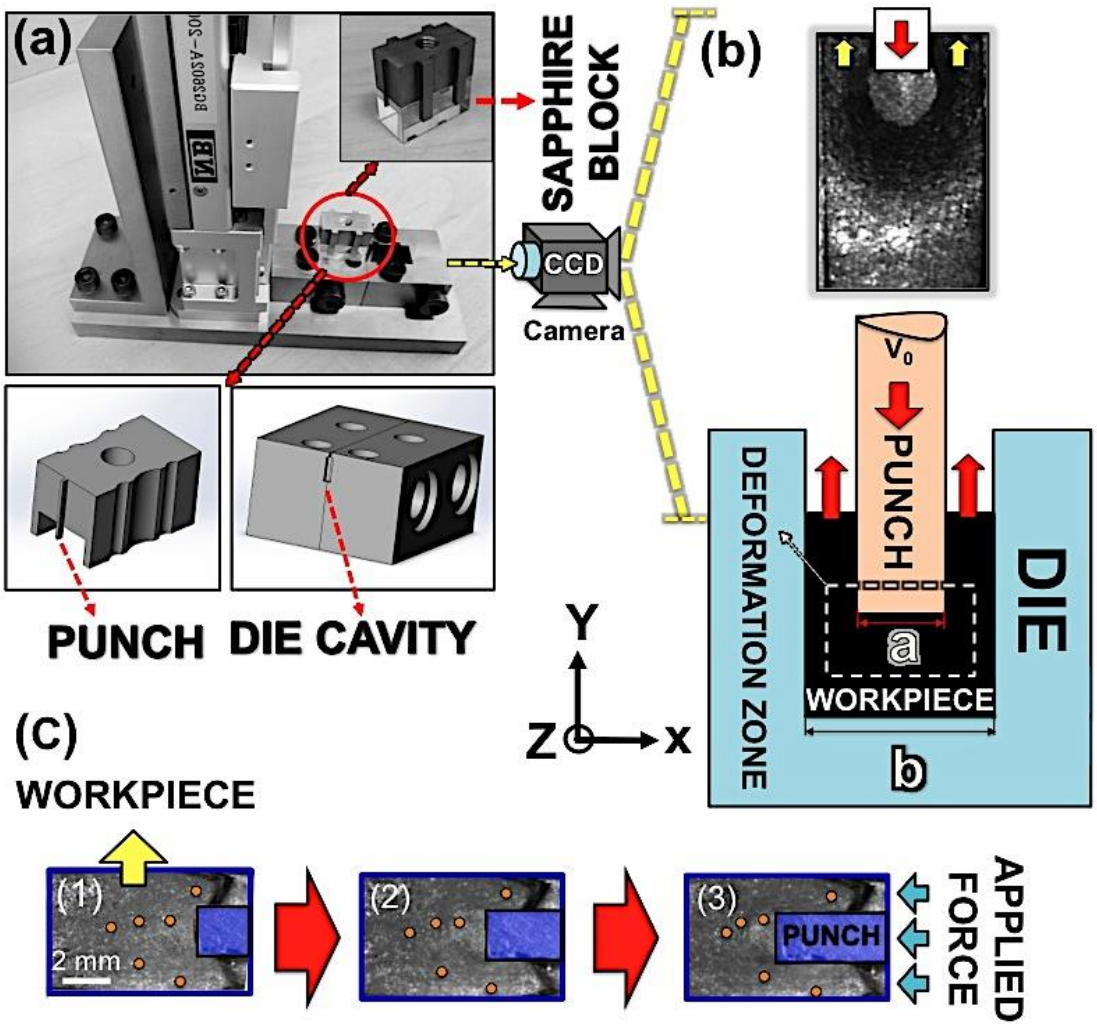

Figure 14: a) Assembled indirect extrusion setup showing die components including die cavity, punch and sapphire block. The sample is placed in the die cavity. Indirect extrusion is performed when the punch is advanced into the sample. Sapphire block provides constraint ensuing plane-strain conditions while allowing for imaging of the deformation. This setup is capable of facilitating *in situ* observation of deformation using high-speed camera. b) Schematic of indirect extrusion process and its parameters, top inset shows the material flow observed through the transparent sapphire block, and c) Sequence of images captures using CCD camera, motion of asperities is observed during deformation of Pb.

5.2.2 Material system

Crystalline metals such as commercially pure Pb, Al 1100, OFHC Cu all having F.C.C. crystal structures were used in which deformations are accommodated by cross slip. Since, the main objective of this effort is to understand the fundamental underpinnings that relate the deformation field variables to the evolving microstructure we will remain focused on pure single-phase metals.

5.2.3 Methods to create various microstructures

Crystalline metals used in this research were subjected to a series of deformation processing and heat treatment to create various microstructures. All aforementioned materials were used in as-received condition. Generally materials in as-received mode consist of a microcrystalline structure with almost uniform grain size distribution. In order to create other desired microstructures, large scale orthogonal machining was employed. This method is known as Severe Plastic Deformation (SPD) techniques whereby very large strains typically involving complex stress state or shear strain are imposed into the metal. Orthogonal machining imposes severe shear using a wedge-shaped cutting edge characterized by the rake angle (α) that advances against a workpiece, which is schematically illustrated in

Figure 15a. When the thickness of the workpiece is much larger than depth of cut (a_0), the plane strain condition is prevailed in the deformation zone (Palmer & Oxley, 1959). Orthogonal machining has a great potential to create various microstructures depending on the material system and processing conditions (Basu, Abolghasem, & Shankar, 2013; Shankar, Chandrasekar, King, & Compton, 2005). Varying deformation conditions by varying the tool rake angle and cutting speed from ~1 up to 2000 mm/s result in a wide range of strain, strain-rate, and temperature and consequently various final microstructures during machining.

Effective strain imposed on the chip in the deformation zone during LSM is given by: $\varepsilon = \frac{\cos\alpha}{\sqrt{3}\,\sin\varphi\cos(\varphi-\alpha)}$, Where φ (shear angle) is a function of ${a_0}/{a_c}$: $\tan\varphi = \frac{{a_0}/{a_c}\cos\alpha}{1-{a_0}/{a_c}\sin\alpha}$ (P Oxley, 1962). As a consequence of the severe imposed shear strain, material forming the chip undergoes severe refinement, featuring a UFG microstructure (Sevier et al., 2006). Additionally, owing to the deformation geometry, the final microstructures in the chip also feature simple shear type of texture (W. Lee & Zhou, 1993). The deformation zone of machining also penetrates into the workpiece underneath the tool edge (Pu et al., 2011); therefore leaving deformed microstructure in its wake.

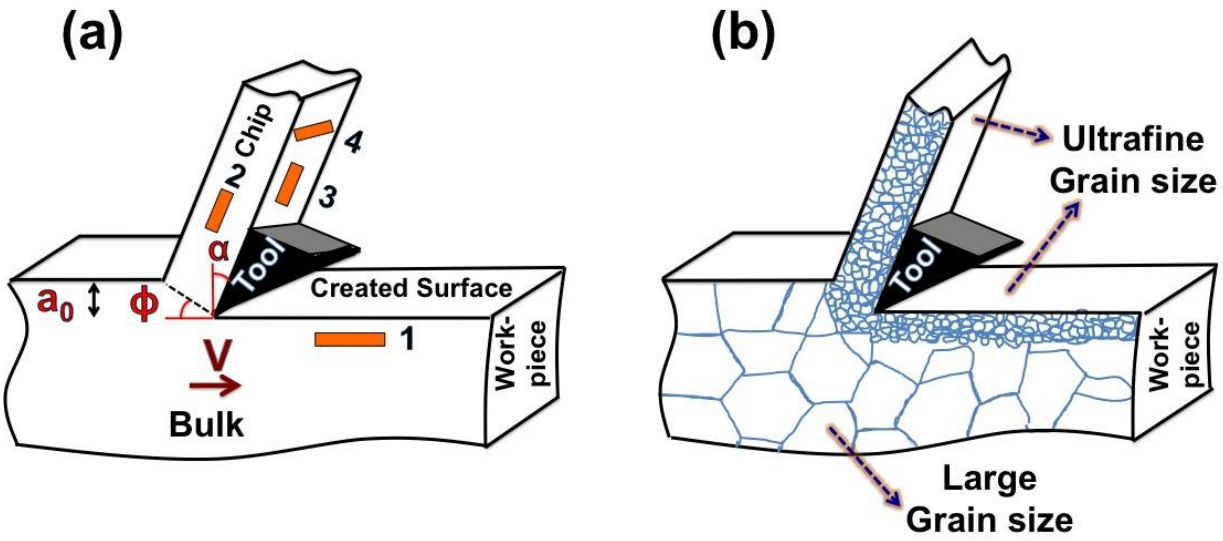

Figure 15:) Schematic of orthogonal machining, showing geometry of the process and deformation parameters. 1, 2, 3 and 4 are locations from which samples for microforming were cut and prepared. b) Schematic shows the gradient of grain size in the workpiece and chip after machining, showing an ultrafine grained microstructure in the chip and on the freshly created surface and large grain size in the bulk.

The contiguity of the deformation zones giving rise to the chip and the freshly generated surface results in microstructures being mirrored between them. It must be noted that material forming the chip undergoes plastic deformation progressively as it traverses through the deformation zone due to the advancing tool.

Figure 15 shows the location in the deformed workpieces machining where the samples were cut. The gradient of grain size in the workpiece after machining. The thickness of ultrafine layer depends on the processing conditions e.g. tool rake angle, speed, depth of cut, etc. and material properties. Location 2 is the direction corresponding to front view of the chip cut during machining, 3 and 4 correspond to the direction of side view in the vertical and horizontal directions in the deformed chip from which samples for indirect microextrusion were cut. Samples cut in the 3, 4 and 5 directions are marked as F, S_H and S_V respectively, corresponding to the front, side-horizontal and side-vertical directions. Location 1 is where the samples cut for deep drawing experiment (next chapter).

5.2.4 Microstructure design and Sample preparation techniques

Al 1100 and OFHC Cu sheets were used in as-received conditions ($Al_{as\text{-}received}$ and $Cu_{as\text{-}received}$) and cut with the required dimension. Effect of grain size is also studied during indirect microextrusion. Heat treatment of Al was done at 823 K for 3 hrs (Al_{3hrs}) and 20 hours ($Al_{full\text{-}anneal}$) to create microstructures featuring various initial grain sizes. Annealing of Cu sheets was performed at 973 K for 20 hrs ($Cu_{full\text{-}anneal}$).

Ultrafine and bimodal/lamellar structures were created using large strain machining (0, 20 ad 40° tool rake angles, 300 μm depth of cut, 5 mm/s cutting speed) of Cu bulk and samples were cut from the chip in different orientations (2,3 and 4. Samples with a rectangular shape were extruded using indirect microextrusion die by applying force in the specified orientations.

5.2.5 Orientation image microscopy (OIM)

Pre and post mortem orientation imaging microscopy was performed on the samples using Electron Back Scattered Diffraction in a Philips XL 30 SEM equipped with a Hikari EBSD detector. Al and Cu samples were mounted in the epoxy and mechanically polished in a Struers down to 0.04 μm using colloidal silica for final step. Accelerating voltage used to perform OIM is typically 20KV and a spot size ranging from 0.05 to 2 μm depending on the grain size was set. Using 'TSL OIM 5.0/6.0' software, broad spectrum of information about the microstructure characteristics e.g. average grain size, sub-grain size, local misorientation, texture, etc. was achieved from EBSD data. 'TSL' provides a series of useful plots/maps for better characterization and analysis of evolved microstructures, among them we used: GOS (Grain orientation spread): shows Strain in isolated grain, the average orientation is first calculated for each grain. The spread is then the average deviation between the orientation of each point in the grain and the grain average; IQ (Image quality): lower IQ is due to the presence of grain boundaries, sub-grains and strains, it can be used to evaluate the amount of deformation; KAM (Kernel average misorientation): One good indicator of strain in crystalline materials are local variations in misorientations shown in KAM maps, for a given point, the average misorientation of that point with all of its neighbors is calculated with the proviso that misorientations exceeding some tolerance value (Maximum misorientation). Higher KAM shows higher internal strains or local strains in the grains, resulted in crystal rotations; Pole Figures: shows the distribution of crystallographic orientation in polycrystalline materials. The ODF is a means of statistically describing the texture or preferred orientation and is the keystone of texture analysis. Additionally, grain boundary characteristics and other quantitative information of these plots/maps are also obtained using 'TSL' software.

5.2.6 Geometrically Necessary Dislocation (GND) density maps

OIM data was utilized to characterize the geometrically necessary density field, ρ_{GND}. This was done using the procedure described in(Demir, Raabe, Zaafarani, & Zaefferer, 2009). ρ_{GND} is approximated as the norm of Nye's dislocation tensor α_{ij} which is calculated using:

$$\underline{\alpha} = \underline{\nabla} \times \underline{\beta} \tag{13}$$

where β_{kl} is the elastic part in the distortion tensor, decomposed additively from the total distortion tensor. β_{kl} can be further decomposed additively into the stretch ϵ_{kl} and the rotation g_{kl} components in which, the stretch is neglected. Previous investigations using this technique have resulted in valuable scientific contributions(Demir et al., 2009). This results in:

$$\underline{\alpha} \approx \underline{\nabla} \times \underline{g} \tag{14}$$

Here, g_{kl} is processed from empirically acquired OIM data. In our experiments, the Bunge components (φ_1, Φ, φ_2) obtained from EBSD are converted to the rotation tensor which is taken as g . Finally, equation (14) is implemented numerically.

5.2.7 Optical microscopy

Another post-deformation analysis of evolved microstructure during microforming was made through the optical image microscopy. Microstructures were characterized using crossed polarized light and the results were compared to OIM graphs. To have a better contrast in optical images, Al and Cu samples were slightly etched using 90:10:15 ml of H_2O, HF, HCl and 90:10 of H_2O_2 HNO_3 for a required time respectively. Digital light-optical microscope that offers

spatial lateral resolutions down to ~500 nm is used for optical imaging. Additionally, roughness/topography of the created surfaces of microproducts deformed by indirect extrusion and deep drawing with respect to the prior microstructure was characterized using a highly versatile Keyence VHX 600 system. It was used for quantitative surface topographical measurements into the realm of sub-micron dimensions.

5.2.8 Texture simulation

Texture evolution in different regions the microproducts produced by indirect microextrusion is simulated using Visco Plastic Self Consistent (VPSC) model (Wang et al., 2010). In VPSC model, each grain is a visco-plastic anisotropic ellipsoidal inclusion embedded in a visco-plastic anisotropic Homogeneous Effective Medium (HEM). A FORTRAN implementation of this model was employed which uses a discretized ODF in the form of a collection of orientations as input. Initial texture (discrete orientations - Euler angles and weights), active slip and twin systems (and their hardening parameters) and macroscopic boundary conditions (strain history obtained by DIC) are input VPSC. Data of 1000 random orientation distributions are input to the VPSC code for performing texture evolution simulations. The Voce material model for Cu is used. To calibrate the VPSC model, deformation history of deformed material by indirect microextrusion in different regions of deformation zone (beneath the plunger, close to the corner of the plunger and extruded side walls) are obtained from empirical measurements using DIC. The velocity vector fields during indirect microextrusion obtained from DIC are input to the VPSC code for simulating texture evolution in microproducts. Simulated textures were then compared with empirical texture measurements

obtained from EBSD data analysis and parameters of the VPSC model were updated until a good match between observed and experimental data is acquired.

Table 3: Deformation parameters measured for indirect extrusion of Pb for punch velocity 2 mm/s. a is Punch width and b is die width (Figure 14b). F_Y is the measured force by load cell in Y direction (Figure 14b). k is extrusion constant (Equation (16)). h_{SF} and θ_{SF} are thickness and angle of deformation zone II (Figure 17b) based on strain-rate field measurements (Figures 16 and 18). h_{RF} and θ_{RF} are thickness and angles of deformation zone II based on rotation field measurements (Figures 20 and 21). $\dot{\gamma}$ and ε_{eff} are average strain-rate and effective strain in zone II measured by DIC.

a (mm)	b (mm)	F_Y (N)	k (MPa)	h_{SF} (mm)	h_{RF} (mm)	θ_{SF} (deg)	θ_{RF} (deg)	$\dot{\gamma}$ 1/s	ε_{eff}
2	5	70	13.7	0.30	0.63	37	30	1.8	1.2
	4	80	14.4	0.24	0.56	30	24	2.1	1.8
	3	120	18.2	0.18	0.43	20	13	2.4	2.5
1	2.5	40	15.6	0.37	0.49	43	40	2.8	1.9
	2	50	18	0.31	0.38	35	30	3.7	3.2
	1.5	70	21.3	0.23	0.32	23	20	4.7	4.3

Table 4: Deformation parameters measured for indirect extrusion of Pb for punch velocity 20 mm/s. a is Punch width and b is die width (Figure 14b). F_Y is the measured force by load cell in Y direction (Figure 14b). k is extrusion constant (Equation (16)). h_{SF} and θ_{SF} are thickness and angle of deformation zone II (Figure 17b) based on strain-rate field measurements (Figures 16 and 18). h_{RF} and θ_{RF} are thickness and angles of deformation zone II based on rotation field measurements (Figures 20 and 21). $\dot{\gamma}$ and ε_{eff} are average strain-rate and effective strain in zone II measured by DIC.

a (mm)	b (mm)	F_Y (N)	k (MPa)	h_{SF} (mm)	h_{RF} (mm)	θ_{SF} (deg)	θ_{RF} (deg)	$\dot{\gamma}$ 1/s	ε_{eff}
2	5	110	21.5	0.45	0.65	40	32	4.8	1.9
	4	136	24.6	0.33	0.53	33	25	5.7	2.7
	3	178	27.1	0.25	0.46	24	16	6.9	3.6
1	2.5	69	27.2	0.46	0.52	44	41	7.2	3.7
	2	77	27.9	0.40	0.39	37	33	10.1	5.3
	1.5	97	29.7	0.33	0.34	26	24	13.4	6.2

Table 5: Deformation parameters measured for indirect extrusion of pure Al with different initial grain sizes (δ). a is Punch width and b is die width (Figure 14b) and punch velocity is 5 mm/s. F_Y is the measured force by load cell in Y direction (Figure 14b). k is extrusion constant (Equation (16)). h_{RF}/b and θ_{RF} are normalized thickness and angles of deformation zone II based on rotation field measurements (Figure 23, insets D, I and N). $\dot{\gamma}$ and ε_{eff} are average strain-rate and effective strain in PDZ I, below the punch measured by DIC (Figure 23, insets B, G, L and E, J, P respectively).

a (mm)	b (mm)	δ (μm)	F_Y (N)	k (MPa)	$h_{RF/b}$ (mm)	θ_{RF} (deg)	$\dot{\gamma}$ 1/s	ε_{eff}
0.5	1.5	150	68	111.8	0.37	38	2.8	1.2
		70	100	164.5	0.26	30	4.2	1.9
		30	140	230.2	0.22	24	5.7	2.9

5.3 RESULTS AND DISCUSSION

In situ experiments were conducted on commercially pure Lead (Pb), Aluminum (Al 1100) and Copper (OFHC Cu) using small length scale indirect extrusion (IE) device. Parameterization of geometry of Plastic Deformation Zone (PDZ) was performed using Digital Image Correlation (DIC) technique in order to study the effects of the macroscopic/microscopic boundary conditions (e.g. deformation rate, deformation ratio, initial grain size, infigureitial texture, etc.) on mechanical responses at diminishing spatial scales. This was accomplished by post-mortem microstructure characterization using Orientation Imaging Microscopy (OIM) to reveal microstructure/texture evolutions with respect to various starting microstructures. Quality of microproducts was examined by characterization of generated surfaces after deformation using Keyence surface profiler. Finally, *In situ* characterization aided by high speed imaging of indirect extrusion coupled with a Visco-Plastic Self-Consistent (VPSC) model was used to predict the evolved textures in different regions of deformation zone and the results were compared to OIM observations. These findings provide a beneficial background about characteristics of plastic deformation zone and its distribution in order to optimize and control the properties of miniaturized components.

5.3.1 Indirect extrusion of Pb

Parameterization of deformation zone geometry was performed in Pb by studying the key elements of deformation mechanics (strain, strain-rate and rotation fields) in order to model deformation behavior for the materials with almost no work hardening capacity as a function of length scale and process parameters. Therefore, the effects arise by microstructural features (e.g. grain size and anisotropy) can be ignored and hence, geometry of deformation can be purely attributed to the process boundary conditions. Here, the assumptions are almost equivalent to

what is prevalent in Slip Line Field (SLF) theory in which there is no account for the effects of work hardening, heat generation and thermal gradients etc. on the deformation field(W.F. Hosford & Caddell, 2011; Rees, 2012). In this section, we present results of the *in situ* measurements to describe scaling effects on the extension/spread of plastic deformation zone.

5.3.1.1 Strain-rate fields

Figure 16 shows the strain-rate fields during IE of Pb in dies with 5, 4 and 3 mm widths and punch with 2 mm width at different deformation speeds. A heterogeneous deformation zone ensues during indirect extrusion of Pb, the morphology of which is shown in higher magnification in Figure 17a corresponding to extrusion ratio (R) 2 (50% cross section area reduction) for strain-rate cut-off below 2 1/s for better demonstration of the details of PDZ. Here, extrusion ratio refers to(William F Hosford & Caddell, 1993):

$$R = {A_0}/{A_f} \tag{15}$$

where A_0 and A_f are the initial and final cross sections of workpiece. The geometry of deformation is also schematized in Figure 17b using bold white lines showing different regions of plastic deformation zone (PDZ) that are marked as zones I, II and III in displacement field obtained by DIC. θ and h, angle and thickness of zone II of PDZ, are demonstrated in Figure 17b as parameters of deformation zone II which is undergoing significant changes by varying the extrusion ratio and scaling of deformation geometry (Figure 16). The morphology of PDZ is relatable to that suggested by SLF analysis for backward extrusion-type problem with extrusion ratio 2 for elastic perfectly plastic material in plane strain condition (Figure 18c and d), corresponding to frictionless and sticking friction conditions respectively(Chakrabarty, 2012; W.F. Hosford & Caddell, 2011). Flow patterns shown in these figures demonstrate trajectories

corresponding to the direction of material flow with maximum shear strain-rates assuming no strain increment/work hardening along these trajectories. From Figure 17 a, paths with high strain-rate are localized in the two arms extended from the corners of the punch to the walls of the die with an angle θ marked as zone II and also a ring shape zone (zone I) that developed below the punch and diffused into the bulk of the workpiece (Figure 17 b). Intimate sticking friction is assumed at the interface of the material and die wall that creates frictional drag between the workpiece and die wall. For sticking friction, from SLF perspective, α/β slip lines meet the perfectly rough surfaces at angles $0^{\circ}/90^{\circ}$. It is seen that flow patterns observed in Figure 16 for different extrusion ratios and speeds follow sticking friction condition pattern (Figure 17 d). It is found that the scale free angle θ is approximated as ~17° for extrusion ratio (R) 2 and d, the normal distance from the corner of the punch (point A in Figure 17 d) to where the slip lines of zone II meet die wall (point C in Figure 17 d) is ~3.31L (Figure 17 d)(Chakrabarty, 2012).

Empirical observations confirm that the constriction of length scales influences the shape of the deformation zone. This is evident from a comparison of insets (A to O) shown in Figure 16. It is observed that the morphology of deformation zone during indirect extrusion of Pb maintains the general shape schematized in Figure 17 b across different punch velocities and die widths. However, it is evident that with increasing the punch velocity, the zones of I and II assumed more diffused and curvilinear morphologies compared with lower ram velocities. Insets in bottom row of Figure 16 (K to O) corresponding to indirect extrusion with 3 mm die width feature significantly shallower angled deformation zones (θ in Figure 17 b) when compared with the top rows insets (A to J) corresponding to indirect extrusion dies with 4 and 5 mm widths.

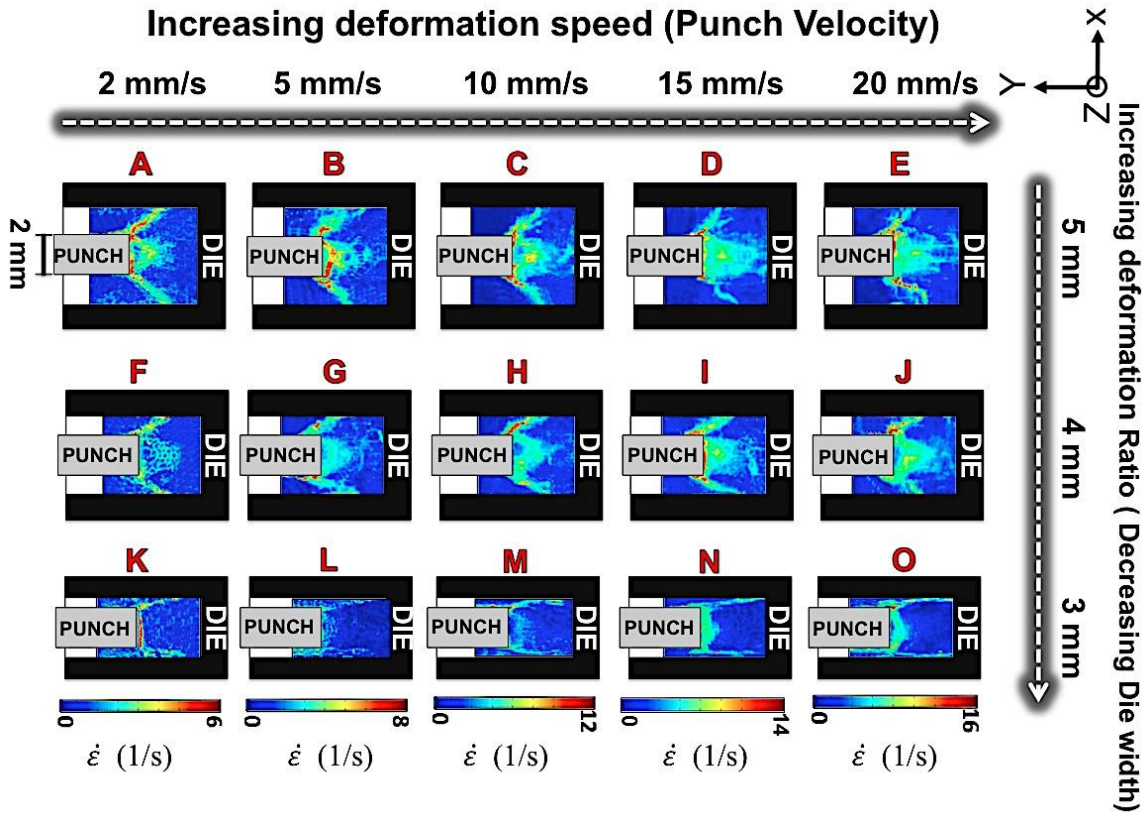

Figure 16: Strain-rate fields revealed by DIC for indirect extrusion of Pb for various deformation geometries and speeds (insets of A to O). Width of the punch is 2 mm in this set of experiments.

Additionally, the thickness of zone II (h in Figure 17 b) changes with increasing the extrusion ratio. Based on equation 15, extrusion ratios are calculated as 1.66, 2 and 3 for dies with 5, 4 and 3 mm widths. Higher extrusion ratios signify higher values for imposed strains ($\varepsilon = ln\, R$)(William F Hosford & Caddell, 1993).

The influence of scale and geometry of IE was quantified by parameterizing the shape of the deformation zone in terms of θ_{SF} and h_{SF} (Figure 17 b). Here, subscript SF refers to strain-rate field. These were quantified using DIC (Figure 16) for results obtained for 2 mm/s and 20

mm/s punch velocities (first and last columns of Figure 17), summarized in Table 3 and 4. It is seen that θ_{SF} changes from 37 ° to 20 ° and h_{SF} from 0.3 to 0.18 with increasing deformation ratio (R) which implies decrease in the thickness of zone II. These are corresponding to measurements obtained for 2 mm/s punch velocity and 2 mm punch width (Table 3). By normalizing the values of h_{SF} with respect to the width of the die for each extrusion ratio in Figure 16, it is found that this value is almost the same for all three extrusion ratios ~ 0.06. Therefore, the normalized thickness of the deformation zone does not change significantly by varying the extrusion ratio.

Table 4 shows same measurements of parameters of deformation zone and their variation by changing deformation ratio for 20 mm/s punch velocity. Results from this quantification reveal that the normalized thickness of deformation zone II ($h_{SF}\ /b$) is approximately 0.085, which shows an increase in this parameter with increasing the deformation speed. It also show that the angle θ_{SF} increases for all extrusion ratios.

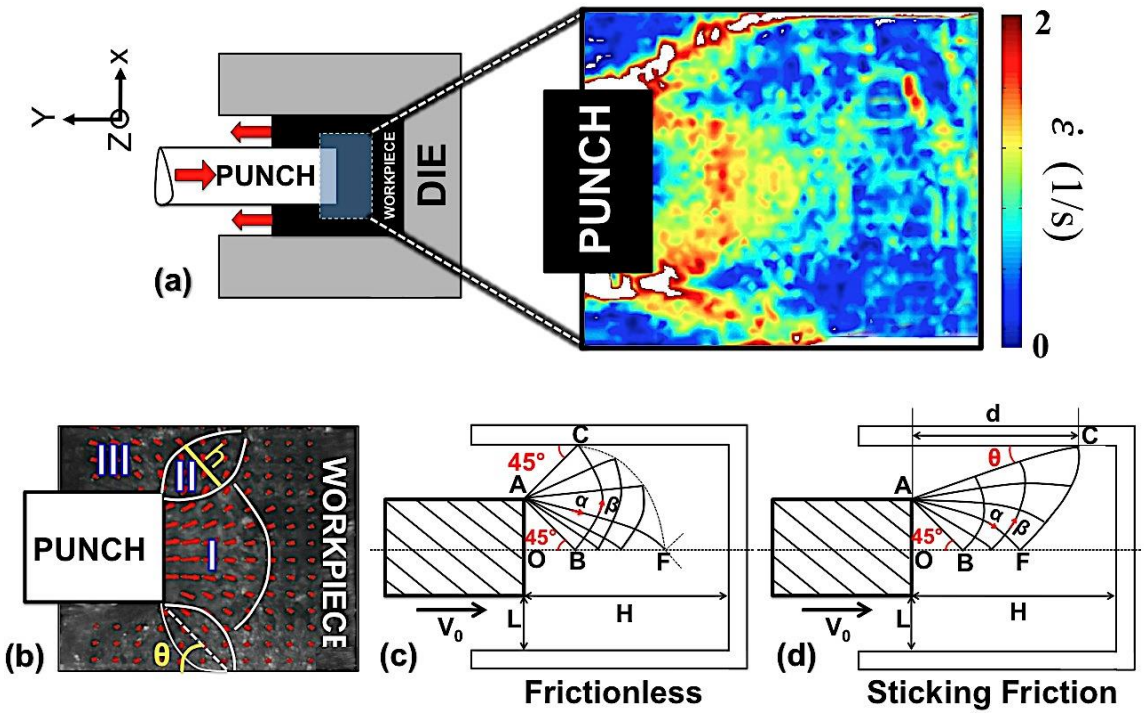

Figure 17:) Schematic of indirect extrusion process, inset shows strain-rate field under the punch for 50% area reduction or extrusion ratio 2 in Pb. Strain-rate filed is represented below the cut-off 2 whereby regions with higher values appeared in white color. b) Different regions of the deformation zone appeared in strain-rate fields marked as zones I and II and III in displacement field developed under the punch during deformation. Additionally angle of zone II with extrusion die wall and also its thickness are marked as θ and h respectively. c) and d) Slip line fields in indirect extrusion for perfectly elastic–plastic material in frictionless and sticking friction conditions respectively(Chakrabarty, 2012).

Figure 18 illustrates the strain-rate fields for 1 mm punch width with 2.5, 2 and 1.5 mm die widths. Within this set, the ratios are kept the same as Figure 16, but the process is scaled down in a geometrically similar manner to ½ of previous dimensions. Similar deformation zone morphologies are obtained compared to strain-rate fields shown in Figure 16. However, it is seen that zone I is more localized and does not spread into the workpiece as compared with results exhibited in Figure 16. It has been argued based on SLF theory that when the ratio H/a (length of the sample over the width of the punch) is >8.75, a localized deformation appears below the punch(W.F. Hosford & Caddell, 2011) (zone I), similar to what is observed during indentation. Here, for 1 mm punch width the ratio H/a is equal to 10. An extended deformation zone I is observed during the IE of Pb for 2 mm punch width (Figure 16) where the ratio H/a is 5. It is also seen that all three zones became almost unified with increasing the extrusion ratio (i.e., insets K, L etc, Figure 18).

Apart from this, θ_{SF} values for 1 mm punch widths (Figure 17) are consistently larger than those prevalent during IE with 2 mm punch width, manifesting through a more diffuse zone II, often merging into zone III (Table 3 and 4). It is important to note that θ_{SF} corresponding to 50 % area reduction (rows 2 and 5 in Table 3 and 4) is significantly larger than θ suggested by scale free slip line model (Figure 17 d). Measurements show that this value is larger than 30° for both scales and velocities, almost twice as what is suggested by SLF theory (~17°)(Chakrabarty, 2012). Larger angles appeared in deformation zone II also result in reducing distance d in Figure 17 d from ~3.31L to a range between ~1.3 to 1.7L depending on the scale and velocity. Therefore, this implies that although the overall geometry of deformation zone almost remains similar by scaling down the process, its quantities do not follow the values predicted for scale free deformation fields suggested by analytical SLF models.

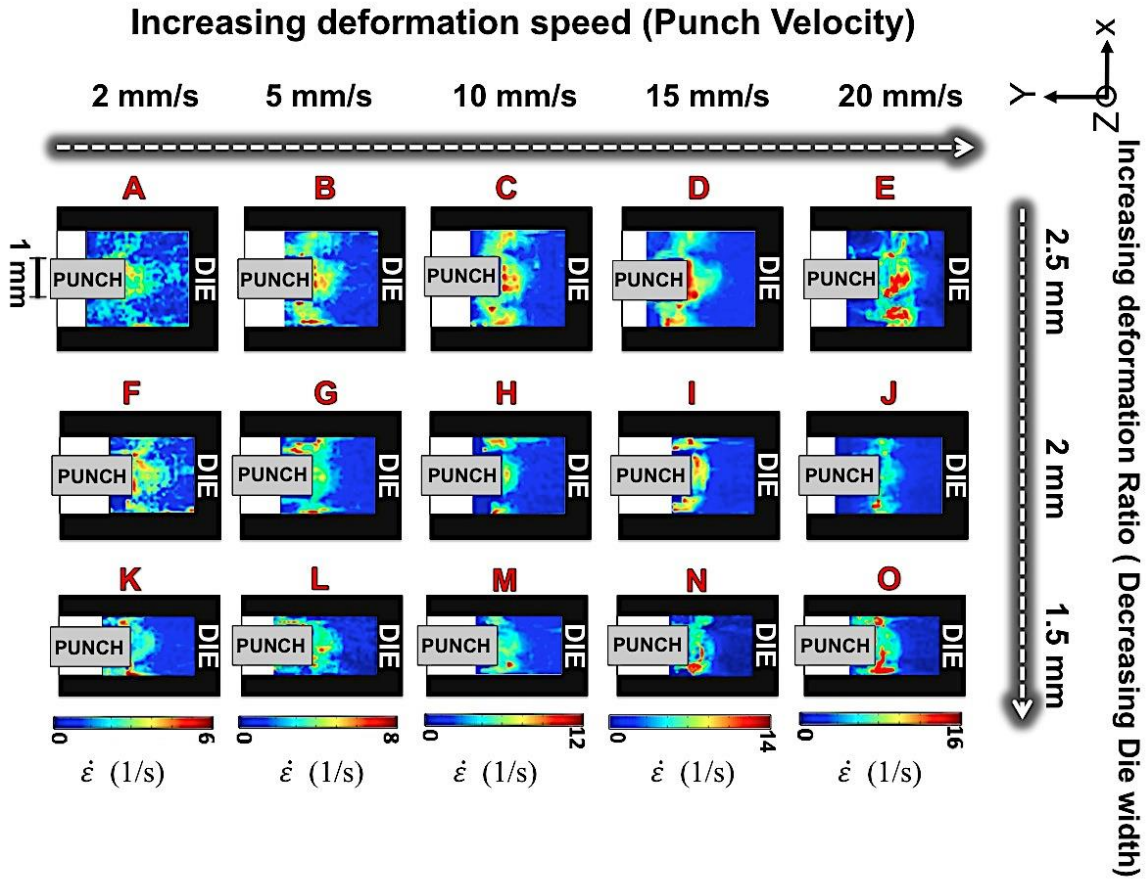

Figure 18: Strain-rate fields revealed by DIC for indirect extrusion of Pb for various deformation geometries and speeds (insets of A to O). Width of the punch is 1 mm in this set of experiments.

Another quantification of deformation zone is normalized values of h_{SF} for punch width 1 mm shown in Table 1 and 2, h_{SF}/b ≈0.15 and 0.20 for 2 and 20 mm/s punch velocities respectively. This indicates that there is an increase in the thickness of zone II in PDZ, instigated by process scale down ($h_{SF}/b \approx 0.06$ and 0.085 for punch widths of 2 mm). Consequently, the normalized thickness of zone II increases by the factor ~2.3-2.5 times with scale down of the process.

From all aforementioned observations of strain-rate fields in Figure 17 and 19 and quantified results in Table 3 and 4, it was observed that the geometry of deformation is not significantly influenced by varying the punch velocity. However, effects of deformation rate might appear to be more significant in parameters pertaining to the ongoing deformation mechanics such as strain-rate and strain that may result in process instability particularly by scaling down the process. These effects will be discussed in the next sections.

Average strain-rate ($\dot{\gamma}$) in zone II, exhibited during IE with conditions shown in Figure 17 and 19 for 2 and 20 mm/s punch velocities, respectively, are illustrated in Table 3 and 4. These values significantly increase upon process scale down. This effect is attributed to a coupled effect of greater interaction of workpiece with die through friction (surface area effect) and more importantly from localization of strain fields. These will result in non-uniformities in microstructures within parts created by IE, likely manifesting instabilities in mechanical response of the fabricated machine element.

To probe these effects further, values of force along the directions X, Y and Z were measured. Results along the extrusion direction (Y direction) are reported in Table 3 and 4. In extrusion process, force along the Y direction (F_Y) is expressed as(William F Hosford & Caddell, 1993):

$$F_Y = k\, A_0\, lnR \tag{16}$$

where k is extrusion constant, an overall factor which accounts for the flow stress of material, friction and inhomogeneity of deformation(E. Lee, Mallett, & Yang, 1977). That is because inhomogeneity in deformation and hence inhomogeneous distribution of plastic strains results in increasing internal stresses that affects the external forces(Prime & Hill, 2002; Teoh & Lee, 1991). The k values were found close to the shear strength of Pb(Handbook, 1979). From Table

3, it is seen that k increases with increasing extrusion ratio as well as scale down of the process. This effect is magnified with increasing the velocity (Table 4). Effectively, the shear strength of elastic perfectly plastic material with almost no work hardening capacity such as Pb does not increase significantly with the imposition of strain during the process. Consequently, this significant evolution represented in Table 3 and 4 for the values of k with scaling down the process and increasing the velocity is related to frictional effect and deformation inhomogeneity as mentioned previously. It is seen that the value of k is increased in a range of ~14-25% with scale down of the process by ½ and ~40-55% with velocity (extracted from Table 3 and 4). These factors suggest more instability in the mechanical response of the material during the process and hence heterogeneity in process outcomes. Inhomogeneity factor, which is responsible for creating strain gradient during deformation, will appear with better resolution in strain fields that will be discussed in the next section.

5.3.1.2 Strain fields

Figure 19 illustrates the strain fields ensuing upon IE on Pb and reveals that the deformation zone is more diffuse and spreads into the workpiece at larger extrusion ratios and smaller length scales. Additionally, it is evident that for a punch width of 2 mm, increasing punch velocities from 2 mm/s to 20 mm/s localizes the strain field within bands in zone I (insets A to F of Figure 19). This discontinuity in strain fields suggests shear localization and banding in the material, and will promote inhomogeneity in resulting microstructure. However, this effect declined with scale down of the process (1 mm punch width: insets G to M of Figure 18) exhibiting more unified and continuous strain field in the vicinity of the punch.

Empirically calculated mean effective strains ε_{eff} (using DIC) in zone II imposed during IE are shown in Table 3 and 4 for process parameters (at 2 and 20 mm/s punch velocity) studied here. The anticipated increase in value varies from ~0.5 to ~0.7 and then to ~1.1 for ratios 1.66, 2 and 3 respectively using $\varepsilon = ln\, R$. This formula for strain is derived analytically, from shape change imposed during IE. However, empirically calculated mean strains in Zone II exhibited larger values than that expected analytically (Table 3 and 4, last columns). This effect originates from friction, coupled with constriction of deformation within a smaller volume of material.

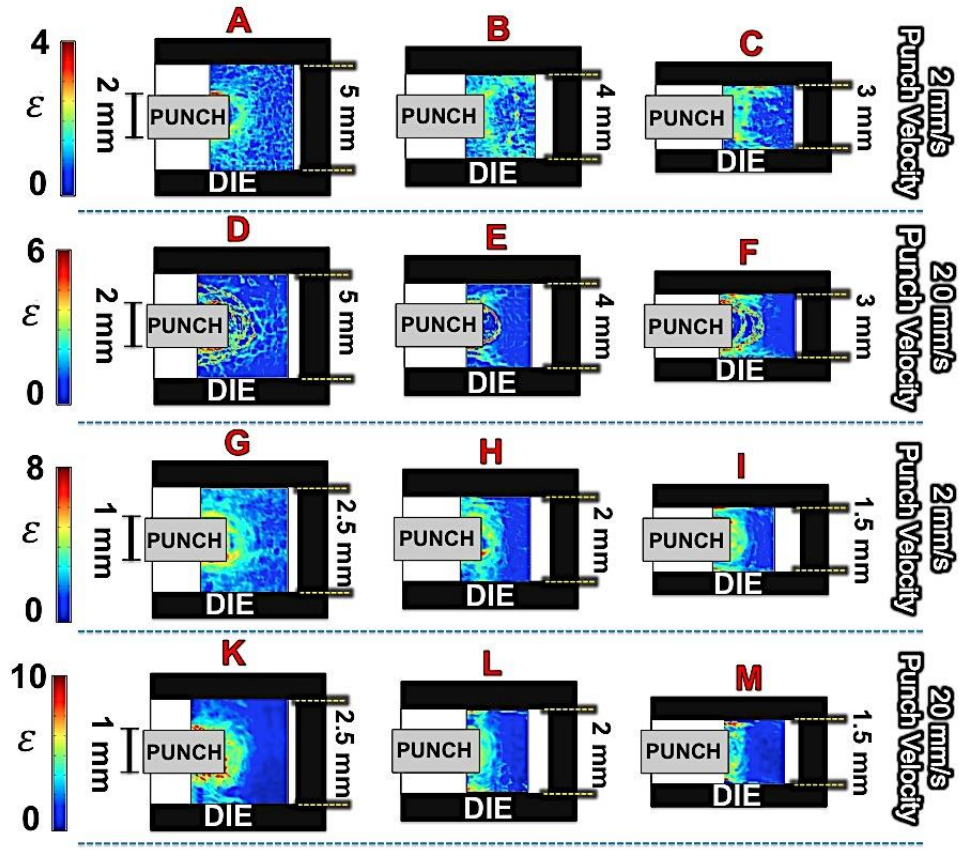

Figure 19: Strain field revealed by DIC for indirect extrusion of Pb for various deformation geometries and speeds (A to M) in dies with 1 and 2 mm punch widths.

5.3.1.3 Rotation fields

Figure 20 and 21 illustrate the result from this calculation for punch widths of 2 mm and 1 mm for different scales and deformation speeds. It is seen that the rotation of material elements is more concentrated in zone II of PDZ for all conditions. However, it is lesser in zones III and I. It is also seen that with increasing ratio of extrusion, magnitude of rotation (ω) increases in zone III and almost merges with zone II.

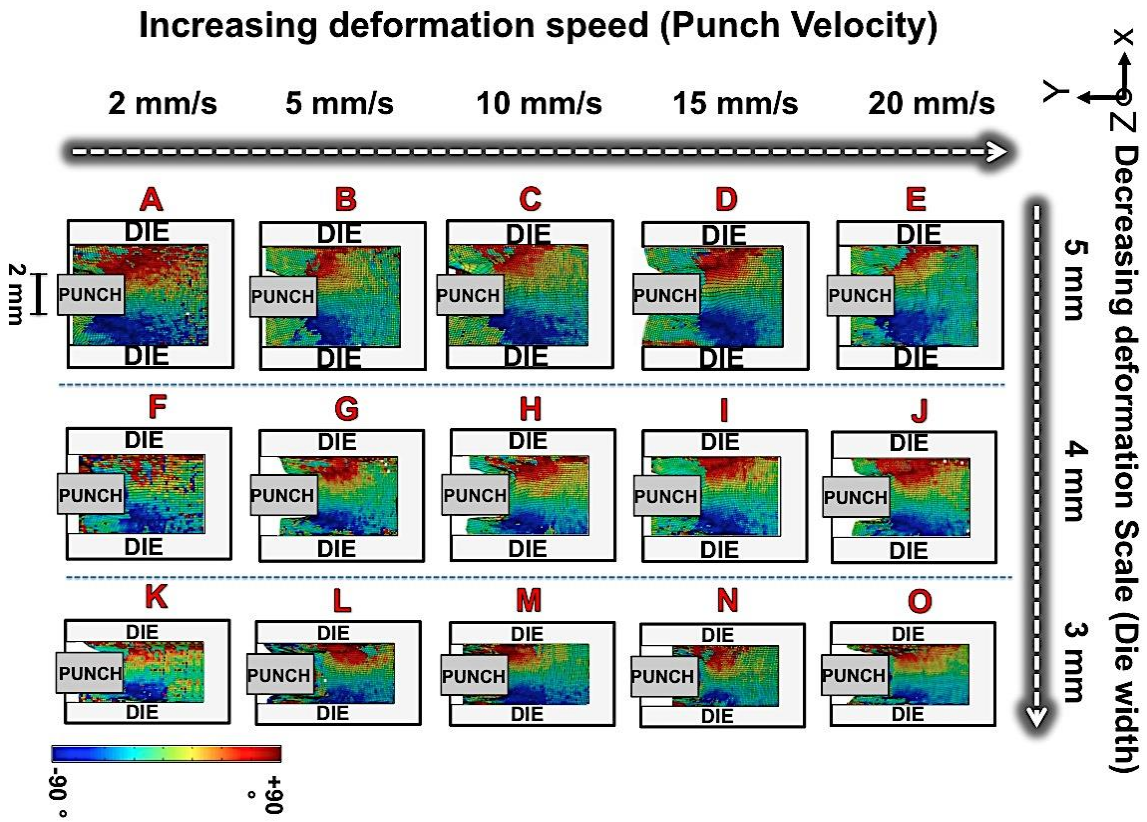

Figure 20: Rotation fields revealed by DIC for indirect extrusion of Pb for various deformation geometries and speeds (insets of A to O). Width of the punch is 2 mm in this set of experiments.

A somewhat similar but more intense phenomenon is seen when the deformation zone is further constricted by reducing the width of the die while keeping the extrusion ratio same (Figure 21). With increasing the deformation speed, rotation increases in the zone I (below the punch), but it does not show a significant increase in magnitude.

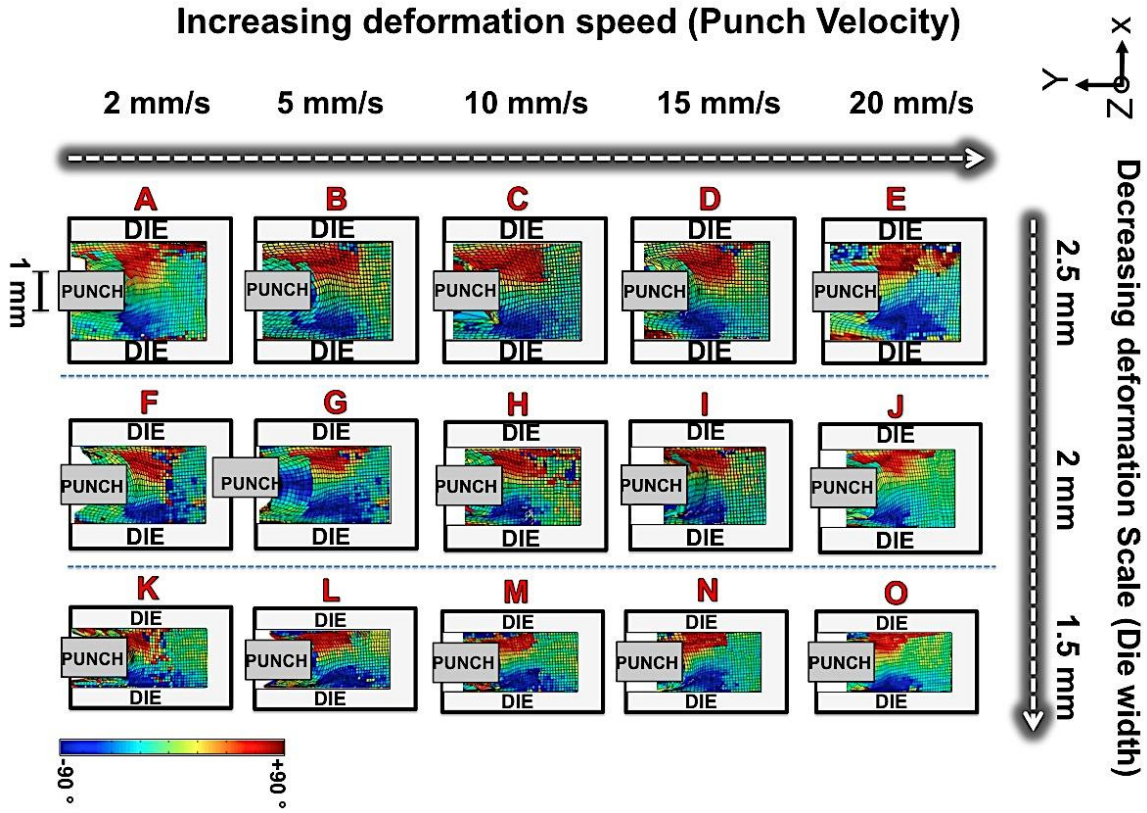

Figure 21: Rotation fields revealed by DIC for indirect extrusion of Pb for various deformation geometries and speeds (insets of A to O). Width of the punch is 1 mm in this set of experiments.

Another manifestation of spatial constriction of the deformation geometry on ensuing plastic flow is observed in the rotation fields. Angles and thickness (θ_{RF} and h_{RF}) measured for zone II of rotation fields are shown in Table 3 and 4 for 2 and 20 mm/s deformation speeds. Here, subscript RF refers to rotation field. It is seen that the normalized thickness of zone II is less sensitive to process parameters here than witnessed from the strain-rate fields (h_{SF}). For instance, it is found that the normalized thickness of zone II increases by ~1.5 times when the scale of the process was decreased to ½.

With scale down of the process, it is likely that rotations will give rise to process instabilities in materials where ductility is limited. It is expected that rotational fields play an important role in the microstructure evolution in PDZ and also in texture reorientation for indirect extrusion of textured material. For instance, the rotation field determines reorientation of initial texture within regions of the workpiece that undergo large rigid body rotations. This phenomenon, which is more pronounced in smaller length scales may result in significant texture changes(Hirsch & Al-Samman, 2013) that instigate flow instabilities and affect quality of miniaturized products fabricated by microforming operations.

5.3.2 Indirect extrusion of Al

It is known that the polycrystalline work hardening in metals depends on the grain size (δ)(Acharya & Beaudoin, 2000; Thompson, Baskes, & Flanagan, 1973) and it is rationalized using the Hall–Petch relation(Armstrong, Codd, Douthwaite, & Petch, 1962; hall, 1951; Petch, 1953). Mechanical behavior is also modulated by dislocation density increments whereby statistically stored or geometrically necessary dislocations are accumulated in different regions of grains (e.g. grain interior and grain boundary)(Ashby, 1970; Holt, 1970; Nabarro, Basinski, & Holt, 1964). It is known that Geometrically Necessary Dislocations (GNDs) affect plastic flow

and result in enhanced work hardening in polycrystalline materials(Al-Rub & Voyiadjis, 2004; Evers, D.M.Parks, Brekelmans, & Geers, 2002). GNDs are produced as a result of gradients in plastic shear that appear either because of the internal microstructure features (e.g. non-deforming phases/precipitates or grain boundaries) or external boundary conditions (e.g. geometry of loading or volume of material undergoing deformation(N.A. Fleck, G.M. Muller, M.F. Ashby, & J.W. Hutchinson, 1993; Poole, Ashby, & Fleck, 1996).

Spatial inhomogeneity in deformation was seen recently during indirect extrusion of micro scale products. This was shown to originate from anisotropy of single crystals, which dominates material flow in small length scales and results in poor part qualities. Such effects were seen to subdue in the presence of an excess of grain boundaries and grains, wherein the anisotropic nature of material is evened out and isotropy in material flow results in better part qualities(Bakhshi-Koybari, 2002; Chang & Wang, 2010; Rosochowski, Presz, Olejnik, & Richert, 2007; W.L.Chan, Fu, & Yang, 2011).

While previous efforts revealed some consequences of grain size effect on the flow behavior and part quality of miniaturized products, a systematic study of describing how the deformation zone geometry scales with the initial microstructure and how it evolves and manifests the process outcomes is still lacking. In this section, we seek to parameterize deformation zone geometries during indirect extrusion of Al 1100 in small length scale as a function of the starting grain size (δ).

5.3.2.1 Mechanics of deformation (stain-rate, strain and rotation fields)

Figure 22 shows the results of metallography on deformed Al 1100 produced using as-received and heat treated starting microstructures by indirect extrusion. The as-received Al featured a grain size of ~30 μm whereas the annealed Al featured a mean grain size of ~70 μm (3

hours at 823 K) and ~150 μm (20 hours at 823 K). From *in situ* observations using CCD camera as well as post-mortem optical metallography, it is seen that a larger Dead Metal Zone (DMZ) as opposed to Pb was formed during indirect extrusion of Al. This is due to larger work hardening capability of Al(Cardarelli, 2000). In addition, from these observations, we see a concentrated PDZ close to the periphery of the DMZ. This is shown schematically in Figure 22 a.

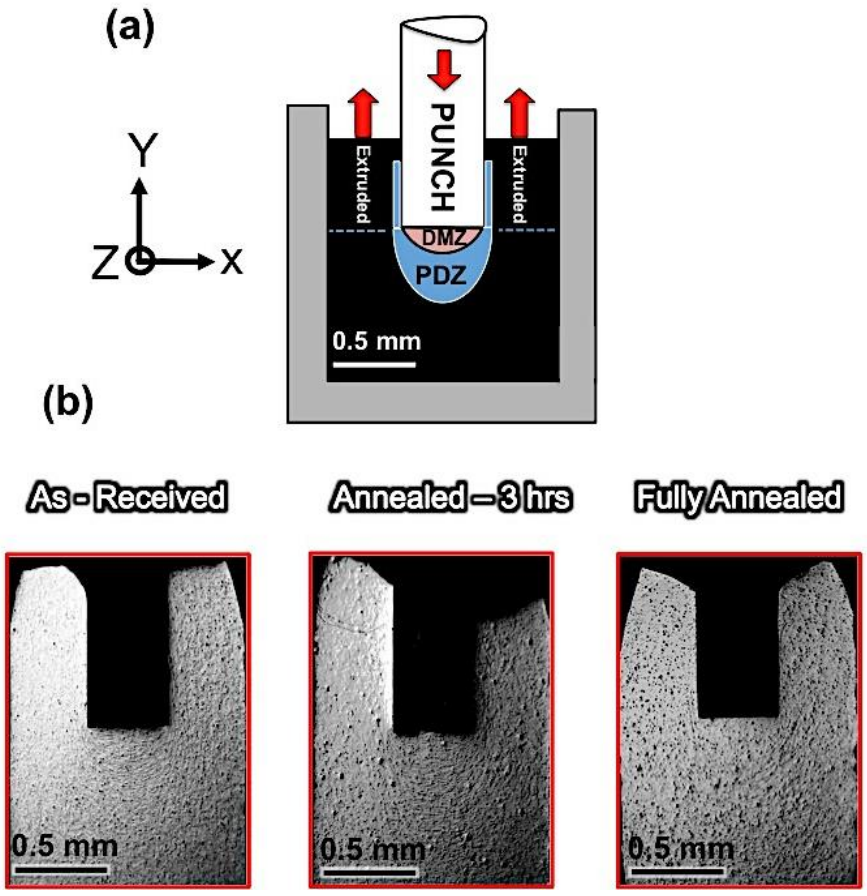

Figure 22: Schematic of indirect extrusion showing different regions of deformation zone. Here, DMZ refers to the area of dead metal zone and PDZ to the area of plastic deformation zone. b) Optical images of polished and etched surfaces of the extruded Al with different initial grain sizes.

It is seen that the quality of deformed products depends on the parameters of initial microstructure (grain size/texture). Here, quality refers to uniformity in internal and top surfaces created in two extruded arms (Figure 22 a). As opposed to the general belief that larger grain sizes are detrimental to the quality of the parts produced in meso/micro scale forming processes(Tiesler & Engel, 2000), we see irregularly shaped parts resulting from Al $_{3hrs}$ parts with medium grain size among all Al samples (Figure 22 b). However, more detailed analysis is needed to clarify simultaneous effects of initial microstructure parameters (grain size/texture) on processing outcomes and their interaction with geometry of the process and macroscopic boundary conditions.

As mentioned above, deformation zone includes two major areas, DMZ and PDZ with a circular morphology formed around the punch (Figure 22 b). A larger DMZ was formed in the sample with largest initial grain size (Al $_{full\text{-}anneal}$) as compared with the other samples (Al $_{as\text{-}received}$ and Al $_{3hrs}$). From the measurement using results shown in Figure 22 b, it is found that the depth of DMZ in workpiece below the punch at centerline is ~130, 170 and 270 μm for Al $_{as\text{-}received}$, Al $_{3hrs}$ and Al $_{full\text{-}anneal}$ conditions respectively.

PDZ appeared as layers of deformed material having a ring-shaped morphology (Figure 22 b). It is seen that PDZ extends further into the workpiece below the punch in Al $_{full\text{-}anneal}$ compared to other conditions. Empirical measurements using optical microscopy revealed that the thickness of PDZ is ~180, 360 and 520 μm for Al $_{as\text{-}received}$, Al$_{3hrs}$ and Al $_{full\text{-}anneal}$ conditions respectively along the centerline. Although the depth of PDZ below the punch is smaller in as-received condition, it has a more localized morphology as opposed to heat-treated conditions.

Figure 23 illustrates *in situ* characterization of mechanics of deformation during IE in Al. Strain-rate and rotation fields are shown at initial and steady states of the process demonstrating

the mechanics of the formation of DMZ and PDZ during IE, caused by the advancing punch. This shows how the paths with high strain-rates evolve during the process and consequently different parts of the deformation zone form. The material at initial state of deformation shows a PDZ with morphology somewhat similar to what is formed during simple compression obtained by slip line solutions(William F Hosford & Caddell, 1993) (insets A, F and K in Figure 24b, c, d). This is because the material initially is in compression mode between the punch and the die before it starts shearing and flowing upward along the die walls. This is obtained by DIC from analyzing the set of images captured from initial state of the deformation. In addition, deformation zone has a branched morphology originating from the interface of DMZ and PDZ in as-received condition. However, these features are absent in the annealed counterparts. This is presumably due to the larger concentration of grain boundaries in the former (as-received) as opposed to the latter (annealed). Therefore, from the observations revealed by DIC, in work hardening material, the geometry of deformation zone has different features compared with non-work hardening materials as discussed in the previous section for model material Lead. It is observed that the evolution of dead metal and plastic deformation zones below the punch (Figure 22 a) during the deformation governs geometry of deformation zone throughout the sample. It is seen that in Al the deformation zone marked as zone II in Figure 17 b did not appear as evident as it appeared in IE of Pb. It also did not originate from the corners of the punch and somewhat shifted towards the bottom part of PDZ.

Grain boundaries are known to act as sites within polycrystalline microstructures where the onset of plastic deformation takes place during imposition of a global strain field (Ming Wang Fu & Wai Lun Chan, 2014). This is because of the ease of activation of dislocation slip on more systems close to grain boundaries in order to maintain compatibility. Therefore, the higher

concentration of grain boundaries presumably manifests in the narrower branching deformation zone along stress concentrations imposed by global boundary conditions in the as-received material as opposed to annealed ones. Irrespective of this, the deformation zone which ensues during IE of Al is significantly more diffuse than that in Pb. Reasons for this is traced back to rate of work hardening which is known to remain positive before saturating at large strains as opposed to that in Pb which features a nearly elastic perfect plastic (negligible work hardening) behavior during plastic deformation. This results in strain localization behavior that manifests in well-defined zones undergoing severe deformation at small spatial scales. Another reason is related to the high homologous temperature of Pb, which makes activation of several slip systems for accommodation of global strains easier. Therefore, the final strain-rate field looks similar to that predicted by slip line fields, which is essentially a kinematically admissible solution. Slip line field is closer to an upper bound theory for isotropic elastic perfectly plastic materials(W.F. Hosford & Caddell, 2011); the difference between lower and upper bounds in plastic deformation is smaller; so Pb offers a better framework to predict plastic flow using slip line fields rather than aluminum; therefore the discrepancies.

Qualitatively similar rotation fields as Pb is observed in Al in aforementioned conditions (insets C, D, H, I, M and N of Figure 24 b, c, d) except for the large dead metal zone (no rotation) appeared in zone I in Al, which is almost negligible in Pb (Figure 20 and 21). It shows that the thickness of zone II (as marked in Figure 17 b) is larger for fully annealed condition as compared with other conditions. The heterogeneity of Al deformation during IE is also shown in the strain field characterization of the deformation zone (insets E, J and P of Figure 24b, c, d). The morphology of PDZ observed in Figure 22 b shows more concentration of strain with larger magnitude in as-received condition as opposed to annealed ones. Table 5 shows results of this

quantification for all three conditions of extruded Al using miniaturized die. It is seen that force values and so the resulting factor k strongly depends on the grain size (δ) of Al samples and increases significantly with decreasing δ. Flow stress of Al 1100 can also be predicted using Hall–Petch relation, ($\sigma_y(\varepsilon,\delta) = \sigma_0(\varepsilon) + k_0(\varepsilon)\delta^{-1/2}$), that relates the flow stress to the grain size (δ), where $\sigma_0(\varepsilon)$ and $k_0(\varepsilon)$ are material constant and function of imposed strain (Armstrong et al., 1962; hall, 1951; Petch, 1953). Hall-Petch relation for Al 1100 was found to have material constants, σ_0 and k_0, 14.3 (MN/m^2) and 0.065 (MN/(m$^{3/2}$) respectively for a range of grain size from 20 μm to 400 μm and strains under 0.5(Thompson et al., 1973). The nominal strain in the geometry used here is 0.4 as mentioned previously. The expected values for flow stress (yield strength) using this equation and material constants are found to be ~19.5, 22 and 26.2 MPa for grain size (δ) 150, 70 and 30 μm respectively. It shows that the expected flow stress increases ~12.5% and 33.7% for grain sizes 70 and 30 μm respectively with respect to large grain size 150 μm. But, the real increase in the flow stress based on the results shown in Table 5 for values of k, as an indicator for flow stress of material in sub (mm) scale, are ~47% and 106% for grain sizes 70 and 30 μm respectively with respect to large grain size 150 μm. These high deviations in flow stress increment by decreasing grain size in indirect microextrusion having the same specimen size are couple manifestations of the thickness of the shear zone that indicates heterogeneity in deformation, and friction. This is supported by the empirical measurements of ε_{eff} and $\dot{\gamma}$ using DIC (Table 3) showing a large difference in these values for Al $_{\text{as-received}}$, Al $_{\text{3hrs}}$ and Al $_{\text{full-anneal}}$. Consequently, the high deviation in real values from expected values using conventional Hall-Petch relation indicates the equation (or material constants) may not be valid in case of microforming. This was shown by many efforts tried to include the specimen size effects using a modified Hall-Petch (Mahabunphachai & Koc, 2008) relation combining with

surface layer model(Miyazaki, Shibata, & Fujita, 1979) in order to rationalize high real flow stresses in microforming scenarios(M. W. Fu & W. L. Chan, 2014). For example, in modified Hall-Petch relation the ratio of the sample size/grain size ($^{D,t}/_{\delta}$) is considered as a variable or in the surface layer model, it is suggested that the deformation behavior of surface material is different from the interior part and hence the sample is divided into two parts with different flow behaviors.

However, all aforementioned parameters show their effects on the geometry of deformation zone e.g. its thickness and extension as shown in the results of thickness of PDZ found for Pb by scaling down and also in Al by varying the initial grain size. Hence, thickness of deformation zone captured by DIC can be suggested as variable that has combined effects of all deformation parameters, e.g. grain size, specimen size, friction, deformation rate, etc. and therefore, it can be used in the Hall-Petch equation in order to predict the flow stress of material. These dimension of PDZ is estimated for example by setting a threshold strain-rate of 0.05 /s for different materials using strain-rate fields obtained by DIC and equation constants is found by plotting flow stress values versus the thickness or area of the PDZ. This verification needs many data points for each material system.

Additionally, it is seen that with the same macroscopic process boundary conditions, mechanical response of material towards the rotation quantified as h_{RF}/b and θ_{RF} in Table 3 is also influenced by initial grain size (δ). The values of these parameters are also dependent on the geometry of DMZ and PDZ below the punch.

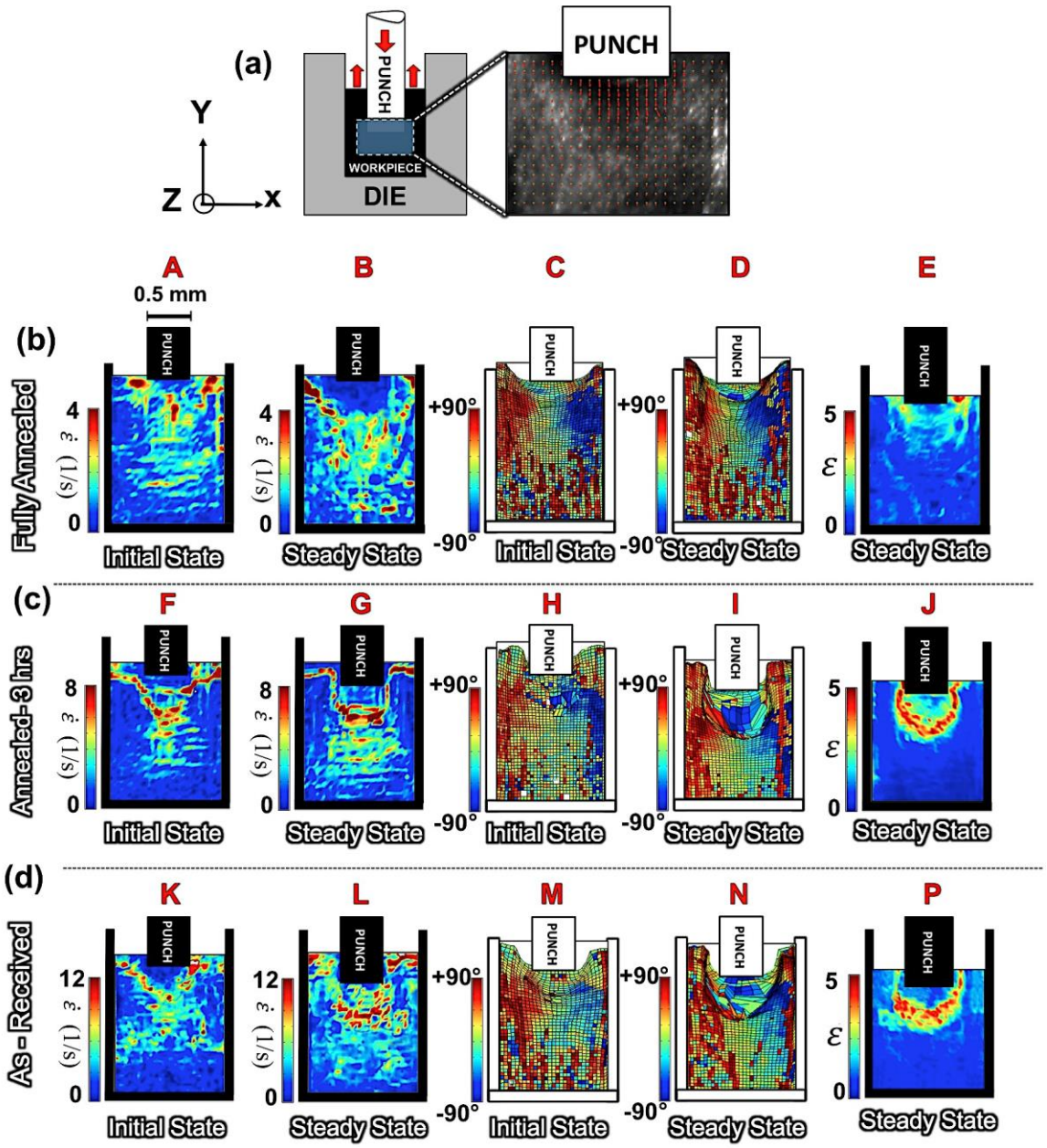

Figure 23: Schematic of indirect extrusion with a transparent window, inset shows displacement field in Al obtained by DIC through *in situ* observations. b), c) and d) Strain-rate, rotation and strain fields obtained by DIC in initial and steady states of deformation during IE of Al with different initial grain sizes (insets A to P).

5.3.2.2 Microstructure and texture evolutions in PDZ

Figure 24 and 25 show OIM of samples made by performing IE on $Al_{full\text{-}anneal}$ and $Al_{as\_received}$. Additionally, the figures also show the crystallographic textures extracted from OIM. With respect to the starting microstructure that featured a random crystallographic texture, both cases feature significant evolution of crystallographic texture in PDZ (Figure 22 a) of the extruded samples (region D) as marked in Figure 24 and 25. However, this evolution is somewhat subdued in $Al_{full\text{-}anneal}$.

Consequences of heterogeneity of deformation are clear from a comparison of microstructures obtained from the deformed material close to the punch corner and PDZ (regions E and D) with that in the extruded arms (region A). The former microstructure features ultrafine grains (suggesting deformation induced refinement) with respect to starting microstructures and those in the extruded arms (region A). A similar feature rich microstructure resulted from indirect extrusion of $Al_{full\text{-}anneal}$.

Here, microstructure in the extruded arms close to the walls of the punch (region B) is seen deformed and elongated in the direction of material flow (upward). However, a larger grain structure is seen close to the center of the extruded arm in fully annealed sample (region A). Region C in Figure 24 and 25 corresponds to area located in zone II as marked in Figure 17b or branches off from the deformation zone diffused from PDZ into the workpiece. From OIM observation, microstructure evolution in region C is not as intense as what is seen in PDZ (regions E and D).

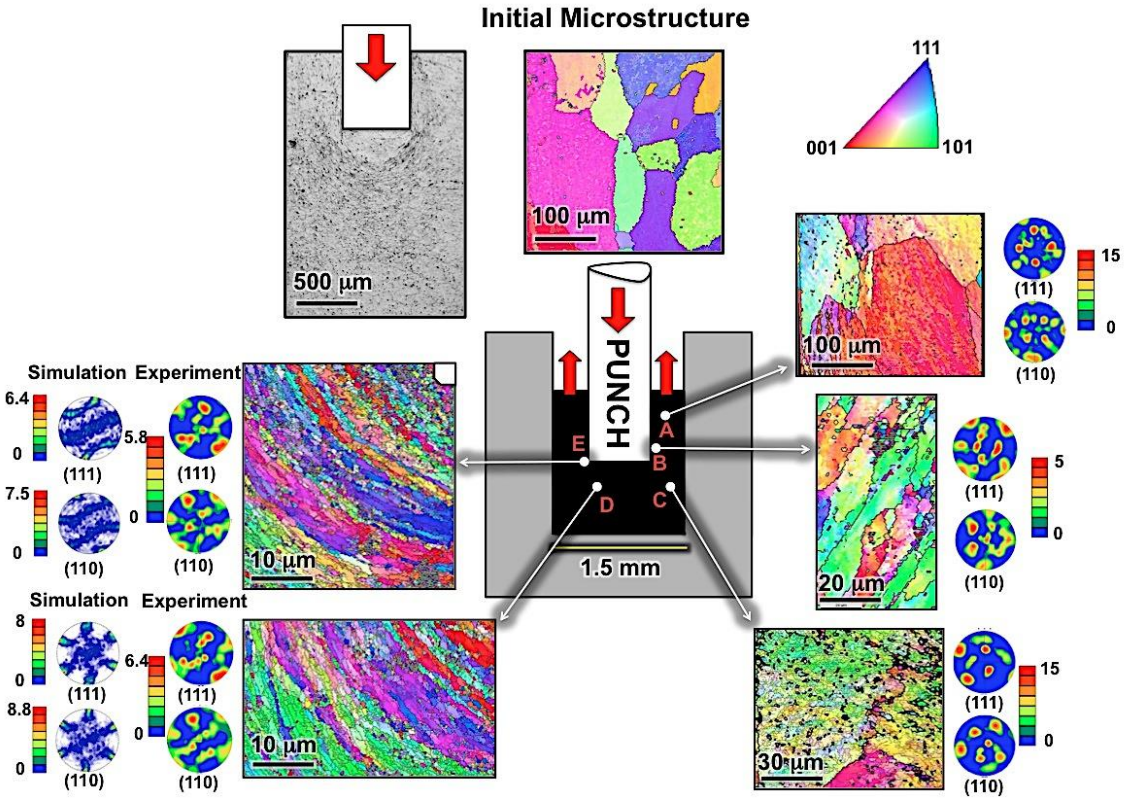

Figure 24: Inverse pole figure obtained from OIM of Al in fully annealed condition before and after indirect extrusion showing initial and final microstructures in different regions (marked as A to E). Empirical and simulated (111) and (110) pole figures show texture evolution across the deformed sample. Inset in top left of the image shows deformed microstructure throughout the sample captured by optical microscopy. Inset on top shows the IPF color code.

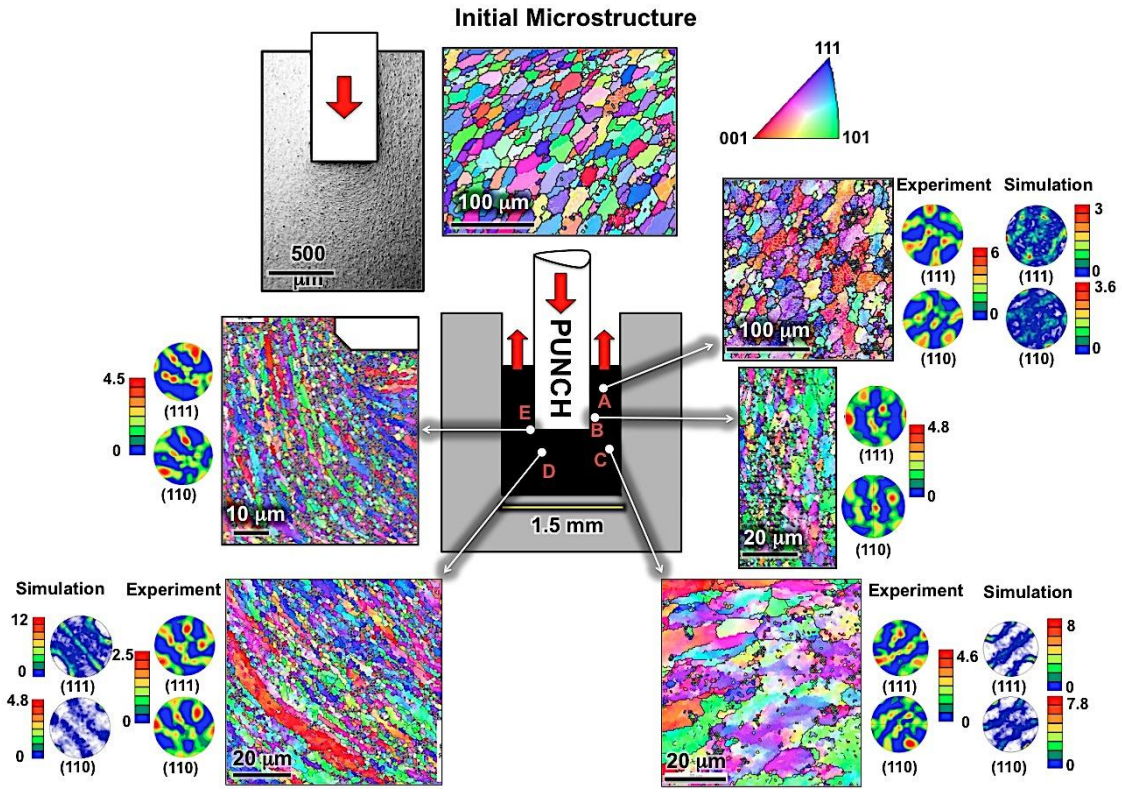

Figure 25: Inverse pole figure obtained from OIM of Al in as-received condition before and after indirect extrusion showing initial and final microstructures in different regions (marked as A to E). Empirical and simulated (111) and (110) pole figures show texture evolution across the deformed sample. Inset in top left of the image shows deformed microstructure throughout the sample captured by optical microscopy.

In addition to grain refinement, note that the evolution of the texture in different parts of Al during IE in small length scale. Empirically obtained textures extracted from EBSD micrographs, it is revealed that texture evolves more significantly in zones undergoing localized straining (regions E and D) in both cases (Figure 24 and 25). Despite the pre-deformed sample featuring large microcrystalline grains, regions D and E feature ultra-fine grains due to the high

local straining in these regions (insets E Figure 23 b). Elongation, reorientation and refinement of polyocrystalline samples Al $_{annealed}$ resulted in evolution of strong textures featuring high maxima in (111) pole figures (Figure 24). This is seen in regions close to the corner of the punch and a similar phenomenon is observed in Al $_{as\text{-}received}$ during IE (Figure 25).

Results of texture simulations using VPSC are also shown in Figure 24 and 25 for regions D and E in fully annealed and A, D and E for as-received samples. It is evident from Figure 24 and 25 that there is significant variation in evolution of crystallographic textures across the deformed sample by indirect extrusion. These observations suggest the simple shear crystallographic texture(Kalidindi, Bronkhorst, & Anand, 1992) in material is created during indirect extrusion, which has highest density below the punch (Region D). We see that VPSC model performs very well for predicting textures evolved in material during indirect extrusion even for annealed condition regardless of the assumption made in VPSC simulation of contribution of thousands of grains and all possible orientations during texture evolution(Lebensohn & Tomé, 1993). It must be noted that in deformation in small length scales particularly for microstructures with very large grain size similar to fully annealed condition used in present work, there is a few number of grains undergo deformation locally in different regions of workpiece. However, simulated results of crystallographic textures by VPSC are in reasonable agreement with empirical observation of local textures obtained by EBSD. Presumably, the microstructure reaches to a certain level of refinement while texture locally evolves. This can account for the efficacy of the texture prediction.

It is evident that in spite of the large variation in the initial grain size (δ) of Al samples; the microstructure undergoes a significant transformation during IE in PDZ. In both cases, the evolved microstructure show features that are predominantly present at medium to high strain

levels in deformed Al(Hughes & Hansen, 1997). This is supported by high strains imposed locally in PDZ and captured by DIC (Figure 23), though the nominal strain ($\varepsilon = ln\, R$) is comparably small (=0.4). Additionally, similar textures evolved in PDZ, where the microstructure underwent a significant refinement for both cases. All these suggest a minor role of the initial grain size (δ) in the texture evolutions in the regions correspond to high local straining (Regions E and D). However, it must be noted the major role of the grain size (δ) is in the gradient/scattering of microstructure characteristics, which determines the geometry of PDZ. Details associated with this effect are discussed in the next section.

5.3.2.3 Characterization of dislocation structure

Figure 26 shows distribution of Geometrically Necessary Dislocation density (ρ_{GND}), Inverse Pole Figure (IPF) and Kernel Average Misorientation (KAM) maps are also shown for both samples in fully annealed and as-received conditions. Results are shown for regions E and D (Figure 10 and 11) that are shown as "corner" and "ring" in Figure 27 a and b respectively.

It is seen that GNDs form within zones that feature largest orientation gradients that are essentially zones close to original high angle grain boundaries or newly formed low/high angle grain boundaries. KAM is essentially a similar parameter as GND density field. This is verified by obtaining KAM maps from the TSL software for the corresponding OIM micrographs. KAM maps are shown for corner and ring zones for fully annealed condition (Figure 27 a and b) and the threshold was chosen to be less than 15° to eliminate any contribution from high angle grain boundaries. In KAM maps, areas of high concentration of local misorientation indicate high orientation gradients, which is closely related to GNDs as discussed above in the methodology described to calculate ρ_{GND} from OIM data. According to KAM diagrams, the average values for local misorientations are calculated and the results are shown in the tables demonstrated in

Figure 26 a and b. Accordingly, the average of KAM is higher for as-received condition in both corner and ring zones (5.62° and 4.16° respectively) as compared with fully annealed condition (3.2° and 2.9°). These results show that how high volume of high angle grain boundaries in as-received sample results in promoting the formation of larger local misorientations during deformation as supported by larger imposed local strains shown in Figure 23d, inset P.

These differences in KAM are relatable to geometry of the PDZ during IE. For instance, it is seen by characterization of flow fields using DIC that the PDZ features a diffuse morphology during extrusion of Al $_{\text{full-anneal}}$ samples. A diffuse PDZ will result in smaller strain gradients and therefore smaller KAM (and ρ_{GND}), compared with a locally constrained PDZ in Al $_{\text{as-received}}$.

Investigations using DIC show that the dimensions associated with the PDZ (and therefore KAM as well as ρ_{GND}) scale with the grain size. This is directly relevant to the concentration of grain boundaries, which are known to be hot spots for dislocation activity in order to maintain compatibility during plastic deformation.

The average of ρ_{GND} over the area that ρ_{GND} maps were generated is ~ 1.6×10^{15}, 6.3×10^{15} for corner (Figure 10 a) and 7.9×10^{14}, 3.4×10^{15} /m^2 for ring (Figure 26 b) in fully annealed and as-received samples respectively. These values show local ρ_{GND} in different regions of PDZ.

However, the overall ρ_{GND} can be roughly estimated by measuring the thickness of the deformation zone (h) by setting a threshold strain-rate of 0.05/s in strain-rate fields and finding the average of effective strain over this thickness (Table 5).

This is done by using strain equations 17-19, described subsequently, whereby ρ_{GND} is related directly to strain gradient (ε/h). Using this argument, values of ρ_{GND} for Al $_{\text{as-received}}$ and Al $_{\text{full-anneal}}$ was estimated as ~5.6×10^{14} and 8.2×10^{13} /m^2 respectively. Although these values do

not match perfectly with the local ρ_{GND} measured using OIM micrographs, they suggest a close approximation of overall ρ_{GND} produced in PDZ during deformation.

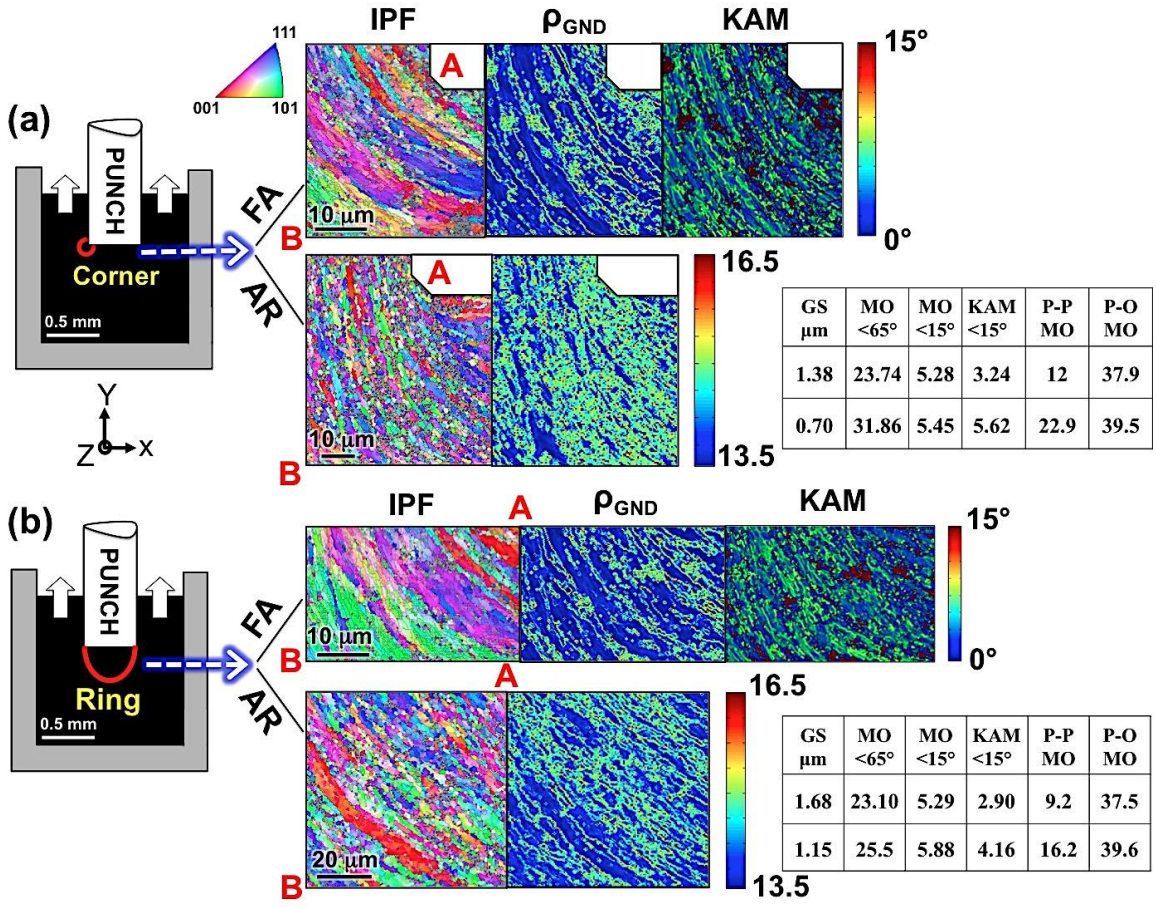

GS µm	MO <65°	MO <15°	KAM <15°	P-P MO	P-O MO
1.38	23.74	5.28	3.24	12	37.9
0.70	31.86	5.45	5.62	22.9	39.5

GS µm	MO <65°	MO <15°	KAM <15°	P-P MO	P-O MO
1.68	23.10	5.29	2.90	9.2	37.5
1.15	25.5	5.88	4.16	16.2	39.6

Figure 26: Inverse pole figure (IPF), geometrically dislocation (GND) density and kernel average misorientation (KAM) maps for regions labeled as corner and ring in PDZ for fully annealed and as-received Al samples. Color scale for GND is at $\log_{10}$ scale. Tables show average of grain size (GS), misorientation (MO), KAM, point-to-point (P-P) and point-to-origin (P-O) misorientations for aforementioned regions. (P-P) and (P-O) were measured from points A to B marked in IPF images.

In the tables demonstrated in Figure 27 a, b, the values of average grain size (GS) and misorientation angles (MO) for angles <62.8 and <15° in evolved microstructures are also shown for aforementioned regions. Results show that in spite of the large difference in the grain size of starting microstructure, the evolved microstructure has almost the same grain size in the regions of interest with intense local strains in both cases (Figure 24 b and 24d, insets E and P) except for corner in as-received condition, which has the smallest average grain size (Tables in Figure 26). Comparing the ρ_{GND} with IPF and KAM maps indicates that refinement is mostly promoted by the formation of GND boundaries during deformation.

Also the average of point to point (P-P) and point to origin (P-O) misorientations are also shown (Tables in Figure 26) along the line connected the corners of IPF maps from A to B (marked in Figure 26). Point-to-point indicates the orientation changes between abutting points while point-to-origin refers to the orientation changes between all points and a reference point which is A in these measurements. It is seen that there is a difference in the average of P-P misorientation between the samples in fully annealed and as-received conditions showing lower values for fully annealed condition. It shows that the local misorientations as well as orientation gradient from B to A is larger in as-received condition.

It is apparent that the misorientation developed during deformation in PDZ and consequently GNDs is considerably larger in as-received condition, presumably due to the high density of high angle grain boundaries in the initial state. It was discussed previously that for the same geometry and boundary condition used in indirect extrusion of Al in both annealed and as-received conditions, the thickness of deformation zone below the punch (Figure 22 a) is approximately 3.7 times larger for former (fully annealed) as compared with later (as-received).

It shows the thickness of the deformation zone changes significantly by changing the initial grain size. In strain gradient plasticity theory, strain gradient is defined as:

$$\eta = {d\varepsilon}/{dx} \tag{17}$$

where ε is strain and x is distance along the X axis(N. A. Fleck & J. W. Hutchinson, 1997). Integration of this equation along each axis gives the length of the zone over which the strain is changing in the deformation zone that is related to the thickness of the deformation zone along the mentioned axis as:

$$h = c \int dx = C_0 \ {\varepsilon}/{\eta} \tag{18}$$

Here, C_0 is constant. The gradients of strain that can create either because of the geometry of deformation or material itself result in GNDs according to(N.A. Fleck et al., 1993):

$$\eta = b \, \rho_{GND} \tag{19}$$

where, b is the Burgers vector. Therefore, thickness of the deformation zone is related to ρ_{GND} by following expression:

$$h = c \int dx = C_0 \ {\varepsilon}/{b \, \rho_{GND}} \tag{20}$$

Thus, it is argued that the thickness of deformation zone is a function of strain and GND density, $h = f(\varepsilon, \rho_{GND})$ having a direct relationship with strain and inverse relationship with density of GNDs.

Both extrinsic and intrinsic material length scales result in generating high density of GNDs(Engel & Eckstein, 2002). Therefore, $\rho_{GND(Total)}$ for Al with different grain size (δ) deformed by indirect extrusion studied here is expressed as:

$$\rho_{GND(Total)} = \rho_{GND(Geometry)} + \rho_{GND(Grain\ size)} \tag{21}$$

In indirect extrusion of pure aluminum, density of GNDs caused geometrically is related to the initial and final width of the sample as:

$$\rho_{GND_{(Geometry)}} = \frac{1}{b}\left(\frac{1}{w_i} + \frac{1}{w_f}\right) \quad (22)$$

where, w_i and w_f are initial and final width of the sample (1.5 and 1 mm respectively) and b is burgers vector (0.286 nm for aluminum). Simple calculation using this equation reveals that ρ_{GND} caused by geometry constrictions for the dimensions used in present work is estimated as ~ 5.83×10^{12} /m^2. This value is constant in all experiments with Al studied here.

Intrinsic source of generating GNDs for pure system studied here is considered to be the grain boundaries, expected to be hard relative to the grains interior(Thompson et al., 1973). Grain boundaries act as constraints that impose long-range stresses in the microstructure accommodated by GNDs. The density of such GNDs and its dependence to grain size was firstly suggested by Ashby(Poole et al., 1996). In his model, it is assumed that in grain boundary regions GNDs are dominant and their density is related to the slip distance (λ^G) and since grain size is a upper bound for slip distance, then it is related to grain size as(Thompson et al., 1973):

$$\rho_{GND_{(Grain\ size)}} = C_1/\delta b \quad (23)$$

where, δ is grain size and C_1 is a constant. In Ashby's model, ρ_{GND} is also related to strain but applies in the limit of low strains only and then becomes independent as strain goes up since increasing strain should not require a proportionate increase in grain boundary accommodation(N.A. Fleck et al., 1993). Neglecting the effect of $\rho_{GND_{(Geometry)}}$in $\rho_{GND_{(Total)}}$ and substituting equation (23) as a measure for $\rho_{GND_{(Total)}}$in equation (20) we obtain:

$$h = c\int dx = C\varepsilon\delta \quad (24)$$

where, C is a constant which is equal to C_0/C_1 and ε is average of strain over the thickness of deformation zone. This simply shows that dimension of deformation zone is related directly to strain (ε) and grain size (δ). Thus, since $\rho_{GND_{(Total)}}$ in equation (23), varies locally throughout

the deformation zone we can use grain size parameter (δ) in order to predict thickness of deformation zone. This is possible by plotting the thickness of deformation zone (h) versus ($\varepsilon\delta$) using accurate imposed strains obtained empirically by DIC for materials with various initial grain size to find the constant value (C) of equation (24) for each material. For the three data points we have for Al, constant C were found to have the value ~0.36 with R^2=0.9. Verification of this value needs more data points. It must be noted that when the scale of deformation is reduced to the order of micron and becomes close to the intrinsic martial length scales e.g. subgrain size etc., the effect of $\rho_{GND\,(Geometry)}$cannot be ignored in determining the thickness of deformation zone(S. Basu & M. R. Shankar, 2014b).

5.3.2.4 Surface quality

Another effect of the deformation zone geometry is on the surface quality/roughness of microproducts. Here, in indirect extrusion we discussed how PDZ geometry scales with sample size as well as the initial grain size. The effects of microstructure characteristics on developing rough surfaces during plastic deformation have been extensively studied (Wu & Lloyd, 2004). Roughening creates surface defects that may develop in the form of necking, cracking and etc. during the operation and cause failure of the products. Hence, formation of such defects requires additional finishing operations, which is limited and almost impossible in microforming products given the dimension constraints. It has been shown that surface roughening evolves linearly with imposed strain and it depends linearly on grain size (Wu & Lloyd, 2004). The origins of roughening microscopically are attributed to spatial grain orientation distribution. They observed that grains lying on the surface deform differently to the grains in the interior of the sample undergoing deformation and so the grain-to-grain compatibility causes the surface grains to

move normally to the surface, leading to surface roughening. It was shown that surface roughening is primarily due to the inhomogeneous distribution of the grain orientation and secondary due to the inhomogeneous deformation within individual grains. Here, we are trying to correlate roughening to the mechanics of deformation and its interaction with microstructure features in microforming. In indirect microextrusion, the outer sides of the sample act as free surfaces that move freely during deformation but die walls that constraint sample from the sides eventually suppress their free movement.

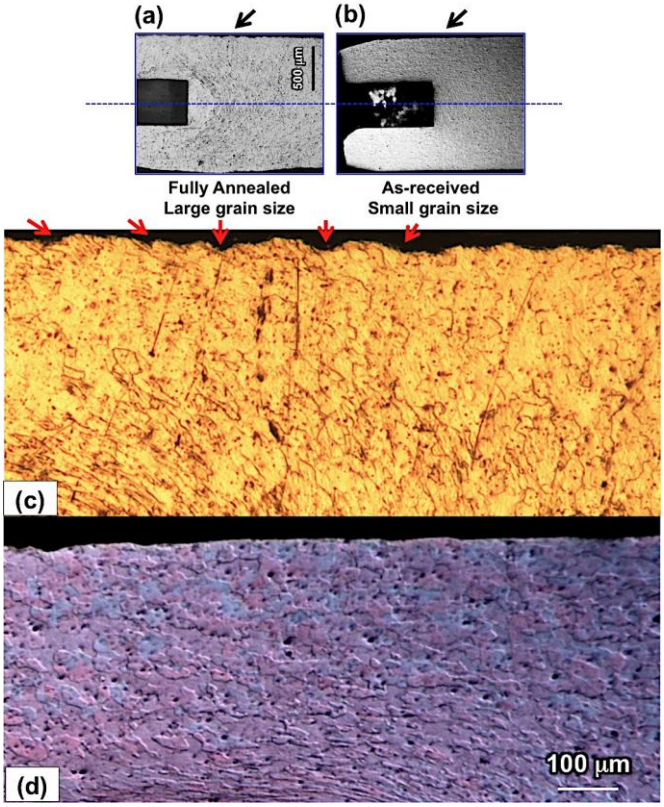

Figure 27: Optical images of Al after indirect microextrusion in a) Fully annealed and b) as-received conditions. Arrows refer to the regions the higher resolution of which are shown in c) and d) for fully annealed and as-received samples respectively.

Figure 27 shows optical images of the surface created on the sides of extruded Al samples in both fully annealed and as-received conditions. It is observed that in fully annealed case, the exterior sides of the sample especially located at the middle part of the surface has a rough outside compared with the as-received one.

Previously it was shown that scaling down the process (sample dimension) as well as grain size determine geometry of PDZ that was discussed in terms of the thickness of the PDZ and also its extension into the workpiece. In Al, it is seen that the thickness of PDZ in $Al_{\text{full-anneal}}$ is larger than $Al_{\text{as-received}}$ (Figure 27 a and b) that was also discussed extensively in previous sections. The PDZ (area shown in Figure 22 a) below the punch in $Al_{\text{full-anneal}}$ is extended into the workpiece so that the edges of it reach to the sides of the sample. This is shown by red arrows in Figure 27 c where at the bottom of each groove formed during deformation there exists a shear flow line of PDZ. We see that the sequence of shear flows during deformation has left a series of groove shaped defects on the free surface. This is a result of the interaction of the microstructure features with the mechanics of deformation that is highly influenced by sample volume. This phenomenon can be clarified by tracing a material point pathline during the deformation. DIC is used as promising method to do this and clarify material flow type with respect to macroscopic and microscopic boundary conditions.

5.3.3 Indirect extrusion of Cu

The work described in this section represents results of the investigation of the effect of the initial grain size and texture rotation in polycrystalline Cu as prototypical work hardening material with larger rate compared with Al. Starting microstructures with desired grain size in a range of small to ultrafine/nano size and also textures created by machining as described previously. Figure 28 illustrated IPF images of starting microstructures used to perform IE in

annealed condition and also obtained by methodology described in Section 4.1.1. The average grain sizes measured empirically using OIM images are ~80, 0.68, 0.42 and 0.24 μm for annealed, 40L, 20 L and 0L respectively. The focus is on parameterization of PDZ and roughening origins and their interactions with respect to the starting microstructure features and mechanics of material flow.

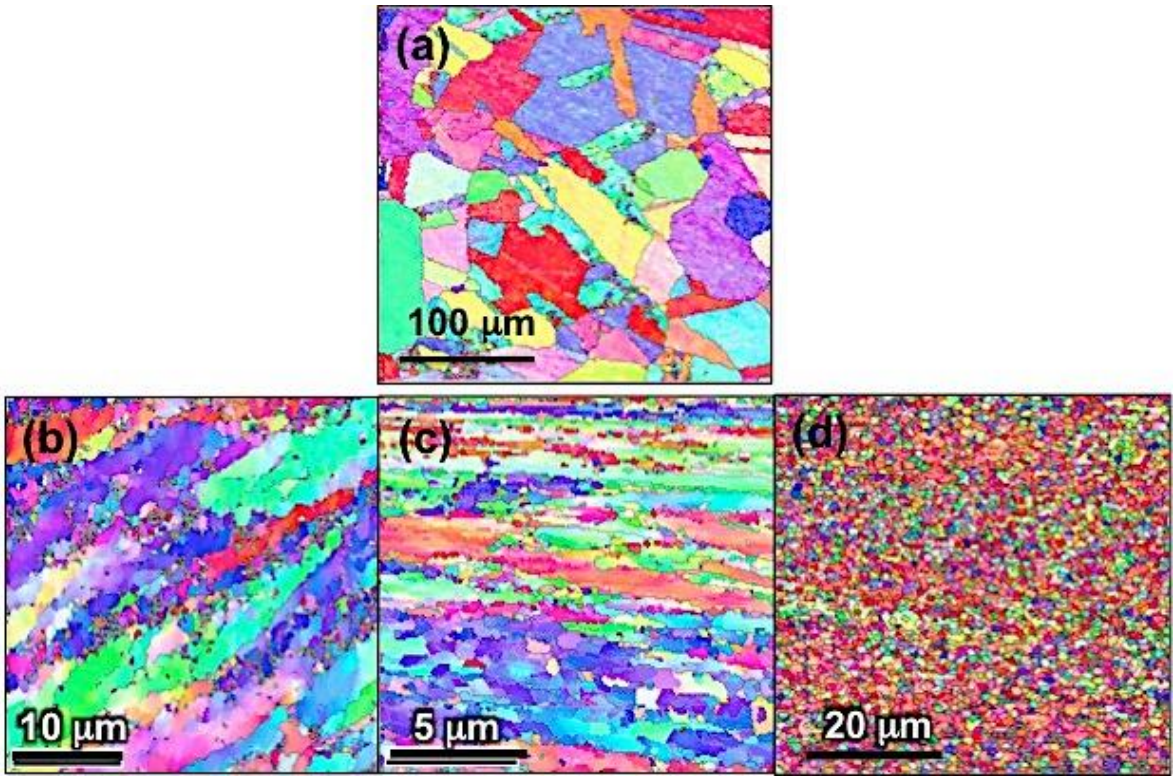

Figure 28: IPF images showing the starting microstructures of Cu samples used in indirect extrusion which are corresponding to: a) annealed, b) 40L, c) 20 L and d) 0L.

5.3.3.1 Surface topography and part quality

We have shown that the volume of ensuing PDZ increases in microforming operation by indirect extrusion and it is comparable to dimension of the sample. Therefore, the mechanics of its formation affect the final shape and quality of microproducts. Here, we describe this behavior in small-scale grain size regime from ultrafine to nano size microstructures as suggested materials for microforming. Figure 29 exhibits the material flow in extruded products with respect to different starting microstructures.

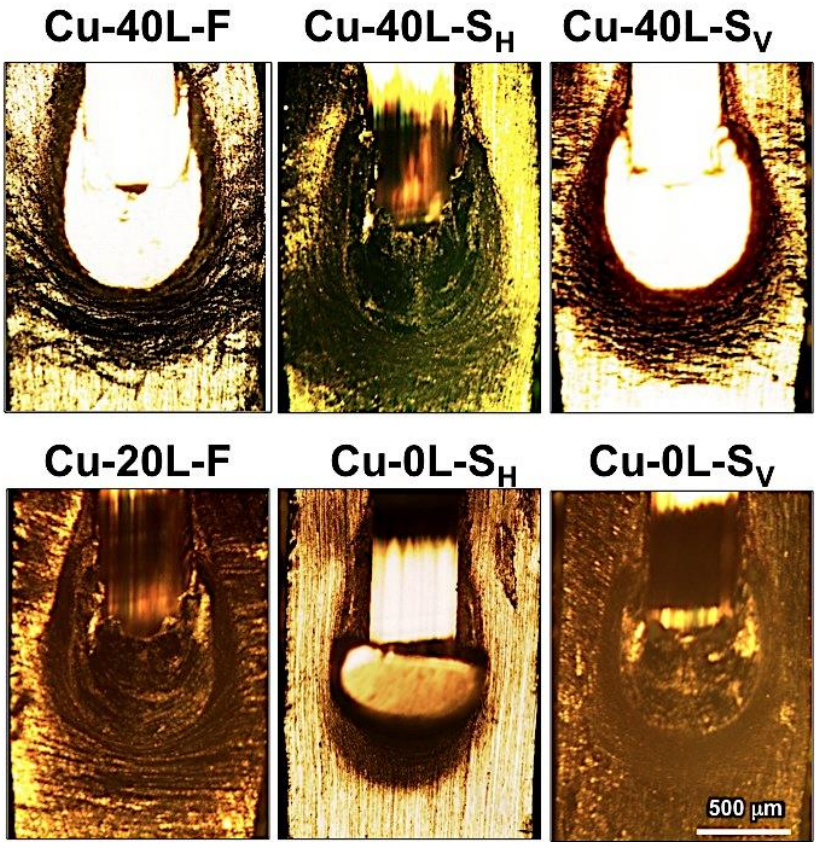

Figure 29: Optical images of extruded Cu samples with different initial microstructures by indirect micoextrusion showing PDZ geometry and material flow type with respect to initial grain size and also rotation of initial texture.

Here, the top row refers to the samples made of Chip in 40L condition with similar grain size but rotated textures. It is clearly seen that rotation of initial texture has significant effect on the geometry of PDZ in terms of its volume and extension into the work piece below the punch as well as sides. For instance, in 40L-F and 40L-S_V, PDZ reached to the sidewall of the die where the layers with localized shear feature were suppressed. This effect is somewhat subdued in case of 40L-S_H shows a smaller volume of PDZ creating around the punch during deformation. This effect is more pronounced in case of 0L-S_H sample with comparably more uniform and smaller grain size. It shows a significant shrink in the volume size of PDZ around the punch in which the sides of the sample are almost unaffected by extended PDZ. This results in better exterior surface quality of products as seen in Figure 30 that compares aforementioned extruded samples by showing optical images after polishing the surface. This was also shown for annealed condition, which results in more irregularity in deformation flow that leaves rough surfaces. Experiments were performed in plane strain condition as described in Section 4.2. Therefore, polishing the surface will not affect the features observed *in situ* through the camera and also by post-deformation optical microscopy.

In producing UFG/ Nano structured materials using SPD methods, depending on the geometry of utilized method and also amount of imposed strain, the created microstructure can feature various grain sizes, textures, etc. In most of them UFG structure is created thorough the large shear and lattice rotations which accelerate grain subdivision. In machining, shear localization occurs at the shear plane (Figure 6 c) where a large strain is imposed on the material. By advancing the tool into the material and further flow of chip material, a sequence of shear bands forms in the chip (Marusich & Ortiz, 1995).

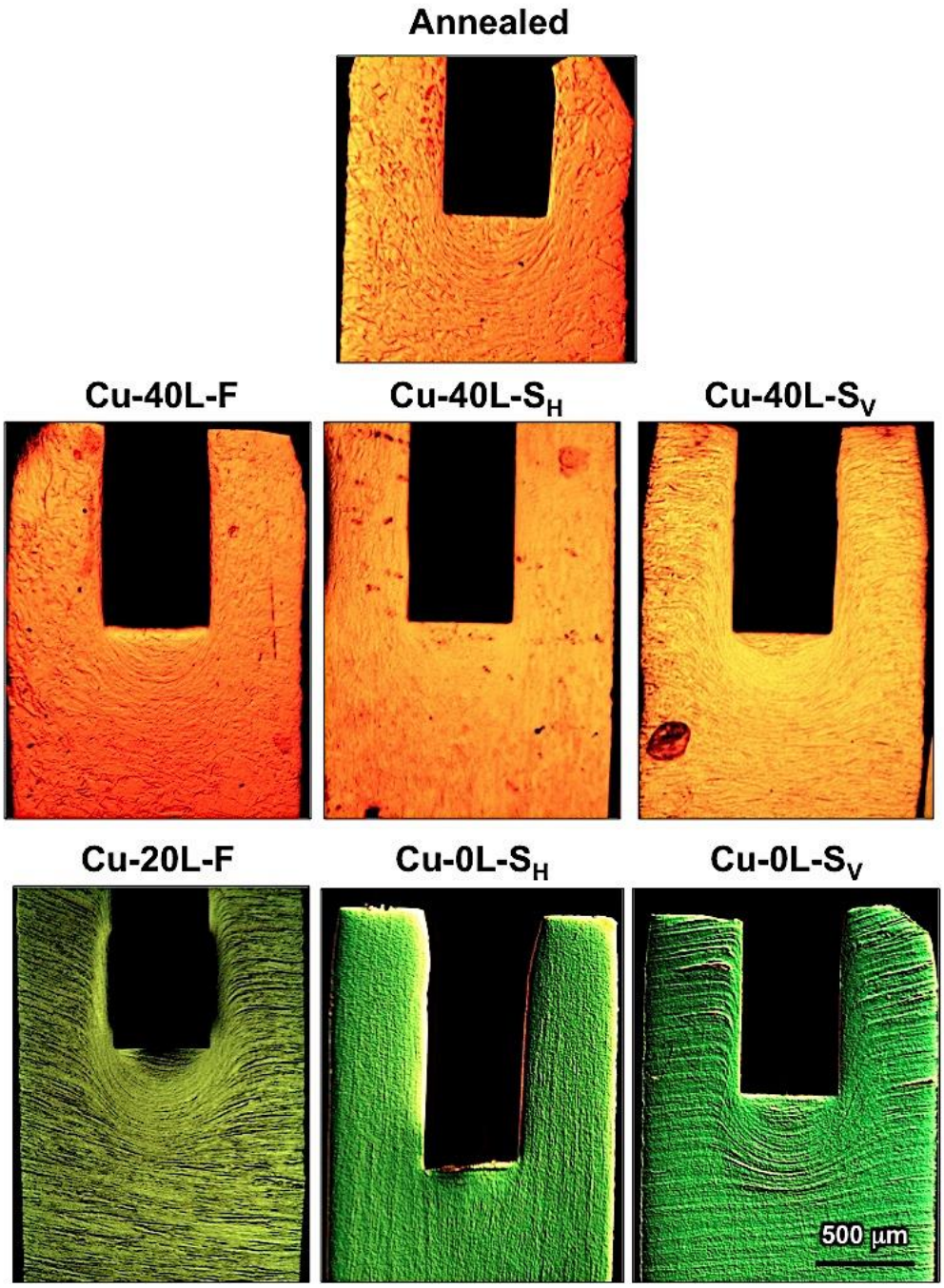

Figure 30: Optical images of extruded Cu samples with different initial microstructures by indirect micoextrusion showing PDZ geometry and material flow type with respect to initial grain size and also rotation of initial texture. This was captured after polishing the surface of samples.

By choosing smaller tool rake angle e.g. 0° tool rake angle, distance between shear bands become smaller and therefore more uniform microstructure with smaller grain size is produced (Figure 28). From Figure 29, it is observed that the shear bands created during machining also affect material flow and control geometry of PDZ even in 0L condition with more uniform microstructure. This effect is almost unavoidable in using UFG microstructures created by SPD methods as starting material, as there always exist features related to shear direction of material during SPD.

Figure 31 shows 3D optical images if the interior surfaces of extruded samples with rotated textures. Interior surfaces refer to the created surfaces during deformation in interior sides of the sample in contact with punch. It is seen that rotation of pre-existing textures also influences quality of aforementioned surfaces. Here, the effect of shear band flow lines oriented in same direction across the sample is also apparent in quality of interior surfaces. As it creates micro-cracks in interior surfaces of 40L-S_V sample as the movement of punch is in the direction which cut the aforementioned shear bands. This effect is not observed on the surface of 40L-S_H sample. This also shows the composite nature effect of material produced by SPD. It is seen that this orientation (S_H) is favorable for reducing the effect of PDZ extension and its interaction with pre-existing shear bands on the quality of extruded microproducts. However, the force results show a large value for this direction as it is about 330 N compared with F and S_H conditions, which is 220 and 210 N respectively. This is corresponding to applied force in Y direction.

The mechanics of deformation and its interaction with microstructure features will be discussed subsequently using DIC method to clarify material flow behavior.

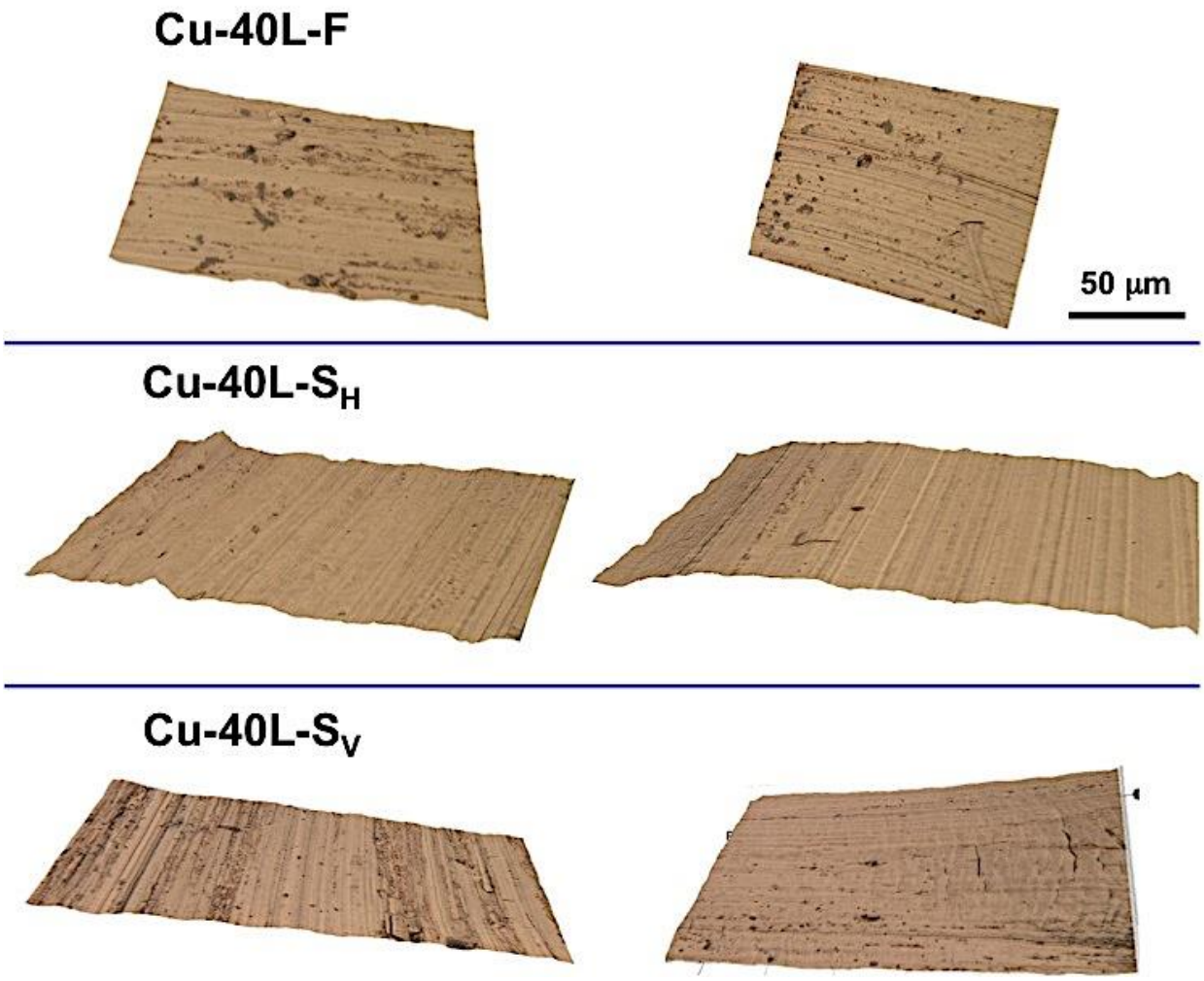

Figure 31: 3D topographic map of the interior surface of extruded Cu samples with same grain size but rotated textures. These surfaces are in contact with punch walls and created during indirect extrusion.

5.3.3.2 Mechanics of material flow

Figure 32 shows the strain-rate and strain fields obtained for some of the conditions explained above. It clearly shows the effect of initial grain size and texture rotation on the morphology and geometry of PDZ as it is more localized and confined to a small region for 0L-

S_H sample. In annealed sample the pathline with high strain-rate extended more into the workpiece as they reached the die walls. This effect is almost invisible in 0L-S_H sample.

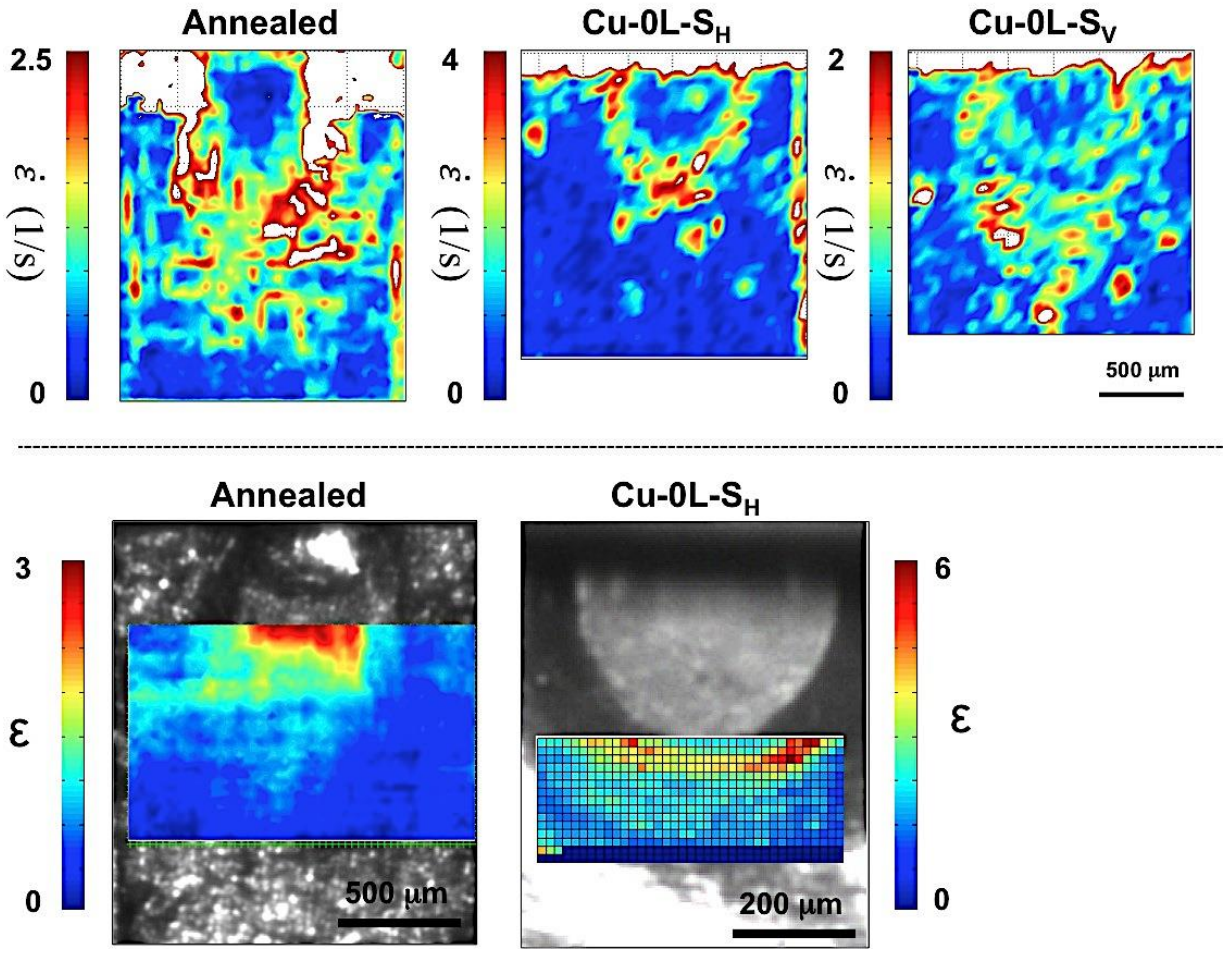

Figure 32: Strain-rate and strain fields obtained by DIC for the microstructures mentioned on top of each image, showing the heterogeneity of deformation zone with respect to grain size and texture rotation and also shear banding in PDZ for UFG material. Strain-rate fileds are represented below the cut-off shown with max value on the color bar whereby regions with higher values appeared in white color.

Previously, we discussed the morphology of PDZ with respect to the grain size and showed for Al that it linearly increases with increasing grain size and imposed strain and used strain gradient plasticity to rationalize this phenomenon. Here, again we see that with increasing grain size a more extended PDZ but less concentration is formed during indirect extrusion. Strain fields obtained empirically by DIC shown in Figure 32 this localization and shear band formation for UFG material. However, one must be noted that even for same initial grain size (0L-S_{Hand} 0L-S_V), the thickness of PDZ is very different. Therefore, this model cannot capture the effect of pre-existing textures or materials with composite microstructures. This is the coupled effect of texture rotation and grain size. Texture rotation changes material pathlines during the deformation. One can be argued here is some pre-existing textures may require large lattice rotation for material to deform as it undergoes deformation and rigid body rotation. Hence, it produces more GNDs, which it density has an inverse relation with thickness of PDZ. Larger lattice rotations result in severe texture evolution and grain refinement and therefore this can be captured by OIM analysis of extruded parts with respect to different prior textures.

5.3.3.3 Microstructure evolution across PDZ

Figure 33-38 illustrate microstructure evolution in different regions of the extruded samples for some of the aforementioned starting microstructures. Similar to Al, a heterogeneous deformation zone with more extended dead metal zone as a result of larger work hardening capacity is formed during indirect extrusion. Here, the microstructure evolution is the couple effect of the grain size as well as texture rotation samples made from chip.

Figure 33 shows this evolution for annealed Cu in different regions of the extruded sample. It is seen that similar to Al, microstructure in extruded arms (region A) does not change significantly and features same grain size microstructure with strained large grains. The texture

in this part is obviously not random texture but also is not evolved severely during deformation. Region B is corresponding to the PDZ formed below the punch during deformation. In this region, a very heterogeneous deformation is seen as layers of deformed/non-deformed materials are formed in this region (back arrows). This shows the non-concentrated nature of this zone for annealed materials.

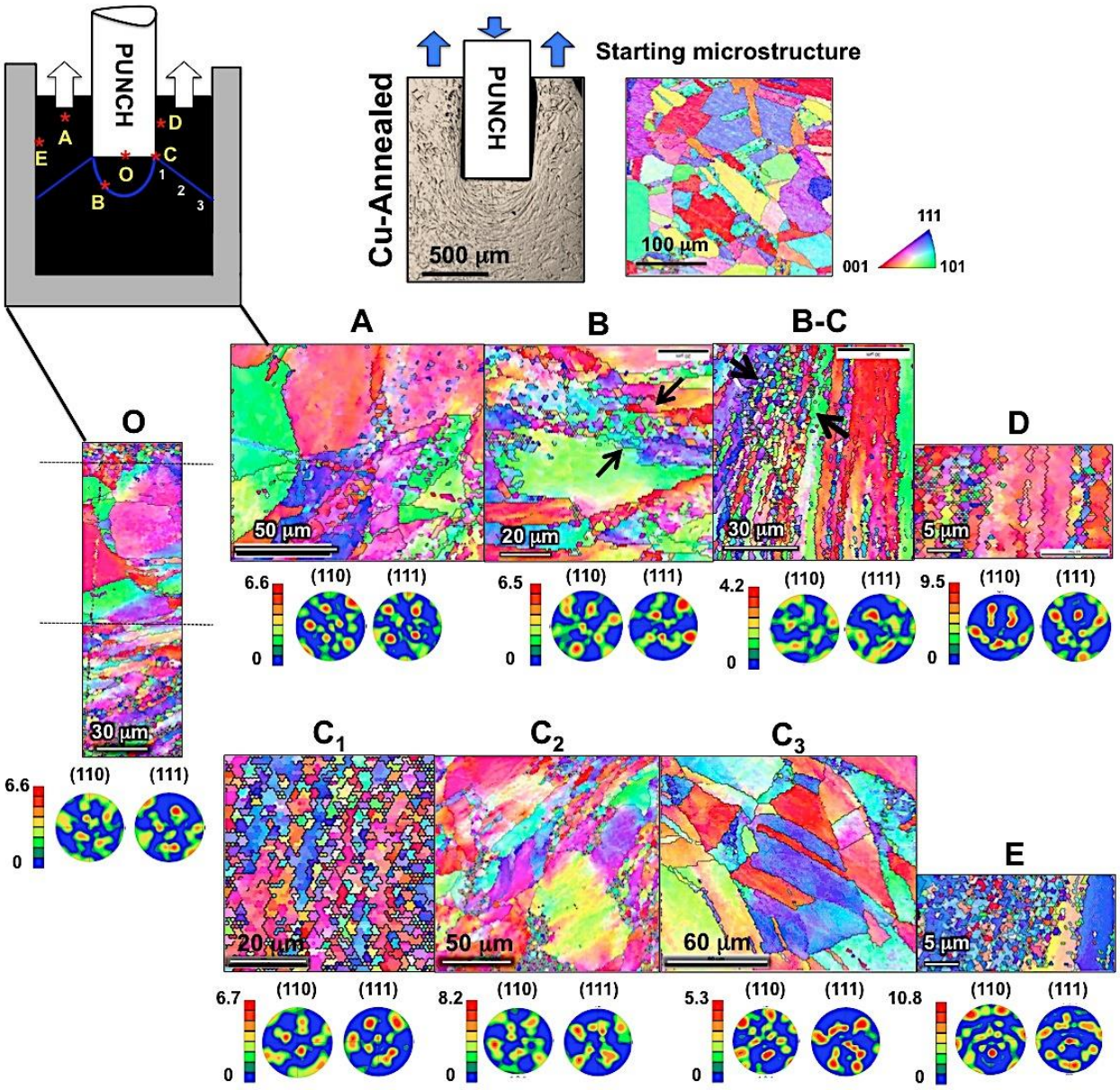

Figure 33: IPF obtained from OIM maps for Annealed Cu before and after indirect extrusion showing initial and final microstructures in different regions (marked with star and named as A-E and O in schematic, top left inset). Empirical (110) and (111) pole figures show texture evolution across the deformed sample. Inset in top left of the image shows optical image of deformed sample by indirect extrusion.

This alternated high/less strained layers is also visible at the interface of B and C regions where a large concentration of shear bands separating extruded part from PDZ is seen. The high level of refinement is also seen at the corner of punch where the material is in direct contact with punch. Additionally, at regions along the C line, microstructure is either un-deformed or slightly strained. In all above cases, there is not much texture evolution associated with annealed sample because of spreading nature of PDZ, which is not concentrated in a confined region. The microstructure corresponding to region O shows that there is a layer of unreformed grains with approximately 100 μm thickness below the punch related to dead metal zone.

Figure 34-36 show microstructure evolution in different regions of the extruded samples for 40L samples with similar grain size but rotated textures. It is seen that in the extruded arms (marked as region A), microstructure has similar features as initial microstructure and it does not undergo significant evolution during deformation for all three cases but it has somewhat more deformed for 40L-S_H. It is seen that mix texture modes (shear/compression) appear locally in different regions of the sample and texture does not follow exact paths corresponding to a specific type of the texture. In 40L-F sample, same type of texture evolved in regions B, B-C and D, which are slightly rotated with respect to each other. Similar but somewhat less strong texture is seen region C_3. It seems that simple type of the texture evolved during deformation in all aforementioned regions with different strength and intensity. Although strong textures formed in this region for other two conditions, they do not feature simple textures. It is seen that in the sample 40L-S_H, texture are very different in different parts of the sample and does not follow the same pattern in those regions. In addition a strong texture evolved at region C_3 compared with other samples. The heterogeneity in texture evolution is also visible in 40L-S_V as it features a strong compression texture in region C_1 while a simple shear texture in region D.

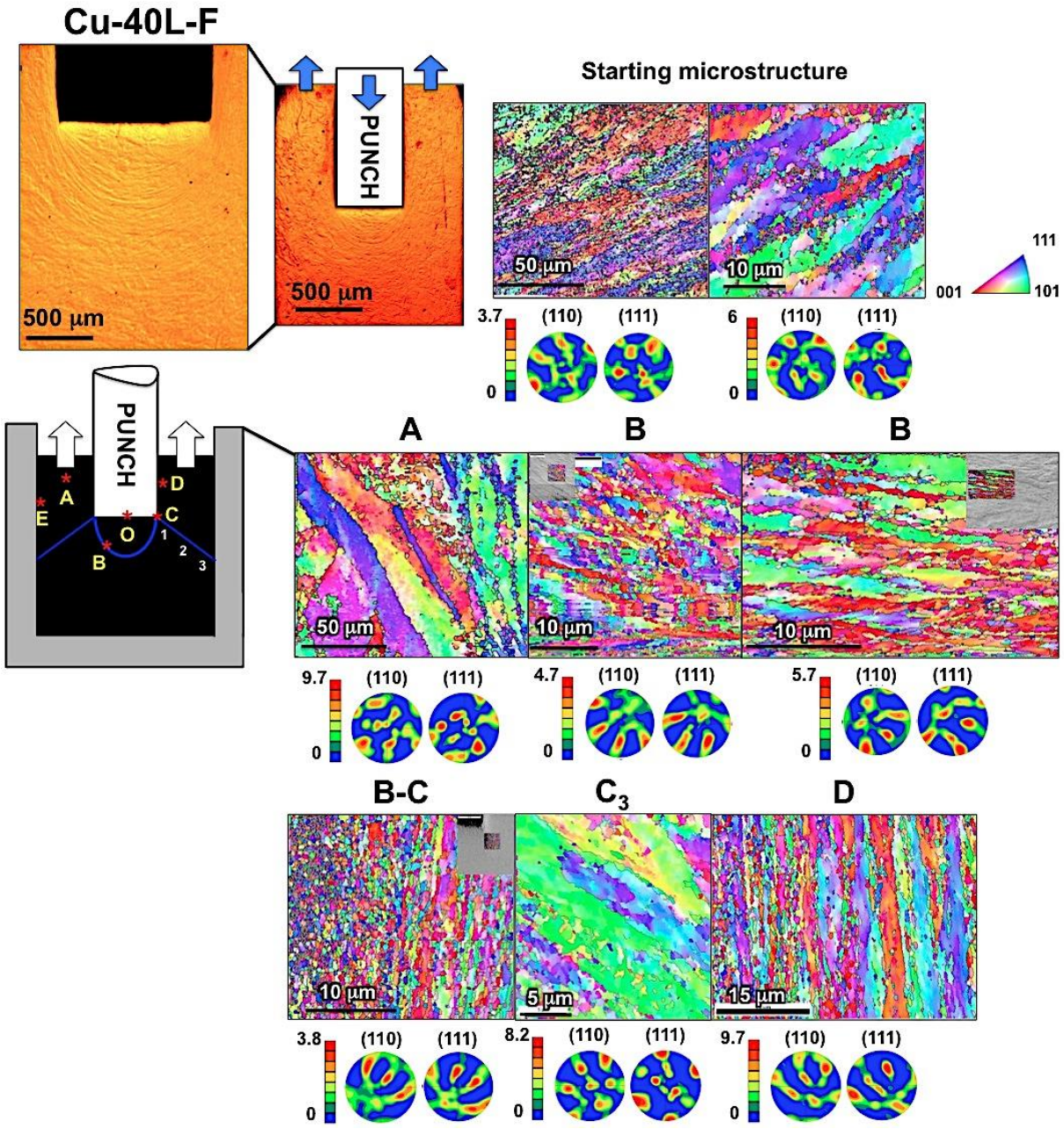

Figure 34: IPF obtained from OIM maps for Cu (40L-F) before and after indirect extrusion showing initial and final microstructures in different regions (marked with star and named as A-E in schematic, top left inset). Empirical (110) and (111) pole figures show texture evolution across the deformed sample. Inset in top left of the image shows optical image of deformed sample by indirect extrusion.

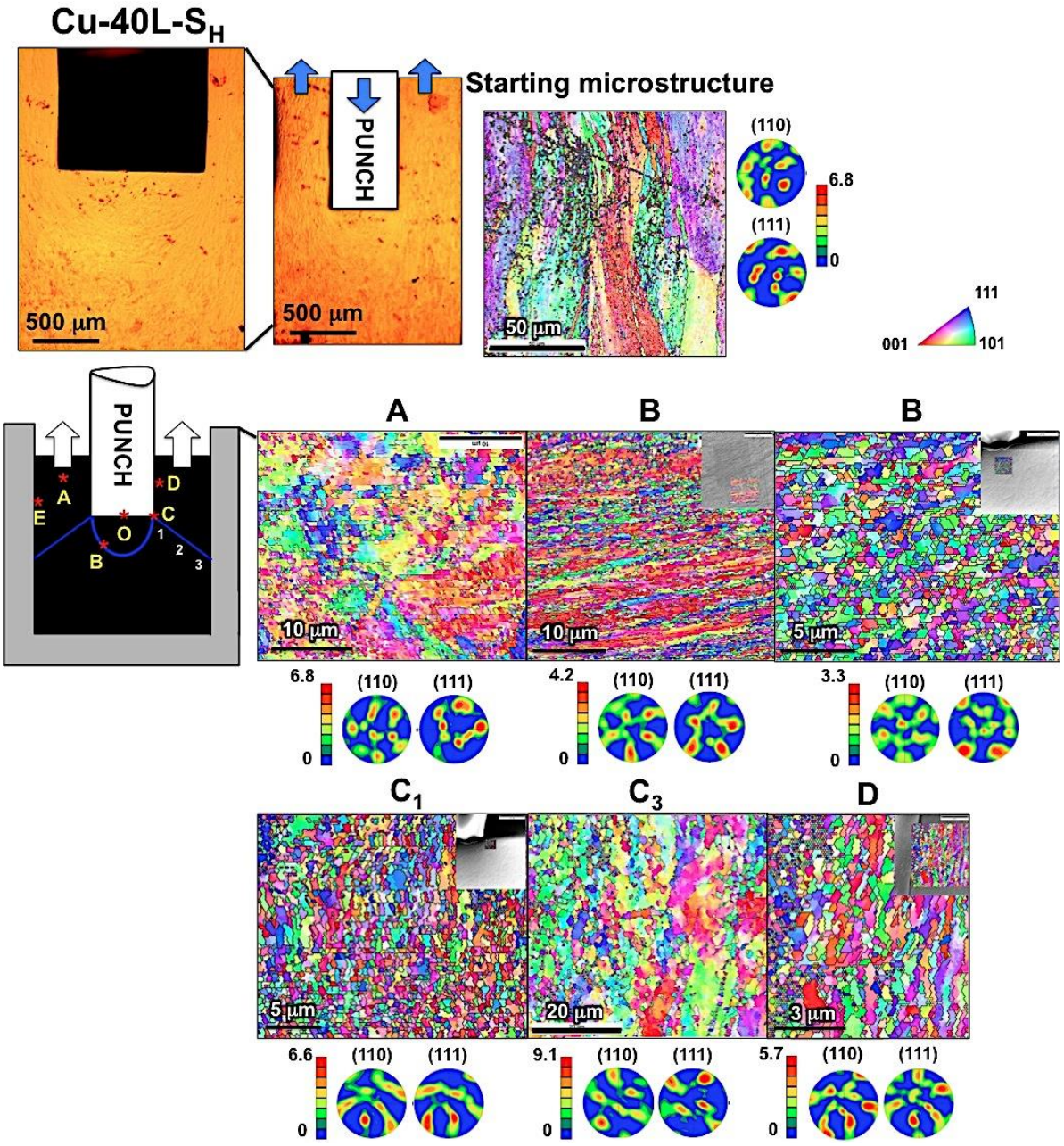

Figure 35: IPF obtained from OIM maps for Cu (40L-S_H) before and after indirect extrusion showing initial and final microstructures in different regions (marked with star and named as A-E in schematic, top left inset). Empirical (110) and (111) pole figures show texture evolution across the deformed sample. Inset in top left of the image shows optical image of deformed sample by indirect extrusion.

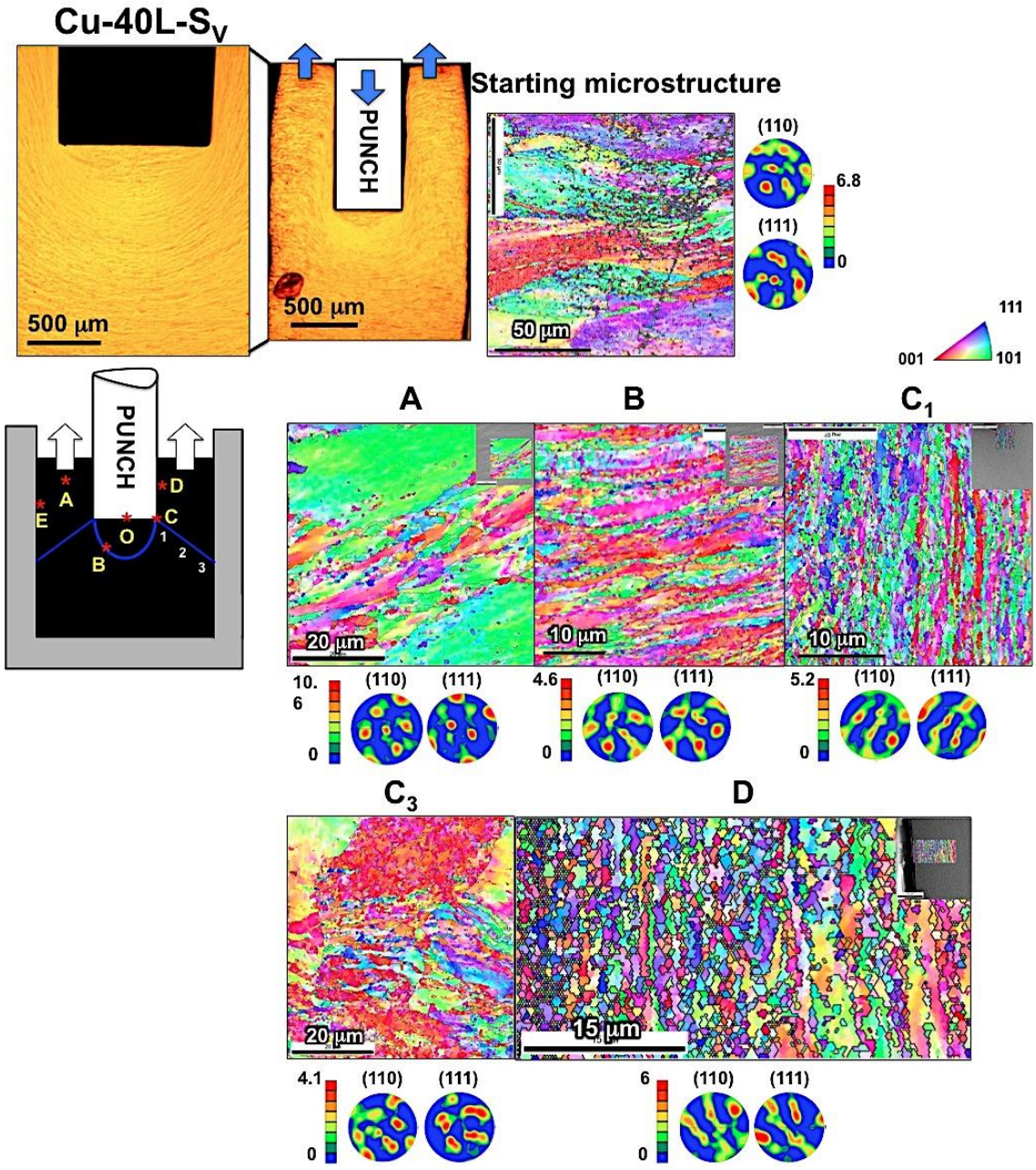

Figure 36: IPF obtained from OIM maps for Cu (40L-S_V) before and after indirect extrusion showing initial and final microstructures in different regions (marked with star and named as A-E in schematic, top left inset). Empirical (110) and (111) pole figures show texture evolution across the deformed sample. Inset in top left of the image shows optical image of deformed sample by indirect extrusion.

Therefore, it is concluded that the initial texture rotation results in different texture/microstructure evolution throughout the sample and hence change properties of micro-parts. This variation in microstructure and texture evolutions is attributed to the interaction of the pre-existing textures with texture are created in different regions of the sample depending on the mode of deformation in aforementioned regions. This conflict results in formation various type of the textures. As we mentioned previously in 40L-S_H, the force required for deformation was significantly larger compared with other two. Therefore, one can be argued here is that the large required force in this case is because of the harder material response to reorientation of pre-existing textures. It must be noted that the orientation of high strained paths (shear band layers) left from machining might be also an important factor in increasing the force values.

Figure 37 and 38 reveal microstructure evolution for 20L-F and 20L-S_H samples. Again less heterogeneous microstructure evolution in seen in sample 20L-F and simple texture evolved in most part of the PDZ. But in sample 20L-S_H, evolved textures in regions B and C are different and it features simple shear type of the texture in region B while it is somewhat close to compression texture at region C. Generally these samples with smaller grain size and more uniform starting microstructure result in more homogeneous microstructure evolution throughout the sample.

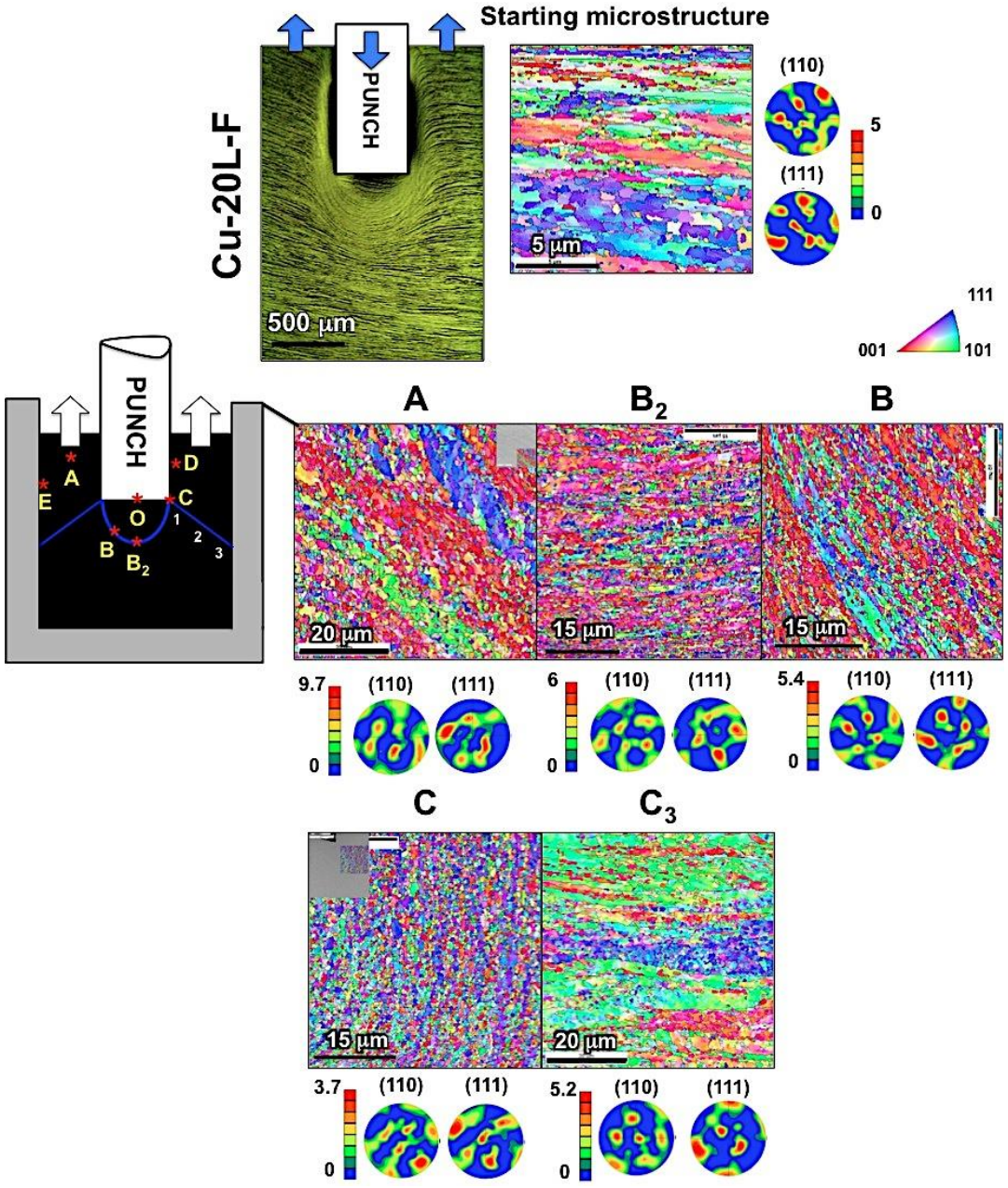

Figure 37: IPF obtained from OIM maps for Cu (20L-F) before and after indirect extrusion showing initial and final microstructures in different regions (marked with star and named as A-E in schematic, top left inset). Empirical (110) and (111) pole figures show texture evolution across the deformed sample. Inset in top left of the image shows optical image of deformed sample by indirect extrusion.

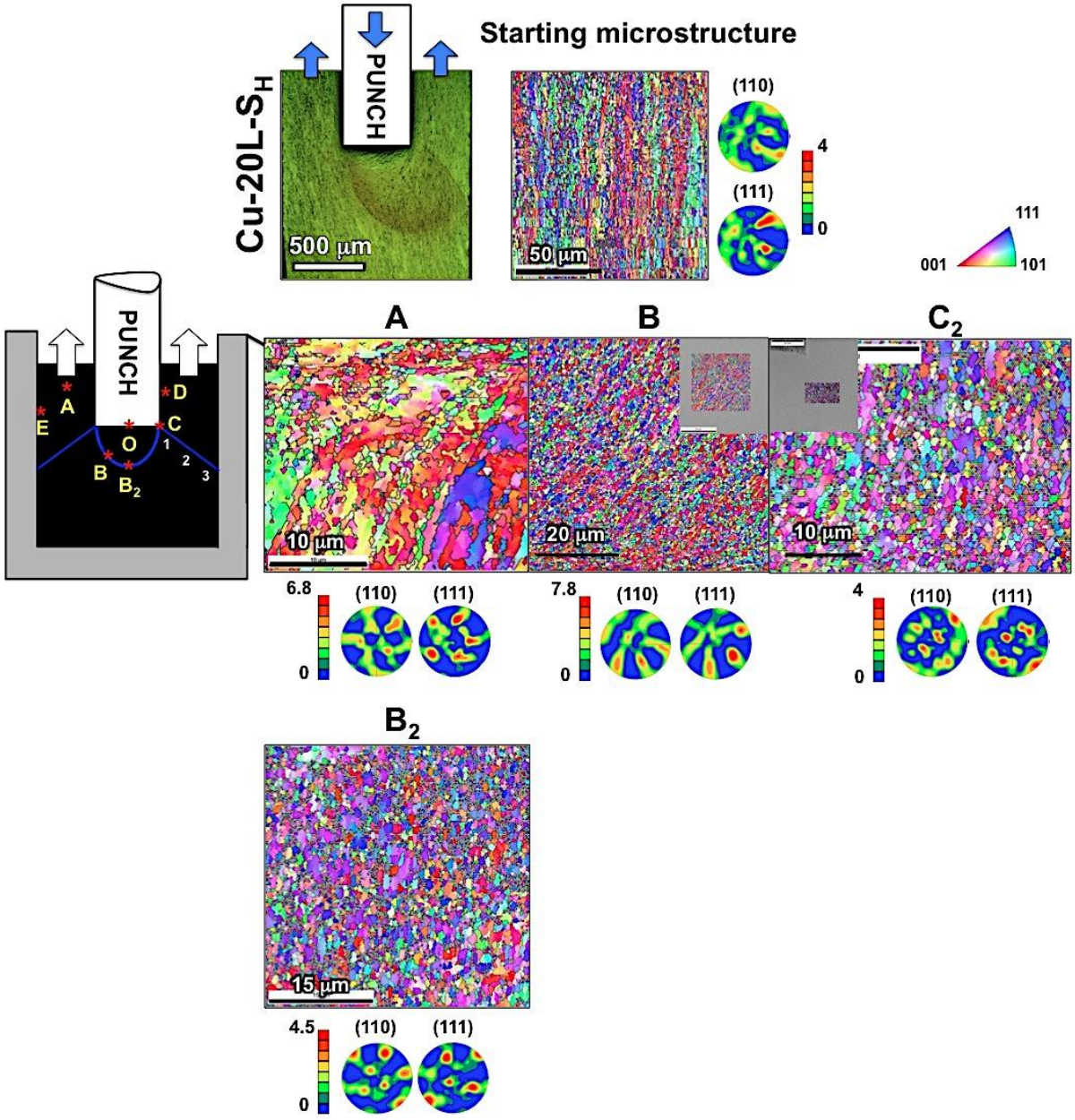

Figure 38: IPF obtained from OIM maps for Cu (20L-S_H) before and after indirect extrusion showing initial and final microstructures in different regions (marked with star and named as A-E in schematic, top left inset). Empirical (110) and (111) pole figures show texture evolution across the deformed sample. Inset in top left of the image shows optical image of deformed sample by indirect extrusion.

5.4 SUMMARY AND FINDINGS

This study was set to explore the effects arise from scaling and geometry constrictions in indirect microextrusion using model material Pb and identify limitations exist in scale free models e.g. SLF theory. To satisfy this objective, indirect microextrusion was performed using *in situ* stages capable of visualizing the deformation across the sample. Major elements of mechanics of deformation such as strain, strain rate and rotation fields were revealed across the length-scales and by varying the deformation rate. Quantifying the aforementioned elements was performed in order to identify the impacts of scaling and deformation rate across the PDZ. Parameterization of PDZ based on DIC measurements was also used to find the effect of mentioned factors on the heterogeneity and extension of PDZ where most of the process outcomes can be related to the phenomena occur at this zone. Next exploration was on the effects of microstructure characteristics including the grain size effects and later on for ultrafine material, finding suitable textures that behave optimally during the deformation by enhancing the flow behavior of material and quality of microproducts.

It is seen that although the morphology of PDZ is relatable to models suggested by SLF analysis for backward extrusion-type, there is a variation in the exact dimensions of deformation field proposed in such scale-free models. It is found that the normalized thickness of the deformation zone increases with scaling down of the process. The normalized thickness increases by the factor ~2.5 times with scale down of the process by ½. However, with increasing deformation rate, the morphology of PDZ and its spread does not change significantly. But, that leads to enhanced strain localization and rotation of material elements, which is further pronounced in smaller scales. These can result in non-uniformities in microstructures within parts created by IE, essentially manifesting in instabilities in mechanical

response and lead to process anomalies. The inhomogeneity factor extracted from the force measurements by finding the extrusion constant parameter k across the length scales is found to increase in a range of ~14-25% with scale down of the process by ½ and ~40-55% with increasing velocity by 10.

Complementing this, effect of grain size on mechanical responses in Al and its microstructure evolution was studied during IE. It is shown that with a larger initial grain size and larger work hardening capacity, the deformation zone is more extended and a large dead metal zone forms below the punch manifesting more heterogeneity in deformation. A VPSC model was employed to simulate local evolved textures in different part of the deformed Al samples and the results were compared to the empirical observations. It is found that there is a significant variation in evolved crystallographic textures across the deformed samples and observations suggest a preponderance of a simple shear crystallographic type of texture resulting from the deformation. Finally strain gradient theory and its relation to microstructure features e.g. grain/sub grain size was used to rationalize the thickness of the deformation zone. IPF maps and DIC measurements were used to find the ρ_{GND} in deformation zone. The average of Local ρ_{GND} is found to be ~7.9×10^{14}, 3.4×10^{15} /m^2 based on IPF maps in PDZ and ~5.6×10^{14} and 8.2×10^{13} /m^2 across the entire PDZ for fully annealed and as-received samples respectively. This suggests DIC technique as a promising method for quantifying microstructure evolution by relating the PDZ parameters to strain gradient.

Empirical observations of performing indirect microextrusion on ultrafine Cu samples having different textures revealed the strong dependency of the PDZ geometry on the prior textures. In micro-scale indirect extrusion, as shown by preliminary experiments by Pb, the size of PDZ increases which ensues more heterogeneity in deformation throughout the sample. It is

found that the interaction of this heterogeneity with created surfaces during deformation will eventually determine the quality of products in terms of the surface finish. Exploring the evolved textures at different regions of deformation zone with respect to the orientation of prior textures shows the evolution of different types of textures e.g. simple shear or compression crystallographic textures or in some regions a mixture of various textures.

6.0 MICRO-DEEP DRAWING

Sheet metal microforming involves a wide range of the processes, which are employed to fabricate a vast amount of micro-products for many applications. In these processes complexities related to size effect e.g. role of strain gradient in heterogeneity of deformation are nontrivial.

Micro-deep drawing involved a sheet metal forming process in which a rectangular blank was drawn into a forming die by advancing a punch (Figure 39). This was done in plane strain condition. Owing to the configuration of the setup, thickness of the highly polished sheet undergoing deformation is exposed unlike in the common radial sheet metal forming configurations.

It is expected that insight gained from the study of deformation behavior of material during micro-deep drawing can be used for a vast array of microforming processes e.g. microembossing, microblanking, micropunching etc.

6.1 QUESTIONS, HYPOTHESIS AND OBJECTIVES

In micro-deep drawing or any micro-sheet metal forming processes, catastrophic failure caused by fast fractures occurs due to the complicated geometries and stress distribution across the sample. Since, the dimension of the sample in one direction (thickness of the sheet) is very small compared to the other two, and then controlling the process and material response in this dimension is crucial to reduce or prevent any catastrophic failure. Due to the bend/drawing, a very high stress concentration is localized at the bent close to the corner of the punch. Therefore, micro-sheet is more likely to fail at this part. So, microstructure design becomes very important to delay or prevent any crack formation and propagation across the thickness of the sheet. The microstructure design need a comprehensive knowledge of the details of how grain size and its distribution, grain boundary characteristics, individual grain orientations or texture of the sheet, etc. affect deformation behavior of material during micro-deep drawing specifically regarding to their interaction with geometry and stress condition.

Similar to micro-bulk forming processes, it is expected that decreasing the grain size of the sample generally will improve the formability of micro-sheets by reducing the effects arise by anisotropy or non-uniformity. While microstructure refinement has several associated benefits, including enhancement of yield strength, better low cycle fatigue properties, etc., it often comes at the price of lower ductility at room temperature and lower thermal stability [53, 54]. So, the question here is: can we design the microstructures with respect to the geometry and loading condition of deep drawing that helps for better formability of the sheet while preventing early fractures due to the stress localization or lack of ductility?

It has been shown that ductility of fine grain size microstructures can be significantly improved by introducing bimodal microstructures [54, 55], lamellar structures [55, 56], and

coherent twin boundaries [56] or by designing a smooth and graded nano-grain/coarse grain interface [57]. In all above cases, variation in the parameters of the microstructure helps material sustain strain during the deformation and effectively delays strain localization and onset of instability at room temperature (microstructure engineering). In deformation geometries like tension in which the material undergoes homogenous deformation, the bimodality feature of microstructure is better to be distributed uniformly throughout the microstructure. However, in more complicated deformation configurations such as deep drawing, distribution of bimodality feature becomes significantly important as the stress is more localized in the regions that have larger contact area with punch- close to the corners of punch. Hence, higher toughness is needed for these regions to sustain strain localization and avoid crack initiation, which results in failure. This problem becomes even more important when the size of workpiece shrinks. In this case, the volume of material undergoing deformation decreases. Toward solving this problem, we hypothesized that Bilayer/multilayer or Graded microstructure provide conditions under which strain localization is avoided by having an ultrafine layer of material on top of the metallic sheets (in contact with punch) which is connected to the bottom layer with larger grain size to enhance ductility and formability.

Drastic thinning also starts happening that results in creating rough and poor quality surfaces at the corners. Based on such observations, the degree of crystallographic rotation is higher at those areas compared to the other parts of the sheet. Additionally, a sudden thinning and extension concentrated in one grain, mostly located below the punch, is observed in deep drawing of micro-sheets with large grain size. Hence, it is hypothesized that lamellar microstructures consist of the alternating layers of material with different grain size distribution-

ultrafine grain size and larger grain size- can avoid these types of process anomalies in material flow behavior during micro-deep drawing.

To complete this study, we are also seeking to investigate the effect of grain size as well as grain boundary characteristics on improving or disproving formability during micro-deep drawing. Coupling all these suggested experiments with SEM based DIC helped the better understanding of material response to deformation during this process.

6.2 METHODOLOGIES AND EXPERIMENTAL TECHNIQUES

Deep drawing facility for micron sized blanks capable of *in situ* Scanning Electron Microscopy (SEM) has been set up to perform the deformation in plan strain configuration. Die components including die cavity, blank holder and punch, all were made of D_2 tool steel. The die was set up onto the device equipped with a motor to apply linear force on the punch and sits inside the chamber of Philips XL 30 Scanning Electron Microscope.

The device was originally designed to perform *in situ* micromachining (Saurabh Basu & M Ravi Shankar, 2014) and utilized inside the chamber of SEM to observe record and analyze *in situ*, associate micro and nano-scale phenomena during micromachining. The design enables detailed characterizations at high magnifications in the SEM, via *in situ* secondary and backscattered electron imaging. The device is also capable of other imaging techniques including *in situ* Orientation Imaging Microscopy (OIM) by Electron Back Scattered Diffraction (EBSD). Controlling micromotions less than 10μm coupled with the force measurement using load cell with sub-micrometer resolution is all three X, Y and Z directions is another capability of this device. The load cell purchased from Michigan Scientific Corporation (Part # TR3D-B 250 lbs) mounted on a little stage that is driven along the slides by the piezo actuator. Details of the design and performance of this device can be found in previous work done in this group (Saurabh Basu & M Ravi Shankar, 2014).

The schematic and assembled of the deep drawing device is illustrated in Figure 39 a and 39b while performing deep drawing, flow of material was recorded in a sequence of secondary electron images. *In situ* characterization of the deformation field was performed using Digital Image Correlation (DIC). DIC as described above is a non-contact technique that tracks a pattern of strong contrast as the material deforms and then calculates the change in distance between

speckles and provides strain/strain-rate/rotation fields of deformation. To quantify the mechanics of deformation and find the heterogeneity of the deformation throughout the microstructure, high-resolution DIC is needed. Therefore, to obtain an accurate measurement of local strains accumulate in the vicinity of the grain boundaries, twin boundaries, etc. high-resolution images using SEM are needed. A low accelerating voltage (10KV) was used whereby physical asperities on the surface of the work piece would be amenable to producing sharper contrast in the secondary electron images. Advancing the punch at low speed, 150 μm/s to avoid temperature rise associated with high strain-rate plastic deformation, performs micro-deep drawing. It should be noted that, in this deformation configuration, the amount of strain imposed into the sample is typically small and for the most of experiments it is less than 0.2 while further plastic deformation results in failure. With the same die geometry; different punch widths, 0.5 mm and 0.8 mm, were used to examine various drawing ratios on the deformation behavior of microsheets. The width of the die cavity is 1mm for all experiments. Microstructure characteristics of sheet before and after deformation using micro-deep drawing set up for some different starting microstructures.

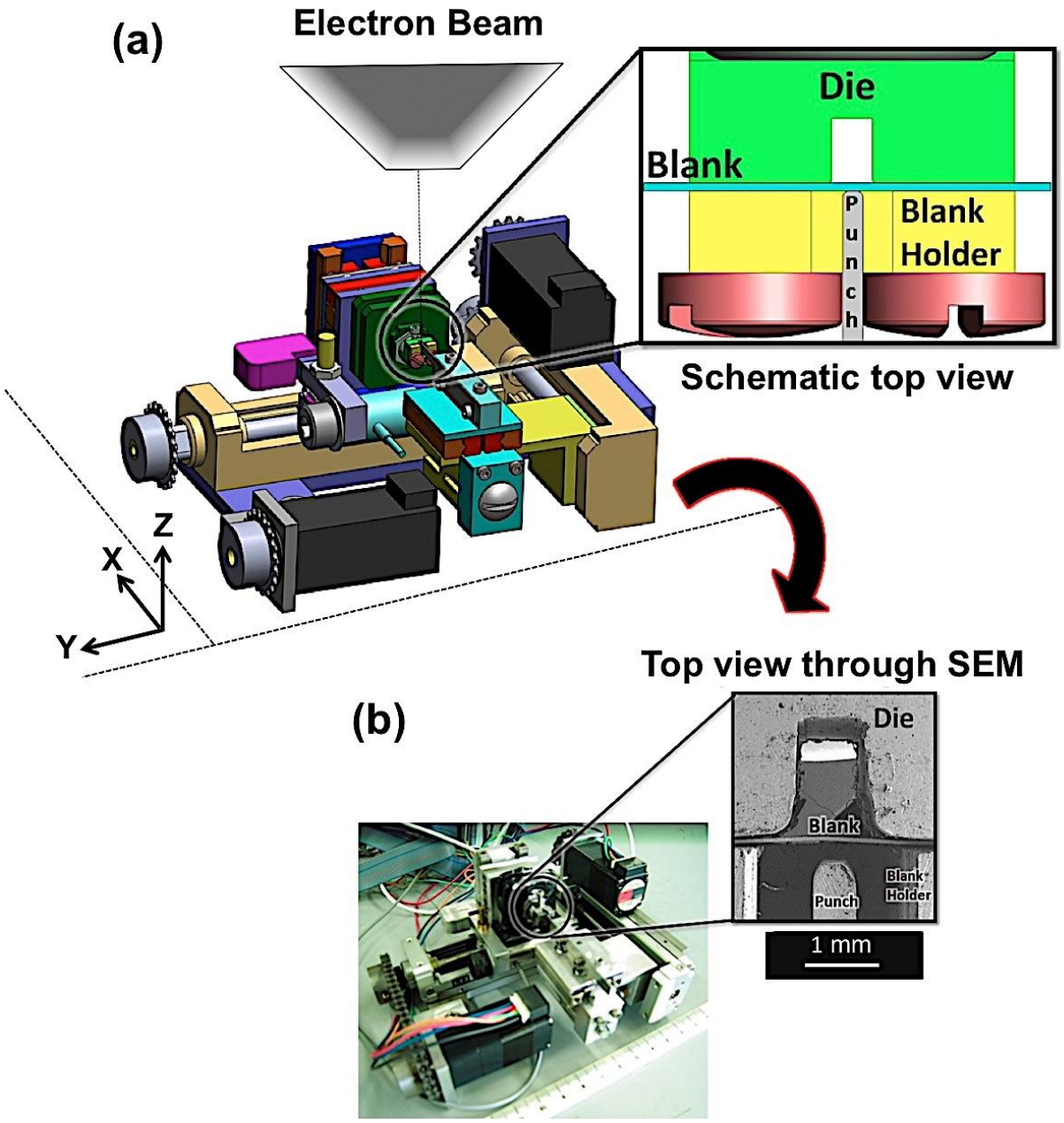

Figure 39: a) Schematic illustrating Micro-deep drawing setup inside the chamber of SEM. b) Deformation stage assembly and top view of the sample through SEM.

6.2.1 Materials and microstructure design

In micro-deep drawing, Ni and Cu sheets with 50, 75, 100 μm thicknesses were used with different initial microstructure parameters. Micro-sheets were prepared with approximately 7 mm length and 3 mm width. Ni and Cu sheets both were tested in as-received conditions. To study the effect of the grain size, very large grain sized Ni micro-sheets were produced by polishing Ni strips that were annealed at 1173 K for 10 hrs with average grain size ~300 μm. To create Ni sheets with fine grain size, machining (20° tool rake angle, 100 μm depth of cut, 5 mm/s cutting speed) was performed on the bulk of annealed Ni (1173 K, 2hrs) and then deformed chip is heat treated at 823 K for 1hr and then grinded down and polished using SiC papers to the desired dimensions (100 μm thickness, 7 mm length and 3 mm width). The resulting microstructure features an average grain size about 5 μm throughout the chip.

Another microstructure examined in micro-deep drawing is graded microstructure, having a layer of ultrafine grain microstructure on top of the sheet and a large grain size layer underneath (location 1 in Figure 15 a). They were produced from freshly created surface of the Ni bulk (Figure 15 b) after machining (0° tool rake angle, 100 μm depth of cut, 5 mm/s cutting speed). Samples were cut from the machined surface and grinded down to 100 μm. Generally the thickness of the ultrafine grain layer is approximately between 15-30 μm. Samples were grinded down carefully from the bulk side to desired thickness and from the ultrafine top side it was polished smoothly to only remove the rough surface left from machining to keep the ultrafine layer on the top. This integrated graded microstructure was created on Ni bulks with large (~200 μm) and medium (~50 μm) grain size microstructures.

Lamellar microstructure was also created in the Ni chips using 40° tool rake angle, 100 μm depth of cut, 5 mm/s cutting speed. Such microstructure features lamellas with fine/ultrafine

grains separated from each other by either original high angle grain boundaries or generated low angle grain boundaries, which oriented vertically across the thickness of the chip/sheet. Similar to previous samples, this sample was also prepared by grinding down the chips in aforementioned cutting condition from both sides to the desired dimension to produce a sheet with lamellar microstructure for micro-deep drawing.Cu sheets were examined in as-received condition as mentioned previously in three different thicknesses: 50, 75 and 100 μm. Additionally the effect of grain boundary characteristic was examined in Cu microsheets by creating special boundaries in ultrafine Cu chips (20° tool rake angle, 100 μm depth of cut, 5 mm/s cutting speed) using short and long annealing time (5 min and 2 hrs) at 473 C°.

6.2.2 Orientation image microscopy (OIM)

In micro-deep drawing, Ni and Cu micro-sheets were mounted in the epoxy and mechanically polished in a Struers down to 0.04 μm using colloidal silica for final step. After polishing, samples were removed from epoxy by dissolving epoxy in acetone and then placed in the deep drawing die, while the polished surface of the sheet was exposed to the SEM beam to perform microforming inside the SEM and to do EBSD before and after each stop of deformation. Additionally, Ni samples were also vibratory polished for several hour using 0.04 μm Alumina solution. Accelerating voltage used to perform OIM is typically 20KV and a spot size ranging from 0.05 to 2 μm depending on the grain size was set.OIM by EBSD performed before deformation on initial microstructure. Post-deformation microstructure characterization was also performed after each stage of deformation to track microstructure/texture evolution grain-by-grain and in different regions of the microsheets during micro-deep drawing.

Table 6: Microstructure characteristics measured for fully annealed Ni sheet with large grain size before the deformation, after first stop and also after failure related to OIM images shown in Figure 41 and 42. Grains 1-8 are numbered in this sample according to Figure 41. Kernel Average Misorientation (KAM), Grain Orientation Spread (GOS), Point-to-Point (P-P) and Point-to-Point (P-O) along local x and y-axes (Figure 41 a), Grain Size (GS) along local x and y-axes (Figure 41 a) and Grain Boundary Misorientation (GB M-O) are shown for each grain and grain boundaries separating aforementioned grains.

Grain ≠	1	2	3	4	5	6	7	8	Ave
KAM (deg)	1 0.6 0.92	0.76 0.85 1	0.66 0.63 0.92	0.54 0.66 0.7	0.58 0.78 0.87	0.82 0.89 0.91	0.66 0.80 -	0.48 0.72 1.14	0.56 - 0.92
GOS (deg)	0.825 0.46 1.1	0.78 0.73 0.78	0.71 0.64 0.9	0.54 0.72 1.2	0.96 1 1.12	0.76 0.67 1	1 0.61 -	0.76 0.87 0.82	0.79 - 0.98
P-P (X) (deg)	0.95 0.5 0.56	0.62 0.68 1.3	0.6 0.53 0.85	0.5 0.57 0.51	0.52 0.54 0.65	0.76 0.9 0.7	0.6 0.62 -	0.33 0.63 0.77	0.61 - 0.76
P-P (Y) (deg)	1.15 1.84 0.72	0.75 0.79 1.1	0.55 0.45 1	0.65 0.73 1	1.98 0.81 1	0.86 1 1	0.47 0.68 -	1.84 - 1.13	1.03 - 1.86
P-O (X) (deg)	2.27 0.92 2.54	2.5 3.49 7.8	2.54 3.29 6.4	3.6 4.72 5.6	1 3.15 2.52	1.86 6.11 5.6	1.41 2.11 -	0.43 6.6 11.8	3.07 - 5.99
P-O (Y) (deg)	5.76 3.51 5.9	1.77 5.9 2.89	0.89 1.79 4.2	7.1 7.8 6.5	2.73 6.3 6.5	3.68 4.3 4.5	3.6 3.9 -	4.9 - 4.2	3.8 - 4.02
GS (X) (μm)	103 103 108	241 247 261	91 88 100	165 168 190	99 95 90	297 283 332	48 44 -	282 272 404	165.76 - 212.15
GS (Y) (μm)	112 100 98	111 110 108	28.6 29.8 32	87 88.84 57	112 115 115	110 105 98	53 46 -	110 90 75	111 - 98
GB ≠	1-2	2-3	2-4	3-4	4-5	5-6	6-7	6-8	7-8
GB (M-O) (deg)	60 60 60	60 60 56	42 44 54	35 34 28	14 14 14	60 56 52	29 32 -	39 41 -	54 54 -

Table 7: Microstructure characteristics measured for as-received Ni sheet with medium grain size before the deformation and after failure for different sections of the sheet (Figure 50 a). Kernel Average Misorientation (KAM), Grain Orientation Spread (GOS), Grain Size (GS) and Grain Boundary Misorientation (GB M-O) are shown for each section and in average for the whole sample.

Section≠	1	2	3	4	5	6	Ave After Failure	Ave Initial State
KAM (deg)	1.54	1.69	2.17	1.82	2.08	1.41	1.78	1.03
GOS (deg)	2.2	1.76	2	1.95	2.4	1.5	2.13	1.16
GB(MO) (deg)	19.25	18.86	22.13	22.25	18.56	26.21	17.5	32.95
GS (μm)	7.8	5.9	5.22	6.13	6.3	7.67	6.51	9.11

Table 8: Microstructure characteristics measured for Ni sheet with small grain size before the deformation and after failure (Figure 55 and 58). Kernel Average Misorientation (KAM), Grain Orientation Spread (GOS), Grain Size (GS) and Grain Boundary Misorientation (GB M-O) are shown both case for the parts of the sheet for which OIM were performed.

	Ave Initial State	Ave After Failure
KAM (deg)	1.57	2.45
GOS (deg)	1.33	4.37
GB(MO) (deg)	29.88	30.98
GS (μm)	4.5	4.37

Table 9: Microstructure characteristics measured for Cu sheet produced by machining and subsequent heat-treating before deformation by deep drawing (Figure 77 a-c). Grain size (GS); Grain boundary-misorientation (GB M-O); %Twin boundaries (Σ3 boundaries); % Low angle grain boundaries (LAGB), >2<15; % High angle grain boundaries (LAGB), >15 and % CSL boundaries are shown for each microstructure in average.

Microstructure type	As-machined	Short-annealed	Long-annealed
GS (μm	0.59	1.63	2.75
GB (MO) (deg)	32.8	27.3	19.9
Σ3 %	0.02	0.11	0.13
LAGB %	0.21	0.43	0.64
HAGB %	0.68	0.39	0.2
CSL %	0.09	0.16	0.14

6.3 RESULTS AND DISCUSSION

6.3.1 Deep drawing of Ni

Commercially pure Ni 200 was used as a work hardening F.C.C. model material to examine the effect of prior microstructures on flow behavior and onset of failure during micro-deep drawing. Various microstructures features were created in Ni sheets using different thermo-mechanical treatments. Pure Ni is easy to polish and provides a chemically stable surface that does not undergo any oxidation/corrosion during microforming, so it was used to track the evolution of microstructure during micro-deep drawing grain-by-grain and in the vicinity of the grain/twin boundaries. Results of this observation will be discussed subsequently.

6.3.1.1 Characteristics of created starting microstructures

Figure 40 shows the starting microstructures created in the Ni microsheets to perform *in situ* micro-deep drawing. The position of the microsheets (blank) and its thickness exposed to the beam inside the SEM for performing *in situ* experiments exhibited in Figure 40a.

Schematic and OIM images of aforementioned type of microstructures examined in this suite of experiment are exhibited in Figure 40b and c, insets i-o. Here, microstructure type i refers to a very large grain size where the grain size is bigger than the thickness of the microsheets (100 μm); type j to the medium grain size microstructure in which the grain size is medium and annealing twins are distributed almost uniformly across the microstructure; type k to the small grain size microstructure with uniform grain size distribution; type l to graded microstructure consists of an ultrafine grained surface layer, a transition layer and a pre-strained sub-layer with large grain size, straining in sub-layer is formed during machining of surface that left an ultrafine layer on the surface and a pre-strained layer underneath depending on the

penetration depth of strain; type m to the same microstructure as type l but the underneath layer has a medium grain size features; type n to same microstructure as type m but flipped over wherein the ultrafine grained layer becomes sub-layer in the sheet; type o to the lamellar microstructures composes of large lamellas strained and consists of low and high angle grain boundaries separated by original grain boundaries in annealed plate that the chip made of. The methodologies employed to create such microstructures were described in section 4.4.1.

Characteristics of aforementioned microstructures and their behavior during micro-deep drawing will be discussed for each case in the following subsections.

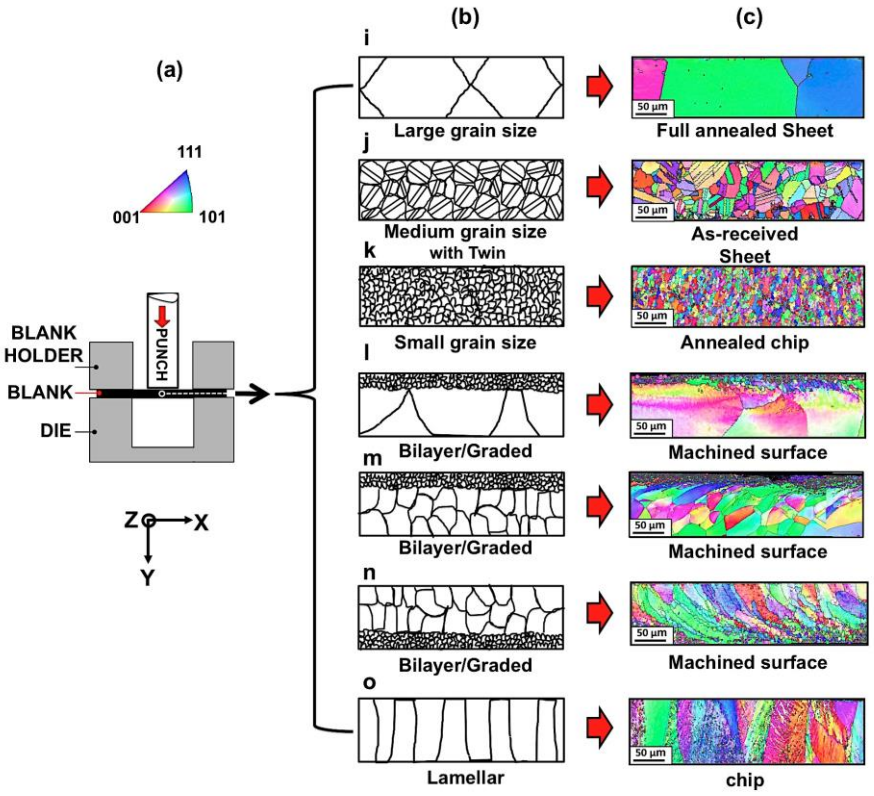

Figure 40: Schematic of deep drawing in plane strain condition showing the exposed surface of the sheet (Blank) to beam with different microstructures. Schematic of examined microstructures in Ni microsheets (i-o) by deep drawing; i: very large grain size showing a grain size larger than the thickness of the sheet, j: medium grain size with distributed annealing twins across the microstructure, k: small grain size, l: graded with large grain size sub-layer, m: graded with medium grain size sub-layer, n: graded with medium grain size top-layer and ultrafine grain size sublayer, o: lamellar consists of deformed large lamellas aligned vertically across the thickness of the sheet. c) OIM images of the suggested initial microstructures obtained before preforming deep drawing experiment (i-o) created by; i: annealing Ni as-received sheets, j: as-received, k: annealing the chips produced by machining, l: machining the surface of annealed Ni plates, m: machining the surface of as-received Ni plates, n: machining the surface of as-received Ni plates, o: chips produced by machining of annealed Ni plates.

6.3.1.2 Large grain size (type i)

Figure 41 shows OIM micrographs of annealed Ni sheet (100 μm) before performing *in situ* deep-drawing experiment. Plane strain configuration is employed to do this in which the polished surface of sample is exposed to the electron beam inside the chamber of SEM and undergoes deformation by advancing the punch. The microstructure revealed by OIM analysis shows a very large grain size in which only few grains (numbered in Figure 41 b) spread across the thickness of the sheet. Figure 41 c demonstrates the KAM maps that show local misorientation distribution inside each grain and in the vicinity of grain boundaries for misorientations below 10°. It is seen that the illustrated annealed grains are almost strain free and spread with random orientations across the microstructure. This provides a condition to track the microstructure evolution grain-by-grain in the interior of grains and in the vicinity of grain boundaries. In order to track the microstructure evolution in the sheet grain-by-grain during micro-deep drawing, the experiment was stopped two times before failure and OIM analysis was performed on the exposed surface of the sheet. Results of this analysis are illustrated in Figure 42. This analysis was also performed on the sample after failure (Figure 42 d). This figure shows irregularity/non uniformity in different parts of the sheet which is related to the properties of the individual grains i.e. size, orientation, etc. and the grain boundaries separating these grains as well as macroscopic boundary conditions i.e. position of the grains in the sheet with respect to the punch and geometry of deformation. To probe this further, microstructure characteristics are analyzed in details after each step of deformation as we perform on the initial state of the microstructure for each grain. Results of these characterizations.

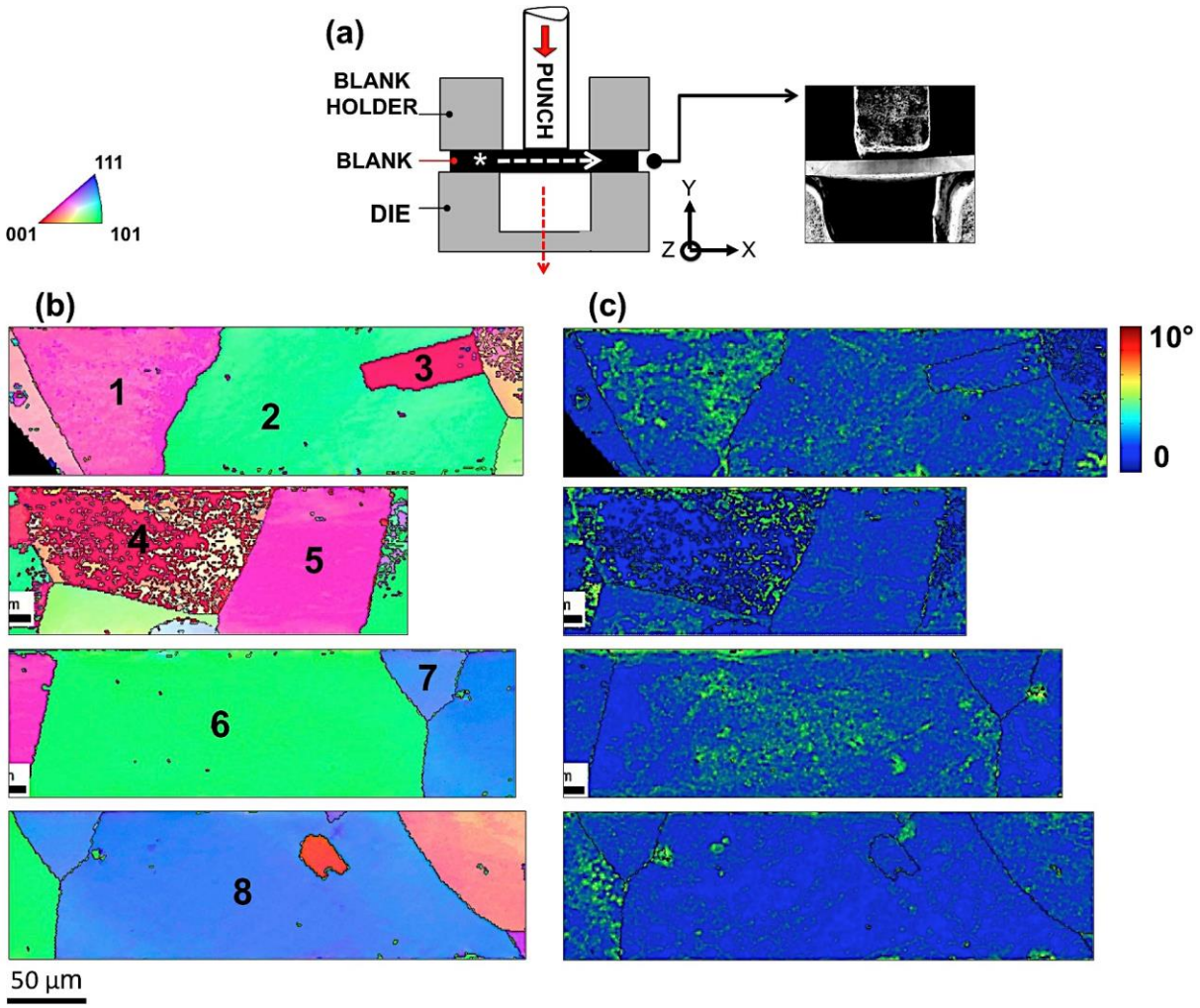

Figure 41: Schematic of micro-deep drawing die showing the position of the blank, (* refers to exposed side of microsheet to SEM electron beam that was polished and its microstructure captured by OIM), inset shows the SEM image of the sheet with 100µm thickness before deformation. b) OIM micrographs show the microstructure of sheet having very large grain size, grains numbered individually along the white arrow, schematic image, c) KAM maps show the local misorientation distribution in each grain, this was shown for misorientations below 10 °.

In this table, measurements for KAM, grain orientation spread, point-to-point and point-to-origin misorientations along the local X and Y axes, etc. for each grain as well as grain boundaries misorientations using TSL-OIM analysis software are shown for aforementioned states corresponding to OIM analysis shown in Figure 41. From this table, it is observed that KAM, which shows the average of local misorientation for each grain, increases by advancing the punch for almost all grains across the sheet. But the rate of increasing local misorientations is larger for grain 8 where the sample fractured compared with other grains (Figure 42 d). This value is lowest for grain 6 located below the punch, which undergoes the significant extension during deformation. Average of GOS is also shown for all grains before and after deformation by micro-deep drawing. Results show an increasing trend for almost all grains except grain 2 that has the same value of GOS in initial and final states showing the homogenous deformation across the grain. P-P and P-O misorientations are also measured for each grain along the local x and y-axes. It is seen that P-P (x) is largest for grain 8 and while P-P (y) has the lowest value for this grain. This indicates that the variation of misorientation between adjacent points within the grain is large along the extension axis (x) but very small across the sheet thickness (y axis). Results for P-O (x) again show the largest variation for grain 8 but it has the lowest variation along the y-axis. All these observations suggest very small crystallographic rotations during the micro-deep drawing of a sheet with large grain size. Grain size was also measured along local x and y-axes showing the thinning phenomenon (extension of each grain). Results reveal that this phenomenon does not happen uniformly in each grain as the grains 6 and 8 undergoes significant extension while grains such as grain 1 almost remains unchanged during the deformation. Additionally, misorientation of the grain boundaries (GB-MO) separating grains from each other was measured after each step of deformation. It is seen that for some grain boundaries e.g. GB 2-

4 separating grains 2 from 4, it does not change while it has an slight increase for GB 6-8 and 6-7 where the material fails and noticeable decrease for GB 3-4 and 5-6 where the grain rotations occur to maintain continuity at the grain boundaries. Consequently, from all above empirical measurements it is suggested that material with large grain size is deformed inhomogenously during micro-deep drawing and it is mostly governed by slip rather than crystallographic rotations.

Non-uniformity in deformation is also observed within the grains especially at the intermediate states of the deformation. Although, KAM maps show localization of deformation in different parts of the sheet during deformation, IQ maps capture better the onset of deformation and its spread in individual grains as shown in Figure 43 for some of grains across the sheet. For instance in grains 2 and 8 it starts at grain boundaries while for grain 6 almost at the interior part of the grain.

It is seen that since the distance between grain boundaries are too large and grain size is larger than the thickness of the sheet, deformation starts inhomogenously from the interior of the grain rather than convectional belief that it necessarily starts from the grain boundaries as parts of the material which resist the deformation of interior. The incompatibility effects become lesser as the deformation mode changes from bending to drawing by advancing the punch into the die results in more homogeneous deformation in each grain.

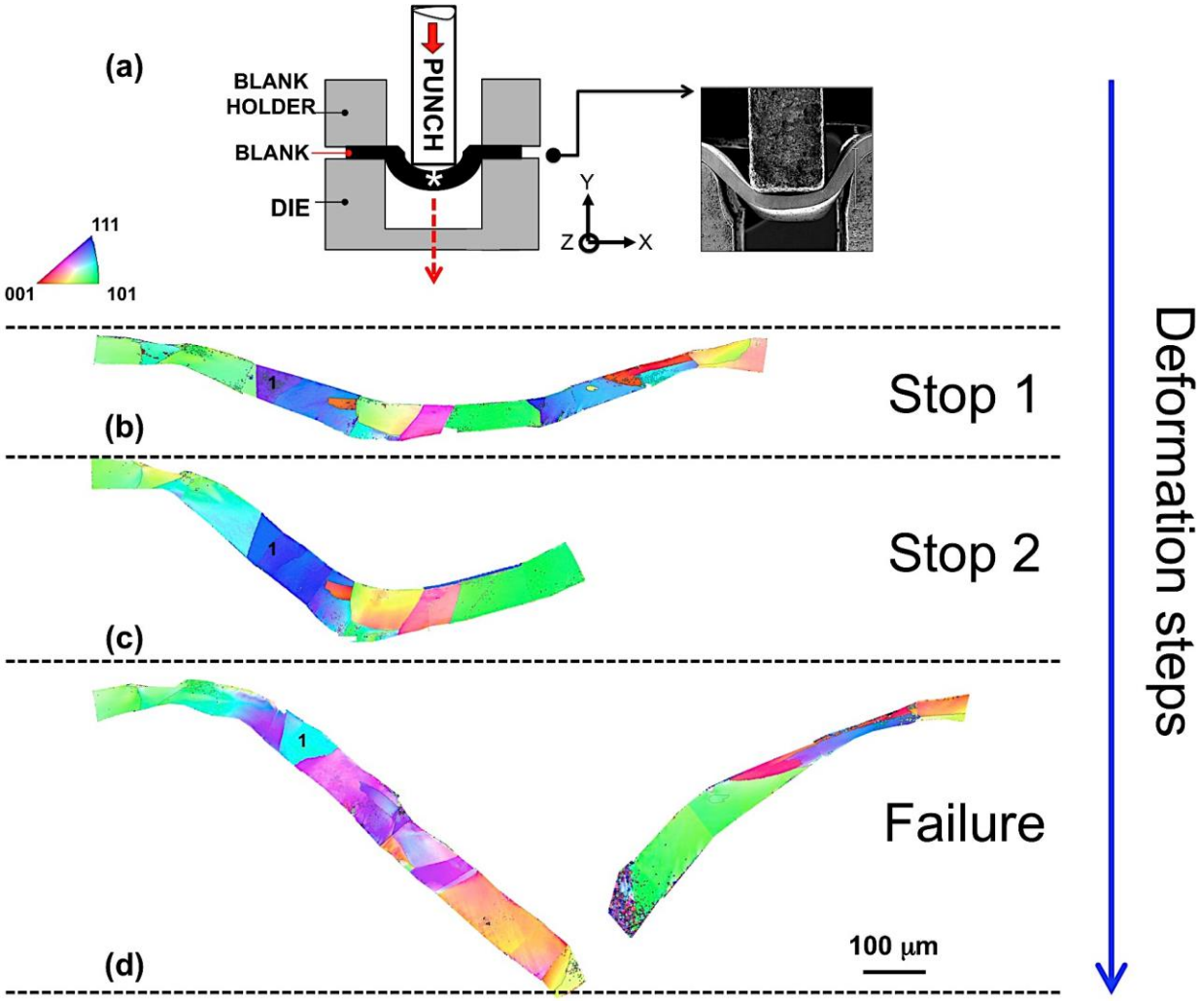

Figure 42: a) Schematic of micro-deep drawing experiment, showing deformed sheet (blank) in the die as a result of advancing the punch through the die cavity, (*refers to the exposed surface of the sheet, the microstructure of which was captured using OIM analysis after several stops and after failure). Right inset shows the SEM image of the deformed sheet captured while performing experiment. IPF from OIM of the polished surface after b) First stop, c) Second stop and d) Failure show the microstructure evolution and deformed grains during microforming.

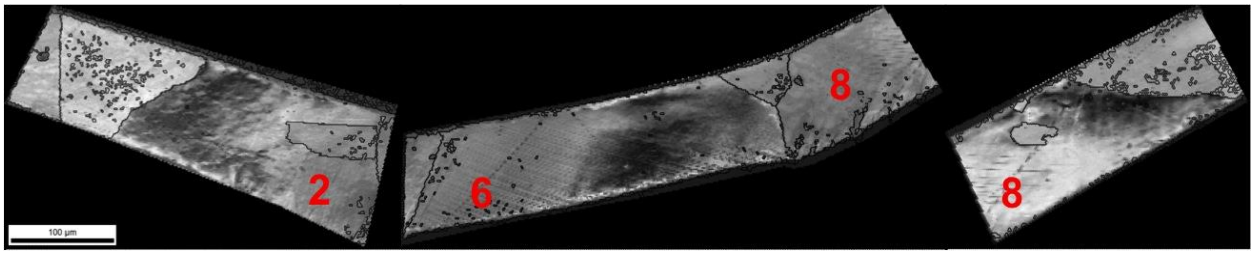

Figure 43: IQ map at stop 1 of deformation showing the onset of deformation in each grain.

In addition to the microstructure evolution, the grains interactions during deformation to maintain compatibility within the microstructure affect the properties of the surface of microproducts. Incompatibility makes the free surface grain move normal to the surface, resulting in the occurrence of surface roughening. Commonly, presence of the twins, twin boundaries, triple junctions, grain boundaries along with grain orientation and location of the grains with respect to the punch and geometry of deformation (macroscopic boundary conditions), result in creating prominent rough surfaces during deformation. This is the manifestation of the broad inhomogeneity during microforming of annealed sheets due to the individual reactions of each grain to the deformation. The amount of rotation to maintain continuity at grain boundaries is suppressed in this type of microstructure across the thickness and therefore, grain rotations are mostly attributed to material response to geometry and macroscopic boundary conditions (rigid body rotation) rather than continuity at grain boundary (lattice rotation). Figure 44 demonstrates this effect on the surface and the consequences of highly inhomogeneous plastic flow in different parts of the sheet in intermediate states of deformation and also after fracture. It shows that further deformation results in more roughening on the free surface of the sheet more pronouncedly at the corners of the punch and also corners of the die where the deformation is more concentrated.

It is observed that steps appeared at the grain/twin boundaries and even within a grain where part of a grain deformed more severe compared with the other parts. This shows the deformation is not distributed uniformly even at grain interiors. This is because part of the big grain located at the bottom edge of the sheet, which is undergoing tension while the upper part is undergoing compression, therefore the discrepancies. Hence, grains such as grain 2 and 4 start expanding from outer side in bottom edge of the sheet at the corners of the punch while grain 7 is popping-up because of compressive stresses at the upper edge and also at the triple junction (Figure 44 b). Figure 44 c shows necking and then a ductile fracture occurred.

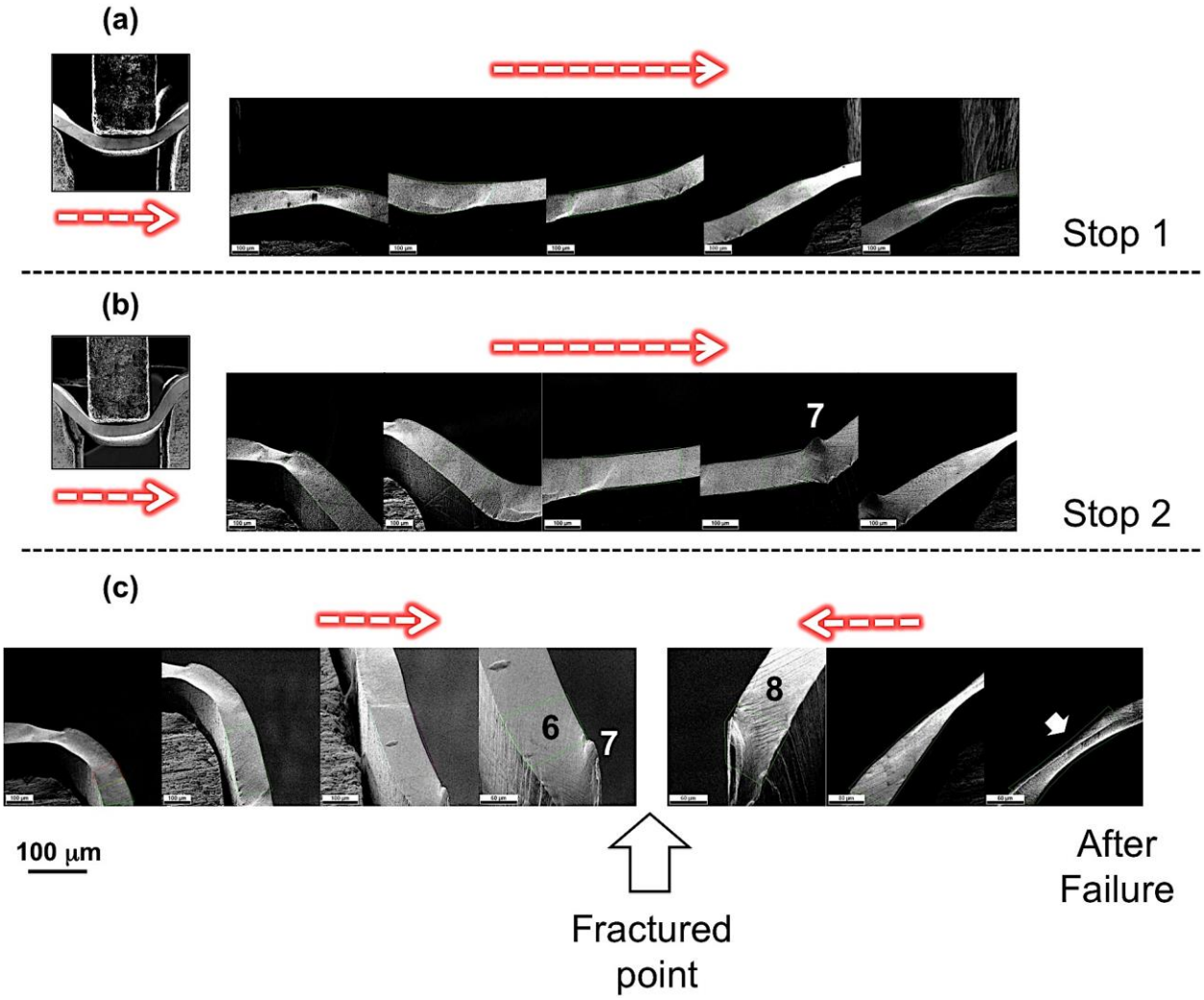

Figure 44: SEM images of the surface of annealed sheet during microforming by deep drawing after a) First stop; b) Second stop and c) Failure. Severe rough surface developed during deformation due to the anisotropic and inhomogeneous deformation Behavior of sample. Arrows show the direction of the sequence of captured images thorough SEM. Numbres 6-8 refer to grains marked in Figure 41, which shows the fractured point in the sheet.

Bending effects at the corners of the die also result in creating of very rough surfaces where the upper edge of the sheet is under tension and bottom edge under compression. This stress conditions and sudden changes in stress mode results in imposing large strain gradients across the thickness of the sheet. Therefore, surface roughening, which is the result of grain interactions to deformation and to maintain continuity at the grain boundaries, is significantly influenced by geometry of grain boundaries. For instance, at the right corner of the die (arrow in Figure 44 c), presence of a long horizontally orientated grain boundary close to centerline of the sheet lead to the formation of a pick on the surface due to the different deformation mode in upper and lower sides of the grain boundary and grain boundary resistance to deformation.

It shows symmetric slips originated from this grain boundary in both upper and lower sides. From SEM observations as was suggested by the grain-by-grain analysis of the microstructure evolution table 6 the deformation is governed by slip (Figure 45) rather than crystallographic rotation. It shows that at grain boundaries, triple junction and etc. (arrows in Figure 45 b and c) deformation reaches to a stage that several slip systems are needed to maintain continuity at these parts of the crystal. But in most part of the grain only one slip system got activated and therefore less crystallographic rotations. Figure 45 c shows this effect at a triple junction (shown by arrow) where high-generated stress is relaxed by second slips in neighboring grains. This was captured after polishing of the fractured surface again. To activate multiple slip systems locally at the vicinity of triple junctions, crystal rotations are required. This high local misorientations results in formation of low angle grain boundaries (Figure 45 j) that extended into the grain as also shown in KAM map (Figure 45 k).

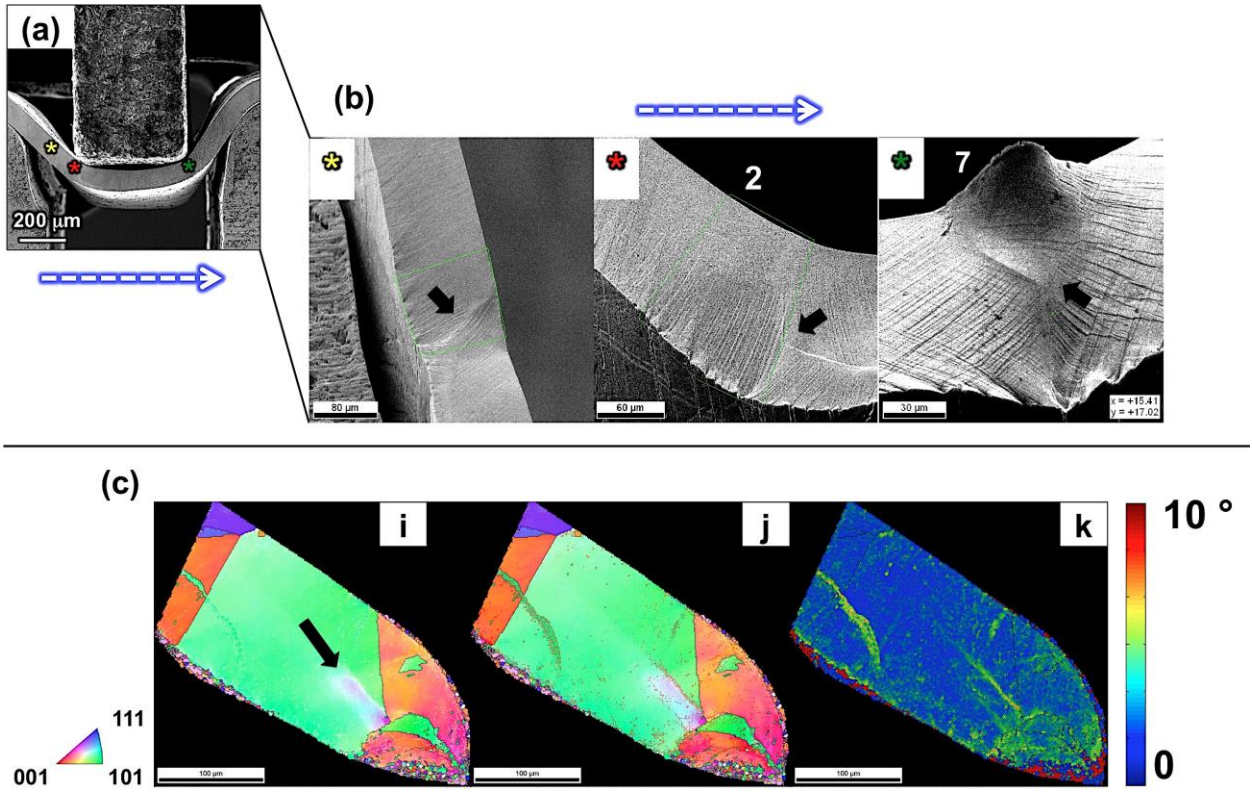

Figure 45: a) SEM image of the annealed sheet undergoing deformation close to the fracture, (* marks with different color refer to the locations of the sample from which the high-resolution SEM images were taken). b) High-resolution images of the regions in the sample (marked with *) close to the corners of the punch and on the side of the sheet, showing the interaction of the grains to the deformation in the outer/inner sides of the sheet as well as in the vicinity of the grain boundary and triple junctions shown by black arrows. c) IPF from OIM of fractured region after repolishing showing the microstructure evolution around the triple junction, insets i, j and k show IPF with high angle grain boundaries, IPF with high and low angle grain boundaries and KAM maps respectively.

Mechanics of deformation

Sequence of SEM images (Figure 46 a-d) recorded during micro-deep drawing reveals deformation of surface grains during deformation. Method used to perform DIC was described in details in section 4.5. Figure 46 e shows the strain-rate field for the deformed sheet. Inset at right shows the locations of the grains with respect to the punch according to numbering in Figure 41. It is seen that deformation is localized at the grain boundaries. The highest concentrations are at the corners of the punch; white arrow shows strain concentration at grain 7, its deformation is illustrated in left inset. From SEM and OIM observations described previously, it is seen that the fracture happens at grain 8. This is also captured by looking at DIC result where the highest localization of deformation is at grain 8, bottom right side of white arrow (Figure 46 e). It must be noted that non-homogeneous deformation is clearly observed along the sheet in each grain and also in grain interiors, which are undergoing different rate of deformation than grain boundaries. This is in agreement with microstructural evolution analysis discussed previously.

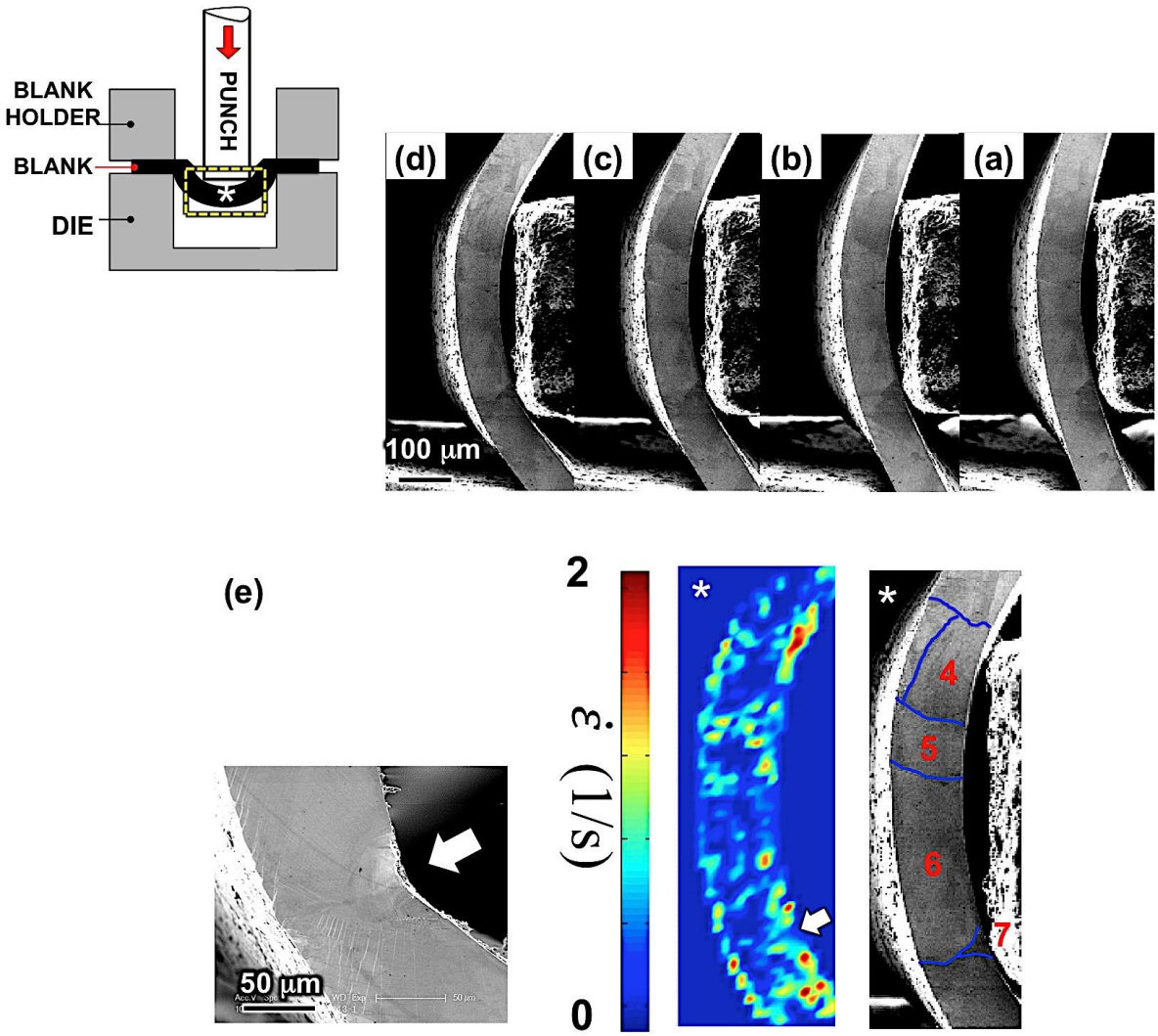

Figure 46: a)- d) Sequence of Secondary Electron Images for performing Digital Image Correlation captured during micro-deep drawing of annealed Ni sheet. The area used to perform DIC is shown by dash line in the schamteic inset on the left. e) Strain-rate field obtained from DIC for micro-deep drawing with V= 150 μm/s. This shows a localization of strain at the grain boundaries marked in right inset with blue color. Nummbers 4-7 are corresponding to grains marked in Figure 41 a. Inset on the left shows a larger magnification of the area shown with white arrow in strain-rate image corresponding to small grain number 7 which popped-up at the corner of the punch during deformation.

Theory of micro-deep drawing (micro-bending)

Generally deformation in micro-bending of sheet metals is associated with the shape changes while in micro-deep drawing it is associated with reducing in the cross sectional area in which a tensile force or pressure is applied to achieve a permanent deformation(Hezong et al., 2011). Theories applied in micro-bending is useful in micro-deep drawing in plane strain condition because of the similarity that exists in their deformation configuration as shown in Figure 47.

SGP models are essentially based on Taylor's work hardening models(G. I. Taylor, 1934) by which the yield shear stress is related to dislocation density by:

$$\tau = \alpha G b\sqrt{\rho_T} = \alpha G b\sqrt{\rho_S + \rho_G}, \sigma = M\tau \tag{25}$$

where α is an empirical material constant ranging from 0.1 to 0.5, G is shear modulus, b is burger's vector, ρ_T, ρ_S and ρ_G are total dislocation density, statistically dislocation density and geometrically necessary dislocation density respectively(Hezong et al., 2011). M is known as Taylor factor which relates tensile yield strength (σ) to shear yield strength (τ). This theory is used to rationalize the extra strength observed in deformation of foils compared with thick sheets of same material by introducing extra term GNDs density effect in hardening behavior of foils during micor-bending. The relation between the plastic strain gradient and GNDs density is assumed as:

$$\nabla\varepsilon = \rho_G b \tag{26}$$

where $\nabla\varepsilon$ is plastic strain gradient and ρ_G can be written as:

$$\rho_G = 1/R_n \tag{27}$$

where $R_n$is the neutral plane radii shown in Figure 47 b after bending which is equivalent to $R_n = R_i + h/2$. Therefore, substituting equation (27) in (26), the strain gradient can be written as:

$$\nabla\varepsilon = \frac{1}{R_n} = k_n \tag{28}$$

where $k_n$is the curvature of the neutral plane after deformation.

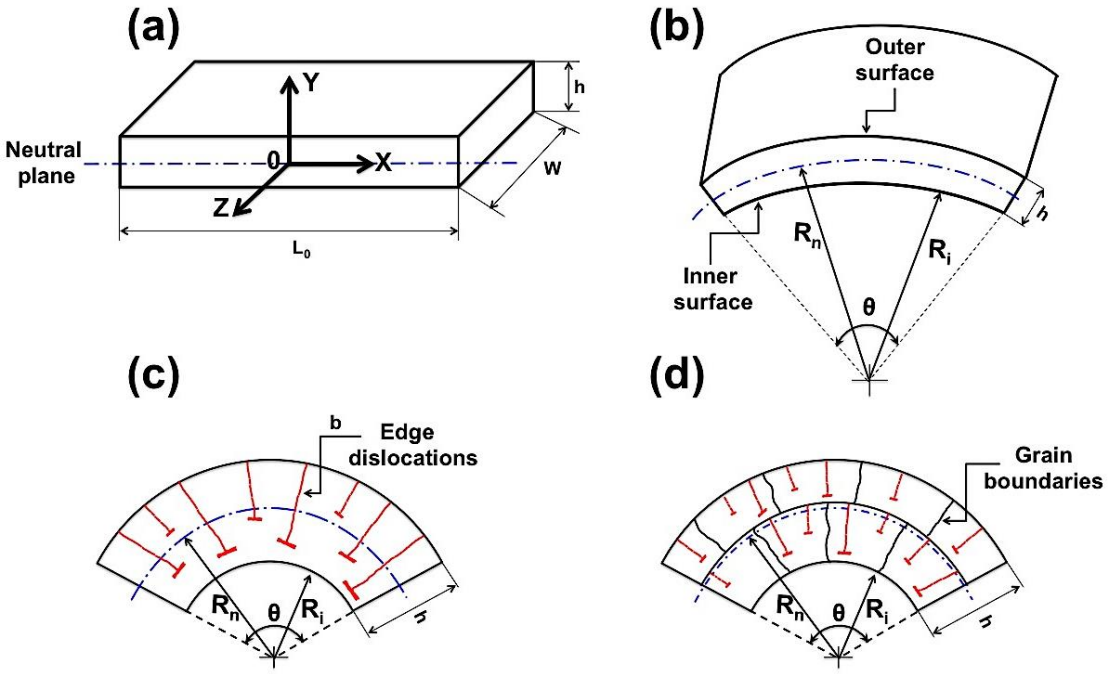

Figure 47: Schematic of the mechanics of micro-bending in thin sheets in plane strain configuration showing a) Initial state of the sheet with length of L_0, width of W and thickness of h. coordinate diagram is assumed at the centered line of the sheet shown with dash blue color corresponding to the neutral plane of the sheet. b) After bending deformation with angle θ shows inner and outer formed surfaces as well as the radii of inner and neutral surfaces. c) Geometrically necessary dislocations morphology and distribution in single crystal sheet and in d) Multilayer sheet having many grains across the thickness.

Strain Gradient Plasticity (SGP) has been used as a strong theory to rationale size effects in the micro-bending of thin foils that was initially introduced by Fleck et al(N. A. Fleck, G. M. Muller, M. F. Ashby, & J. W. Hutchinson, 1993) in which the extrinsic (dimensional) constraint was suggested as variable that determines strain gradients.

Although extrinsic dimensions effects utilizing ρ_G term in Taylor hardening model is used to describe the strengthening behavior of thin foils, it has been shown that the geometry and distribution of this type of dislocations results in reducing or increasing this effect. Meaning that it may completely disappear in ultrafine sheets where a large number of grains across the thickness of the sheet suppress effects arise by GNDs on the microstructure evolution. This phenomenon is shown graphically in Figure 47 c and d for a single crystal sheet where there is only one grain across the thickness of the sheet and a bilayer sheet where there are two layers of the grains across the thickness of the sheet (polycrystal).

Here, for the identical curvature and hence the same average ρ_G for both single and polycrystal thin sheets, the geometry and distribution of GNDs are different. In micro-bending due to the length difference ($= h\theta$) between outer and inner edges, a series of extra half planes (edge dislocations/GNDs) is inserted to maintain lattice continuity throughout the sheet during bending deformation (Figure 47 c and d). The inner edge is under compressive stress while the outer edge under tensile stress. This is while the centerline or neutral line shown with blue color in Figure 47 has zero stress. Therefore, it is assumed that theses compressive and tensile stresses have their maximum value ($e_{Max} = \frac{h/2}{R_n}$) at the edges with opposite sign. It is argued that in case of single crystal sheet (Figure 47 c), GNDs are formed and extended from the outer edge to the middle parts and inner edge of the sheet while this effect is suppressed in polycrystalline sheet (Figure 47 d) due the presence of grain boundaries oriented parallel to the edges of the sheet and

hence hinder the extension of GNDs from outer edge to the inner edge. This hypothesis essentially argues that lattice rotations around the GNDs created during bending decreases in case of polycrystalline sheet materials and it is limited mostly to the outer edge. In this case, the movement of dislocations is also hindered by grain boundaries and therefore the effects of statistically stored dislocations (SSDs) become more significant in hardening and strengthening of thin sheets while GNDs effects almost vanishes.

According to the SGP, in micro-bending, the displacement field in the local coordinate system shown in Figure 47 a is represented as(Stölken & Evans, 1998):

$$u_1 = k_n x_1 x_2,\ u_2 = -k_n\,({x_1}^2 + {x_2}^2),\ u_3 = 0 \tag{29}$$

where x_1 and x_2 are spatial displacements along the X and Y directions according to coordinate system shown in Figure 47. From it, deformation gradient tensor is obtained as:

$$F = {\partial u_i}\big/{\partial x_j} = \begin{bmatrix} k_n x_2 & k_n x_1 & 0 \\ -2k_n x_1 & -2k_n x_2 & 0 \\ 0 & 0 & 0 \end{bmatrix} \tag{30}$$

This is the deformation gradient tensor that can also be found from DIC for deformation zone. This can be used to find Taylor factor maps having initial orientation of each material point that obtained by OIM maps.

Scaling down the sample size

Figure 48 a shows the initial microstructure of the 50 μm Ni sheet with large grain size in which the grain size is larger than the thickness of the sheet. Grains are numbered from left to right. Figure 48 b-d shows the SEM image, IFP and KAM maps for the sheet at the corner of the punch where failure occurs. This was captured few steps before the fracture. It is seen that

material flow is not accompanied by activation of many slip systems across the grains and it is highly localized in grain 3 while it is very small in other grains. Shear banding occurs at this corner before material undergoes a significant deformation. The step formed due to shear banding started from grain 2 and passed through the grains 3, 4 and 5. Shear banding occurs in ductile metallic materials as the concentration of plastic flow and it is characterized by massive collective dislocation activity in a narrow region while the matrix undergoes a low and homogenous plastic flow (Jia, Eisenlohr, Roters, Raabe, & Zhao, 2012). This is promoted when homogeneous dislocation slip is inhibited. Similar behavior us observed in material flow during deep drawing of Ni sheet by scaling down the thickness by half.

The driving force for such behavior is attributed to very high local misorientations and lattice curvature at the corner where the high GNDs are generated by comparably high rate of material thinning to other part of the sheet. This is caused by large variation in deformation rate in different parts of the sheet. A further deformation results in material failure at the corner before the deformation in other parts of the sheet reaches to an almost homogeneous state, as was observed in 100 μm Ni sheet close to the failure.

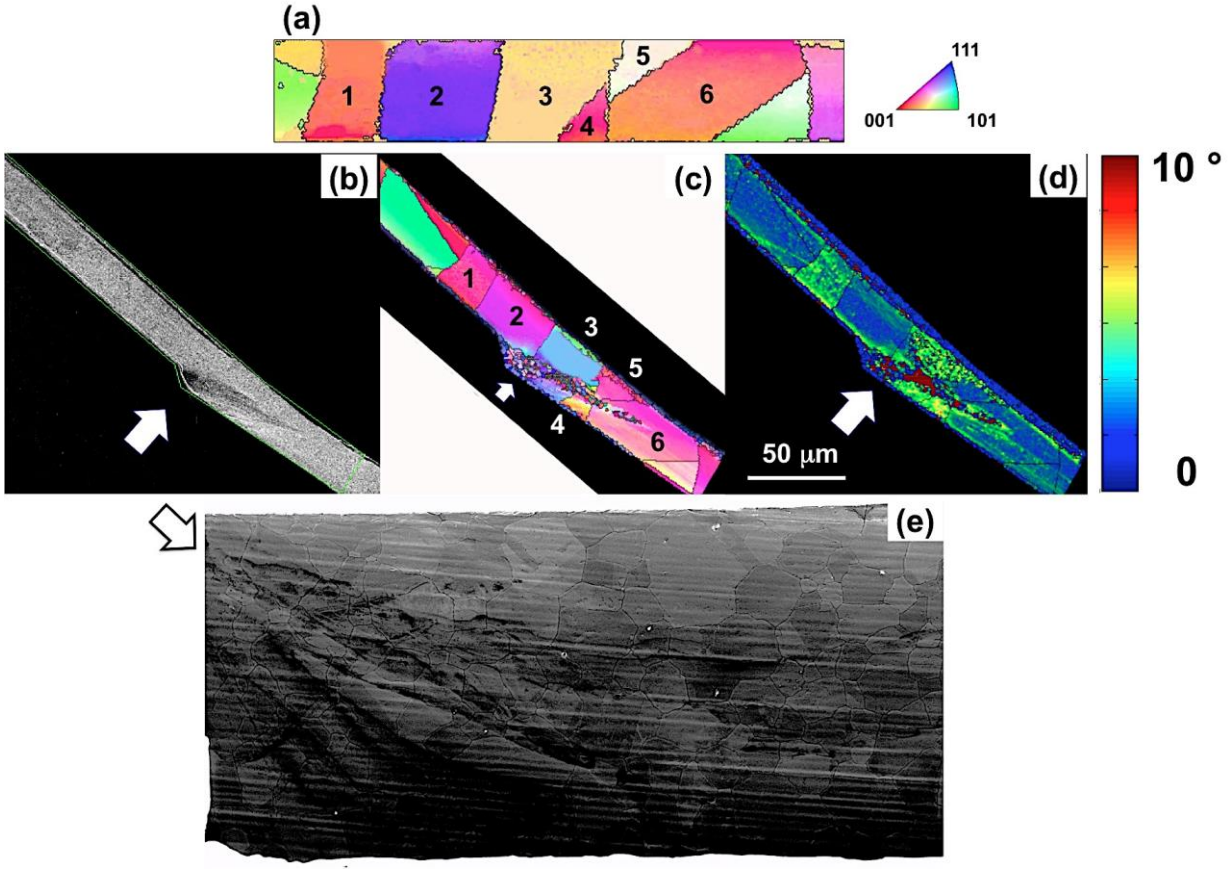

Figure 48: a) and b) IPF from OIM of starting microstructure of 50 μm annealed Ni sheet from different part of the sheet; grains are numbered to track the microstructure evolution after deformation in each grain. b-d) SEM, IPF and KAM images of the sheet after deformation from the region located at the corner of the punch where shear banding (white arrows) occures and material starts to fail. e) Back side of the sheet shows the onset of shear banding at the corner of the punch, which goes through the width of the sheet.

Increasing the deep drawing ratio

Figure 49 show micro-deep drawing for 100 μm Ni sheet at larger ratio, punch width 0.8 mm compared with 0.5 mm used in all previous microforming conditions. Similar deformation behavior and fracture to results Figure 42 was observed in this sample. Figure 49 a shows the initial microstructure (Type i, Figure 40) of the sheet at the corner of the punch where failure occurred. Figure 49 b and c are the SEM images of the deformed sheet close to fracture and after that respectively corresponding to the grains illustrated in Figure 49 a. It is seen that fracture occurred at grain 2 as a result of necking in interior of this grain. Grain boundary separating grains 1 from 2 is shown by red arrow in Figure 49 c. IPF and KAM maps again show a very slight deformation across the grains few steps before the fracture (Figure 49 d).

The results of this observation also show the effect of twins and their interaction with matrix towards the deformation. Although the failure accelerated by increasing the deformation ratio, the presence of such long twins might expedite failure at the corner. They act as obstacles to deformation and unlike the matrix, they are hard to deform by slip and therefore result in irregularity in the deformation. This results in developing high compressive stresses at the corner close to the punch (white arrow, Figure 49 c) and hence material deforms severely there and folds on the surface. Consequently, big annealing twins accelerate onset of localization in microforming and promote roughening on the surface.

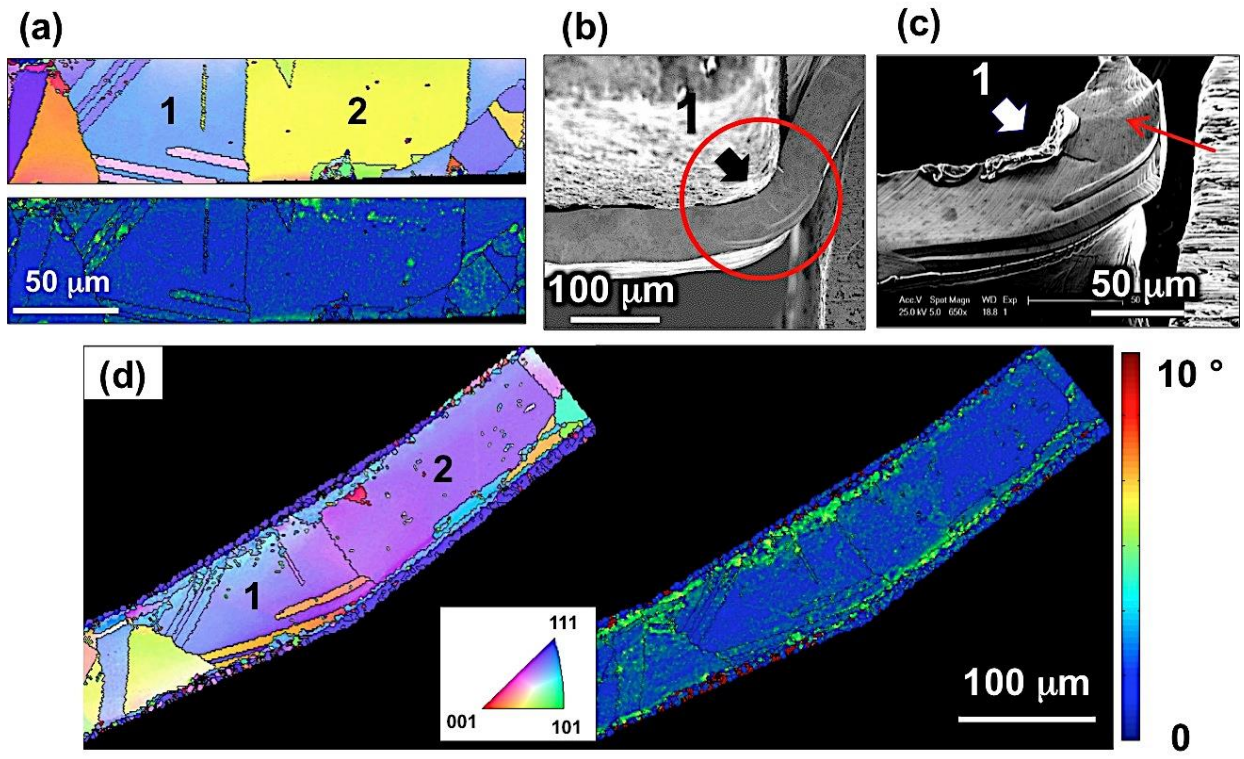

Figure 49: a) IPF from OIM and KAM of starting microstructure of 100 μm annealed Ni sheet from the region located at the corner of the punch. The width of the punch is 0.8 mm. Grains are numbered to track the microstructure evolution after deformation in aforementioned grains. b) SEM image of the sheet showing the deformed sheet at the corner of the punch, grain 1 is shown by black arrow. c) SEM image of the sheet at the corner of the die after fracture shows the area in the red circle in part b, here grain 1 is shown by white arrow while the grain boundary separating grains 1 and 2 is shown by red arrow. Necking occurred in the interior part of grain 2. d) IPF from OIM and KAM of the sheet in grains 1 and 2 after micro-deep drawing close to fracture.

6.3.1.3 Medium grain size (type j)

Initial microstructure of as-received 100 μm Ni sheet is shown in Figure 50. IPF, GOS and KAM maps show that aforementioned sheet has a medium grain size microstructure and annealing twins are observed almost in all grains. Because of previous thermomechanical processes for fabrication of the sheets, microstructure shows some pre-strained grains across the sample (Figure 50 b and c). In order to examine the microstructure evolution in this type (type j) of microstructure during micro-deep drawing, sheet was divided to several sections as shown in Figure 50 a.

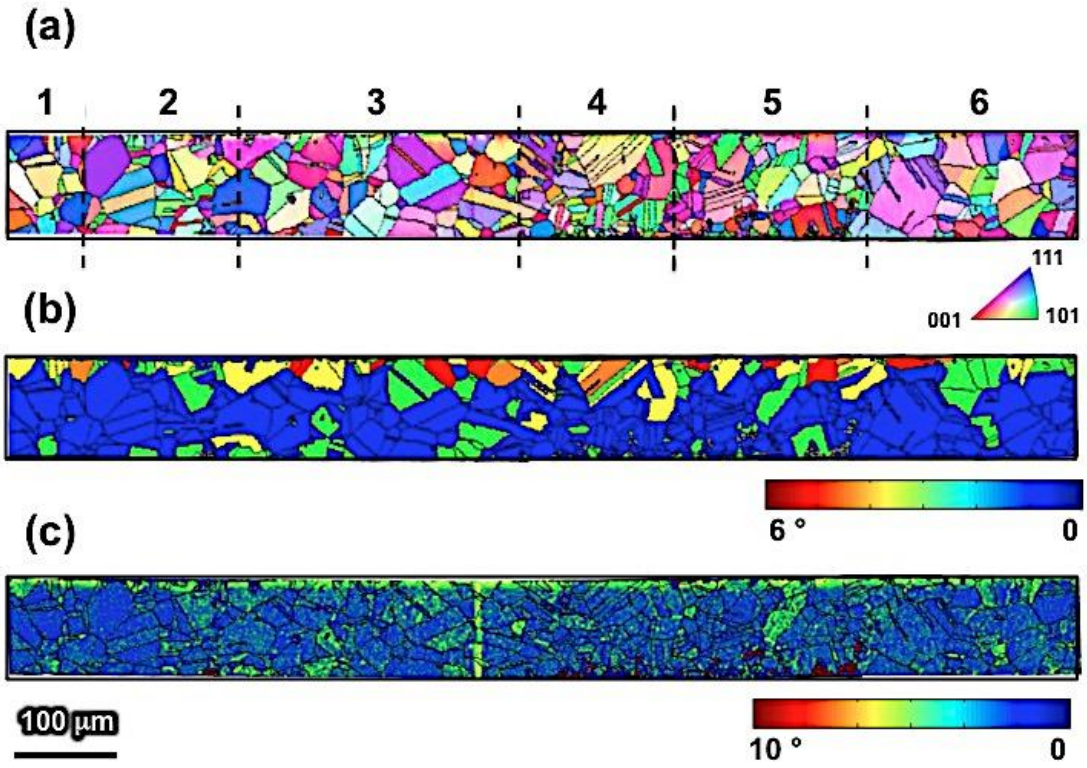

Figure 50: a) IPF from OIM, b) GOS, and c) KAM of starting microstructure of 100 μm as-received Ni sheet. Numbers 1-6 refers to sections of the sheet for which the microstructure evolution during micro-deep drawing was characterized.

Characteristics of initial microstructure for each section and for the whole sheet in average is shown in table 7, section 4.3. This analysis was also performed on each section after failure, the microstructure of which is shown in Figure 51 a-f. It is seen that the microstructure evolution has a faster rate in section 5 of the sample where deformation is localized. According to the results shown in Figure 51, sample was failed at the interface of sections 3 and 4. It is seen that the microstructure evolution in as-received sheet has a faster rate compared with the annealed sheet. Results indicate that average KAM during deformation till failure has an increase about 75% in as-received sheet while it is 55% in annealed one. The increment for GOS is 83% whereas it is 24% for annealed sheet.

It is seen than the average GB misorientation has a significant decrease in as-received sheet around 88% while it does not have a constant trend of increasing or decreasing for all grain boundaries in annealed sheet. Significant decrease in GB misorientation is attributed to compatibility of the microstructure to deformation and grain rotations to maintain continuity at the grain boundaries and also towards the macroscopic applied stresses.

Misorientation in both cases varies along the grain boundary after deformation while it is almost constant with low variation before microforming. Therefore, from all above empirical measurements, it is concluded that microstructure evolution has a faster rate in overall in as-received sheet compared with the annealed sheet.

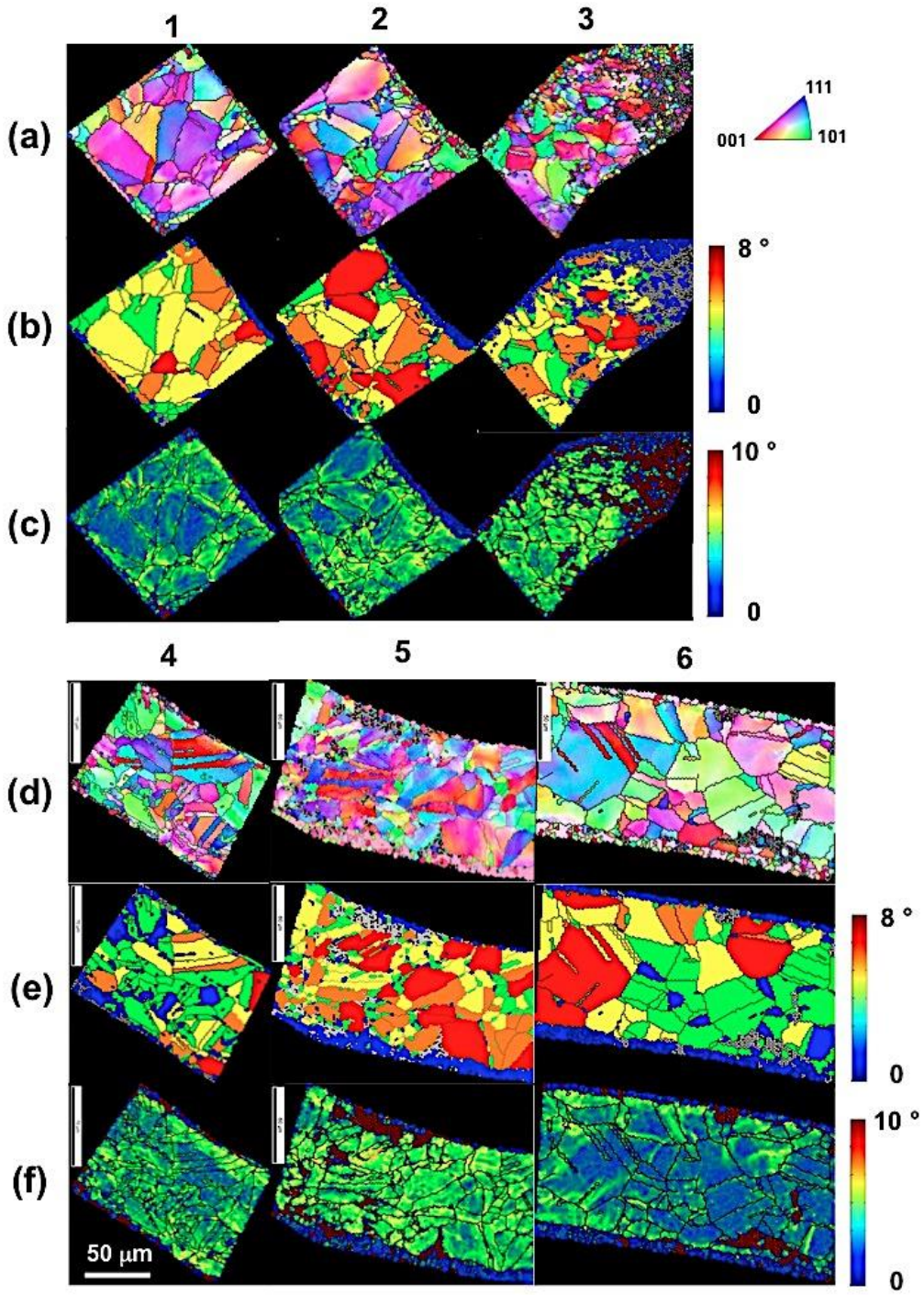

Figure 51: IPF from OIM, GOS, and KAM of microstructure of 100 μm as-received Ni sheet after fracture for sections a-c) corresponding to sections 1-3 and d-f) corresponding to sections 4-6 that marked in starting microstructure.

Surface topography after fracture

Figure 52 a shows SEM images of the as-received Ni sheet after fracture. It is seen that a rough surface formed on the free surface of the sample exposed to SEM beam. A and B are corresponding to the fractured edges of the sheet, showing a ductile fracture.

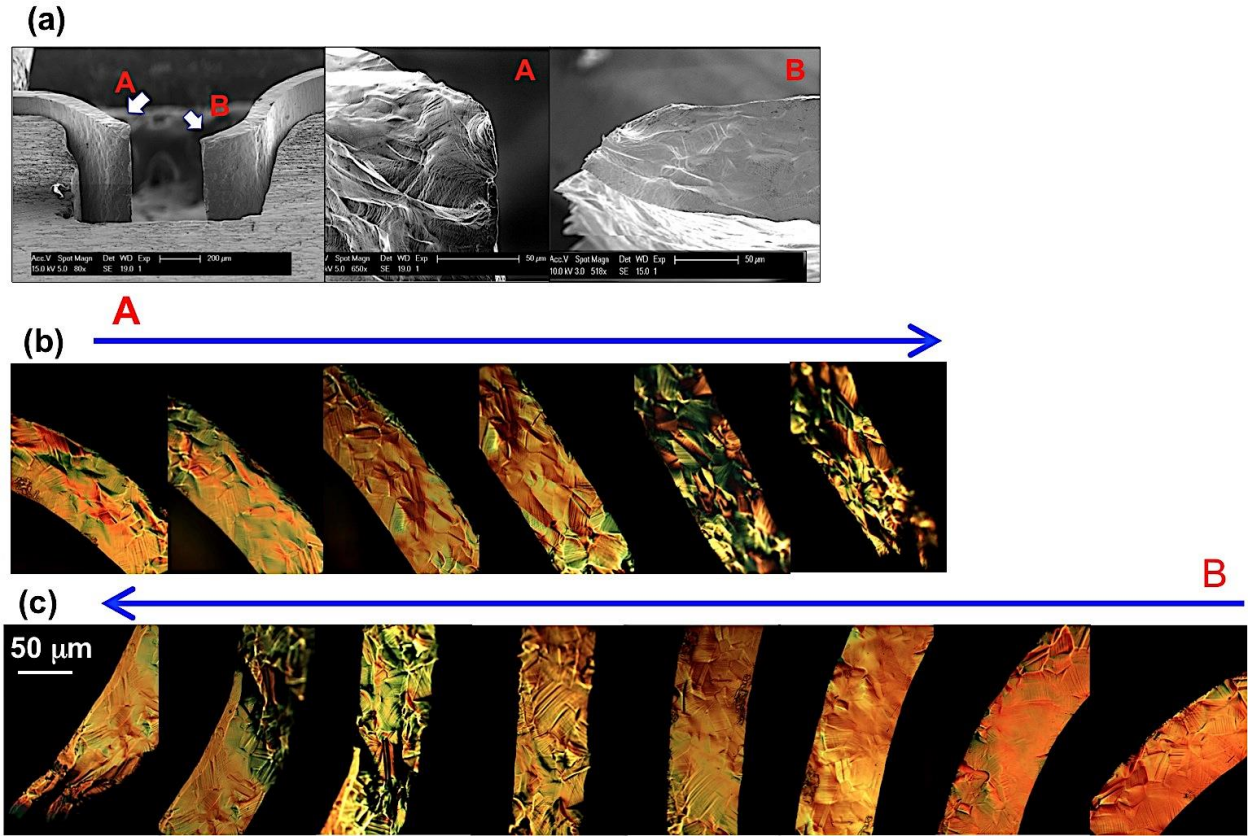

Figure 52: a) SEM images of fractured 100 μm as-received Ni sheet. A and B refer to left and right sides of fractured sample. b) and c) Optical images of the surface of fractured sample; arrows show direction of taking images in sides A and B. Images show a very inhomogeneous roughness on the surface after deformation.

Figure 52 b and c show the optical images of different parts of the sheet after the fracture. A non-homogeneous surface roughening depending the location of the grains with respect to the punch and die corners formed during deformation. Blue arrows show the surface roughness evolution in the two parts A and b along the direction from the corner of the die to the corner of the punch. It is seen that a very rough surface formed during the deformation of this type of microstructure. A sever roughening is observed at the corner of the punch. Grains deformed by slip. However in some grains several slip activated to maintain continuity. They are corresponding to grains with high GOS and KAM shown in Figure 51. This requires larger lattice rotation and therefore developing local misorientations within a grain. It is seen that large steps occur at the twin boundaries, especially those located close to the punch corner. This is while groove shape defects are formed at triple junctions. Surface roughness are also promoted within the grains where they are not deformed uniformly as in part of a grain several slip system are activated while other parts deformed only by one slip system.

Scaling down the sample size

Figure 53 show microstructure evolution in 50μm as-received Ni sheet. This Figure features deformation mechanics (Figure 53 a) and microstructure evolution (Figure 53 b-e) in medium grain size Ni sheet as a result of scaling down the thickness by half with respect to condition described in previous section. Again the concentration of deformation is observed in the corners of the punch. However, by looking carefully at DIC (Figure 53 a) and IQ images (Figure 53 b), it is seen that the deformed grains, which appear with dark color in IQ map are corresponding to where there be a high localization of strain-rate in DIC image (arrows in Figure 53 a and b). Similar to annealed case described previously by scaling down the thickness, shear

banding is accelerated in the sample, right arrow in Figure 53 b. Deformation is somewhat uniform compared to the large grain size sample. Although the deformation is more concentrated at inner and outer edges based on bending theory explained previously, it is not zero at the centerline. At the early stages of deformation it quickly spreads across the thickness at the corners and results in failure.

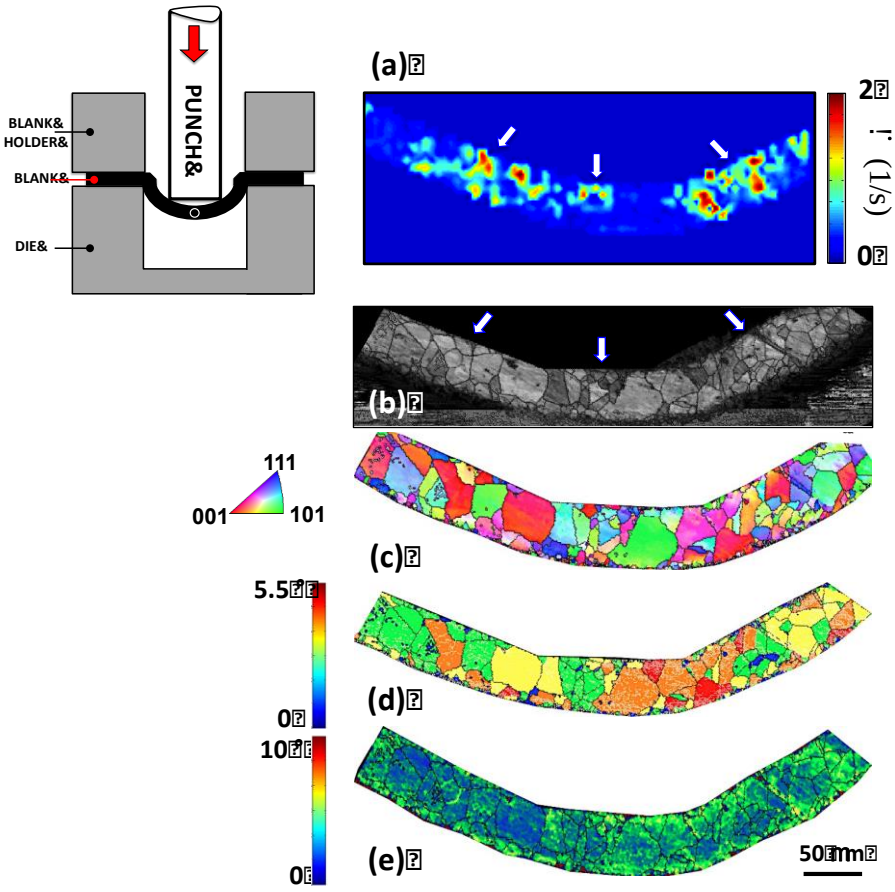

Figure 53: Deformation mechanics and microstructure evolution of fractured 50 μm as-received Ni sheet. a) Strain-rate field obtained by DIC. b) IQ c) IPF from OIM. d) GOS, and e) KAM maps of microformed sheet right before the fracture. Arrows in parts a) and b) show the regions with high localization of deformation.

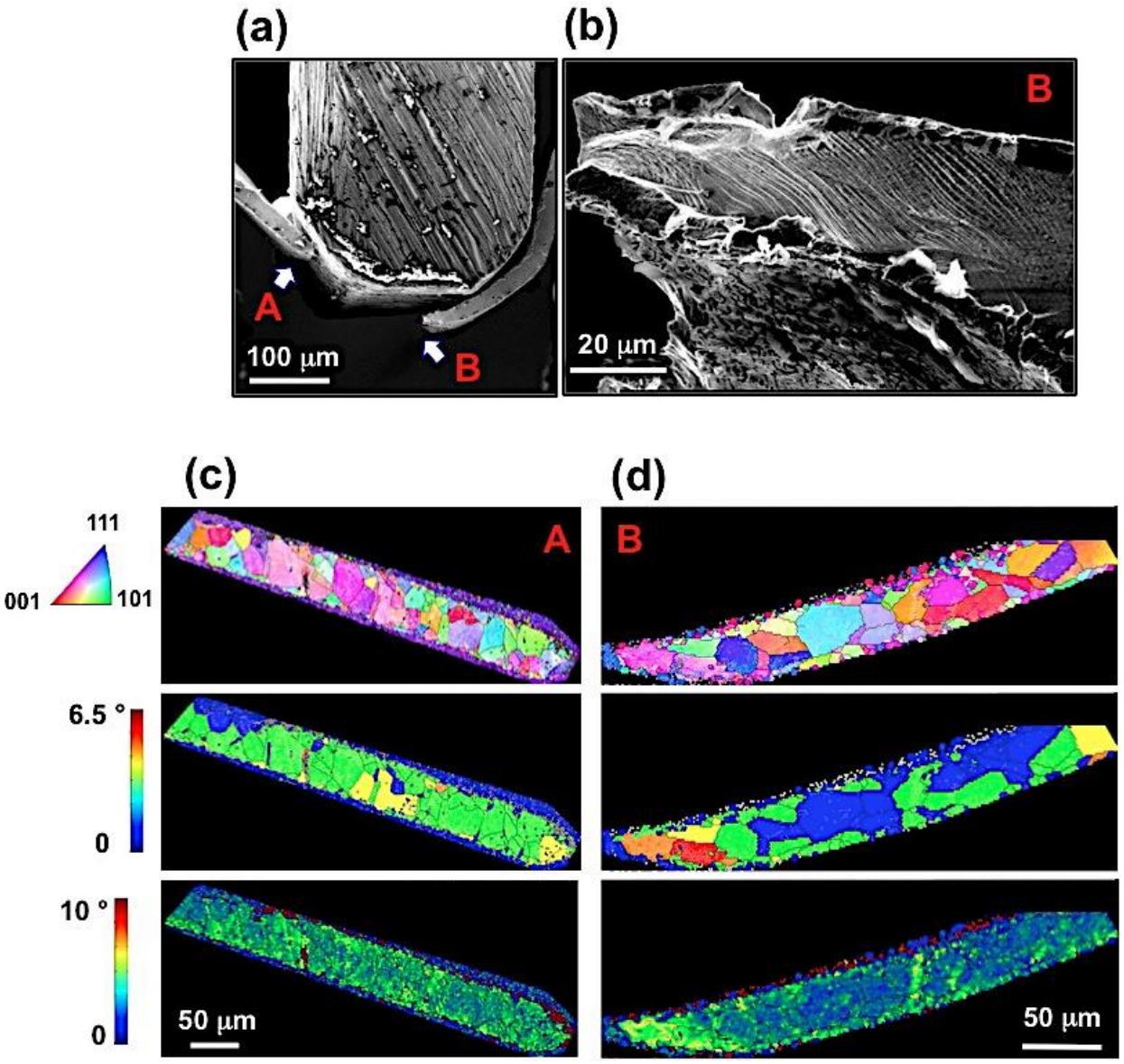

Figure 54: a) SEM image of 50 μm as-received Ni sheet after fracture; A and B show the two fractured surfaces. b) High magnification SEM image of fractured surface B. c) and d) IPF from OIM, GOS and e) KAM maps of fractured surfaces A and B after polishing respectively.

Figure 54 a show SEM images of aforementioned sample after the fracture. Severe localization of deformation is seen in one side of the fractured sample (edge B, Figure 54 b), the microstructure of which is shown in Figure 54 d after polishing the surface again. The microstructure of edge A is illustrated in Figure 54 c. We see that side A of the fractured sample almost undergoes homogeneous deformation according to GOS and KAM maps whereas in side B, the deformation is localized in almost 2 grains. The highly concentrated deformation at this part suggests that once instability occurs in this part, progressive deformation slows down in other parts of the sample and localization accelerates failure in that region.

6.3.1.4 Small grain size (type k)

Micro-deep drawing was also performed on the sheet with small grain size, the microstructure of which is illustrated in Figure 55. The characteristics of this type of microstructure are shown in Table 8, Section 4.3.

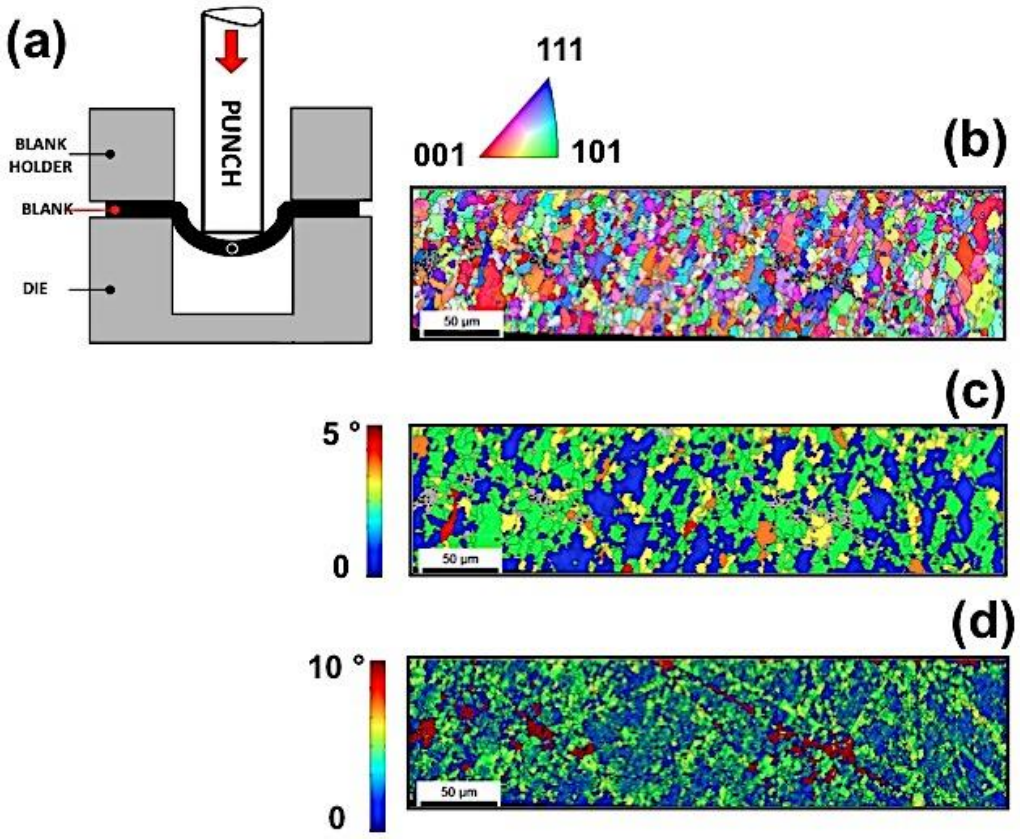

Figure 55: a) IPF from OIM, b) GOS, and c) KAM of starting microstructure of 100 µm small grain size Ni sheet.

Sample was homogenously deformed compared microstructures discussed previously, the mechanics of which is illustrated in 56. It is seen that deformation is more concentrated at the inner and outer edges of the sheet rather than the corners. DIC was performed on the sample few steps before failure occurs as the corners.

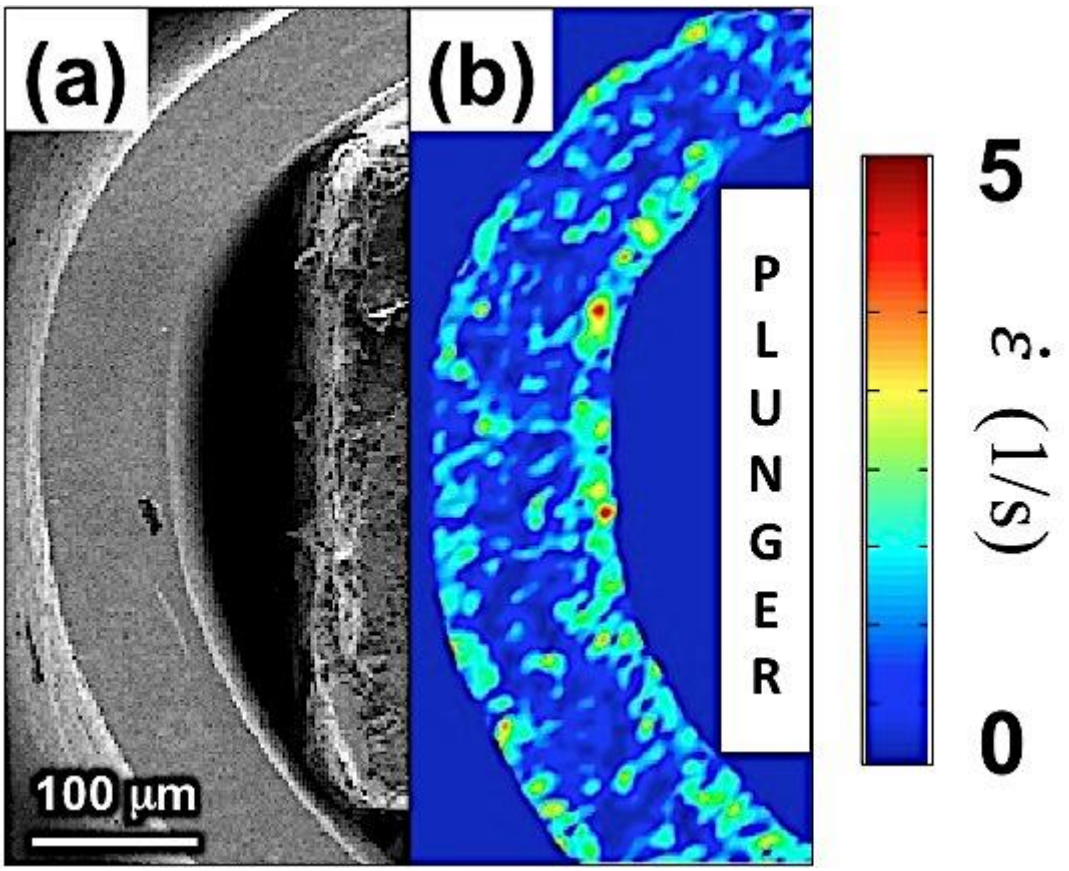

Figure 56: Strain-rate field obtained from DIC for Small grain size 100 µm Ni sheet during micro-deep drawing with V= 150 µm/s.

Figure 57 a shows the surface topography of the sheet, which failed at the outer edge and also corners of the punch. This was captured optically using Keyence surface profiler. From surface topography analysis we see that material in outer edge starts folding on the surface.

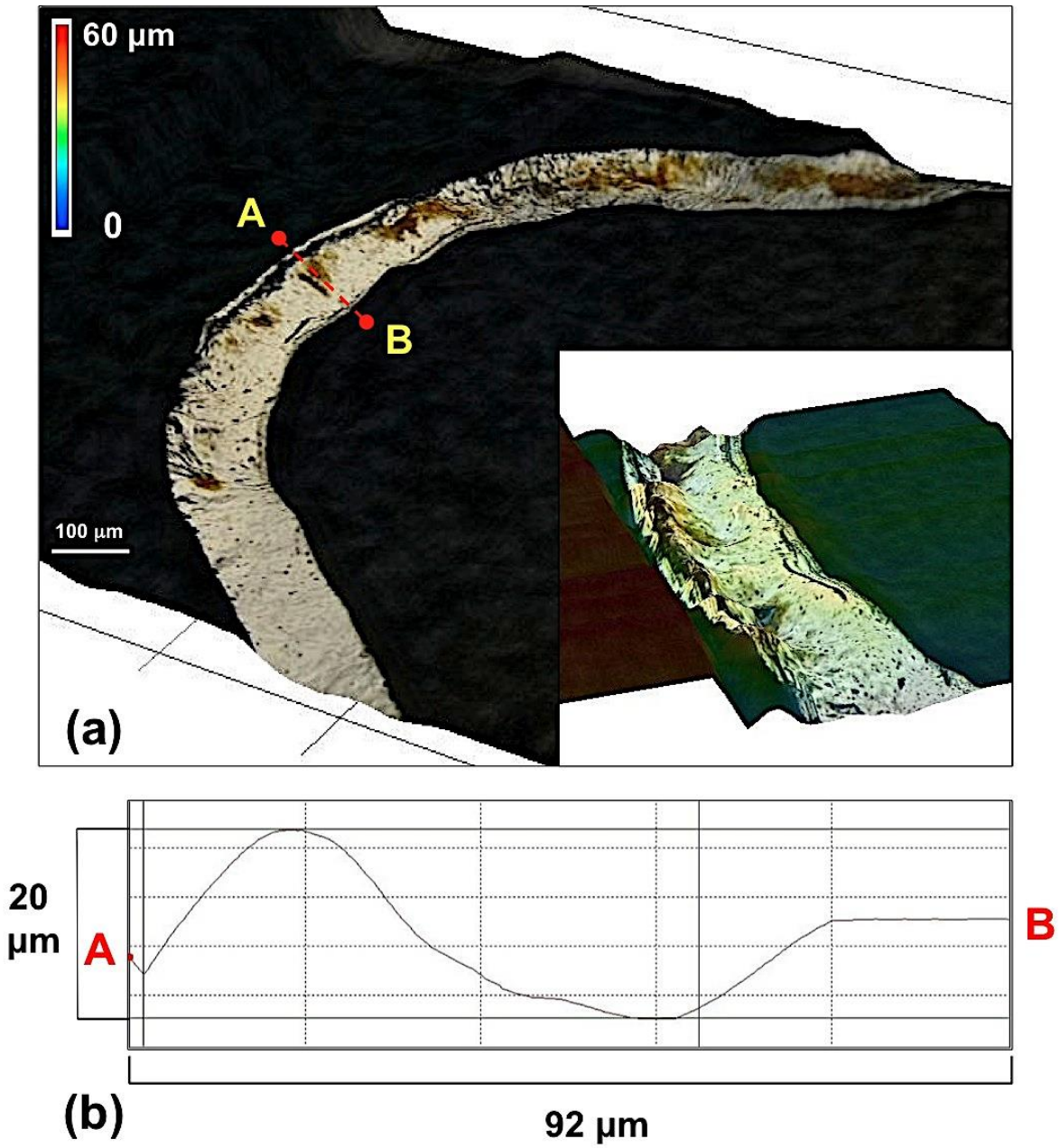

Figure 57: a) 3D topographic map of the surface of 100 µm Ni sheet close to failure showing the surface features developed during micro-deep drawing; bottom right inset shows a larger magnification of the middle part of the sheet corresponding to where folding defect appeared. b) Profile of the surface from marked points A to B across the thickness of the sheet.

It is seen that in addition to the folding defect, material is also wrinkling at the corners. Inset at the bottom right of Figure 57 a shows a larger magnification of the middle part of the sheet where thinning is non-uniform and accompanied by material folding.

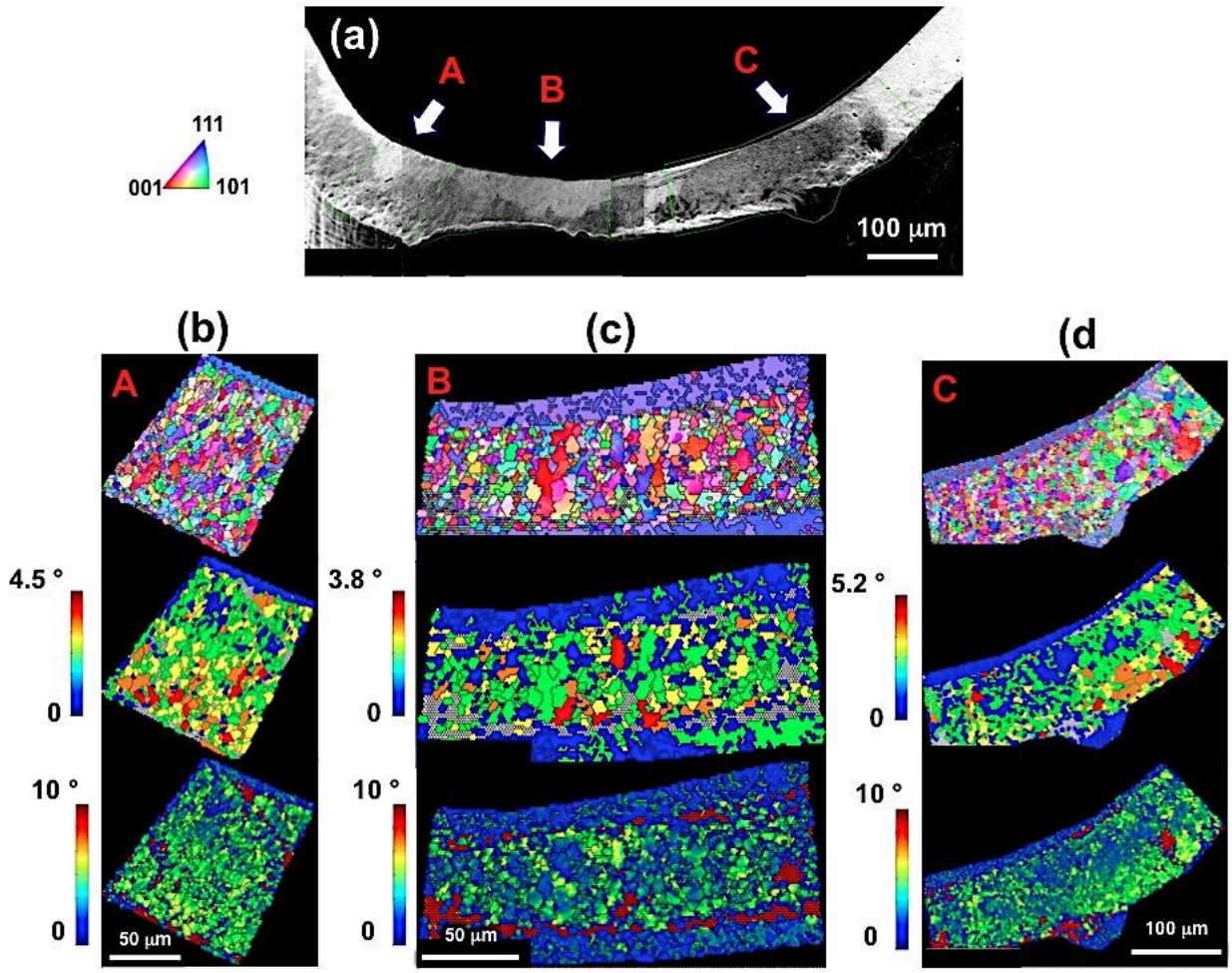

Figure 58: a) SEM image of small grain size sheet close to fracture showing thinning phenomenon at the middle part, below the punch. A, B and C refer to the regions that their microstructures are shown in parts b)-d), corresponding to IPF from OIM, GOS and KAM maps respectively.

Figure 58 b shows the profile of the surface corresponding to a line drawn from outer edge to the inner edge of the sheet (marked as A to B) indicating the height of the defect. This might be because of hardening effect as a result of high stretches at the outer corner as material gets harder at the outer edge and further stretch is no sustained at this part.

Figure 58 shows the microstructure of part of the sheet for which the surface profile is shown above in previous figure. Figure 58 a is SEM image of this part in which the location of performing OIM analysis is shown by arrows and marked as A, B and C. Characteristics of microstructure from this empirical measurements for aforementioned regions are averaged and results are provided in Table 8, Section 4.3.

It is seen that there is no significant changes in grain size (GS) and grain boundary misorientation (GS-MO) by deformation and the value for later did not drop unlike other previous microstructures examined so far in previous sections. However, the rate of increasing values for KAM and GOS (microstructure evolution) is significantly larger than annealed and as-received sheets.

6.3.1.5 Lamellar microstructure (type o)

Figure 59 illustrates the OIM images of lamellar microstructure used to perform micro-deep drawing. The lamellas are original annealing grains severely deformed during machining and orientated in the same direction (Figure 59 a). High density of local misorientations developed during the machining results in the formation of high and low angle boundaries within each lamella (Figure 59 b). The high resolution of a selected area (red circle in Figure 59 a) at the grain boundary separating two lamellas is shown in Figure 59 c-f before deformation and after the failure. This type of microstructure shows the lowest ductility among other tested microstructures as we see a very slight microstructure evolution in the selected area with almost

no change in the orientation of grains as well as local misorientation development within this area. However, it is observed that the high stress concentration at the interior edge of the sheet leads to the appearance of a hill at grain boundary.

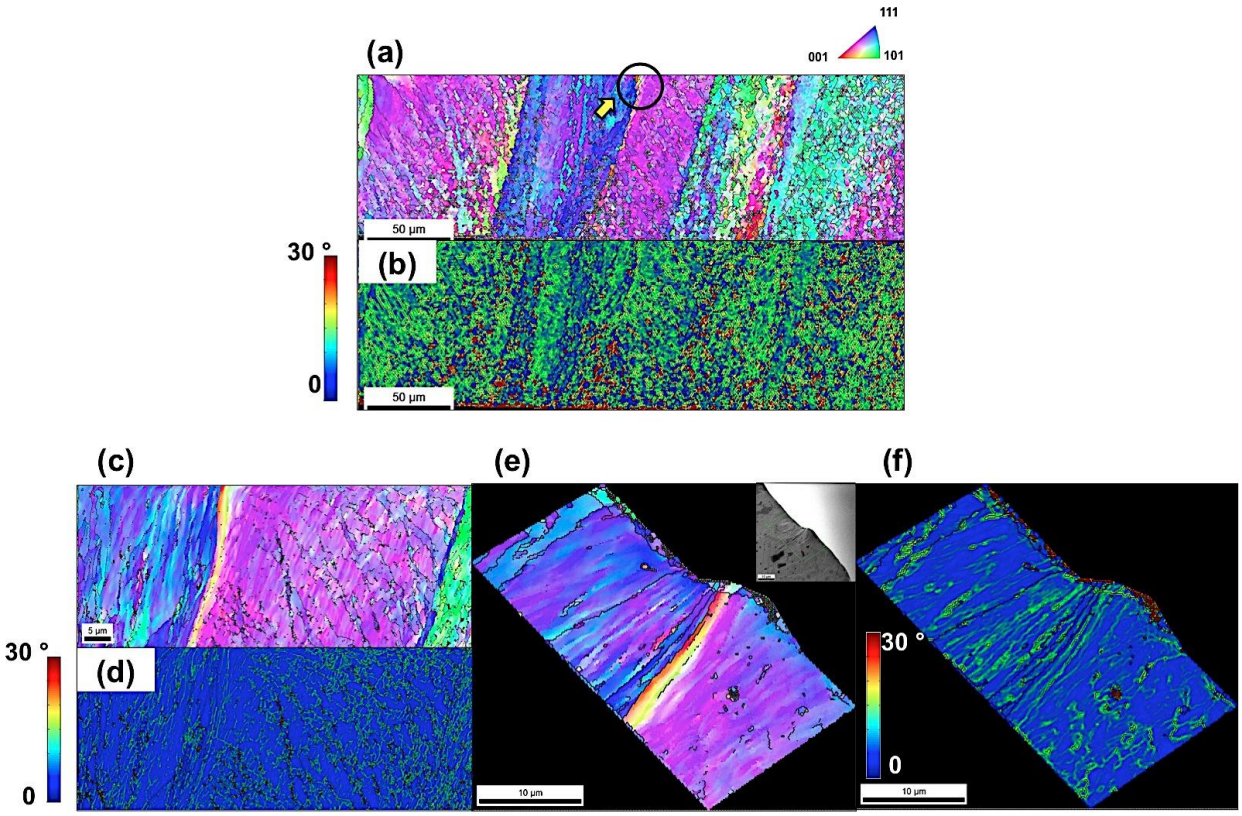

Figure 59: a) IPF from OIM and b) KAM of lamellar microstructure of 100 µm Ni sheet at initial state (before deformation). c) and d) IPF and KAM of selected area shown by circle in part a) in high magnification before deformation showing the deformed microstructure with lamellar features. e) and f) IPF and KAM of selected area shown by circle in part a) after deformation by deep drawing.

Such defects are observed across the sample at the grain boundaries close to the punch (Figure 60 a). In this Figure, a very small deformation occurs only at the outer edge, which stopped there and did not go through the thickness of the sheet. Based on the mechanism discussed in 47d, it seems the formation of the extra half dislocation planes at the outer edge and its extension through the thickness is hindered due to the presence of high and low angle grain boundaries in lamellas. Figure 60 b-d shows SEM images and IPF map of fractured part, which its location is shown in Figure 60 a by white dash line. It is seen that deformation is only concentrated in one/two lamella at the corner of the punch and almost other part of the sheet is slightly deformed and unaffected by deformation and sample fractures at the grain boundary. Less ductility in deformation and fractured surface is seen in Figure 60 c and d. It is concluded that in spite of the small grain size produced during creation of this type of microstructure by machining, the morphology of created grain and grain boundaries, their geometry and orientation play an important role in the mechanical response of material during deep drawing.

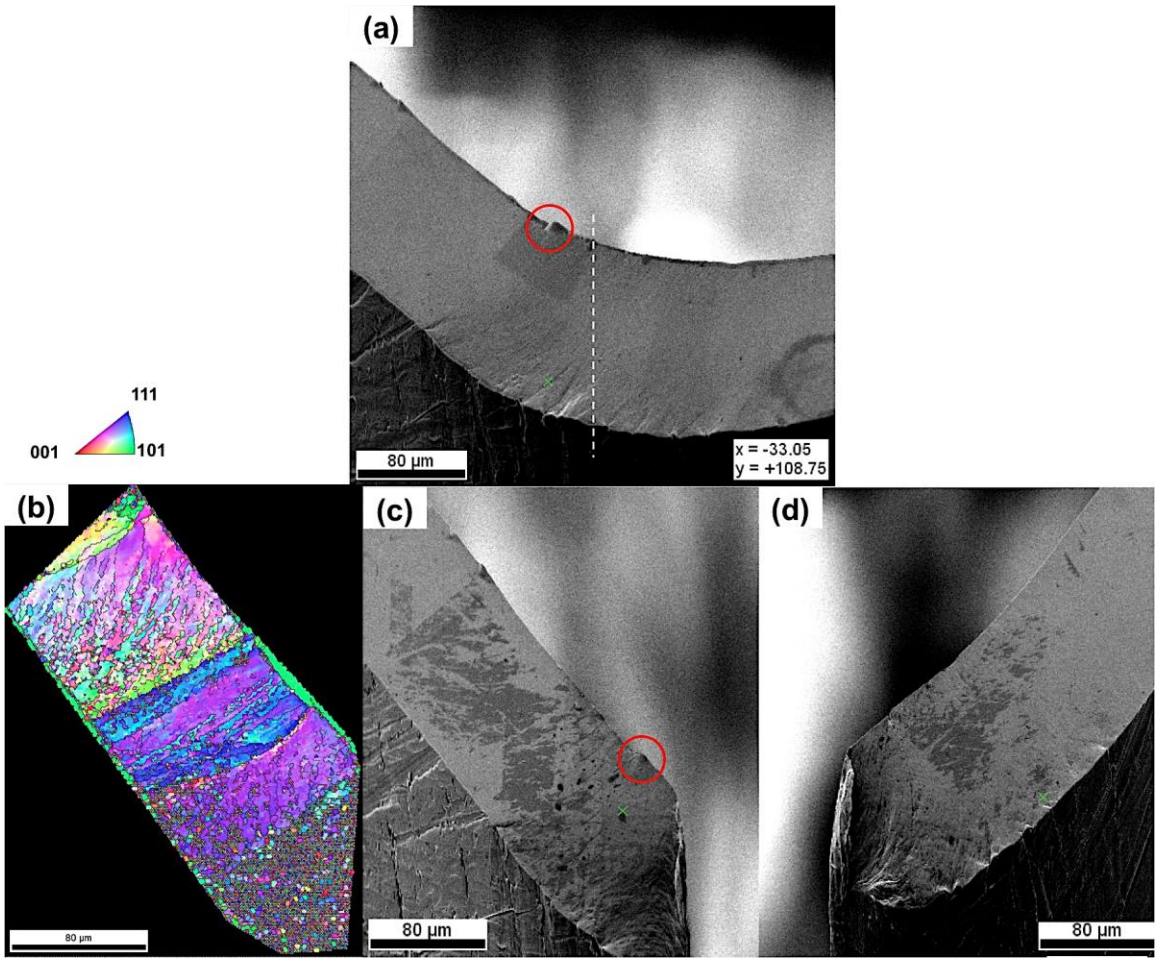

Figure 60: a) SEM image of deformed sample right before failure; dash line is corresponding to where the sample fails. b) IPF from OIM of fractured part. c) and b) SEM images of the sample after failure. Red circle refers to the region the microstructure of which shown in previous figure.

Mechanics of deformation captured by DIC is shown in Figure 61 b corresponding to SEM image on the left (Figure 61a). Black arrows show the location of original high angle grain boundaries separating lamellas appeared with high strain-rate lines in DIC image.

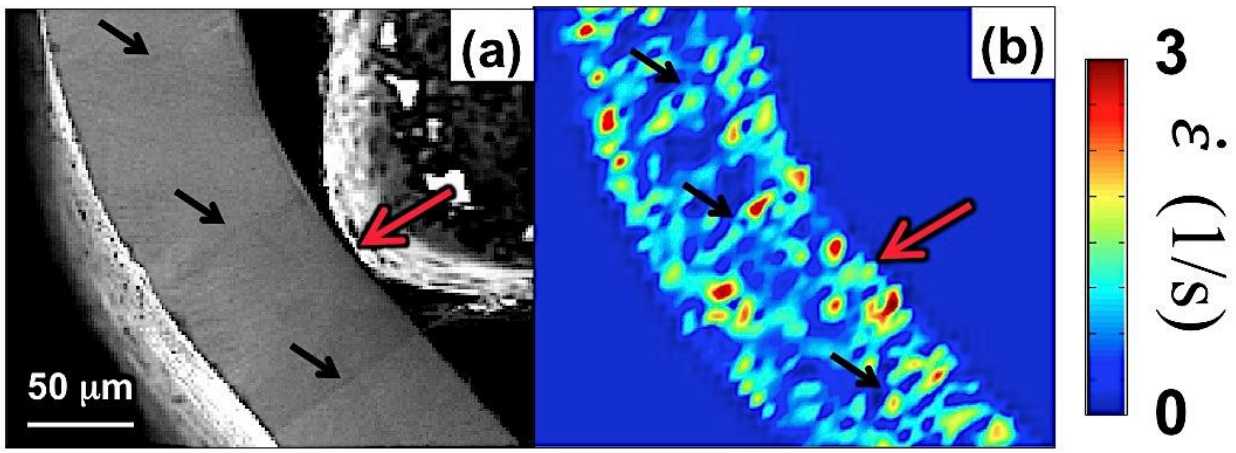

Figure 61: Strain-rate field obtained from DIC for 100 μm Ni sheet with lamellar microstructure during micro-deep drawing with V= 150 μm/s.

6.3.1.6 Graded microstructure (Types l, m and n)

Type l

Figure 62 shows the graded microstructure created by machining. IPF and KAM maps of different parts of the sheet are exhibited in this figure before the deformation by deep drawing. Top surface consists of a UFG layer and a sub-layer with very large grains, numbered to track microstructure evolution during deformation (Figure 62 a-d). A high resolution IPF and KAM images of UFG layer from selected region shown by black rectangle in Figure 62 c is illustrated in Figure 62 e. It is seen that there is a transition pre-strained layer at the interface of UFG and large grain size underneath layer. This microstructure shows a very high distortion at the UFG and its interface with large grain size sub-layer resulting in very high local misorientation developments.

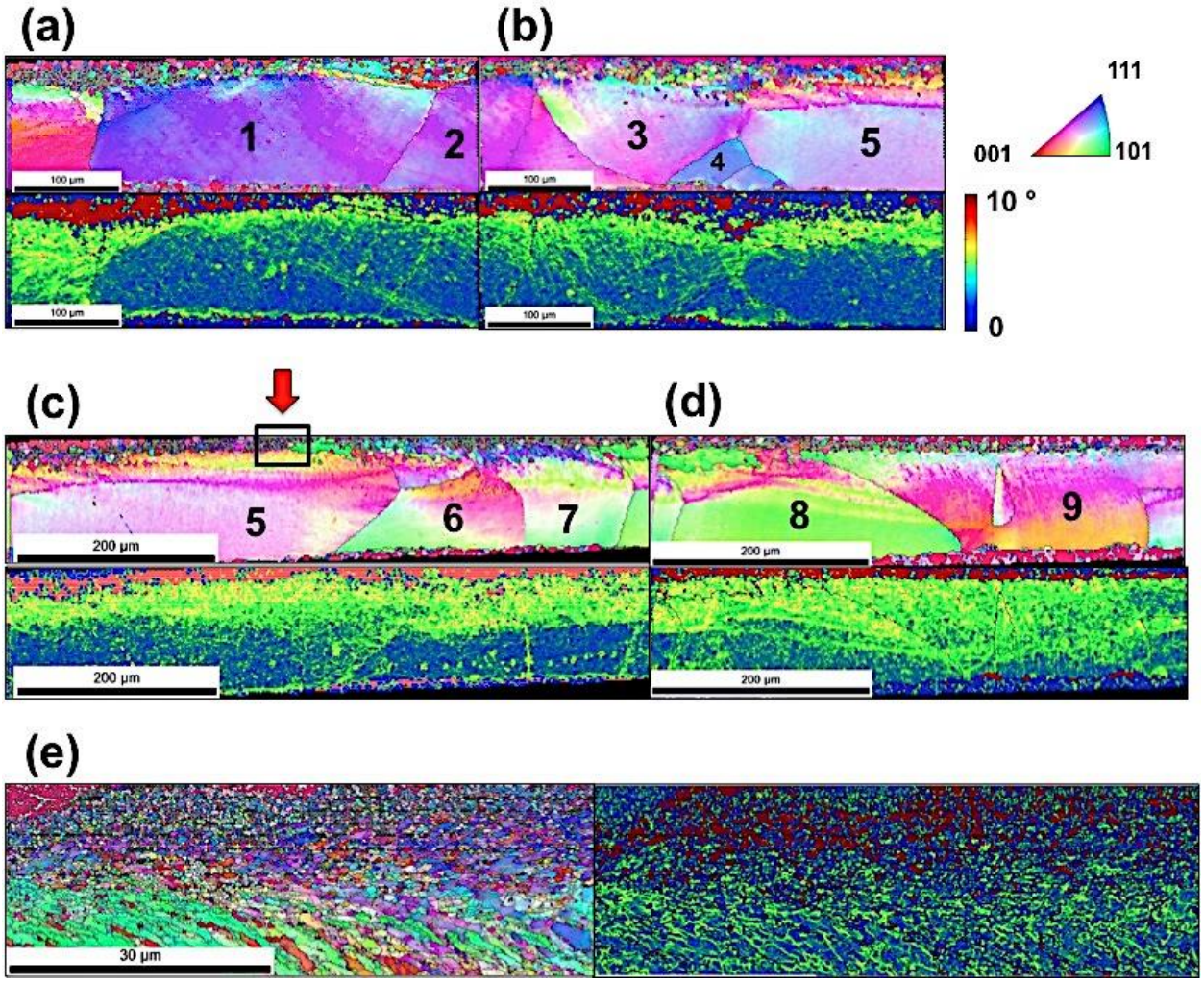

Figure 62: a-d) IPF and KAM of graded microstructure (ultrafine grains on top layer and large grains underneath) of 100 µm Ni sheet before deformation by deep drawing. Grains on sub-layer were numbered as 1-9. e) High magnification of selected region in part c, showing the microstructure of ultrafine layer in IPF and KAM maps.

Figure 63 a shows the IPF and KAM maps of deformed microstructure at the intermediate state of deformation corresponding to SEM images shown in Figure 63 b. It shows nonuniformity in different grains specifically at grains located at the corners of punch, grains 4 and 7. We see the high local misorientation at the outer edge of grains 6 and 7 as well as grain boundary at interface grains 3 and 4. It seems at this corner; stress is concentrated at the tripe junction, grains 3, 4 and 5. This effect is also observed at the grain boundary grains 9 and 10 at the corner of die. These phenomena result in severe roughening of free surface, the topography of which was captured by 3D Keyence optical surface profiler (Figure 64).

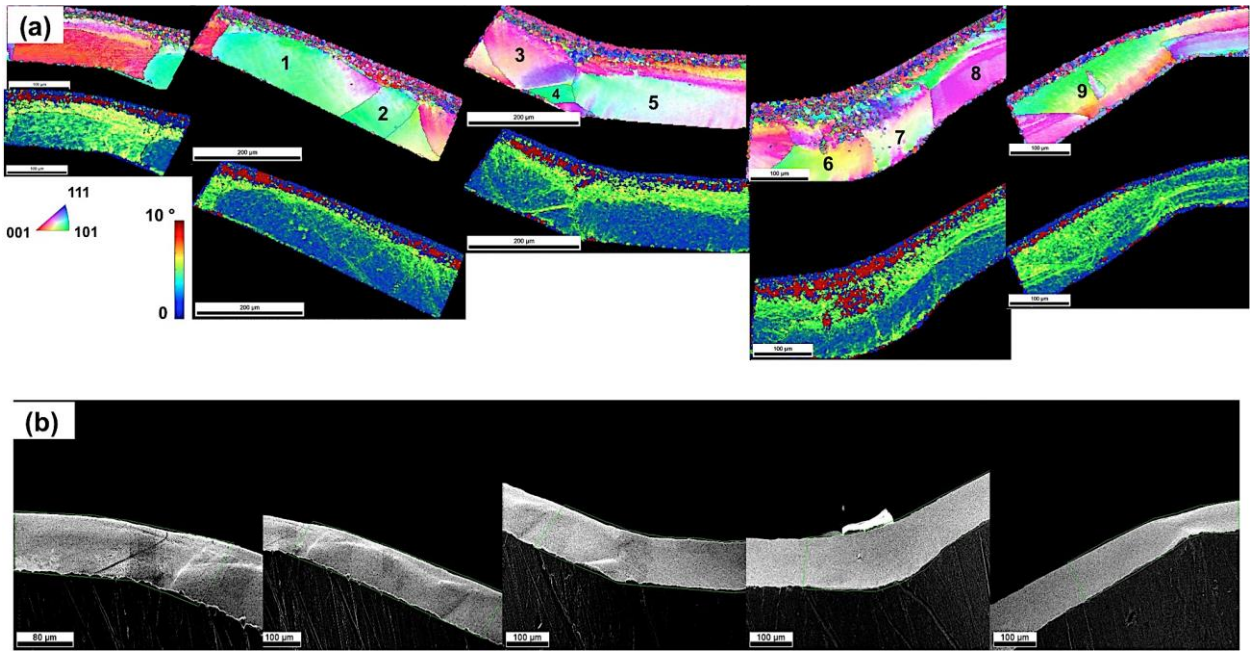

Figure 63: a) IPF from OIM and KAM maps of Ni sheet with graded microstructure obtained few steps before fracture showing microstructure evolution in numbered grains. b) SEM image of sample at the aforementioned state of deformation, showing the roughening evolution on the surface.

Figure 64 shows slip at the outer edge where the large grains are located. It clearly shows that the penetration of deformation stopped at the interface of large grain size layer with UFG layer. Similar type of the defects as those observed in deformation of very large grain size sheet is also seen here such as groove shaped defects at triple junction (Figure 64 c) and steps at grain boundaries (Figure 64 d).

At triple junction shown in Figure 64 c, it is observed how secondary slips activated in order to relax stress in this point and to maintain continuity. Severe slip also is happening at corner shown in Figure 64 d, the interface of grains 4-5 to which does not go through the top layer. Figure 64 e-f demonstrate the profile of aforementioned surfaces showing the roughness of surface across the sheet and also the profile of hills and grooves at grain boundaries and triple junctions.

The mechanics of deformation at the corner of the punch captured by DIC and its corresponding SEM image is shown in Figure 65. This shows a high concentration of straining at the corners where the material is in contact with the punch corner. It also shows high strain-rate paths along the slip planes formed during deformation corresponding to slip lines at bottom corner of Figure 65 a.

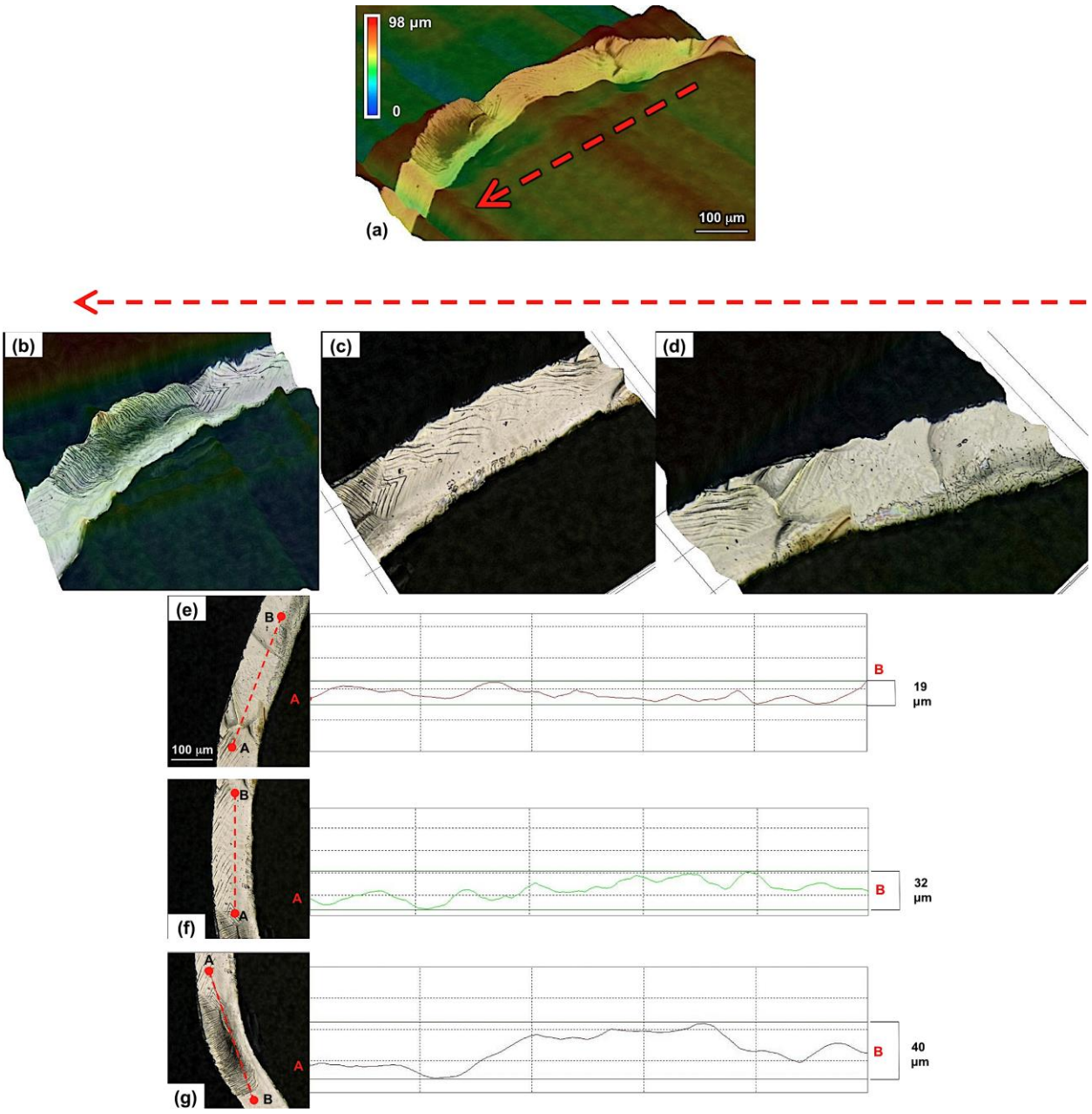

Figure 64: a) 3D topographic map of the surface of 100 µm Ni sheet with graded microstructure captured few steps before failure, showing the surface features developed during micro-deep drawing. b-d) High resolution images of different parts of the sample in the direction shown by red arrow in part a. Profiles of the surfaces shown in parts b-d from marked points A to B across the sheet.

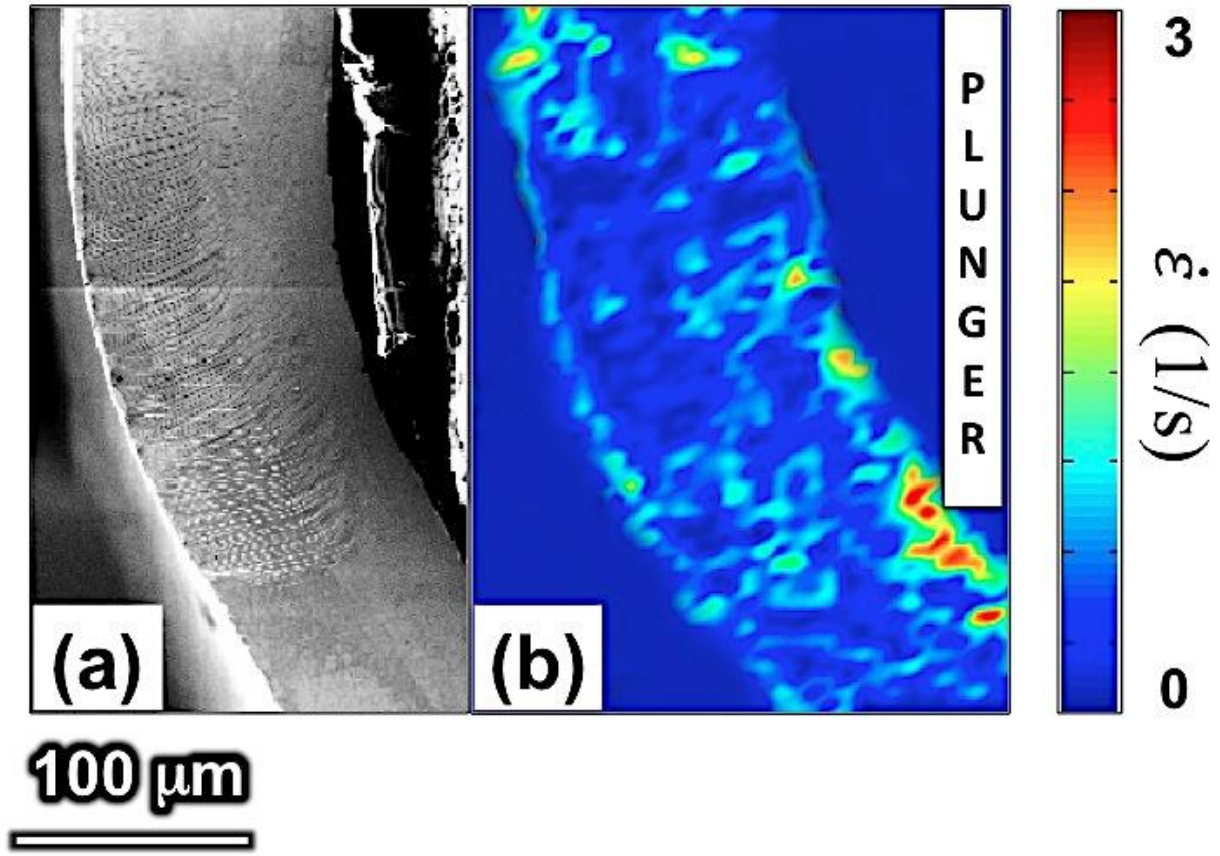

Figure 65: Strain-rate field obtained from DIC for 100 µm Ni sheet with graded microstrucutre during micro-deep drawing with V= 150 µm/s.

By further progress in deformation, it is observed that the sample fractures from the corner of the die unlike all aforementioned microstructures examined so far (Figure 66 a) in which the samples fracture at the corner of the punch. This is where the high concentration of local misorientation is developed and shown in KAM maps Figure 63 a.

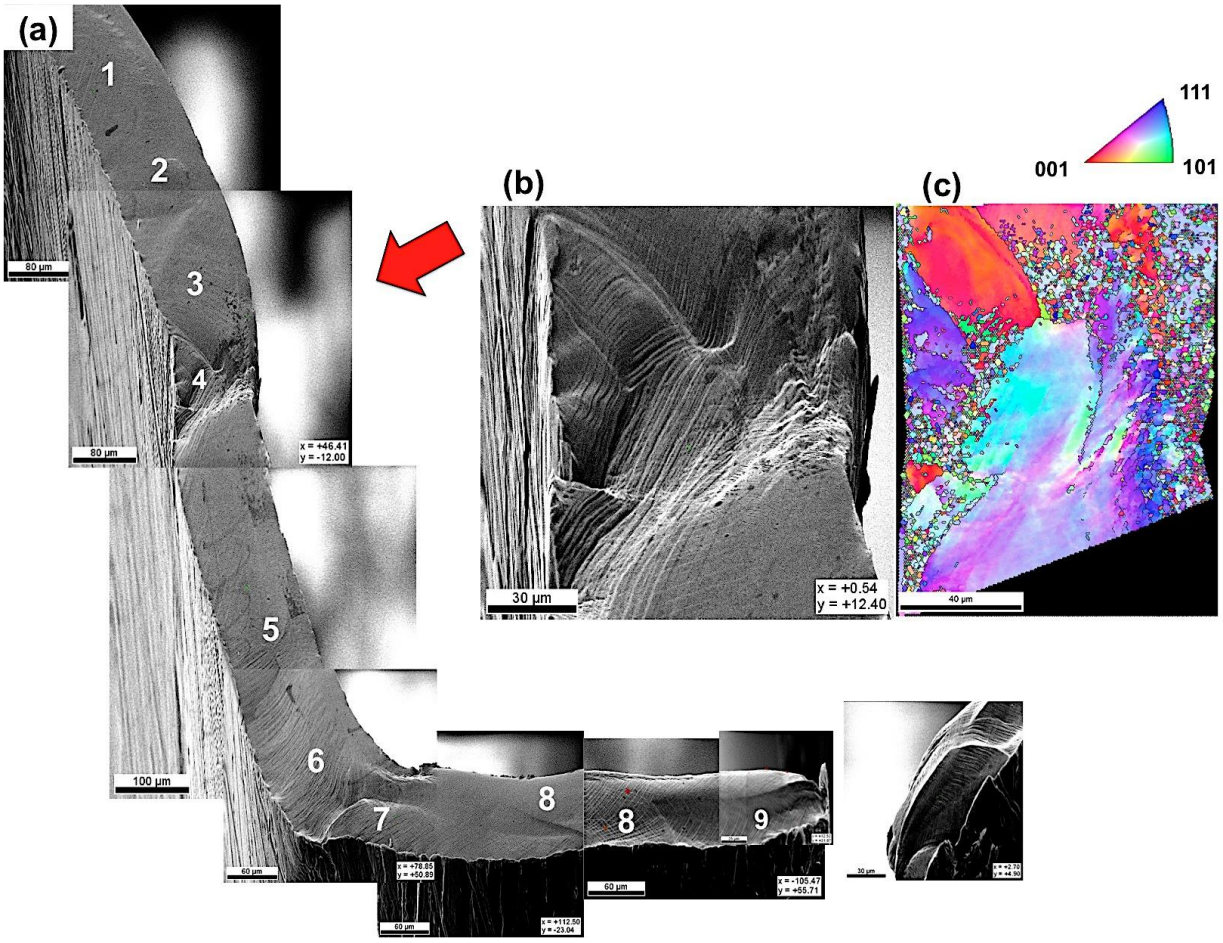

Figure 66: a) SEM image of Ni sheet with graded microstructure after failure, showing the roughening evolution on the surface and deformation in numbered grains. b and c) High resolution SEM image and IPF map respectively of the region located at the corner of the punch and deformed severely during deep drawing.

Despite severe deformation at corners of punch, corresponding to grains 4 and 6-7, the sample fails at the corner of the die, grain 9. However, a maximum formability is observed in this type of microstructure compared with others. We can argue that the top layer with UFG structure provides enough strength for material to sustain local stresses at this edge of the sample when high crystal lattice rotations caused by adding extra half dislocation plans leads to localization and then fracture. On the other hand, the presence of large grain size sub-layer provides enough ductility and it starts stretching by advancing the punch. Consequently UFG layer delays fracture as it can sustain higher level of straining. Therefore, this directional variation in properties is very useful in complicated deformation geometries such as deep drawing if thin sheets.

Figure 66 b and c show high resolution SEM image and its corresponding IPF map for one of the corners corresponding to the location of grains 3, 4 and 5, shown by red arrows. This image clearly shows how UFG layer postponed the fracture and also the formation high density of slip at this layer. A very large lattice rotation is observed at the triple junction of aforementioned grains.

As we mentioned, fracture occurs at the corner of the die, grains 9 and 10. This is because the UFG layer at this corner is positioned at outer edge and hence under tension and large grain size layer under compression. Consequently, high tensile stresses are created at UGF layer at outer edge of the sheet. Therefore, due to the tensile mode of deformation and also lack of ductility in UFG layer to accommodate large crystal distortions at that edge, sample fails from this part. It again shows a ductile fracture at the surface of fractured parts.

Figure 67 shows IPF and KAM maps of the sheet after fracture. Interestingly, almost all surface grains oriented towards the 001 and 111 directions.

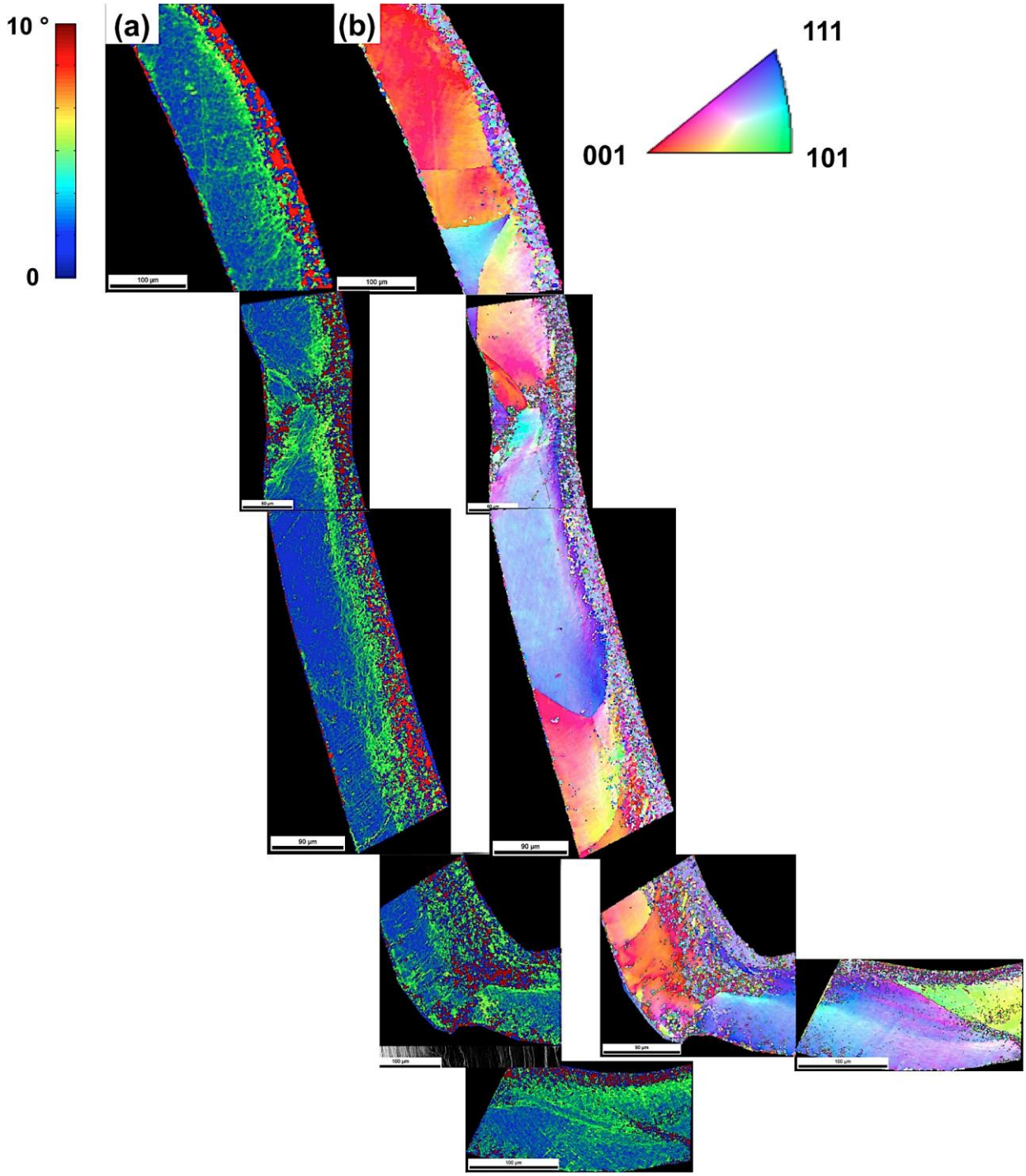

Figure 67: a) KAM and b) IPF maps of Ni sheet with graded microstructure after failure, showing the microstructure evolution in different regions of the sample.

Type m

Graded microstructure was also created on the surface of medium grain size Ni sheets in order to reduce irregularity in shape of the sheet after deep drawing and promote uniformity in deformation along with high level of formability expected in such microstructure. Figure 68 illustrates this type of microstructure created to perform deep drawing. Again UFG layer on top and a transition layer at the interface of UFG and sub-layer with high local misorientations produced during machining of the surface are observed.

Similar defects and deformation behavior as microstructure type l is observed during deformation of this microstructure with somewhat more uniform deformation and less surface roughening.

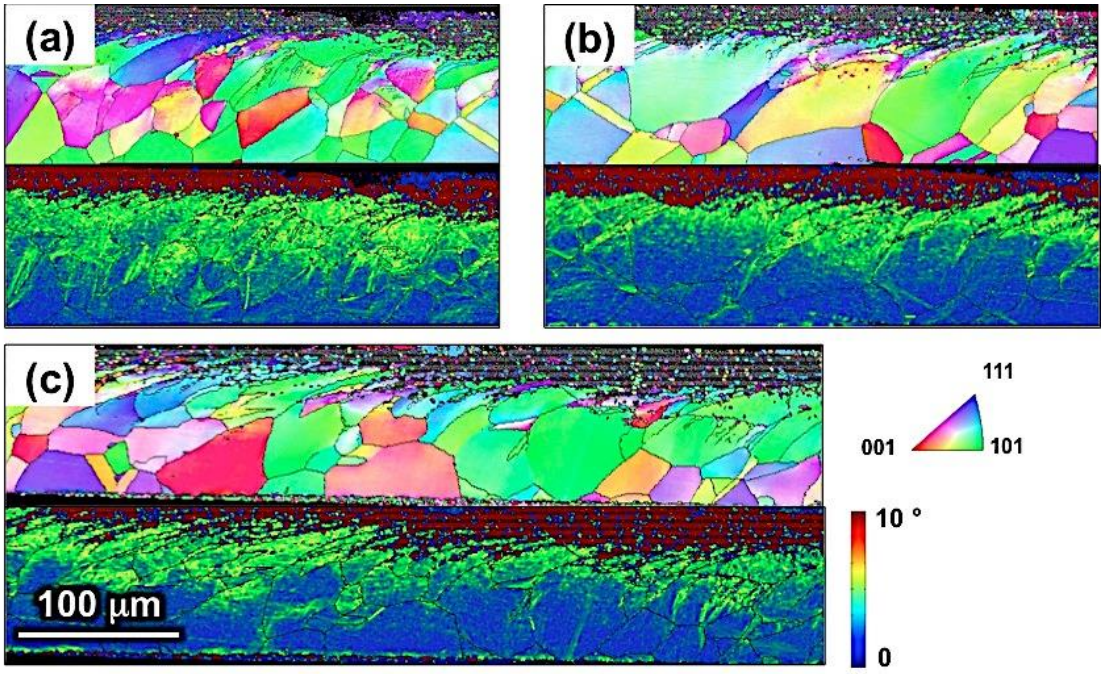

Figure 68: a-c) IPF and KAM maps of graded microstructure (ultrafine grains on top layer and medium size grains underneath) of 100 µm Ni sheet before deformation by deep drawing.

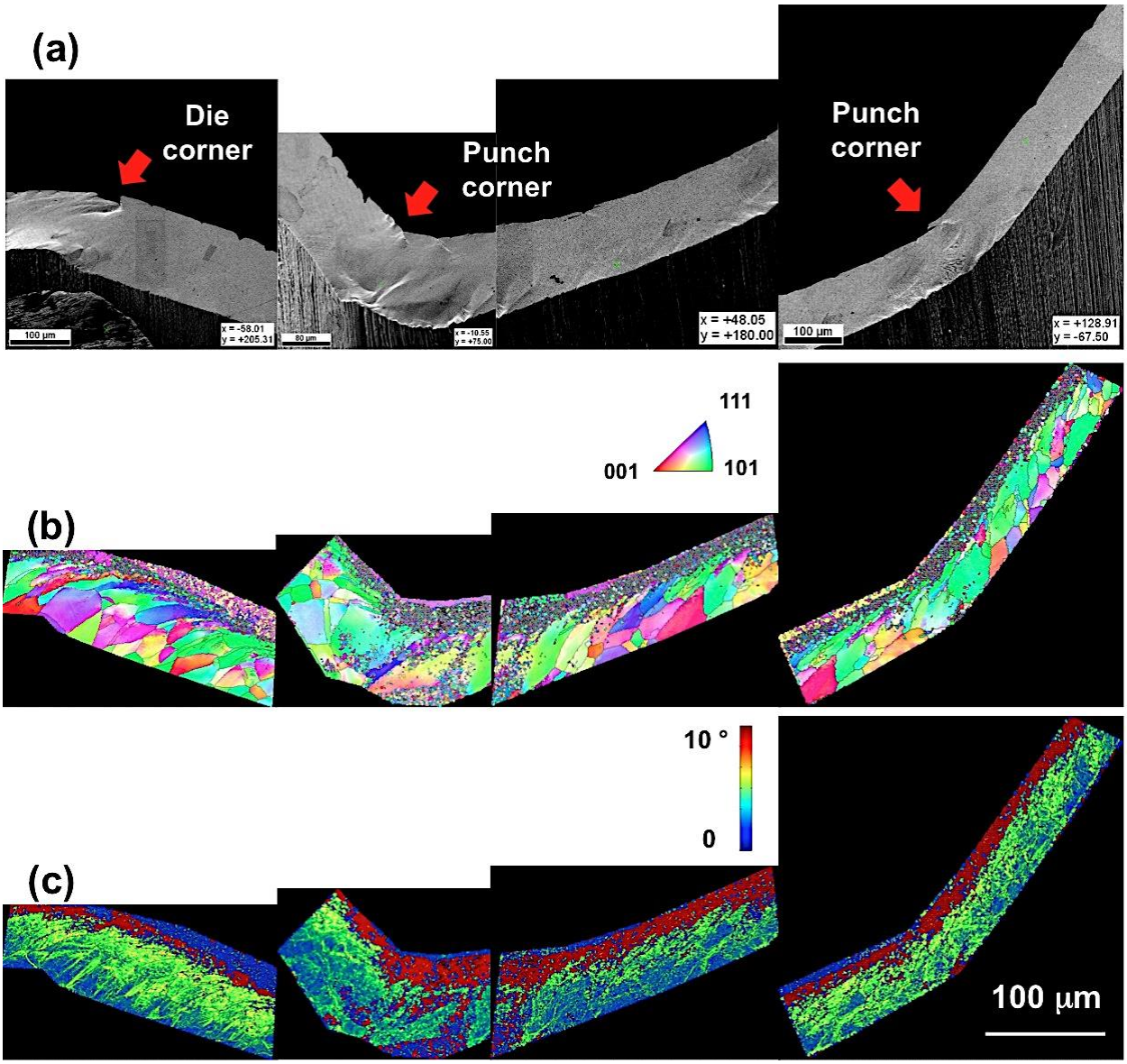

Figure 69: a) SEM image of Ni sheet with graded microstructure obtained few steps before fracture showing the roughening evolution on the surface. b) IPF from OIM and c) KAM maps at the aforementioned state of deformation, showing the microstructure evolution in sub-layer.

The microstructure evolution and surface topography of this type is shown in Figure 69. An interesting type of defect is seen in this microstructure type at the corner is free movement of grains interiors to the direction normal to the surface. This is due to constrain applied by UFG top layer and grain boundaries at sub-layer. Therefore, the interior of the grains is popping-up as the grain boundaries resist to deformation. This is also captured by DIC at the corner of the punch. High concentration of deformation is observed at the corner and at the grain boundaries surrounding the popping-up grains. A very less deformation appears at the interior of the grains based on the DIC observation.

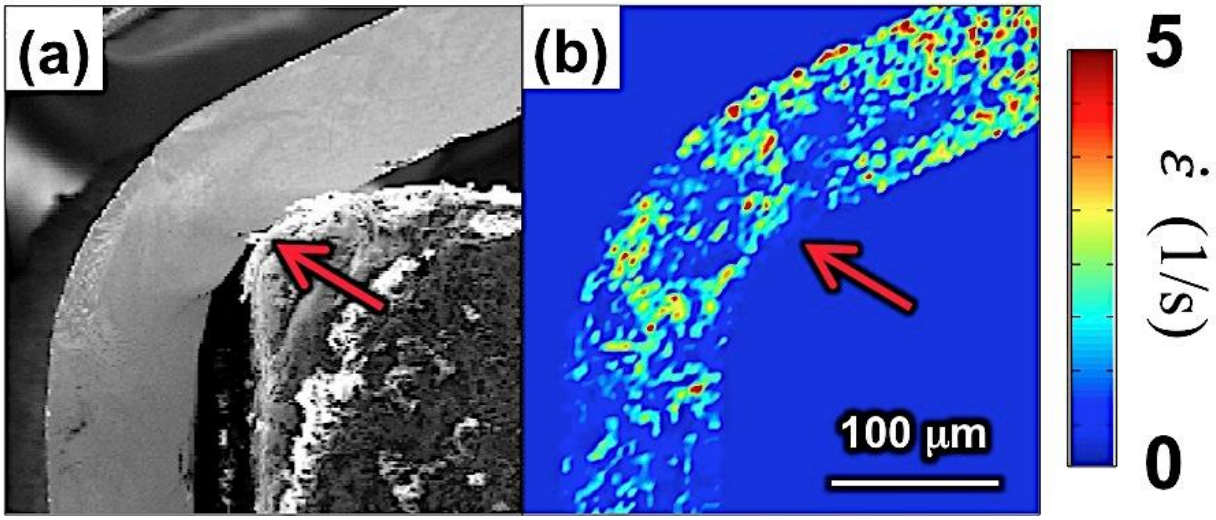

Figure 70: Strain-rate field obtained from DIC for 100 µm Ni sheet with graded microstrucutre dkuring micro-deep drawing with V= 150 µm/s.

The maximum formability and most uniform deformation are observed in this type of microstructure. Figure 71 shows the microstructure of the deformed sheet at the corners of the punch after progressing the deformation for a few more steps before failure. The surface of the sample was polished before performing OIM. A more homogeneous deformation is observed across the sample. However grains at the corner stretching and instability in the form of necking starts happening. Stretching of the sub-layer grains continues until the sample fails and a significant deformation is achieved during deep drawing.

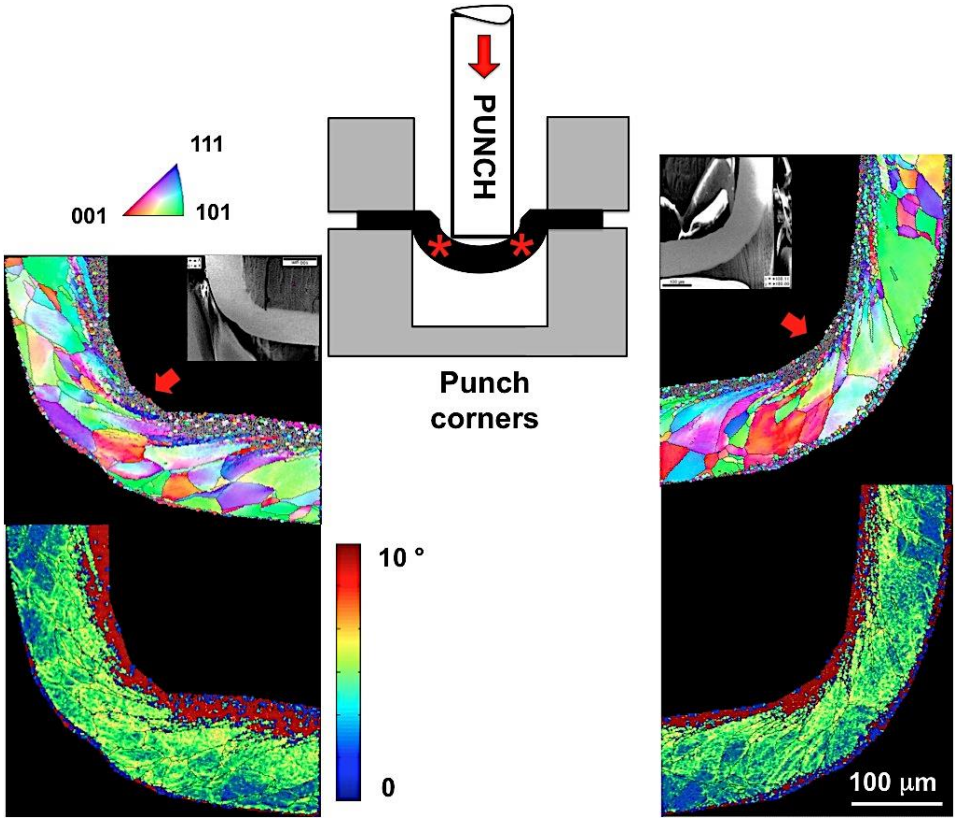

Figure 71: IPF from OIM and KAM maps of Ni sheet with graded microstructure obtained few steps before fracture showing microstructure evolution at the corners.

Figure 72 shows microstructure at the fracture parts and also across the sheet after failure. We see that the thickness of the UFG layer even after significant thinning is unchanged and the sub-layer underwent a noticeable stretch during deformation. Although we observe the gradient microstructure from top to bottom edges of sheet significantly improves the formability in micro-deep drawing of Ni sheets.

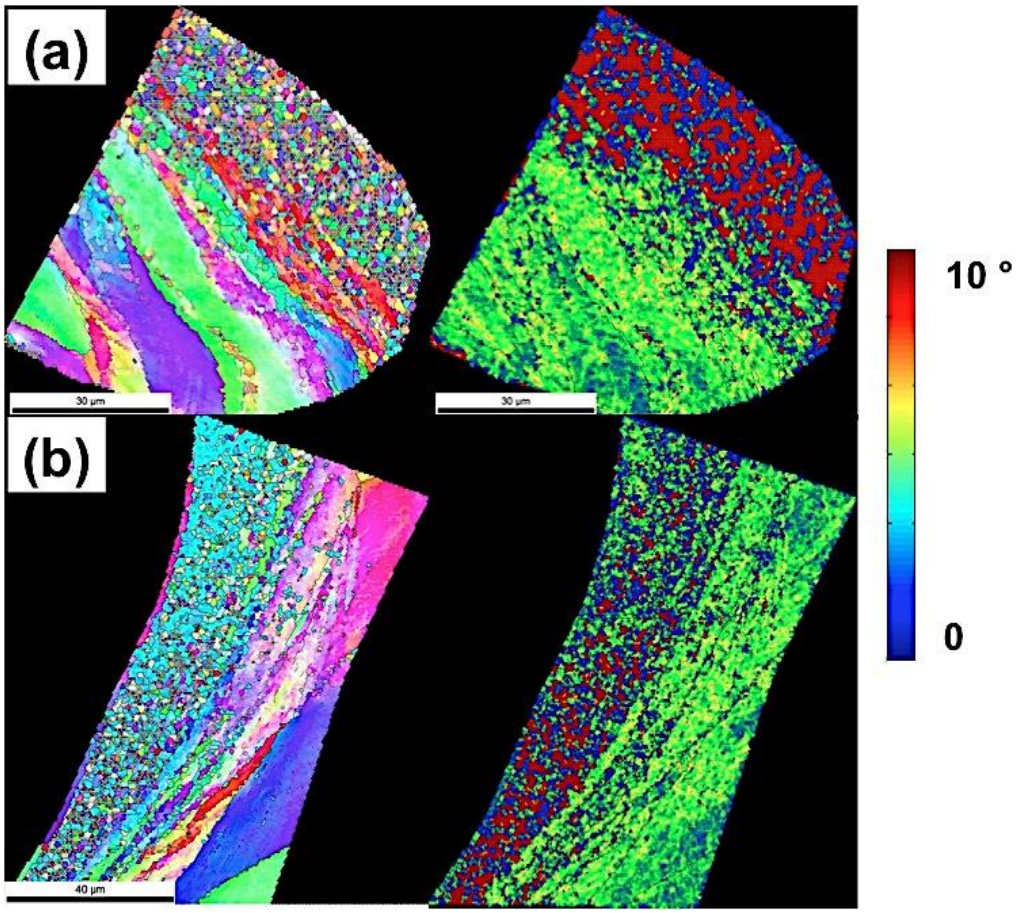

Figure 72: IPF from OIM and KAM maps of Ni sheet with graded microstructure after fracture showing microstructure evolution at the a) fracture point and also b) across the thickness of the sheet. This was obtained after polishing the surface of the fractured sample.

Type n

Figure 73 a shows the starting microstructure of type n, where the UFG layer is positioned at the bottom edge of the sheet. Experiments reveled that this microstructure typed fails at early stage of deformation and shows the lowest formability among all other microstructure types. As expected, since the tension edge made of UFG structure, then cracks formed from there and results in early failure in the sample. This sample fails at the corner of punch.

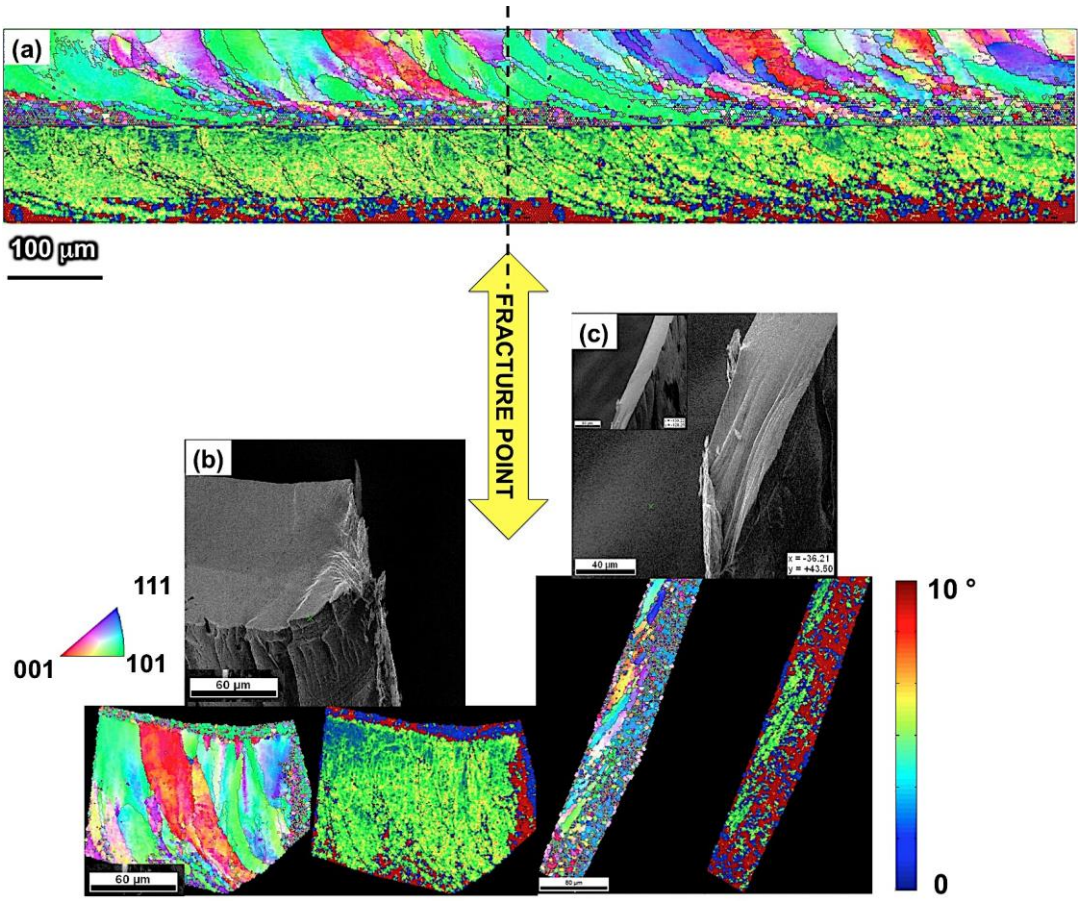

Figure 73: IPF and KAM maps of Ni sheet with graded microstructure (medium size grain on top layer and ultrafine grain layer underneath) before deformation by deep drawing. b) and c) SEM images and corresponding IPF and KAM maps of the sample after failure at fracture parts.

6.3.1.7 Formability based on microstructure type

Figure 74 summarizes formability behaviors of all microstructures described in this section. Figure 74 a shows SEM image of the sample located in the die and captured before starting deep drawing process inside the SEM. Figure 74 b shows the final stage of the aforementioned deformed sheets right before the failure captured by SEM and compares formability during micro-deep drawing with respect to the different starting microstructures. All the images are aligned with respect to a point in the die (shown by red star in Figure 74 a). Blue arrows are the location of this point that show the depth of drawing for each sample with respect to this point of die. A very poor formability is seen for microstructure type i with larger punch width (deep drawing ratio) as well as similar type but 50 μm thickness (scaled-down).

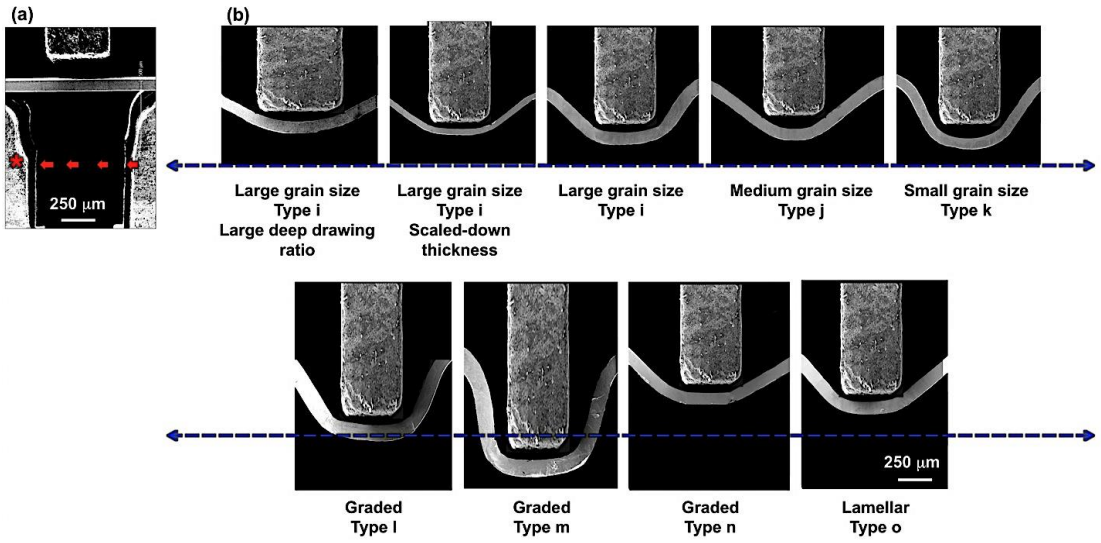

Figure 74: a) Initial state of the Ni sheets in the deep drawing die before the deformation captured by SEM. b) Final state of deformed Ni sheets right before the fracture for different starting microstructures captured by SEM. Images are aligned (blue arrows) with respect to the point shown by red star in the die (part a) to compare the formability in different samples.

More uniform deformation but slightly larger formability is seen in microstructure type j and k with decreasing the grain size. Microstructure type k showed largest and most uniform curvature across the sheet after deformation compared with other microstructure types. Graded microstructure (type l) showed better formability compared with other types as it crosses the blue line and drown deeper in the die. This even got improved in microstructure type m, having the medium grain size sub-layer in terms of both formability and uniformity. Type n showed very low formability having a reverse direction of microstructure gradient compared with type l and m. Lamellar microstructure is again another unfavorable microstructure that showed a very poor formability during deep drawing.

6.3.2 Deep drawing of Cu

In order to validate deformation behavior trends observed in micro-deep drawing, this experiment was also performed on micro Cu sheets as prototypical F.C.C material with high potential application in micro-products.

Sample size effect

Mechanics of deformation for deep drawing of 50, 75 and 100 μm Cu sheets in as-received conditions are shown in Figure 75 a, b and c respectively. We see that a more homogeneous deformation across the length scales as compared with Ni sheet in as-received condition. Similar localization of stain is observed at the corner of the punch. However, deformation does not accompany with high surface roughening as what is observed in Ni sheets during deformation. It is also seen that phenomenon like shear banding did not occur at the early stage of the deformation and material undergoes a significant thinning and deformation before

failure even in 50 µm sheet. This can be attributed to more diffuse deformation zone at the corner for cu compared with Ni as is captured by DIC.

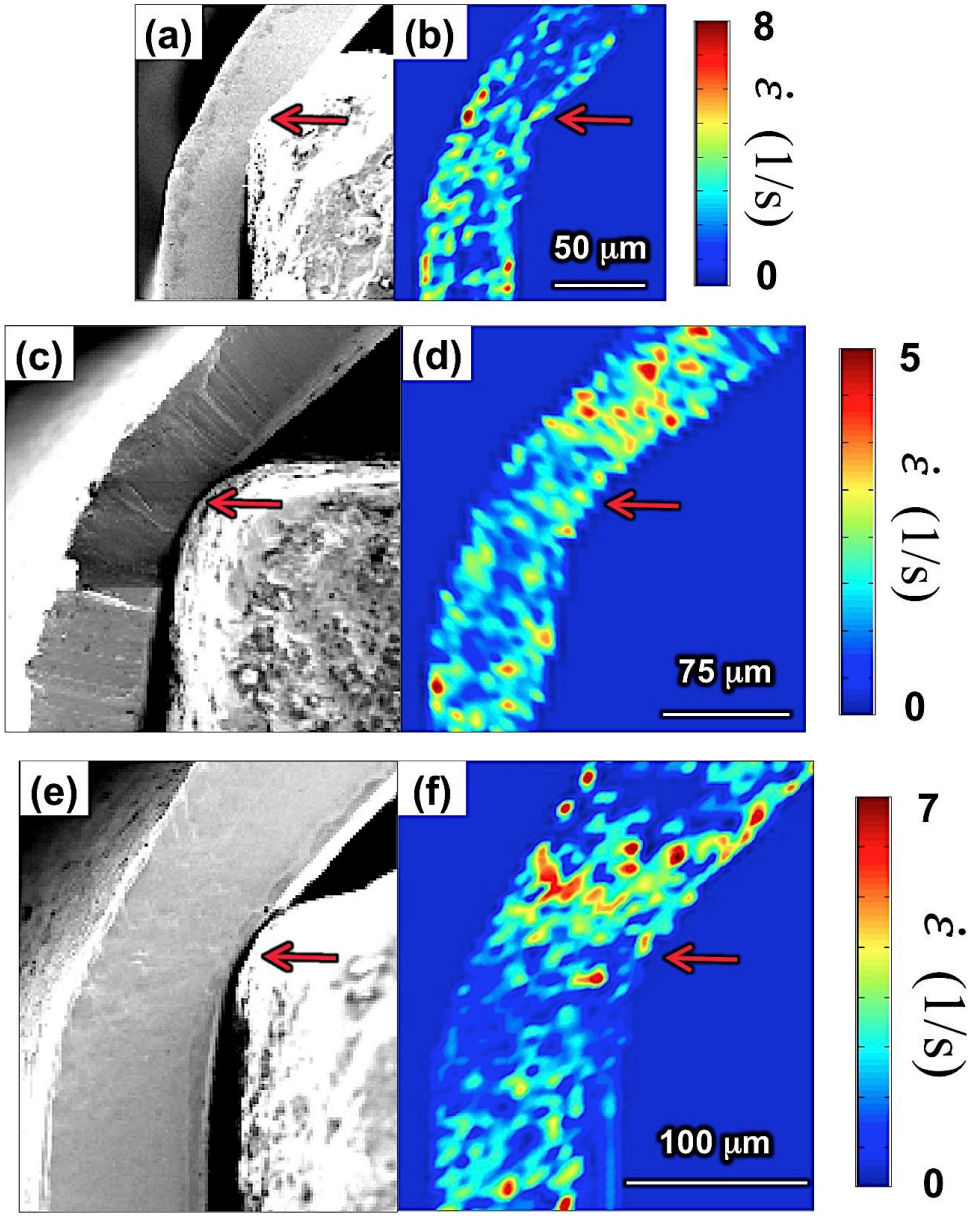

Figure 75: Strain-rate field obtained from DIC for as-received Cu sheets during micro-deep drawing with different thicknesses; a) and b) 50 µm. c) and d) 75 µm. e) and f) 100 µm with V= 150 µm/s.

As an example, the microstructure of 50μm Cu sheet is shown in Figure 76 before the deformation (Figure 76 a) and also after failure in Figure 76 b-d corresponding to bottom, middle and top parts of the sample.

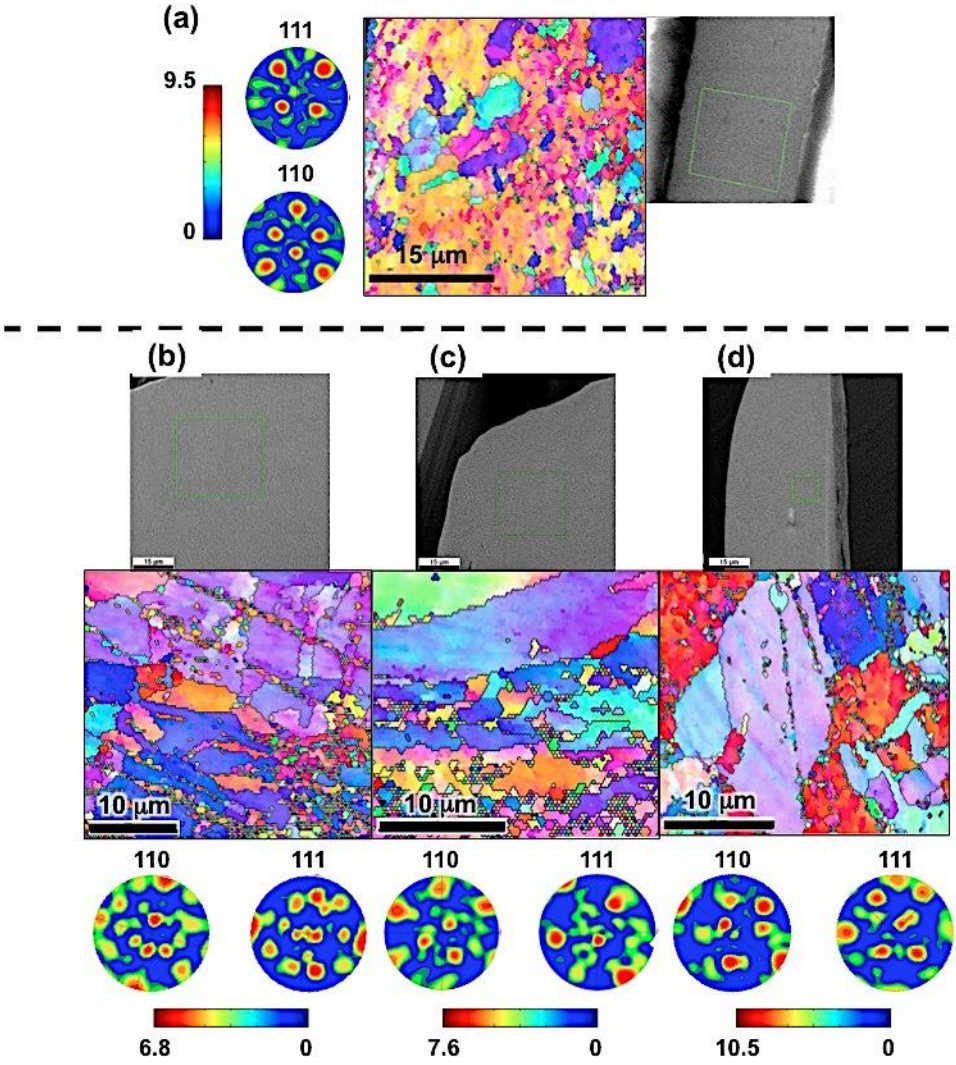

Figure 76: a) IPF, (110) and (111) pole figures of initial microstructure of as-received 50 μm Cu sheet. IPF, (110) and (111) pole figures of microstructure after the failure from: b) Top, c) Middle and d) Bottom regions of fractured part, showing the microstructure evolution in aforementioned regions.

We see that in spite of the less refinement in the microstructure during deformation, material texture evolved during the deformation as it features a somewhat similar to tension type of the texture at the bottom part of the sheet (Figure 76 b) and simple shear at the middle part. The formability of such samples will be discussed subsequently.

Microstructure characteristics effect

Here we examined ultrafine microstructure behavior in Cu sheets and also effect of grain size as well as grain boundary characteristics in Cu sheets. Figure 77 a-c shows starting microstructures created by machining of Cu and post heat-treating as explained in chapter 4.4.

A highly textured UFG material showing simple shear texture was produced in the sheet after machining (Figure 77 a) that underwent some changes by heat-treating for short (Figure 77 b) and long times (Figure 77 c). Characteristics of starting microstructure are shown in Table 9. From this table, the average grain size is about 0.59 μm for as-machined case while it is increasing to the 1.63 and 2.75 μm respectively. We see that there is also a significant change in misorientations as the percentage of low angel grain boundaries increases during heat-treating. There is also a significant increase in percentage of twin boundaries with heat-treating, which is not influenced by heat-treating time. Figure 77 d and e show the microstructure of sheet for as-machined and long annealed condition after the failure respectively.

The mechanics of deformation for all aforementioned microstructures is shown in Figure 78. We see a very uniform deformation in as-machined sheet as opposed to other short and long annealed ones. Here the mechanics of deformation and its variation in different samples cannot be purely related to the grain size factor, as it does not increase significantly during annealing compare to grain size variation examined in Ni experiments.

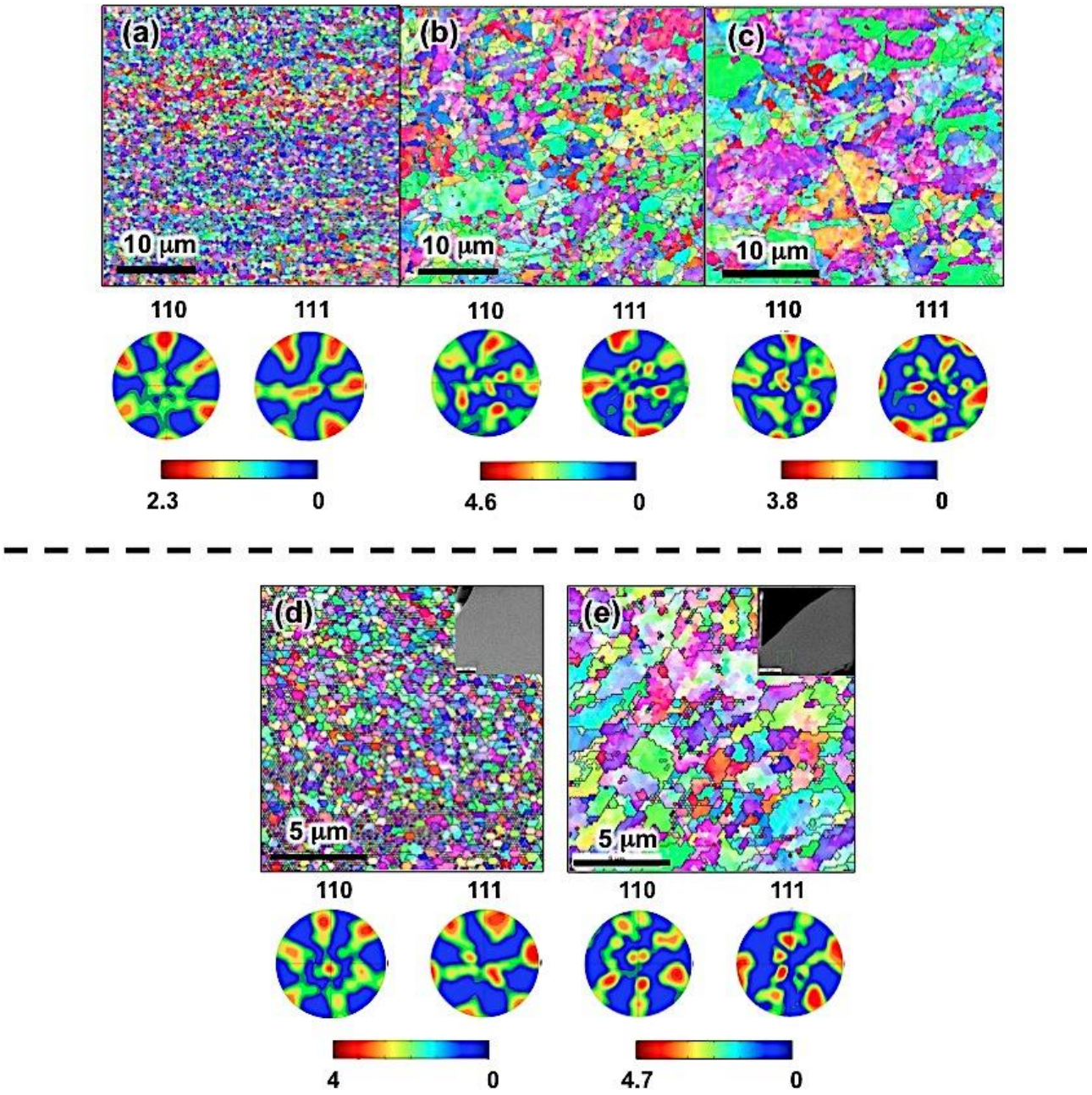

Figure 77: a) IPF, (110) and (111) pole figures of initial microstructure of 100 μm Cu sheet with a) Ultrafine grain microstructure obtained by machining along with: b) Short time and c) Long time annealing of aforementioned microstructure. d) and e) IPF, (110) and (111) pole figures of microstructure after the failure at the middle region of fractured part for microstructure described in parts a) and c) respectively.

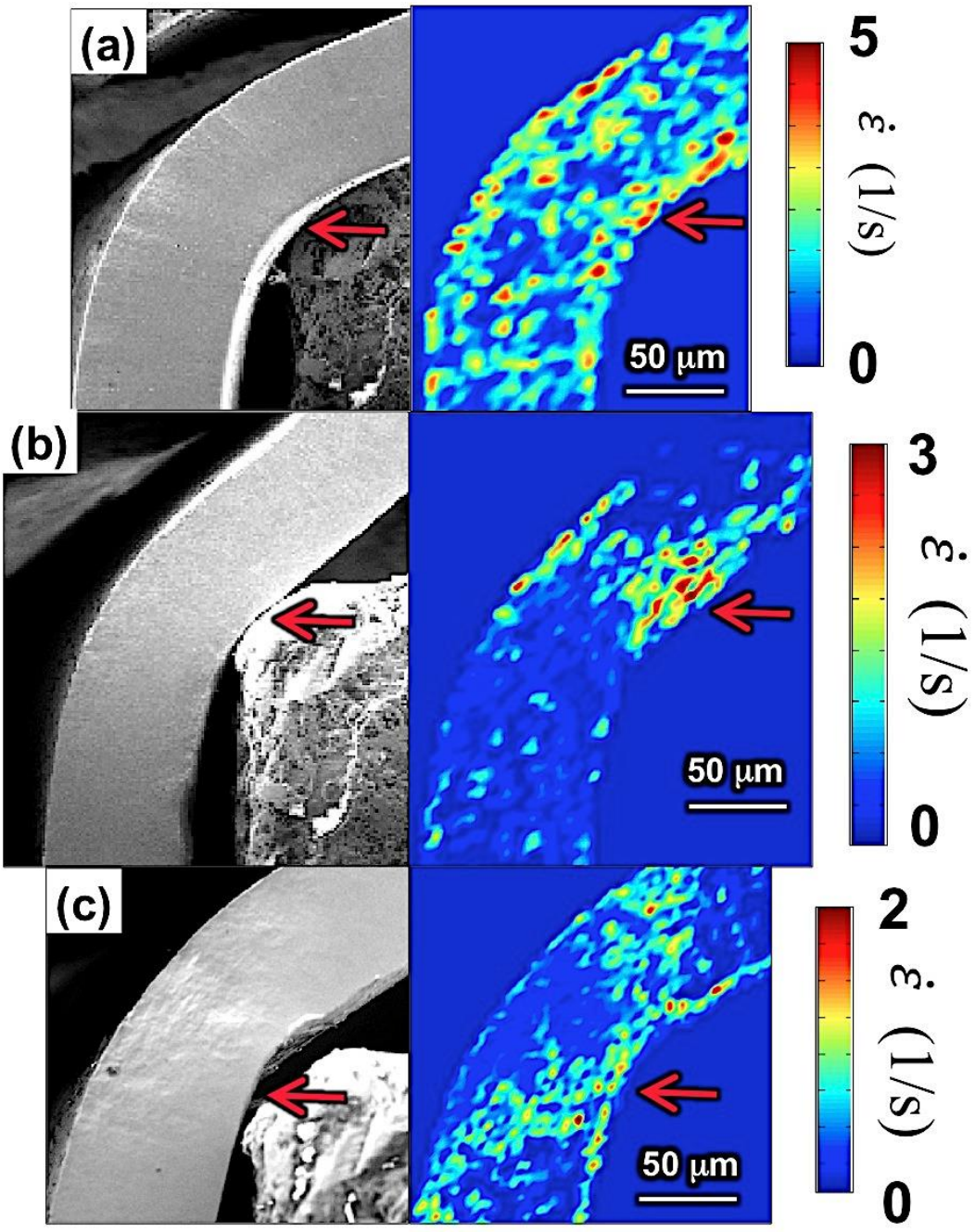

Figure 78: Strain-rate field obtained from DIC for 100 μm Cu sheets during micro-deep drawing with different microstructure: a) Ultrafine, b) Short annealed and c) Long annealed with V= 150 μm/s.

It is observed that the deformation zone at the corner has an expanded morphology in long annealed sample compared with the short annealed one. This might be the result of larger grain size as well as large density of low angle grain boundaries that provides a condition for deformation to diffuse across the sheet in larger area. The formability of aforementioned microstructures will be discussed subsequently.

Formability

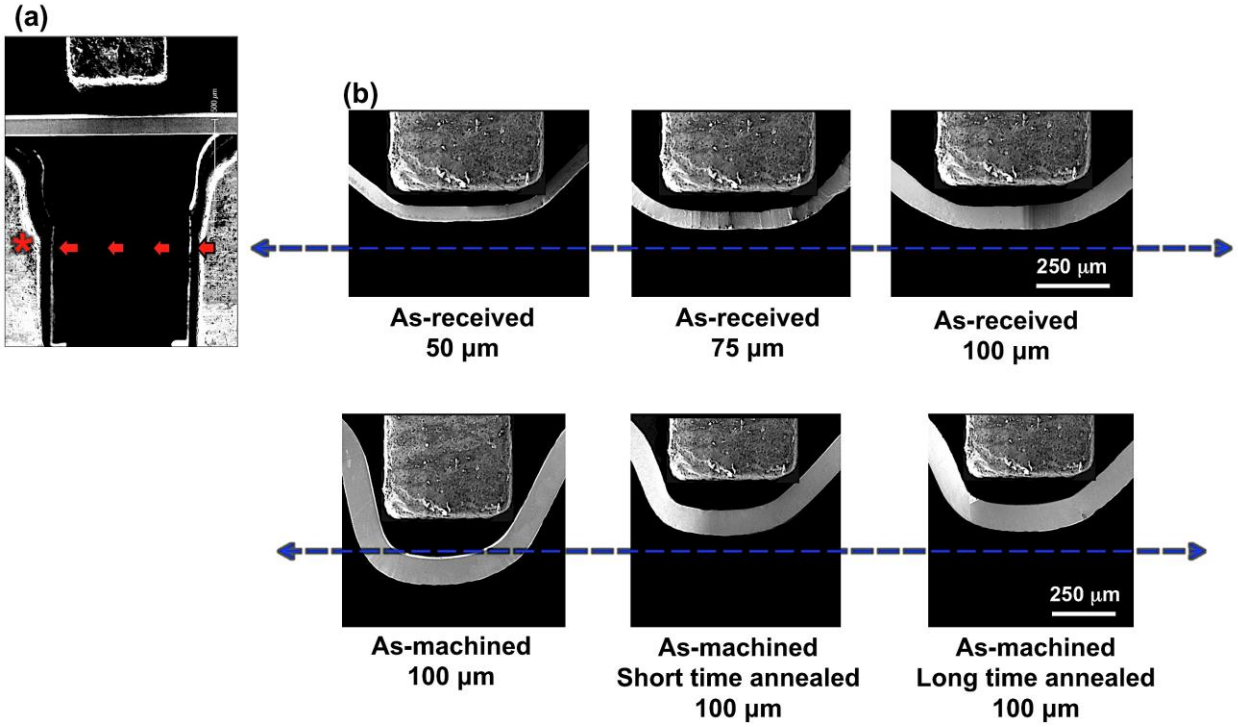

Figure 79: a) Initial state of the Cu sheets in the deep drawing die before deformation captured by SEM. b) Final state of deformed Cu sheets right before the fracture for different starting microstructures captured by SEM. Images are aligned (blue arrows) with respect to the point shown by red star in the die (part a) to compare the formability in different samples.

Figure 79 summarizes formability behavior of Cu sheets for all conditions discussed previously. Similar to Ni, SEM images were captured few steps before the failure. It shows although, Cu sheets show better formability compared with Ni having similar thicknesses in as-received case, their formability does not change significantly with increasing the thickness within the tested ranges. This might be due to the fast rate of failure once the instability starts in localized deformation zone. Comparison of formability in Cu samples with respect to grain size and a microstructure characteristic also indicates a highest formability for UFG sheet and almost similar behavior for annealed sheets.

6.4 SUMMARY AND FINDINGS

This study was set to explore the effects of the microstructure parameters on formability of microsheets. Suitable microstructures were designed in Ni and Cu sheets aiming to enhance the formability and prevent early fracture. Using *in situ* micro-deep drawing stage sitting in the chamber of SEM, the material flow behavior was observed and mechanics of deformation was captured through post processing of the images using DIC technique.

It is found that microstructure evolution is very non-uniform across the sheet especially for the sheets with large grain size as it is different from grain-to-grain depending on the orientation and location of the grains with respect to the punch. Results of tracking the microstructure evolution shows that there is not much of the grain refinement or fragmentation phenomena associated with deformation even close to failure in most types of the microstructures. Additionally there is not much the crystallographic rotation in individual grains as well as near the grain boundaries that varies in different grains. Very rough surface is formed during the deformation as a result of inhomogeneity of deformation in different grains as some of them undergo a very large thinning while others buckles especially those located at the corner of the punch. It is found that in addition to non-uniform deformation across the thickness from top edge to bottom edge, grain boundaries, triple junctions and twin boundaries are also locations for strain localization which results in the formation of hill, groove and step-types of defects/features on the surface respectively and produce rough surfaces during deformation. All this suggests that the microstructure becomes very unstable at the beginning stage of the deformation and it fails as there is not much of the microstructure evolution associated with deformation. Therefore, local phenomena govern this process and result in early fracture before the microstructure undergoes a serious evolution. Using SEM based DIC, it is found that there is strain localization phenomena

at high stress concentration regions around the corners of the die. It also captures locations with high strain at microscopic level close the grain boundaries, triple junction and etc.

More uniformity in deformation is achieved throughout the sheet by decreasing the grain size. However, poor formability is observed due to the lack of ductility in such microstructures and the sample fails before undergoing a significant microstructure evolution.

We have also demonstrated that variation in the microstructure features e.g. grain size distribution results in improving both uniformity and formability. It is found that graded microstructures enhances the formability significantly and delays fracture because of the interaction of slip systems with the interface of ultrafine and large grain size layers.

Similar results are found in repeating microforming of Cu sheets for some of the aforementioned microstructures created in Ni sheets. However, Cu shows a more uniform and ductile behavior comparably as deformation zone captured by DIC shows a more diffuse and extended morphology at the corners of the punch for all microstructure types examined in Cu sheets. It is found that ultrafine Cu sheets with strong texture produced by SPD behave very uniformly and smoothly during micro-deep drawing with high degree of formability. This characteristic is somewhat subdued by annealing the aforementioned sheets as in addition to the grain growth, it produces different types of grain boundaries as well as a random texture across the sheet.

7.0 CONCLUSIONS

We have demonstrated a remarkable influence of microstructure engineering on enhancing the formability and improving the process outcomes with respect to the macroscopic boundary conditions prevail in different microforming geometries: Equal Channel Angular Pressing (ECAP), Indirect Extrusion (IE) and Deep Drawing (DD). High resolution *In situ* observation methods in plane strain condition were established for each geometry and post image processing using DIC techniques were developed and modified for each configuration to measure the mechanics of deformation prevail in deformation zone. Pre and post-characterization of microstructure was performed to track the microstructure evolution in relation with its initial state and correlate with the *in situ* observations of material response to deformation.

Commercially Pure metallic systems including Ni 200, Oxygen Free High Conductivity (OFHC) Cu, Al 1100 and Pb were used in order to perform microforming. We found a direct relation between the process outcomes/anomalies e.g. microstructure evolution, surface roughening, sudden failure, etc. and mechanical/microscopical phenomena that take place in plastic deformation zone (PDZ). We have shown that the geometry and morphology of PDZ is scaled by dimension of the counterparts as well as their starting microstructure features. It is found that the normalized thickness of the deformation zone increases with scaling down of the process. However, with increasing deformation rate, the morphology of PDZ and its spread does not change significantly. But, increasing deformation rate leads to enhanced strain localization

and rotation of material elements, which is further pronounced in smaller scales. These can result in non-uniformities in microstructures within parts created by ECAP and IE, essentially manifesting in instabilities in mechanical response and lead to process anomalies.

Strain gradient theory was used to relate PDZ scale in IE to the grain size and DIC based analysis was established in order to find the geometrically necessary dislocation density across the PDZ and correlate with the mechanics of deformation. This was verified by local measurements of geometrically necessary dislocation density using OIM data.

A VPSC model integrated with DIC was developed to simulate local evolved texture in different part the samples deformed by indirect microextrusion and the results were compared to the empirical observations by OIM. There is a significant variation in evolved crystallographic textures across the deformed samples and observations suggest a preponderance of a simple shear crystallographic type of texture resulting from the deformation. Additionally, we demonstrated the role of prior textures in scaling and morphology of PDZ and also in quality of created surfaces for ultrafine-grained Cu samples deformed by indirect microextrusion. This study revealed for certain prior textures, the quality of micro-products is improved remarkably.

In microforming of thin sheets, we successfully showed that using composite/graded microstructures lead to prevent localization phenomena and delay early fracture. The directional variations in the properties of such microstructures postpone failure and improve formability in micro-deep drawing due to the interaction of slip systems with the interface of bilayer.

All these characterizations are expected to offer a framework for identifying the underlying process-structure mappings and subsequently offer control strategies for mitigating process anomalies and tailoring product functionalities.

BIBLIOGRAPHY

Abolghasem, S., Basu, S., & Shankar, M. R. (2013). Quantifying the progression of dynamic recrystallization in severe shear deformation at high strain rates. *Journal of Materials Research, 28*(15), 2056-2069.

Abolghasem, S., Basu, S., Shekhar, S., Cai, J., & Ravi Shankar, M. (2012). *Mapping Microstructures Resulting from Severe Simple Shear Deformation.* Paper presented at the AIP Conference Proceedings.

Acharya, A., & Beaudoin, A. J. (2000). Grain-size effect in viscoplastic polycrystals at moderate strains. *Journal of the Mechanics and Physics of Solids, 48*(10), 2213-2230.

Adrian, R. (1997). Dynamic ranges of velocity and spatial resolution of particle image velocimetry. *Measurement Science and Technology, 8*(12), 1393.

Al-Rub, R. K. A., & Voyiadjis, G. Z. (2004). Analytical and experimental determination of the material intrinsic length scale of strain gradient plasticity theory from micro- and nano-indentation experiments. *International Journal of Plasticity, 20*(6), 1139–1182.

Armstrong, R., Codd, I., Douthwaite, R. M., & Petch, N. J. (1962). The plastic deformation of polycrystalline aggregates. *Philosophical Magazine, 7*(73), 45-58.

Ashby, M. F. (1970). The deformation of plastically non-homogeneous materials. *Philosophical Magazine, 21*(170), 399-424.

Bakhshi-Koybari, M. (2002). A theoretical and experimental study of friction in metal forming by the use of the forward extrusion process. *J Mater Process Technol, 125*, 369–374.

Barrett, C. S., & Massalski, T. B. (1966). *Structure of metals* (Vol. 631): McGraw-Hill New York.

Basu, S., Abolghasem, S., & Shankar, M. R. (2013). Mechanics of Intermittent Plasticity Punctuated by Fracture During Shear Deformation of Mg Alloys at Near-Ambient Temperatures. *Metallurgical and Materials Transactions A, 44*(10), 4558-4566.

Basu, S., & Shankar, M. R. (2014a). Microstructure Evolution during Severe Shear Deformation at Small Length-Scales. *Scripta materialia, 73*, 52-54.

Basu, S., & Shankar, M. R. (2014). Spatial confinement-induced switchover in microstructure evolution during severe plastic deformation at micrometer length scales. *Acta Materialia, 79*, 146-158.

Basu, S., & Shankar, M. R. (2014b). Spatial Confinement-Induced Switchover in Microstructure Evolution During Severe Plastic Deformation at Micrometer Length Scales. *Acta Materialia, 79*, 146–158.

Bate, P. (1999). Modelling deformation microstructure with the crystal plasticity finite–element method. *Philosophical Transactions of the Royal Society of London. Series A: Mathematical, Physical and Engineering Sciences, 357*(1756), 1589-1601.

Bishop, J., & Hill, R. (1951). CXXVIII. A theoretical derivation of the plastic properties of a polycrystalline face-centred metal. *Philosophical Magazine Series 7, 42*(334), 1298-1307.

Bruck, H., McNeill, S., Sutton, M. A., & Peters Iii, W. (1989). Digital image correlation using Newton-Raphson method of partial differential correction. *Experimental Mechanics, 29*(3), 261-267.

Bunge, H. (1979). Texture and Anisotropy. *Zeitschrift fur Metallkunde, 70*(7), 411-418.

Cardarelli, F. (2000). *Materials handbook*: Springer London etc.

Chakrabarty, J. (2012). *Theory of plasticity* (Vol. U.K.). U.K.: Butterworth-Heinemann.

Chan, W., & Fu, M. (2011). *Integrated product and process design for micro-product development via microforming.* Paper presented at the International conference on innovative methods in product design, Venice, Italy.

Chan, W., Fu, M., & Yang, B. (2011). Study of size effect in micro-extrusion process of pure copper. *Materials & Design, 32*(7), 3772-3782.

Chang, C. C., & Wang, T. C. (2010). Effects of Grain Size on Micro Backward Extrusion of Copper. *Advanced Materials Research, 83-86*, 1092-1098.

Demir, E., Raabe, D., Zaafarani, N., & Zaefferer, S. (2009). Investigation of the indentation size effect through the measurement of the geometrically necessary dislocations beneath small indents of different depths using EBSD tomography. *Acta Materialia, 57*(2), 559-569.

Dong, Y., Zhang, Y., Alexandrov, I., & Wang, J. (2012). Effect of high strain rate processing on strength and ductility of ultrafine-grained Cu processed by equal channel angular pressing. *Rev. Adv. Mater. Sci, 31*, 116-122.

Eisenlohr, A., Gutierrez-Urrutia, I., & Raabe, D. (2012). Adiabatic temperature increase associated with deformation twinning and dislocation plasticity. *Acta Materialia, 60*(9), 3994-4004.

Engel, U., & Eckstein, R. (2002). Microforming—from basic research to its realization. *Journal of Materials Processing Technology, 125-126*(9), 35-44.

Evers, L. P., D.M.Parks, Brekelmans, W. A. M., & Geers, M. G. D. (2002). Crystal plasticity model with enhanced hardening by geometrically necessary dislocation accumulation. *Journal of the Mechanics and Physics of Solids, 50*(11), 2403–2424.

Fleck, N., & Hutchinson, J. (1997). Strain gradient plasticity. *Advances in applied mechanics, 33*, 295-361.

Fleck, N. A., & Hutchinson, J. W. (1997). Strain Gradient Plasticity. *Advances in Applied Mechanics, 33*, 295–361.

Fleck, N. A., Muller, G. M., Ashby, M. F., & Hutchinson, J. W. (1993). Strain gradient plasticity: Theory and experiment. *Acta Matallurgica Materialia, 42*(2), 475-487.

Fleck, N. A., Muller, G. M., Ashby, M. F., & Hutchinson, J. W. (1993). Strain gradient plasticity: Theory and experiment. *Acta Metallurgical et Materialia, 42*(2), 475-487.

Fu, M. W., & Chan, W. L. (2011). Geometry and grain size effects on the fracture behavior of sheet metal in micro-scale plastic deformation. *Materials & Design, 32*(10), 4738–4746.

Fu, M. W., & Chan, W. L. (2013). A review on the state-of-the-art microforming technologies *The International Journal of Advanced Manufacturing Technology, 67*, 2411–2437.

Fu, M. W., & Chan, W. L. (2014). *Micro-scaled Products Development via Microforming*

Fu, M. W., & Chan, W. L. (2014). *Micro-scaled Products Development via Microforming*: Springer.

Gau, J.-T., Principe, C., & Yu, M. (2007). Springback behavior of brass in micro sheet forming. *Journal of materials processing technology, 191*(1), 7-10.

Geiger, M., Kleiner, M., Eckstein, R., Tiesler, N., & Engel, U. (2001). Microforming. *CIRP Annals - Manufacturing Technology, 50*(2), 445-462.

Geiger, M., Kleiner, M., Eckstein, R., Tiesler, N., & Engel, U. (2001). Microforming. *CIRP Annals-Manufacturing Technology, 50*(2), 445-462.

Gong, F., Guo, B., Wang, C. J., & Shan, D. B. (2010). Effects of lubrication conditions on micro deep drawing. *Microsystem technologies, 16*(10), 1741-1747.

Greer, J. R., & De Hosson, J. T. M. (2011). Plasticity in small-sized metallic systems: Intrinsic versus extrinsic size effect. *Progress in Materials Science, 56*(6), 654-724.

hall, H. O. (1951). The Deformation and Ageing of Mild Steel: III Discussion of Results. *Proceedings of the Physical Society, B64*(9), 747.

Handbook, M. (1979). Properties and selection: nonferrous alloys and pure metals. *American Society for Metals, Metals Park, OH*.

Hezong, L., Xianghuai, D., Qian, W., Yu, S., Diehl, A., Hagenah, H., . . . Merklein, M. (2011). Determination of material intrinsic length and strain gradient hardening
in microbending process. *International Journal of Solids and Structures, 48*, 163-174.

Hill, R. (1965). Continuum micro-mechanics of elastoplastic polycrystals. *Journal of the Mechanics and Physics of Solids, 13*(2), 89-101.

Hirsch, J., & Al-Samman, T. (2013). Superior light metals by texture engineering: optimized aluminum and magnesium alloys for automotive applications. *Acta Materialia, 61*(3), 818-843.

Holt, D. L. (1970). Dislocation Cell Formation in Metals. *Journal of applied physics, 41*(8).

Hosford, W. F., & Caddell, R. M. (1993). *Metal forming*: Prentice Hall.

Hosford, W. F., & Caddell, R. M. (2011). *Metal Forming: Mechanics and Metallurgy*: Cambridge University Press.

Hughes, D. A., & Hansen, N. (1997). High Angle Boundaries Formed by Grain Subdivision Mechanisms *Acta Metallurgica, 45*(9), 3871-3886.

Hutchinson, J. (1976). Bounds and self-consistent estimates for creep of polycrystalline materials. *Proceedings of the Royal Society of London. A. Mathematical and Physical Sciences, 348*(1652), 101-127.

Iwahashi, Y., Horita, Z., Nemoto, M., & Langdon, T. G. (1998). The process of grain refinement in equal-channel angular pressing. *Acta Materialia, 46*(9), 3317-3331.

Iwahashi, Y., Wang, J., Horita, Z., Nemoto, M., & Langdon, T. G. (1996). Principle of equal-channel angular pressing for the processing of ultra-fine grained materials. *Scripta Materialia, 35*(2), 143-146.

Jia, N., Eisenlohr, P., Roters, F., Raabe, D., & Zhao, X. (2012). Orientation dependence of shear banding in face-centered-cubic
single crystals. *Acta Materialia, 60*, 3415-3434.

Kalidindi, S. R., Bronkhorst, C. A., & Anand, L. (1992). Crystallographic texture evolution in bulk deformation processing of FCC metals. *Journal of the Mechanics and Physics of Solids, 40*(3), 537–569.

Kanjarla, A. K., Van Houtte, P., & Delannay, L. (2010). Assessment of plastic heterogeneity in grain interaction models using crystal plasticity finite element method. *International Journal of Plasticity, 26*(8), 1220-1233.

Kim, H. S. (2001). Prediction of temperature rise in equal channel angular pressing. *Materials transactions-JIM, 42*(3), 536-538.

Kim, H. S., Hong, S. I., & Seo, M. H. (2001). Effects of strain hardenability and strain-rate sensitivity on the plastic flow and deformation homogeneity during equal channel angular pressing. *Journal of Materials Research, 16*(03), 856-864.

Kim, H. S., Seo, M. H., & Hong, S. I. (2001). Plastic deformation analysis of metals during equal channel angular pressing. *Journal of Materials Processing Technology, 113*(1), 622-626.

Kleiner, M., Geiger, M., & Klaus, A. (2003). Manufacturing of lightweight components by metal forming. *CIRP Annals-Manufacturing Technology, 52*(2), 521-542.

Kocks, U., Kallend, J., Wenk, H., Rollett, A., & Wright, S. (1995). popLA.

Krishnan, N., Cao, J., & Dohda, K. (2007). Study of the Size Effect on Friction Conditions in Microextrusion—Part I: Microextrusion Experiments and Analysis. *Journal of Manufacturing Science and Engineering, 129*(4), 669-676.

Kroner, E. (1978). Self-consistent scheme and graded disorder in polycrystal elasticity. *Journal of Physics F: Metal Physics, 8*(11), 2261.

Kumar, M., Schwartz, A. J., & King, W. E. (2002). Microstructural evolution during grain boundary engineering of low to medium stacking fault energy fcc materials. *Acta Materialia, 50*(10), 2599–2612.

Lapovok, R., Tóth, L. S., Molinari, A., & Estrin, Y. (2009). Strain localisation patterns under equal-channel angular pressing. *Journal of the Mechanics and Physics of Solids, 57*(1), 122-136.

Lebensohn, R. A., & Tomé, C. N. (1993). A self-consistent anisotropic approach for the simulation of plastic deformation and texture development of polycrystals: Application to zirconium alloys. *Acta Metallurgica et Materialia, 41*(9), 2611-2624.

Lee, E., Mallett, R., & Yang, W. H. (1977). Stress and deformation analysis of the metal extrusion process. *Computer Methods in Applied Mechanics and Engineering, 10*(3), 339-353.

Lee, H. J., Lee, N. K., Lee, S. M., Lee, G. A., & Kim, S. S. (2006). Development of Micro Metal Forming Manufacturing System. *Materials Science Forum, 505-507*, 19-24.

Lee, W., & Zhou, M. (1993). A theoretical analysis of the effect of crystallographic orientation on chip formation in micromachining. *International Journal of Machine Tools and Manufacture, 33*(3), 439-447.

Li, S., Hoferlin, E., Bael, A. V., Houtte, P. V., & Teodosiu, C. (2003). Finite element modeling of plastic anisotropy induced by texture and strain-path change. *International Journal of Plasticity, 19*(5), 647-674.

Mahabunphachai, S., & Koc, M. (2008). Investigation of size effects on material behavior of thin sheet metals using hydraulic bulge testing at micro/meso-scales. *International journal of machine tools and manufacture, 48*(9), 1014-1029.

Manabe, K., Shimizu, T., Koyama, H., Yang, M., & Ito, K. (2008). Validation of FE simulation based on surface roughness model in micro-deep drawing. *Journal of materials processing technology, 204*(1), 89-93.

Marusich, T., & Ortiz, M. (1995). Modelling and simulation of high- speed machining. *International Journal for Numerical Methods in Engineering, 38*(21), 3675-3694.

Mason, J., Rosakis, A., & Ravichandran, G. (1994). On the strain and strain rate dependence of the fraction of plastic work converted to heat: an experimental study using high speed infrared detectors and the Kolsky bar. *Mechanics of Materials, 17*(2), 135-145.

Mathur, K. K., & Dawson, P. R. (1989). On modeling the development of crystallographic texture in bulk forming processes. *International Journal of Plasticity, 5*(1), 67-94.

Miyazaki, S., Shibata, K., & Fujita, H. (1979). Effect of specimen thickness on mechanical properties of polycrystalline aggregates with various grain sizes. *Acta Metallurgica, 27*(5), 855–862.

Moradi, M., Basu, S., & Shankar, M. R. (2015). In situ measurement of deformation mechanics and its spatiotemporal scaling behavior in equal channel angular pressing. *Journal of Material Research, 30*(6), 798-810.

Mughrabi, H., Wang, R., Hansen, N., Horsewell, A., Leffers, T., & Lilholt, H. (1981). *Deformation of polycrystals: mechanisms and microstructures.* Paper presented at the Proc. 2nd Risø Int. Symp. on Metallurgy and Materials Science, N. Hansen, A. Horsewell, T. Leffers, and H. Lilholt, eds., Risø National Laboratory, Roskilde, Denmark.

Nabarro, F. R. N., Basinski, Z. S., & Holt, D. B. (1964). The plasticity of pure single crystals. *advances in Physics, 13*(50), 193-323.

Nes, E. (1997). Modelling of work hardening and stress saturation in FCC metals. *Progress in Materials Science, 41*(3), 129-193.

Oxley, P. (1962). Shear angle solutions in orthogonal machining. *International Journal of Machine Tool Design and Research, 2*(3), 219-229.

Oxley, P., & Hastings, W. (1977). Predicting the strain rate in the zone of intense shear in which the chip is formed in machining from the dynamic flow stress properties of the work material and the cutting conditions. *Proceedings of the Royal Society of London. A. Mathematical and Physical Sciences, 356*(1686), 395-410.

Palmer, W., & Oxley, P. (1959). Mechanics of orthogonal machining. *Proceedings of the Institution of Mechanical Engineers, 173*(1), 623-654.

Paul, H., Baudin, T., & Brisset, F. (2011). The effect of the strain path and the second phase particles on the microstructure and the texture evolution of the AA3104 alloy processed by ECAP. *Archives of Metallurgy and Materials, 56*(2), 245-261.

Petch, N. J. (1953). The Cleavage Strength of Polycrystals. *Journal of Iron Steel Institute, 174*, 25-28.

Poole, W. J., Ashby, M. F., & Fleck, N. A. (1996). Micro-hardness of annealed and work-hardened copper polycrystals. *Scripta materialia, 34*(15), 559-564.

Prime, M. B., & Hill, M. R. (2002). Residual stress, stress relief, and inhomogeneity in aluminum plate. *Scripta materialia, 46*(1), 77-82.

Pu, Z. W., Caruso, S., Umbrello, D., Dillon, O., Puleo, D., & Jawahir, I. (2011). Analysis of surface integrity in dry and cryogenic machining of AZ31B Mg alloys. *Advanced Materials Research, 223*, 439-448.

Quang, P., Krishnaiah, A., Hong, S. I., & Kim, H. S. (2009). Coupled analysis of heat transfer and deformation in equal channel angular pressing of Al and steel. *Materials transactions, 50*(1), 40.

Raab, G., Soshnikova, E., & Valiev, R. (2004). Influence of temperature and hydrostatic pressure during equal-channel angular pressing on the microstructure of commercial-purity Ti. *Materials Science and Engineering: A, 387*, 674-677.

Raffel, M. (2007). *Particle image velocimetry: a practical guide*: Springer.

Ravichandran, G., Rosakis, A. J., Hodowany, J., & Rosakis, P. (2002). On the conversion of plastic work into heat during high-strain-rate deformation. *American Institute of Physics, Conference Proceedings, 620*.

Rees, D. (2012). *Basic Engineering Plasticity: An Introduction with Engineering and manufacturing* Butterworth-Heinemann.

Rice, J. R. (1971). Inelastic constitutive relations for solids: an internal-variable theory and its application to metal plasticity. *Journal of the Mechanics and Physics of Solids, 19*(6), 433-455.

Rollett, A., Humphreys, F. J., Rohrer, G. S., & Hatherly, M. (2004). *Recrystallization and related annealing phenomena*: Elsevier.

Rosochowski, A., Presz, W., Olejnik, L., & Richert, M. (2007). Micro-extrusion of ultra-fine grained aluminium. *The International Journal of Advanced Manufacturing Technology, 33*(1-2), 137-146.

Roters, F., Eisenlohr, P., Hantcherli, L., Tjahjanto, D., Bieler, T., & Raabe, D. (2010). Overview of constitutive laws, kinematics, homogenization and multiscale methods in crystal plasticity finite-element modeling: Theory, experiments, applications. *Acta Materialia, 58*(4), 1152-1211.

Sachs, G. (1928). Plasticity problems in metals. *Trans. Faraday Soc., 24*, 84-92.

Saotome, Y., & Iwazaki, H. (2001). Superplastic backward microextrusion of microparts for micro-electro-mechanical systems. *Journal of materials processing technology, 119*(1), 307-311.

Schmid, E., & Boas, W. Plasticity of Crystals (1968): London.

Sevier, M., Lee, S., Shankar, M. R., Yang, H. T., Chandrasekar, S., & Compton, W. D. (2006). *Deformation mechanics associated with formation of ultra-fine grained chips in machining.* Paper presented at the Materials Science Forum.

Shankar, M. R., Chandrasekar, S., King, A. H., & Compton, W. D. (2005). Microstructure and stability of nanocrystalline aluminum 6061 created by large strain machining. *Acta Materialia, 53*(18), 4781-4793.

Shekhar, S., Abolghashem, S., Basu, S., Cai, J., & Shankar, M. R. (2012). *Interactive Effects of Strain, Strain-Rate and Temperatures on Microstructure Evolution in High Rate Severe Plastic Deformation.* Paper presented at the Materials Science Forum.

Shekhar, S., Cai, J., Basu, S., Abolghasem, S., & Shankar, M. R. (2011). Effect of Strain-rate in Severe Plastic Deformation on Microstructure Refinement and Stored Energies. *Journal of Material Research, 26*, 395-406.

Shekhar, S., Cai, J., Wang, J., & Shankar, M. (2009). Multimodal ultrafine grain size distributions from severe plastic deformation at high strain rates. *Materials Science and Engineering: A, 527*(1), 187-191.

Shi, X., Pang, H., Zhang, X., Liu, Q., & Ying, M. (2004). In-situ micro-digital image speckle correlation technique for characterization of materials' properties and verification of numerical models. *Components and Packaging Technologies, IEEE Transactions on, 27*(4), 659-667.

Simof, J., & Hughes, T. (2008). Computational inelasticity.

Srinivasan, V., Radhakrishnan, S., Zhang, X., Subbarayan, G., Baughn, T., & Nguyen, L. (2005). *High resolution characterization of materials used in packages through digital image correlation.* Paper presented at the ASME 2005 Pacific Rim Technical Conference and Exhibition on Integration and Packaging of MEMS, NEMS, and Electronic Systems collocated with the ASME 2005 Heat Transfer Summer Conference.

Stoica, G., Fielden, D., McDaniels, R., Liu, Y., Huang, B., Liaw, P., . . . Langdon, T. (2005). An analysis of the shear zone for metals deformed by equal-channel angular processing. *Materials Science and Engineering: A, 410*, 239-242.

Stölken, J. S., & Evans, A. G. (1998). A microbend test method for measuring the plasticity length scale. *Acta Materialia, 46*, 5109-5115.

Taylor, G. I. (1934). The mechanism of plastic deformation of crystals. Part I. Theoretical. *Proceedings of the physics society of London A, 145*, 362-387.

Taylor, G. I. (1938). Analysis of plastic strain in a cubic crystal. *Stephen Timoshenko 60th Anniversary Volume*, 218-224.

Teoh, S. H., & Lee, K. H. (1991). *Fracture of Engineering Materials and Structures*. England: Elsevior Scinece Publishers LTD.

Thompson, A. W., Baskes, M. I., & Flanagan, W. F. (1973). The dependence of polycrystal work hardening on grain size. *Acta Materialia, 21*(7), 1017-1028.

Tiesler, N., & Engel, U. (2000). *Microforming- effects of miniaturization.* Paper presented at the 8 th International Conference on Metal Forming.

Valiev, R. Z., & Langdon, T. G. (2006). Principles of equal-channel angular pressing as a processing tool for grain refinement. *Progress in Materials Science, 51*(7), 881-981.

Vollertsen, F. (2008). Categories of size effects. *Production Engineering, 2*(4), 377-383.

Vollertsen, F., & Hu, Z. (2010). Analysis of punch velocity dependent process window in micro deep drawing. *Production Engineering, 4*(6), 553-559.

Vollertsen, F., Niehoff, H. S., & Hu, Z. (2006). State of the art in micro forming *Journal of Machine Tools and Manufacture, 46*(11), 1172.

W.L.Chan, Fu, M. W., & Yang, B. (2011). Study of size effect in micro-extrusion process of pure
copper. *Materials & Design, 32*(7), 3772–3782.

Wang, H., Wu, P., Tomé, C., & Huang, Y. (2010). A finite strain elastic–viscoplastic self-consistent model for polycrystalline materials. *Journal of the Mechanics and Physics of Solids, 58*(4), 594-612.

Wenk, H.-R. (2002). Texture and anisotropy. *Reviews in mineralogy and geochemistry, 51*(1), 291-329.

Wu, P. D., & Lloyd, D. J. (2004). Analysis of surface roughening in AA6111 automotive sheet. *Acta Materialia, 52*, 1785–1798.

Yen, Y. C., Jain, A., & Altan, T. (2004). A finite element analysis of orthogonal machining using different tool edge geometries. *Journal of Materials Processing Technology, 146*(1), 72–81.

Zehetbauer, M., Stüwe, H., Vorhauer, A., Schafler, E., & Kohout, J. (2003). The role of hydrostatic pressure in severe plastic deformation. *Advanced Engineering Materials, 5*(5), 330-337.

Zienkiewicz, O. a. G., PN. (1974). Flow of plastic and visco- plastic solids with special reference to extrusion and forming processes. *International Journal for Numerical Methods in Engineering, 8*, 1-16.